Cranfield University

Tom-Robin Teschner

A generalised multi-directional characteristic-based Godunov-type framework for elliptic, parabolic and hyperbolic pressure-based incompressible methods

School of Aerospace
Transport and Manufacturing
Centre for Computational Engineering Sciences

PhD Thesis

Academic Year: 2015 – 2018

Supervisor: László Könözsy
Associate Supervisor: Karl W. Jenkins
February, 2018

Cranfield University

School of Aerospace
Transport and Manufacturing
Centre for Computational Engineering Sciences

PhD Thesis

Academic Year: 2015 – 2018

Tom-Robin Teschner

A generalised multi-directional characteristic-based Godunov-type framework for elliptic, parabolic and hyperbolic pressure-based incompressible methods

Supervisor: László Könözsy
Associate Supervisor: Karl W. Jenkins

February, 2018

This thesis is submitted in partial fulfilment of the requirements for the degree of Doctor in Philosophy in Aerospace

Abstract

The objective of the current research is to construct numerical methods based on physical principles to reduce modelling errors in the field of computational fluid dynamics. In order to investigate the non-linearities of the convective flux term, a multi-directional characteristic-based scheme has been developed in this work to capture the anisotropic behaviour of the incompressible Navier–Stokes equations. To avoid the pressure-velocity decoupling and to promote stability at high Reynolds numbers, the Riemann problem has been incorporated into the scheme which creates a multi-directional Godunov-type framework. In order to capture the pressure correctly, which through its coupling to the velocity field is depending on the velocity's non-linear effects, it is postulated that the pressure should have its own transport equation which should have a parabolic type. This is necessary to align the pressure with the mathematical properties of the Navier–Stokes equations. Thus, a novel incompressible method has been developed which features a pressure transport equation which is referred to as the Fractional-Step with Velocity Projection (or FSVP) method. It is further extended through a perturbed continuity equation of the Artificial Compressibility (AC) method to hyperbolise the first Fractional-Step of the system of equations, while the second Fractional-Step retains the required parabolic behaviour, which is called the FSAC-VP method in turn. Through the hyperbolic Fractional-Step, the multi-directional Godunov-type framework is directly applicable to the newly developed method.

Parametric simulations for the lid driven cavity, backward facing step, sudden expansion and Taylor–Green vortex problem have been performed using the AC, FSVP, FSAC-VP and the Fractional-Step, Artificial Compressibility with Pressure Projection, or FSAC-PP, method. The FSVP and FSAC-VP method showed superior convergence properties compared to the AC method for unsteady flows, where a speed up of a factor up to 193.0 times has been observed. Since the parabolic pressure transport equation has a memory of the time history of the flow, smooth error curves have been produced over time while the other methods showed oscillatory profiles. Generally speaking, the most accurate results have been obtained with the FSAC-PP method, closely followed by the FSAC-VP and FSVP method. The inclusion of the multi-directional Godunov-type framework showed generally better or equally well resolved results compared to the benchmark numerical scheme for the FSAC-PP and FSAC-VP / FSVP method. Furthermore, the multi-directional scheme by itself showed its capabilities to predict vortical flows better than a simple numerical reconstruction scheme. The FSAC-VP method has shown a higher degree of scheme independence where velocity and pressure curves showed little variations compared to reference data. This was particularly pronounced for the sudden expansion which had consequences on the prediction of the correct bifurcation behaviour. Finally, it has been argued that what the numerical scheme development is to the non-linear term of the Navier–Stokes equations should be similarly done with incompressible flow method development to capture the correct pressure behaviour. This work shows that differences between elliptic, parabolic and hyperbolic pressure treatments do exist which can have a significant effect on the overall prediction of the flow features.

Acknowledgements

This work has been greatly affected by friends, supporters and Cranfield university staff members to whom I'd like to express my sincere gratitude. My work was positively influenced by the facilities and support I received where I would like to thank Emma Turner from the library and the IT support and HPC staff for providing me with advice and computational resources. I was greatly supported by Serena Slattery and Hayley Ferrier-Kerr for all non-academic and administrative related matters for which I am grateful. This work has been influenced by the anonymous reviewers of submitted conference and journal manuscripts to whom I am especially thankful. Their comments and insights have been incorporated into the writing of this Thesis which has improved the quality of the work.

I'd like to thank my former colleague Michael Kio for his invaluable guidance in the initial phase of my studies. I am thankful to my colleagues Harshavardhana Srinivasan for making me a chocoholic, Jamie Townsend for his discussions on PhD study related (and sometimes unrelated) topics and Soren Rasmussen for discovering the synth-pop musician within me. It all helped to balance my stress levels during the past three years.

I am grateful for the discussions and support I received from the members of the Computational Engineering Sciences Centre at Cranfield University for all their discussions, directions and support which helped me to widen my horizon and understand fluid mechanics from a new perspective. My deepest gratitude goes to my supervisors László Könözsy and Karl W. Jenkins who made a real difference in my overall experience as a PhD student. They gave me the right guidance and support when required but also enough freedom to explore, mould and shape this work based on my own findings. I am especially thankful for all those countless hours we spent discussing fluid mechanics, particle physics, mathematics and philosophy. Those discussions contributed substantially to the findings and developments found in this work.

Last but not least I'd like to express my sincere love and gratitude to Jiyoung Kim for her continuous support over the past years and to my parents Monica Teschner and Hans-Günther Teschner for their perpetual support, shelter and freedom who made me the person I am today.

Contents

List of Figures

List of Tables

List of Symbols

Latin Symbols

Symbol	Description	Units
a	Speed of Sound	[m s^{-1}]
$\mathbf{a}$	Acceleration	[m s^{-2}]
f	Characteristic Surface	[-]
f_τ, f_x, f_y	Characteristic Surface Components	[-]
$\mathbf{g}$	Gravitation	[m s^{-2}]
h	Characteristic Height	[m]
k	Kinetic Energy per Unit Mass	[m^2 s^{-2}]
m	Dimensions	[-]
$\mathbf{n}$	Unit Normal Vector	[-]
n_τ, n_x, n_y	Unit Normal Vector Components	[-]
p	Pressure	[N m^{-2}]
p_k	Rank of Characteristic Surface k	[-]
t	Time	[s]
Δt	Time-step, Real Time	[s]
$\mathbf{u}$	Velocity Vector	[-]
u, v	Velocity Vector Components	[m s^{-1}]
u^*, v^*	Intermediate Velocity Vector Components	[m s^{-1}]
$\Delta x, \Delta y$	Mesh spacing	[m]
$\mathbf{x}$	Coordinate Vector	[m]
x, y	Coordinate Vector Components	[m]

Symbol	Description	Units
A	Surface Area	[m^2]
$\mathcal{A}, \mathcal{B}, \mathcal{C}, \mathcal{T},$	Coefficient Matrices	[-]
$\mathcal{B}_j$	Preconditioning Vector	[-]
D	Artificial Dissipation	[m^2 s^{-1}]
DX	Difference in reattachment lengths	[m]
$\mathbf{F}(\mathbf{U})$	Inviscid Flux Vector / Force Vector	[-]
$\mathbf{I}$	Identity Matrix	[-]
J	Jacobian	[-]
L	Characteristic Length	[m]
L_0, L_1	Error Norms	[-]
$\vec{N}$	Normal Vector	[-]
$\mathbf{Q}$	Primitive Variable Vector	[-]
R	Specific Gas Constant	[J kg^{-1} K^{-1}]
S	Characteristic Height	[m]
S^+	Signal Velocities	[m s^{-1}]
T	Temperature	[K]
V	Volume	[m^3]
X_{r1}, X_{r2}	Reattachment length	[m]

Greek Symbols

Symbol	Description	Units
β	Convergence Parameter	[-]
ε	Convergence Threshold	[-]
λ	Eigenvalue	[-]
λ_{max}	Maximum Signal Velocity	[m s^{-1}]
μ	Dynamic Viscosity	[Pa s]
ν	Kinematic Viscosity	[m^2 s^{-1}]
ν_{num}	Numerical Dissipation	[m^2 s^{-1}]
ξ, η	Curve-linear Coordinates	[-]
$\xi_x, \xi_y, \eta_x, \eta_y$	Metric Coefficient	[-]
$\tilde{\xi}$	Characteristic Interval	[-]
$\dot{\xi}$	Characteristic Speed	[s^{-1}]
ρ	Density	[kg m^{-3}]
σ	Shear Stresses	[Pa]
τ	Pseudo-time / Viscous Stress Tensor	[-]
$\Delta\tau$	Time-step, Pseudo Time	[s]
ϕ	Generic Flow Variable	[-]
Λ	Spectral Radius of Flux Jacobian	[-]
Φ	Extensive Flow Variable	[-]
Ψ	Characteristic Stream or Wave Surface	[-]

List of Abbreviations

AC	Artificial Compressibility
AD	Artificial Dissipation
CB	Characteristic-based
CBS	Characteristic-based Split
CFD	Computational Fluid Dynamics
CFL	Courant Friedrichs Levy (number)
DNS	Direct Numerical Simulation
ENO	Essentially non-Oscillatory
FS	Fractional-Step
FS-PP	Fractional-Step, Pressure Projection (method)
FSAC-PP	Fractional-Step, Artificial Compressibility (method) with Pressure Projection
FSAC-PP	Fractional-Step, Artificial Compressibility (method) with Velocity Projection
FSVP	Fractional-Step, Velocity Projection (method)
GCI	Grid Convergence Index
HLL	Harten, Lax, van-Leer (Riemann Solver)
HLLC	Harten, Lax, van-Leer, Contact (Riemann Solver)
HPC	High-performance Computing
ILES	Implicit Large Eddy Simulation
LES	Large Eddy Simulation

MCB	Multi-directional Characteristic-based (scheme)
MOC	Method of Characteristics
MUSCL	Monotonic Upwind Scheme for Conservation Laws
ODE	Ordinary Differential Equation
PDE	Partial Differential Equation
PP	Pressure Projection
RANS	Reynolds-Averaged Navier–Stokes
RHS	Right-hand Side
RP	Riemann Problem
RS	Riemann Solver
SCB	Single-directional Characteristic-based (scheme)
SIMPLE	Semi-Implicit Method for Pressure Linked Equations
TV	Total Variation
TVD	Total Variation Diminishing
WENO	Weighted Essentially non-Oscillatory

Chapter 1

Introduction

1.1 Motivation with a Historical Perspective

The Navier–Stokes equations govern the behaviour of fluid dynamics on a macro scale. The underlying equations — conserving mass, momentum and energy — can be equally used for compressible and incompressible, as well as laminar and turbulent flows. With modifications, the equations can be extended, for example, to treat hypersonic, multiphase and multiphysics flows. Fluid dynamic research was limited to theoretical and experimental studies until the 1950s and 1960s when the transistor and computer revolution made computational resources available to solve the Navier–Stokes equations numerically. It soon became apparent that computer-based simulations would supplement theoretical and experimental investigations and research on numerical methods commenced.
At first, numerical simulations used simplistic finite-difference schemes of first-order in both space and time which were, however, too dissipative. Numerical scheme development was initially focused on creating robust numerical schemes of second-order, which were easy to implement and thus required only a moderate increase in computational time. The Lax–Friedrich scheme [1] was one of the first proposed schemes which used second-order in space and time for its approximation of the convective flux term. Later, the Lax–Wendroff scheme [2] was introduced where time derivatives were expressed as space derivatives which were re-introduced into the equations through the Taylor-series. This resulted in a second-order scheme and its robustness meant that it is still in use nowadays. These two schemes, probably the two most prominent schemes of its era, kick-started the development of second-order schemes around the 1960s and a certain belief prevailed in the CFD community that second-order schemes are mandatory to escape the highly dissipative nature of first-order schemes. At the same time, Sergei Godunov presented a vastly different approach which was put forward in his dissertation in 1959 [3]. Instead of making the scheme of higher-order, Godunov accepted the dissipative but conservative properties of first order schemes and, in the context of the finite-volume method, provided a high-resolution approach to reconstruct the primitive variables at cell interfaces. Godunov realised that the numerical discontinuity at the cell interfaces represented essentially a Riemann problem and so he used an exact Riemann solver to reconcile the two left- and right-states at the cell interface which resulted from

the interpolation procedure. Godunov did not trust his work enough to continue working on it. He might have been discouraged to some degree by the almost religious belief in second-order schemes where his first-order approach may have not seemed to fit in. However, Godunov stated that all schemes which have an order higher than one, are necessarily non-conservative. This presented a problem for discontinues flows, where shock wave capturing was difficult to capture accurately with the schemes available at that time. An array of schemes were proposed with different dissipative and dispersive error behaviours to circumvent these issues and dominated the research for the coming two decades. An excellent review of classical schemes is given by Hoffmann [4], where the interested reader may find more information.

Fast forward to 1974, the young scientist and prodigy by the name of Amiram Harten just graduated from the Courant Institute at the New York University under the supervision of Peter Lax. Harten would become know as one of the single most important figures in the numerical scheme developments community whose methods are still widely used today and are the de-facto industrial standard. Harten continued as a research scientist at the Courant institute before moving back as a senior lecture to his home town in Tel Aviv in 1977. Here, he continued his work on shock wave capturing schemes and introduced the monotonic upwind scheme for conservation laws (MUSCL) [5] in 1983 which showed favourable conservative properties. A scheme specific constant can be set in such a way that the scheme yields a fully upwind (first- or second-order) or a polynomial reconstruction of third-order. This allowed the same scheme to be operated near discontinuities through upwinding, or as a high-resolution scheme in smooth regions. Furthermore, Harten also introduced the notion of total variation diminishing (TVD), a property a scheme is said to have if its total variation (TV) does not grow but rather decays over time. The classical numerical schemes, which are reviewed by Hoffmann [4], all possess some form of dispersive error near discontinuities, which for some schemes is increasing over time. Those schemes are not TVD, and thus are prone to divergence. Harten introduced the TVD approach through so called limiters, which ensured that even discontinuous signals would not introduce any spurious oscillations. In this approach, limiters would be switched on in discontinuous regions which results in a first-order reconstruction scheme. Thus, even the third-order MUSCL scheme could be used to capture shock waves. The TVD approach meant that Godunov's theorem — that only first-order schemes are conservative — could be extended to second-order schemes as well. Near discontinuities the scheme reverts back to first-order through the limiter, however, sufficiently far away a higher-order of the solution could be guaranteed. For more information on TVD schemes, the reader is referred to the book of Versteeg and Malalasekera [6].

In the same year, Harten, together with Lax and van Leer, proposed a new Riemann solver which became known after the initials of the Authors; the HLL Riemann solver [7]. By this time, Godunov's research on using Riemann solvers instead of sophisticated numerical schemes was accepted knowledge and Harten, among other researchers, proposed new ways of extending and improving Godunov's original idea. By now, high-resolution schemes, like the MUSCL approach, could be paired with new sophisticated Riemann solvers, like the HLL, and the results showed a remark-

able achievement in the field of compressible flows. Discontinuous signals could now be captured to a high degree of accuracy without introducing spurious oscillations. Harten came up with yet another approach to treat discontinuous data and introduced the essentially non-oscillatory (ENO) schemes [8], where different stencils were used to reconstruct inter-cell fluxes of which the smoothest stencil would be used as the final flux. The ENO approach did find an overwhelming acceptance and usage after its introduction and it did not take long before the scheme was fundamentally revised. Seven years after its original introduction, Liu [9] realised that the order of the scheme could be increased by using a weighted combination of all stencils for the final reconstructed value. This scheme became known as the weighted essentially non-oscillatory, or WENO, scheme and is nowadays the most popular scheme for compressible flows when it comes to shock wave capturing schemes.
Around the same time, in 1981, Jameson *et al.* [10] revived the second-order scheme development through their central scheme with artificial dissipation. Although being fundamentally different from the approach pursued by Harten and co-workers, this scheme had a right on its own and started the development of a new class of schemes. To understand the importance of their simplistic but powerful scheme, we need to introduce yet another important figure in the field of fluid dynamics. In 1930, one year after graduating with a PhD from the Moscow State University, Andrey Kolmogorov, a mathematician by choice, went to Germany to work among people like Richard Courant and Edmund Landau on probabilistic systems. Here he was working on random processes under the influence of diffusion. He became a professor at the Moscow State University where he focused on turbulent flows during the second world war. In 1941 [11], he published the mechanism of the energy cascade in turbulent flows which is one of the few accepted universal laws of turbulent flows. Here, Kolmogorov stated that all turbulent kinetic energy is dissipated at the smallest scales. Later, Kolmogorov would define what those smallest scales are which we now know as the Kolmogorov microscales. For the current discussion, all that we are concerned with is that dissipation is a process associated with the smallest scale in the flow. Back to the 1980s, computational resources were scarce and even two dimensional flows challenging to simulate. Thus, the computational grids were by far not able to resolve the smallest scales in the flow and thus the dissipative process was not captured correctly. For laminar flows, this did not cause any issues, however, in turbulent flows, this meant that an imbalance of turbulent kinetic energy production and dissipation was created. While Harten and co-workers tried to remove the dissipative and dispersive errors from the scheme, which is a sensible approach for compressible and high Reynolds number flows where the viscosity and thus dissipation plays a decreasing role, Jameson *et al.* re-introduced the unfavourable dissipative nature of numerical schemes through numerical dissipation. This dissipation turned out to be of the order of the physical dissipation which could not be modelled due to the coarse mesh restrictions. Their scheme, however, had the shortcoming that it required user-defined closure coefficients which controlled the amount of dissipation added to the solution. In theory, the scheme would need to be fine-tuned for each new flow scenario, however, it was found that a set of closure coefficients was applicable to a wide range of flows which made the scheme popular, especially for incompressible flows. This approach turned out to

be very similar to the Reynolds-averaged Navier–Stokes (RANS) approach, where the neglected turbulent dissipation is modelled through the Reynolds stress tensor, which in turn is obtained through transport equations for model specific turbulent transport properties. Essentially, the dissipation is locally computed using a RANS approach while the central scheme with artificial dissipation is defining the strength of the dissipation globally which is then locally scaled by the velocity gradient. The scheme was furthermore simple to implement and thus computational inexpensive while being directly applicable to implicit methods which meant that it too celebrated widespread acceptance and use. More importantly, with the introduction of this scheme, a new view was spread that numerical dissipation is not always a negative side-effect of numerical schemes but a necessity to match the physical dissipation that would otherwise be lost due to the computational mesh. This view would later be used to justify implicit large eddy simulations (ILES), where unlike in traditional LES, the sub-grid scales would be modelled through the numerical dissipation and not by a sub-grid scale model.

The numerical scheme development described above saw a parallel development of a numerical procedure known as the method of characteristics, which had been employed long before the Navier–Stokes equations were integrated numerically. The method of characteristics is applicable to any set of ordinary and partial differential equations and sometimes attributed to the great Italian mathematician Joseph-Louis Lagrange. Historical evidence suggests, however, that it was the less known French mathematician Paul Charpit who presented the method first to the Académie on June the 30th, 1784 [12, 13]. In 1963, around the time when the Lax–Friedrich and Lax–Wendroff scheme enjoyed their widespread use, Viktor Vladimirovich Rusanov [14] presented a generalised derivation of the method of characteristics for the Euler equation and showed how the method can be transformed into a characteristic-based (CB) scheme that is equally applicable to the Euler equations with very little extra implementation effort compared to the competing numerical schemes at the time. The scheme required a hyperbolic system of equations which limited its use to the compressible form of the Navier–Stokes or Euler equations. However, the added complexity introduced physical features into the scheme based on the local eigenstructure of the system of equations. This gave the scheme a competitive advantage over the purely mathematical schemes, although its complexity also meant that it found little use in the numerical scheme development community. Initial development improved aspects of the CB scheme which eventually faded until the focus was purely on numerical schemes based on mathematical properties. In 1994 the CB scheme experienced a renaissance and renewed interest when Drikakis *et al.* [15] introduced the CB scheme for incompressible flows based on the Artificial Compressibility (AC) approach of Chorin [16], which was introduced in 1967 as a purely hyperbolic method for incompressible flows. In their scheme, Drkikakis *et al.* realised that all CB schemes to date were lacking the so called transportiveness property, which would usually be guaranteed through an upwinding procedure. In order to provide the transportiveness, i.e. taking the direction of the flow into account, they proposed their scheme together with a Riemann solver to provide the necessary upwinding based on the local eigenvalues. In this way, a relative simple

numerical interpolation scheme could be used to provide input values for their CB scheme which then produced values that did not violate the transportiveness and conservativeness properties. Here, a numerical scheme is said to contain the transportiveness property if it respects the direction of the flow and uses upwind cells for its interpolation (i.e. it can differentiate between upwind and downwind cells). A scheme can further be conservative if the overall flux in the domain, through all cells, is conserved. The development by Harten and co-workers was the opposite, they proposed to make those properties part of the numerical interpolation scheme. Thus, by the end of the 20^{th} century, researchers were faced with two possible and viable routes to treat the convective flux term. Either, use a high-resolution scheme that would take care of any numerical dissipative and dispersive errors or, to use a more physical approach through a CB scheme combined with a Riemann solver to make traditional properties linked to numerical schemes part of the CB framework. Due to its simplicity, it is easy to understand that the former approach still prevails in the current numerical scheme landscape but further numerical insight is required to advance the CB scheme development to capture complex physical situations. The CB scheme introduced by Drikakis *et al.* [15] was based on characteristic lines which were considered in the Taylor-series expansion in space and time. Due to this approach, it is also termed the single-directional CB, or SCB, scheme, as it only features a single direction in its derivation. In order to apply it to a higher dimensional space, the scheme is simply aligned with each normal direction which results in an isotropic characteristic treatment. Fluid dynamics, and especially complex turbulent flows, are highly anisotropic. Thus, to capture those aspects correctly, an anisotropic CB scheme is required. This has been introduced by Razavi *et al.* [17] in 2008 for the AC method and we refer to it as the multi-direction CB, or MCB, scheme. Their scheme was fundamentally different, not just in the sense that it was multi-directional, but also in the sense that it lacked the transportiveness and even conservative properties of the SCB scheme. Thus, in order to use the MCB scheme it was necessary to use a more sophisticated numerical interpolation scheme while the SCB scheme could be operated using relative simplistic reconstruction approaches. Therefore, one of the aims of this project is to generate a multi-directional CB scheme including the Riemann problem to provide a robust numerical framework to capture the non-linear behaviour correctly where a single-directional approach could fail or perform worse. It will be highlighted in the following how this aim was achieved and its applicability will be shown through various numerical experiments.

Before proceeding, we need to first look at the different methods that are available to treat incompressible flows. It is often said that an adiabatic flow through a pipe or channel cannot be solved with the compressible Navier–Stokes equations. The argumentation is that, in a constant density and constant temperature flow the pressure could not change, although a pressure gradient exists in such a flow. The argumentation is flawed by the fact that no flow has a constant temperature and constant density. From a theoretical point of view, a solution could still be obtained with the stiff system of equations, the computational cost would be, however, demanding for even such a simple flow. Thus, a series of numerical procedures have been proposed for the solution of incompressible flow methods, of which Chorin

was among the first to introduce his AC method [16] in 1967. Here, the continuity equation retains the density derivative which is exchanged for a pressure time derivative. In absence of a working equation of state approach for incompressible flows, the functional relation between the density and pressure is not known and thus the time derivative becomes non-physical. In the limit of a steady state flow, however, the time derivative vanishes and a correct pressure field is obtained. Only a year later, Chorin introduced the notion of the Pressure Projection (PP) [18] method which was later mathematically proven by Temam [19]. The PP method is based on the Helmholtz-Hodge decomposition which enforces a divergence free velocity field. Through a fractional step procedure, a Poisson equation for the pressure can be constructed which provides the pressure and in turn can be used to calculate the velocity field. Both methods are classical and accepted methods in the field of computational fluid dynamics (CFD) and were supplemented by Patankar and Spalding [20] in 1972 who introduced an approximate PP concept which they termed the semi-implicit method for pressure linked equations, or SIMPLE. Here, a simplified momentum equation provides an intermediate velocity field which then can be used to update the pressure. The pressure is then inserted into the continuity equation through an appropriate transformation to iteratively solve for the updated velocity field. The SIMPLE algorithm and its derivatives are the most commonly used methods in the CFD community, however, they are known to have rather slow convergence properties for the pressure and thus require a substantial amount of computational resources. At the same time, the PP method of Chorin requires a substantial amount of Poisson iterations which converges slowly, especially close to Reynolds numbers that are approaching zero [21, 22]. In-fact, it can be shown that the continuity equation of the SIMPLE algorithm can be reduced to a Poisson equation where the only difference to the PP method is the implicit treatment of the convective term and the simplified momentum equation, while in the PP method the pressure is treated implicitly. Since the 1970s, there was little to no effort to improve upon this situation. Improvements to the methods themselves were proposed which, however, may have at best only improved the methods for specific flow scenarios. In 2014, Könözsy [21] proposed a unification of Chorin's AC and PP method which coupled both the hyperbolic properties of the AC method with the elliptic features of the PP method. It was termed the fractional-step, artificial compressibility with pressure projection (FSAC-PP) method and it showed reduced computational times for low Reynolds number flows but also showed a certain invariance towards numerical schemes; low- and high-resolution schemes alike produced a similar level of accuracy where the other methods (AC, PP and SIMPLE) showed a high dependence of the accuracy on the numerical interpolations schemes. It was argued that the Poisson solver introduced a physical smoothing property into the scheme which accelerated the flow but at the same time stabilised the pressure field. Other methods to stabilise the pressure or velocity field included methods of artificial dissipation, for example the central scheme of Jameson *et al.* [10]; the development of the FSAC-PP method showed that once again the properties once linked to numerical schemes can now be thought of properties of the incompressible flow method, in this case, the accuracy and stability.

Under those considerations, it is worth to examine the current state of the art of

incompressible methods. Considering that the design of incompressible algorithms can affect the stability and accuracy, it would appear logical to use a physical rather than numerical closure approximation. The AC method is an artificially constructed method that is not based on any physical considerations. The PP method is based on a mathematically rigorous framework which does align with physical properties of incompressible flows. However, the purely elliptic behaviour — albeit favourable for stability and convergence acceleration — has no physical justification as purely elliptic equations can only exist for steady state flows. The SIMPLE algorithm may be regarded as an approximate pressure projection algorithm and thus suffers from similar shortcomings as Chorin's PP method. The FSAC-PP method has shown favourable properties over the AC and PP method [21, 22], it does however still feature the pseudo time derivative and elliptic Poisson solver. It is important to highlight that from a numerical point of view, all these methods have a right to exist. They are based on numerical, and sometimes physical, assumptions to form an incompressible method. Speaking from a strictly physical point of view, however, there are some shortcomings which this Thesis aims at provide answers to, at least in parts. This will be discussed in Section 1.2.

This short historical perspective of numerical scheme and incompressible method development was aimed at highlighting one recurring theme, that the classical numerical properties associated to numerical schemes can be incorporated into characteristic frameworks and even into the incompressible flow method. The advantage is that it provides a robust environment where relative simplistic interpolation schemes can be used to reduce modelling errors. CFD research has focused, as discussed above, at providing numerical schemes capable of capturing the correct flow physics for specific flow applications. This has led to the belief in the CFD community, that higher-order schemes are necessary to capture complex flow physics correctly. Through the numerical examples provided in this Thesis, it will be shown that the incompressible method itself can have a significant influence on the accuracy and performance. Coupled with a sophisticated multi-directional Godunov-type characteristic-based scheme, a framework to tackle complex physical problems of anisotropic nature is presented in the following.

1.2 Aims and Objectives

Section 1.1 highlighted the need to focus on CB methods in order to introduce physical properties into the scheme. Although a MCB scheme has already been proposed in the literature, it lacked some of the favourable properties of the SCB scheme due to the missing Riemann solver. The first aim is to develop a generalised MCB scheme that can be used with any incompressible flow solver, as long as it is hyperbolic. In a second stage, the MCB scheme needs to be supplemented with an approximate Riemann solver to provide transportiveness and conservativeness. This by itself provides a multi-directional Godunov-type framework which is capable of predicting anisotropic flow features where a single-directional approach may fail. The success of the CB scheme, as for any other numerical interpolation scheme, is measured by how well it captures the non-linear behaviour of a given flow scenario.

The development of numerical schemes has thus focused on the non-linear term while the rest of the equation was interpolated using simple numerical schemes. As we have discussed above, the success of capturing the non-linear behaviour is not just scheme, but also method dependent. The introduced numerical methods for incompressible flows are all based to some degree on mathematical constraints and considerations. In this Thesis, a novel incompressible flow method is proposed that is derived from first principles which focuses on providing a correct pressure field. From the presented methods, the mathematical behaviour of the system of equations is either purely hyperbolic (AC method), purely elliptic (PP and SIMPLE method) or a mix of hyperbolic and elliptic (FSAC-PP method). From observations an argument can be made that the pressure should in reality have an parabolic behaviour in the limit of incompressible flows. Furthermore, while we have transport equations for velocity, density, temperature, turbulent quantities and species, we do not have an independent pressure transport equation which means that the pressure is following the flow. However, it is the pressure which is inducing flow and so the pressure should be able to develop according to its own, parabolic transport equation from which the velocity and the other transport properties follow. The development of such a transport equation and its according method will be shown in Section 3.3.4. To summarise, the aims of the Thesis are as follows:

1. The development of a generalised multi-directional characteristic-based scheme for incompressible flow, applicable to any hyperbolic system of equations.

2. The pairing of the multi-directional characteristic-based scheme with an approximate Riemann solver to extend the method to a multi-directional Godunov-type framework.

3. The evaluation of the proposed scheme for different flow scenarios using low dissipative numerical schemes.

4. The development of a parabolic transport equation for the pressure with a corresponding novel incompressible method.

The objectives by which the above aims are to be achieved are given bellow as

1. The development of a 2D Navier–Stokes solver for cartesian grids, capable of running the channel, lid driven cavity, backward facing step, sudden expansion flow cases and other multi-block domains.

2. Derivation of a generalised multi-directional characteristic-based scheme for any incompressible hyperbolic system of equations.

3. Derivation of a pressure transport equation from physical considerations and implementation into the 2D Navier–Stokes solver to test its performance.

4. Conducting a parametric study for various benchmark cases for different Riemann solvers and characteristic-based scheme combinations to judge their influence on the overall accuracy and convergence rate using different incompressible methods.

1.3 Contributions to the Scientific Knowledge

The contribution to the scientific knowledge may be summarised as follows:

1. Development of a general and rigorous mathematical framework for the multi-directional characteristic-based scheme for any hyperbolic incompressible system of equations.

2. Extension of the multi-directional characteristic-based scheme to include the local Riemann problem to introduce the property of transportiveness and conservativeness into the scheme.

3. Extension of the multi-directional characteristic-based scheme to unsteady flows through a dual time stepping procedure.

4. Development of a novel (FSAC-VP), three stage algorithm based on a velocity projection concept whose mathematical properties are based on statistical mechanics considerations.

5. Application of the multi-directional characteristic-based scheme to the FSAC-PP and FSAC-VP method.

6. In depth analysis of the multi-directional characteristic-based scheme to standard test cases. This has already been done in the literature but the presented results were either contaminated by obvious implementation errors and/or strongly biased in favour of the multi-directional characteristic-based scheme over the reference data. A fair comparison has shown similar trends on a global scale while the scheme itself may not always be as strong as originally claimed when it was introduced.

1.4 List of Publications

1. Tom-Robin Teschner, László Könözsy, Karl W. Jenkins, “Progress in particle-based multiscale and hybrid methods for flow applications”, Microfluidics and Nanofluidics, Vol. 20(4), pp. 1–38, 2016

2. Tom-Robin Teschner, László Könözsy, Karl W. Jenkins, “Numerical investigation of an incompressible flow over a backward facing step using a unified fractional-step, artificial compressibility and pressure projection (FSAC-PP) method”, MultiScience - XXX. microCAD, Miskolc, Hungary, 21–22 April 2016

3. Tamás István Józsa, Máté Szőke, Tom-Robin Teschner, László Könözsy , Irene Moulitsas, “Validation and verification of a 2D lattice Boltzmann solver for incompressible fluid flows”, VII European Congress on Computational Methods in Applied Sciences and Engineering, Crete Island, Greece, 5–10 June 2016

4. Vaios Lappas, Antonios Tsourdos, Panagiotis Tsoutsanis, Tom-Robin Teschner, László Könözsy, Stavros Kindilydes, "Lunar In-situ thermal regolith storage and power generation using thermoelectric generators", Acta Astronautica, (under review)

5. Kori Smith, Tom-Robin Teschner, László Könözsy, "On approximate Riemann Solvers within the unified fractional-step, Artificial Compressibility and Pressure Projection method", MultiScience - XXXI. microCAD, Miskolc, Hungary, 20–21 April 2017

6. Tom-Robin Teschner, László Könözsy, Karl W. Jenkins, "A three-stage algorithm for solving incompressible flow problems", MultiScience - XXXI. microCAD, Miskolc, Hungary, 20–21 April 2017

7. Tom-Robin Teschner, László Könözsy, Karl W. Jenkins, "On Godunov-type multi-directional characteristic-based schemes for hyperbolic incompressible flow solvers", IV Eccomas Young Investigator Conference, Milan, Italy, 13–15 September, 2017

8. Tom-Robin Teschner, László Könözsy, Karl W. Jenkins, "A generalised and low-dissipative multi-directional characteristic-based scheme for incompressible flows in conjunction with approximate Riemann solvers", Computer Physics Communications, (under review)

9. Tom-Robin Teschner, László Könözsy, Karl W. Jenkins, "Predicting Non-Linear Flow Phenomena Through Different Characteristics-based Schemes", Special Issue in "Computational Aerodynamic Modeling of Aerospace Vehicles", (under review)

10. Antonio Figueroa-González, José Oliveira, Tom-Robin Teschner, László Könözsy, Irene Moulitsas, Karl W. Jenkins, "Validation of an in-house lattice Boltzmann solver for multiphase flow applications", 7th European Conference on Computational Fluid Dynamics, Glasgow, UK, 11–15 June, 2018

1.5 Thesis Structure

The remaining structure of this Thesis is as follows. In Chapter 2, the literature dealing with the single- and multi-directional characteristic-based scheme is reviewed. Furthermore, Riemann solvers applied to incompressible flows are also reviewed along with advancement in the field of incompressible method development.

In Chapter 3, the governing equations for an incompressible flow are derived. It is shown how to mathematically classify a system of equations consisting of first-order partial differential equations so as to determine the behaviour of the Navier–Stokes equations and the incompressible flow methods that are used to solve them. The Chapter closes with a description of different incompressible flow methods, including the new Fractional-Step with Velocity Projection (FSVP) and Fractional-Step, Artificial Compressibility with Velocity Projection (FSAC-VP) method.

In Chapter 4, the characteristic-based scheme is reviewed for the single-directional version found in the literature and a full derivation is given for the multi-directional characteristic-based (MCB) scheme. The derivation is shown for the Artificial Compressibility (AC) method but is generalised so as to be applicable to any hyperbolic incompressible flow method discussed in this work. The Riemann problem is reviewed next and its solution discussed in the form of approximate Riemann solvers in the context of incompressible flows. A multi-directional closure is given for the Riemann problem to make it multi-directional in a geometrical sense to be compatible with the multi-directional characteristic-based scheme.

In Chapter 5, numerical considerations are given for the discretisation procedure. First, the finite volume method is reviewed and it is shown how derivatives are approximated for the chosen data-structure. Boundary conditions are reviewed and explained next, followed by a description of the numerical schemes that are used, both in space and time.

In Chapter 6, the results are shown for different flow scenarios to test different aspects of the characteristic-based schemes and the newly developed incompressible methods. Classical numerical schemes and incompressible methods are used as a benchmark to assess the performance of the newly proposed schemes and methods.

Chapter 7 provides a concluding discussion on the results and summarises the overall work. Potential extensions to the newly developed schemes and methods are listed at the end.

Chapter 2

Literature Review

The following discussion is intended to highlight the current development of characteristic-based schemes from a historical perspective and its current use for incompressible flows. The literature dealing with the Riemann problem is reviewed and supplemented by a discussion on incompressible methods. The current gap in the knowledge is highlighted at the end of each section.

2.1 Method of Characteristics for Incompressible Flows

Around 1950, the first publications appeared that were using the method of characteristics in a computational sense applied to fluid dynamics. In 1963, Rusanov [14] provided a generalised theory which was applicable to the compressible Euler equations. More importantly, Rusanov showed that only a mix of compatibility equations along different characteristic surfaces would sufficiently constrain the system and put the characteristic-based scheme into a rigorous mathematical framework. The CB scheme is different from the method of characteristic in that it is applicable to a computational grid and does not require the unit process [23], a process in which characteristic lines are intersected and used to update the primitive variables at the intersection. Rather, the characteristic lines, or surfaces, intersect with the computational grid and thus the primitive variables are updated where grid lines intersect. The same locations are used in finite-difference calculations so that the method can be directly implemented in the finite-difference framework. There are, however, different ways to intersect the characteristics with the grid, a process which is known as characteristic networks. For example, characteristics can propagate from the current time level to the next (a forward network) or from the future time level the past (a backward network). Some research was dedicated in optimising those networks of which an excellent review can be found in the work of Zucrow and Hoffman [24] and Delaney [25]. A comparative study of different characteristic networks was conducted by Cline and Hoffman [26], where advantages and disadvantages were highlighted. Ransom *et al.* [27] focused on a second-order accurate network and showed its applicability by investigating a source and Prandtl-Meyer expansion flow.

One of the first applications of the method of characteristics for the Euler equation can be found in Ferrari [28], who in 1949 investigated the interference of wing-body configurations. The initial development was limited to simple shapes and so Chushkin and Katskova [29], as well as Rakich and Cleary [30] were investigating the flow around generic bodies of revolution that features blunt noses. An upgrade to the method was presented by Sauerwein [31], who presented a characteristic-based scheme capable of handling magnetic fields, chemical reactions, non-equilibrium and multi-component flows. Cline and Hoffman [32] also used a chemical reactive CB scheme approach and showed that their three-dimensional approach resolved the cross-flow behaviour better than a quasi three-dimensional method. In 1974, Hoffman [33] investigated the thrust misalignment in thrust vector controlled nozzles using a three-dimensional characteristic approach while Delaney and Kavanagh [34] focused on a turbine cascade two years later. This marked the peak time for the CB scheme but a change in the numerical scheme development was about to happen with the work of Harten and co-workers. Marcum and Hoffman [35] continued to investigated simple flows through nozzles with a resolved transient behaviour in 1985, however, by now the MUSCL scheme and HLL Riemann solver were introduced. The focused shifted towards Godunov-type methods and the interest in CB schemes declined. The review provided by Roe [36] — although titled "Characteristic-based schemes for the Euler equations" — focused on the already more popular Godunov-type approaches. It is important to highlight that the Riemann problem shares many similarities to the method of characteristic. Thus, it is indeed sensible to talk about a characteristic approach when dealing with Godunov-type methods, however, the CB scheme as debated by Roe was not the same as Rusanov's CB scheme [14].
An excellent primer on the CB scheme for the Euler equations can be found in the books of Zucrow and Hoffman [24, 37], which may be supplemented by the work of Delaney [25], Sauerwein [38] and Rusanov [14].

While the Godunov-type scheme development captivated the compressible flow community, Drikakis *et al.* [15] realised that with the hyperbolic nature of the AC method of Chorin [16], the CB scheme — and in general Godunov-type methods — could be also used in the context of incompressible flows. They introduced the CB scheme based on the derivations of Eberle [39], who proposed a different approach to treat the characteristics in the compressible framework. In their approach, the CB scheme was derived for a one dimensional flow and then subsequently applied to each direction of the governing equations. Two-dimensional flows over a circular arc-cascade and backward facing step were considered. This approach effectively made it a single-directional approach under which it has become known in the literature. Drikakis [40] extended the original SCB scheme to handle three-dimensional flows while comparing the performance of shared and distributed parallelisation strategies. Further extension to assess the CB scheme in conjunction with a full multigrid, full approximation storage (FMG-FAS) was done by Drikakis *et al.* [41]. Despite the hyperbolic nature of the AC method, for which multigrid methods — originally developed for elliptic systems — are prone to lose their favourable convergence acceleration properties, they reported a speed-up orders of magnitudes higher, compared to a solution obtained without a multigrid. It should be mentioned that the original

SCB scheme has received some criticism in the literature. Neofytou [42] revised the original derivation given in [15] and pointed out some mathematical inconsistencies and more importantly stated that the derivation of the compatibility equation has been done in an incorrect manner. In fact, while the original derivation was less mathematical stringent, allowing for more degrees of freedom, Neofytou showed that the coefficient arising in the derivation of the compatibility equations are interdependent and the compatibility condition is not satisfied "regardless of the values of the coefficients" [15, p. 673]. Neofytou derived a consistent set of compatibility conditions which were then compared with the original compatibility equations by Su *et al.* [43]. They concluded that, although a mathematical difference exists between both formulations, numerical results and convergence rates where almost identical. Furthermore, they concluded that the compatibility equations in [15] were not derived inconsistently, rather, simplifications have been introduced which have shown to reduce the mathematical complexity while still retaining the favourable convergence and accuracy properties.

Tai and Zhao [44] implemented the SCB scheme into a two-dimensional unstructured solver using a multigrid and further used a message passing interface approach to parallelise their solver in a single program, multiple data fashion. In their first study, they applied their solver to the flow around a circular cylinder which Tai *et al.* [45] extended to a three-dimensional approach in which they investigated the lid driven cavity. They further refined their parallelisation strategy using a combined shared / distributed memory hierarchy. Tai *et al.* [46] further modified their solver to incorporate matrix-free implicit time marching in their solver for arbitrary CFL numbers and introduced the notion of the immersed object method [47], similar to the immersed boundary method. Here, arbitrarily shaped objects can be placed inside the domain while the immersed object procedure assures that the velocity inside the object is at rest, effectively making it a solid body. Further tests were performed for three-dimensional flows around a circular cylinder. For all cases considered, including their previous work, they showed good agreement with reference data and the applicability of the SCB scheme to these flows in a complex solver environment.

Zhao and Zhang [48] presented an implementation of the SCB scheme into an unstructured, three-dimensional solver were they computed the flow around single and multiple cylinders as well as the flow over a backward facing step. They stressed that a first-order upwind method is not sufficient to capture the upper recirculation area and that higher-order schemes were needed, in conjunction with the SCB scheme, to accurately capture vortical structures, here using an upwind scheme of third-order.

Shapiro and Drikakis [49, 50] further extended the original method to include also variable density flows. Their derivation presented three distinct formulations which, in the limit of a constant density flow, recovered the original system of equations in a different form. The implementation of a multigrid procedure was described and the new formulations applied to simple test cases.

A new form of the compatibility equation was derived by Abdollah *et al.* [51], where an improved prediction of the characteristic speed gave a higher-order version of the original SCB scheme. They applied their version to the lid driven cavity and backward facing step problem and showed the increase in accuracy compared with

the SCB scheme of Drikakis [15].

Soon after the introduction of the SCB scheme, researchers have tried to include multi-directional effects as well into the derivation for a more physical description of the flow. Atashbar Orang [52] included multi-directional information propagation in his CB scheme, still based on the original single-directional approach, and applied it to the flow around a circular cylinder and NACA 0012 aerofoil as well as the flow over a backward facing step. Furthermore, the calculations were done using the Spalart–Allmaras turbulence model and thus a turbulent version of the SCB scheme was solved. However, strictly speaking, the single-directional behaviour was still inherent to the derivation.
Razavi *et al.* [17] and Zamzamian and Razavi [53] introduced the first fully multi-directional CB, or MCB, scheme for incompressible flows in the AC framework. Their derivation was based on the fully compressible, multi-directional scheme as found in the classical literature [14, 24, 25, 37, 38, 54]. Here, the governing equations of the AC method are multiplied by a characteristic surface and no assumption about the direction is made, i.e. the governing equations are not split as in the version of Drikakis *et al.* [15]. The compatibility equations are then derived along the characteristic surface and solved in a similar fashion as the SCB scheme. After the introduction of the MCB scheme, it found little interest in the field of hyperbolic, incompressible flow methods and further investigations did not surface. Only recently, a renewed interest by the original research group has sparked a series of publications, extending the original method along with investigations on more application in conjunction with their MCB scheme. Hashemi and Zamzamian [55] introduced a new set of far-field boundary conditions for incompressible flows, where the compatibility equation was used from the MCB scheme to devise an equation for the open boundary. Following up on their work, Zamzamian and Hashemi [56] further enhanced the solid boundary treatment by introducing ghost-cells at the boundaries, which were populated by extrapolation, according to the prescribed Neumann or Dirichlet boundary condition. Fathollahi and Zamzamian [57] included further characteristic surfaces to derive twice as many compatibility equations compared to the standard multi-directional version. However, they found that the accuracy of the solution did not improve but the convergence rate was favourably affected. Hashemi and Zamzamian [58] showed the extension of the MCB scheme to unstructured grids and tested it on the flow past a circular cylinder. Barar and Razavi also investigated the cylinder and further the lid driven cavity and gave considerations to extend the multi-directional scheme to three dimensions. As will be shown in Section 4.1.2, once the compatibility equations are found for the primitive variables, the set of equations is over constrained, i.e. more compatibility equations than primitive variables are found and the pressure is usually taken as an arithmetic mean over all characteristics. Fathollahi and Zamzamian [57] were faced with the same issue and thus no increase in accuracy was found when more compatibility equations were used and averages of the primitive variables along different characteristics were taken. Razavi and Hanifi [59] derived an explicit version for the pressure equation from the continuity equation and applied it to the flow over parallel flat plates, backward facing step and the lid driven cavity at high Reynolds

numbers. They further used the Spalart–Allmaras model to treat the turbulent effects at high Reynolds numbers. To further investigate non-isothermal flows, Razavi and Adibi [60] included the temperature equation to investigate forced convection between parallel flat plates as well as forced and mixed convection in a lid driven cavity flow. Using different Reynolds, Grashof and Prandtl numbers, they gave an parametric overview for the aforementioned flow cases. Finally, Atashbar Orang *et al.* [61] used the Spalart–Allmaras turbulence model to investigate the flow around a cylinder at high Reynolds numbers. They concluded that the MCB scheme produced superior accuracy, convergence rate and stability when compared to reference data or simulations. However, they also mentioned the use of local time stepping and residual smoothing as accelerating techniques. The problem is that it is not clear where the speed-up in convergence and possibly the stability is coming from. The investigations mentioned above showed similar convergence plots but were sparse on the information given as to how these were obtained, i.e. no acceleration techniques were mentioned and it has to be assumed none were used. The controversy is further fuelled by inconsistent comparisons as for example found in Razavi *et al.* [17] where different, maximum allowable CFL numbers were computed for both the single and MCB scheme but it is not clear from the text if in-fact those were also used to define the time-step In that case, both solutions would essentially march with different time-steps towards a steady state solution which cannot be used for a fair comparison of the two schemes.

There has been a third development of CB-based schemes which has emerged in the field of finite element methods. Zienkiewicz and Codina [62] and Zienkiewicz *et al.* [63] introduced the characteristic-based split (CBS) method in which a three step algorithm updates the primitive variables along the characteristics. In the first step, an intermediate velocity field is predicted and used to obtain either the pressure or density from the continuity equation. The third step updates the velocity field. This process has high resemblances to the PP method, where the pressure is decoupled from the continuity equation through a fractional step (FS), or "splitting" procedure and solved via a Poisson equation. Hence, the name characteristic-based split. The second step of the procedure can either solve for the pressure or density which further unifies compressible and incompressible flows, i.e. their algorithm is invariant to the Mach number. There has been some development within the CBS framework but only a few will be highlighted, as the fundamental approach is different from that employed throughout the rest of this work and thus only the idea is conveyed. Nithiarasu [64] investigated several incompressible flow test cases using the CBS scheme. Specifically, the method was applied to the lid driven cavity, the backward facing step, the flow past a circular cylinder and an ellipsoid-like shape in a stokes flow regime. It was further extended to handle non-isothermal flows by Nithiarasu *et al.* [65] and applied to a flow past an array of cylinders (2D) and spheres (3D). Nithiarasu and Liu [66] further investigated the effects of turbulence and compared the Wolfstein, Spalart–Allmaras and k-ϵ model for the same test cases as in [64]. They further investigated the flow in an upper human airway to demonstrate the applicability of the method to complex geometries. Malan and Lewis [67] further investigated the CBS scheme and tested it against a cylindrical vessel filled with

randomly packed graphite spheres to simulate porous media flows for which experimental was available and showed excellent agreement.

From the above given literature review on the CB scheme for incompressible flows, there has been a recurring theme. All published literature, except concerned with the CBS scheme, were using the AC method for the incompressible CB scheme. Based on the argumentation given in the previous Chapter, the incompressible flow method does make a difference when computing the flow. Some authors argued that higher-order schemes were necessary to capture some flow features which could not be resolved with a lower-order scheme. Since the FSAC-PP method has shown a weak invariance of the numerical scheme on the accuracy. A natural extension would be to use the CB scheme with the aforementioned method. The FSAC-PP method has been originally introduced with the SCB scheme and no extension to the multi-directional scheme has been proposed yet. Thus, one of the aims of the current Thesis is to fill this gap and combine the favourable properties of the MCB scheme with those of the FSAC-PP method. However, at the same time, the comparisons done with the MCB scheme were not always done in a strict scientific manner, where results that were compared were not obtained in the same way. A fair comparison between non CB and CB treatments is necessary which is provided in the following for all test cases. Furthermore, the transportiveness and conservativeness property of the SCB scheme is missing through the application of a Riemann solver. This property can either be supplied by the numerical interpolation scheme, or, be introduced into the MCB framework through the usage of an approximate Riemann solver. Those gaps in the knowledge align with the aims of this Thesis and changes are proposed accordingly in the following Chapters.

2.2 Riemann Solvers for Incompressible Flows

Not many authors tried to solve the Riemann problem (RP) in fluid mechanics before Godunov [3] introduced his framework. Godunov used and exact Riemann solver to solve the Euler equations and the application of RS remained exclusive to the field of compressible flows for decades to come. Rusanov introduced a novel scheme in 1961 [68] to capture shock waves. It was later shown that the HLL RS would result in Rusanov's scheme if the propagation speed were all equal. Further research on RS in conjunction with fluid mechanics stalled and experienced a regain in interested two decades later. Roe [69] introduced a Riemann solver well known in the modern literature, where he linearised the Jacobian (obtained through the chain rule of the inviscid flux vector) for which he then postulated four conditions (which he referred to as "Property U" for uniform), according to which an exact solution to the approximation could be obtained and the physical wave speeds were included in the Jacobian through the solution of the RP. Harten *et al.* [7] provided yet another RS in which approximations for different states according to the eigenvalues were given. It is named after the authors initials and known as the HLL RS. Toro *et al.* [70] later introduced the missing state for the contact surface in the HLL RS and it has become known as the HLLC RS. Toro [71] later popularised exact and approximate RS while Drikakis and Rider [72] summarised extensions to

incompressible flows. Saurel *et al.* [73] investigated both exact and approximate RS and concluded that exact RS provided the highest accuracy but also the highest computational time. Approximate RS were said to have less accuracy but provided much faster computations.

While the RP and its corresponding RS had arrived and were fully accepted in the compressible community, incompressible methods did not see RS applied to their governing equations for another decade. Around the same time when the SCB scheme was introduced into the hyperbolic AC method, first developments took place which saw the inclusion of a RS to incompressible flows. Roger and David [74] introduced Roe's RS into the incompressible framework and applied it to the flow around a NACA 0012 aerofoil. Their investigation was concerned with finding an optimum relaxation factor for their implicit lower-upper / approximate-factorisation (LU/AF) time integration procedure. Other authors adopted the same RS for their studies. Sheng *et al.* [75] investigated the flow around a simplified submarine configuration for various angles of attack and drift. The authors stressed that their multigrid implementation showed favourable convergence rates. Aiming *et al.* [76] used the Baldwin–Barth turbulence model to investigate the flow around micro air vehicle configurations for different aspect ratios and camber of the wing in the pre-stall flow regime. Furthermore, surface flow structures were presented for the parameter space explored. Azhdarzad and Razavi [77] investigated the standard lid driven cavity and flow past a cylinder to validate Roe's RS for standard incompressible test cases. Good agreement with reference data was found. Wang and Wang [78] studied various test cases applicable to ocean engineering, where they investigated the interaction of paired and parallel cylinders entering water, the slamming of a ship hull geometry into water and the entering of a lifted payload, operated from a ship. Where possible, they compared their results against calculations from a boundary element method and showed good agreement, however, while the reference solution produced smooth solutions, the inclusion of the RS allowed small-scale fluctuations to be resolved. Extending their work, Wang *et al.* [79] further investigated the entrance of a wedge into water while studying the overall energy transformation and conversion of the fluid-wedge system. Lee and Lee [80] compare a preconditioned version of the compressible Navier–Stokes equations with the modified AC method of Turkel, using Roe's approximate RS for the inviscid flux part. They applied their solver to the flow over a backward facing step, a turbulent bump and a NACA 0012 aerofoil including Menter's k-ω SST two-equation turbulence model. Their investigation showed that the modified AC method performed best in terms of convergence rate, closely followed by the standard AC method. The preconditioned version of the Navier–Stokes equations did not converge for all cases. However, where it did converge, its convergence rate was the least favourable among the different methods tested. Lee and Lee [81] further investigated the flow around a flat plate and cylinder in the turbulent regime and investigated the added relaxation parameter in the modified AC version of Turkel and its effect on the convergence rate. While numerical discontinuities naturally exist at the interface of control volumes, physical discontinuities enter the solution in multiphase flows where the application of a RS is further of great interest. Ma *et al.* [82] investigated the Rayleigh-Taylor instability and the

breaking of a water column inside a tank and used a detached eddy simulation for the turbulent side of the calculation. Stokos further extended the AC method with Roe's RS to non-isothermal flows and investigated the differentially heated squared and cubic cavity, internally heated cavity and mixed convection past a cylinder.

The application of Roe's RS prevailed in the field of incompressible flows. It took some time until the HLLC RS made its first appearance in the incompressible flow regime. In 2009, Niu *et al.* [83] developed an AC solver using the HLLC RS for the convective fluxes and validated it against the lid driven cavity flow and the oscillatory flat plate flow. They further applied it to a human aorta to simulate Newtonian blood flow, to simplify the procedure. However, initial results revealed cross flow patterns and vortical structures which were to be expected. Mandal *et al.* [84] investigated a channel flow with changing cross section elements over time for which the Arbitrary Lagrangian-Eulerian formulation was used. They further extended their investigation to treat non-isothermal flows [85] where they investigated the differentially heated, rotating cavity flow. Mandal and Sonawane [86] also investigated the heat transfer inside a CANDU-6 nuclear reactor in which they investigated the effect of different inlet velocities and the location and angle of the moderator inlet diffusers on the heat transfer rate. Qian and Lee [87] investigated the flow past a cylinder, over a flat plate and around a S809 aerofoil and later [88] also included the flow through a 90 degree curved square duct. Taylor *et al.* [89] used a variety of non-isothermal test cases, including a heated flat plate and natural, mixed and turbulent convection inside a squared cavity. Following their validation test cases, they applied their approach to a more complex engineering test cases, here the two-phase ribbed tubulator. For the available experimental data they were able to match the results with high accuracy.

The application of the HLLC and Roe's RS have dominated the incompressible regime but some authors embarked on a different route which will be discussed briefly below. Golay and Hulley [90] showed the application of an exact version of a Riemann solver applied to incompressible flows through a preconditioned low Mach number corrected version of the Euler equations. A multiphase flow test case, in the form of wave breaking in shallow water, was presented. The equation of state was modified for their specific purposes and can be regarded as an empirical version for wave breaking flows, where the speed of sound was fixed. Two different versions of the equation of state were presented for isothermal and non-isothermal flows. This approach was further extended by Sambe *et al.* [91, 92] where macro roughness elements were added to the seabed and different parameters of those roughness elements were explored. Further extension to three-dimensional flows were also presented and showed that impact, splash-up and rebounds can be strongly impaired by designing the roughness elements accordingly. Hyams *et al.* [93] used a Rusanov-like flux treatment to investigate the flow around a class-8 truck where they investigated several drag reduction devices and showed their effect on the fuel efficiency. Li *et al.* [94] highlight the need for a low dissipative and dispersive scheme for Implicit Large Eddy Simulations. In order to keep the dissipation low, they applied the minimum dispersion and controllable dissipation scheme for the calculation of the

reconstructed variables and used a simple low-dissipation AUSM Riemann solver for the convective fluxes. They used a compressible version of the Navier–Stokes equations applied to low Mach number flows and tested their solver for the Taylor-Green vortex problem where good agreement with DNS and experimental data was given.

The literature presented above showed that the Roe and HLLC RS found most usage among researchers in the incompressible flow community. Roe's RS is based on a linearised system and thus not a prime candidate for studying the non-linear effects of the Navier–Stokes equations. The HLLC RS, and therefore the HLL RS as well, do not linearise the system and thus would be a natural choice to be used in conjunction with incompressible flows. Smith *et al.* [95] showed, however, that the application of the HLL and HLLC RS to the FSAC-PP method is problematic due to the absence of a pressure gradient in the momentum equation. Furthermore, all RS are strictly speaking only applicable to one dimensional flows. They are extended to higher dimensions in much the same way the SCB scheme is extended to higher dimensions. The RS of Rusanov found little application in the context of incompressible flows. In-fact, San and Kara [96] showed a comparison between different RS and stated that the Rusanov's RS is rather dissipative. In the context of high Reynolds and Mach number flows, the dissipative nature may be of little interest as the importance of dissipation scales with the inverse of the Reynolds number. For incompressible flows, especially for low Reynolds numbers, dissipation regains importance and numerical dissipation through a numerical scheme or RS may even be seen as a favourable approach where coarse computational grids are used. Thus, the Rusanov RS does provide a relative simple scheme whose dissipation can be used in conjunction with low-dissipative interpolation schemes. It is, however, also single-directional in nature. Balsara *et al.* [97–99] showed how RS can be extended to a multi-directional RS and for a truly multi-directional framework the same approach should be adopted. In this Thesis, however, we supply the multi-directional features through the use of the MCB scheme and only make use of the Rusanov RS to access its favourable transportiveness and conservativeness properties. It could be argued that this does not promote a truly multi-directional framework. Nonetheless, we argue that the multi-directional feature is provided through the MCB scheme and the that no further physical insight would be added through a multi-directional RS. Thus, we propose a simple geometrical extension to the Rusanov RS, which is equally applicable to the HLL and HLLC RS, to make it compatible with the MCB scheme.

2.3 Numerical Methods for Incompressible Flows

The discussion of the development of incompressible flow methods will be limited to those based on the original AC or PP method introduced by Chorin [16, 18]. Developments based on the SIMPLE (Patankar and Spalding [20], later popularised by Patankar [100]), or SIMPLE-like methods (such as the popular derivative, the PISO scheme, of Issa *et al.* [101]) are not considered. There are several reasons to prefer the classical AC and PP method over SIMPLE-like schemes. Most importantly, the AC and PP methods are both non-linear whereas the SIMPLE algorithm

has to linearise the convective flux term due to its semi-implicit nature. Secondly, its elliptic nature does not allow the application of the method of characteristics to the convective term (strictly speaking this is also true for the PP method, however, the unification of the AC and PP method in the FSAC-PP method does allow the characteristic treatment to be introduced into the PP framework).
A thorough review of various PP formulations is given by Guermond *et al.* [102], where the available formulations have been further classified into pressure projection, velocity correction and consistent splitting methods and a comparative table has highlighted advantages and disadvantages of each method. Bell *et al.* [103, 104] attempted to introduce the Godunov framework into the PP method. They first made use of slope-limited reconstructed values at the cell interface and in a second step used upwinding to make a decision about the incoming flow direction. From a theoretical point of view, upwinding can be regarded as a solution to the Riemann problem, however, the Riemann problem itself is not solved, rather, the most physical value is chosen. Thus, it can be regarded as a semi Godunov-type procedure. Furthermore, their terminology of "characteristic extrapolation" is simply a second-order Taylor series approximation. It needs to be pointed out, however, that at the time of publishing, the method of characteristics had not yet been introduced into the incompressible framework and their terminology was based on previous works of other authors. In an effort to unify the incompressible with the compressible framework, Xiao [105] presented a novel procedure in which the compressible Euler equations were used as the basis. Expanding the convective part using the product rule, the incompressible effects were included by deriving a Poisson equation for one of the terms through thermodynamic considerations. Subsequent tests on a one-dimensional shock tube showed first the applicability of the method to compressible flows, in which the incompressible terms vanished from the governing equations. Later tests done by Xiao *et al.* [106] showed the compressible, cylindrical explosion and implosion test case as well as the incompressible flow inside a lid driven cavity. For all test cases, results agreed well with reference data. The method requires a staggered grid arrangement for its integration procedure which has limited its applicability to more complex cases. A similar development has been undertaken by Turkel [107] who used the AC formulation as the foundation and further added a pseudo time derivative of the pressure to the momentum equations. These time derivatives were supplied with a further convergence parameter and were multiplied with the velocity. The coupling of pressure and velocity acted as a preconditioner and convergence could be accelerated. No results were presented, however, later investigations showed the favourable convergence properties predicted by Turkel, see [72].
Tang and Sotiropoulos [108] developed the so called FSAC method in which the idea of the pressure projection method is retained by using a fractional step procedure. In the first fractional step, the pressure from the previous time-step is employed while at the second fractional step, the pressure at the next time level is used via a fully implicit procedure. The equations of the second fractional step are compatible with the implicit formulation of the AC method, hence the name FSAC. Compared to the standard AC method and applied to the oscillating lid driven cavity flow, flow in a corner, 2D decaying vortex problem and the flow around a circular cylinder,

it was shown to be 30% to 60% more efficient than the AC method. The speed-up was attributed to the inclusion of the first fractional step where an intermediate velocity is predicted. This method was an important development as it showed that a combination of methods may speed-up the solution significantly. This idea was further extended by Könözsy [109] and Könözsy and Drikakis [21] where the AC method was unified with the PP method into a single framework. In the first fractional step, the perturbed continuity equation of the AC method is used to predict an intermediate pressure field. The momentum equation is consistent with the PP method, where the pressure gradient term is dropped. In the second fractional step, a Poisson equation is derived in which the predicted pressure from the continuity equation is used as an initial guessed pressure field. Since the pressure is not only obtained through the Poisson equation, but also from the continuity equation, the Poisson solver does not need to iterate until the pressure field has converged as in the original PP method. Thus, a significant speed-up can be obtained by partially solving the Poisson solver (typically of the order of ten iterations). The intermediate velocity obtained in the first fractional step is then updated with the new pressure to complete the procedure. The so called FSAC-PP method did not just unify the AC and PP method, but also their mathematical properties. From the AC method, the hyperbolic nature was retained which allows to treat the convective fluxes through a characteristic-based scheme and also the application of a Riemann solver which makes the FSAC-PP method an incompressible Godunov procedure. Furthermore, the elliptic features of the PP method introduced smoothing of the pressure field and thus speed-up and stability of the solution. It was shown that the interaction of these methods allowed the FSAC-PP method to be used for much lower Reynolds number than the AC or PP method alone [21, 109] which made the FSAC-PP method a prime candidate for microflow applications in the Stokes regime. Further results were presented by Könözsy and Drikakis [110] for a multi-species, variable density flow in a Y channel. Könözsy *et al.* [22] included a novel acoustic model into the FSAC-PP method and simulated the trapping and positioning of cryogenic propellants via acoustic liquid manipulation and compared it with their experiments. Such a procedure is found in space applications where low temperatures prevail. Using the vortex-pairing problem, the FSAC-PP method was compared against a compressible Navier-Stokes solver using a low Mach number correction. The investigation showed that the FSAC-PP method performs equally well with lower and higher-order of reconstruction scheme, where the results showed little difference, even when changing the mesh size. These findings are consistent with previous findings [21, 109]. Secondly, the numerical dissipation was found to be almost non-existing for higher order schemes which compared favourable to the compressible solver. However, acoustic fluctuations were not captured by the incompressible solver by default. The method has been further investigated for separated flows by Teschner *et al.* [111], where the separation length of a backward facing step geometry was used to compare the FSAC-PP method against the AC method using first and third-order reconstruction schemes. The results showed a general faster convergence rate for the FSAC-PP method and the reattachment point was in close agreement for both methods, compared to experimental data.

Following the idea of Chorin's AC and PP method, there has been little development to improve current incompressible flow solvers. As stated previously, SIMPLE-like procedures are dropped from the discussion as these are based on linearisation. Furthermore, they do not try to incorporate a physical foundation into the governing equations. Due to the mixed hyperbolic and elliptic features of the incompressible version of the Navier–Stokes equations, the FSAC-PP method is the first of its kind to match the expected mathematical behaviour (i.e. both hyperbolic and elliptic features of both the AC and PP method are incorporated into a single framework). This is a collective behaviour of the system but no consideration is given to the pressure, for which in general no transport equation is available. In Section 3.3.4, the expected behaviour of the pressure is derived from kinetic gas theory considerations. It will be shown that the expected mathematical behaviour of the pressure alone should be parabolic and thus a parabolic transport equation for the pressure is needed. Indeed it is the pressure which causes most of the troubles for incompressible flow calculations and it should be regarded with high scepticism that all primitive variables plus transported scalar and vector quantities have their own transport equation while the pressure has to be either obtained through the equation of state (for compressible flows) or through a numerical procedure (incompressible flows) which does not need to represent the physical behaviour of the pressure.

Therefore, along with the introduction of a physical multi-directional Godunov-type CB scheme to capture the non-linear term in the Navier–Stokes equations, a first attempt is made to construct a parabolic pressure transport equation to solve incompressible flows. The details will be given in the following Chapters.

Chapter 3

The Navier–Stokes Equations for Incompressible Flows

In this Chapter, the governing equations for an incompressible flow are derived from the most basic conservation laws. The derivation is followed by a generalised procedure to mathematically characterise the governing equations as hyperbolic, parabolic and elliptic and numerical methods to solve the governing equations are presented at the end.

3.1 Derivation of the Incompressible Navier–Stokes Equations

Before we can derive the full Navier–Stokes equations, we need to first investigate how a flow property evolves over time. For this, we consider a volume V which is depicted for some time t in Figure 3.1. At time t, we have $V(t) = V_0$ but after some time $t + \Delta t$ the control volume can change to $V_0 + \Delta V$. Consider an extensive flow property Φ which is conserved within the control volume. We can state that it changes according to

$$\Phi = \int_V \phi \mathrm{d}V. \tag{3.1.1}$$

It follows from Eq.(3.1.1) that ϕ is the density of Φ. If we consider Φ to be mass, then ϕ becomes the density of the fluid referred to as ρ. If Φ represents the impulse, than ϕ becomes the impulse density $\rho\mathbf{u}$. This will become important when we derive the

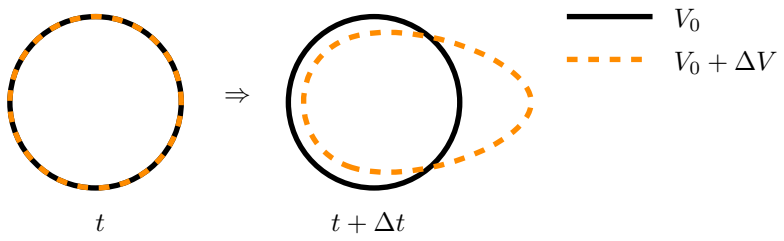

Figure 3.1: Evolution of an arbitrary control volume over time.

conservation laws for fluid mechanics. We are further interested in how Φ changes over time so that we can write

$$\frac{\mathrm{d}\Phi(t)}{\mathrm{d}t} = \frac{\mathrm{d}}{\mathrm{d}t}\int_{V(t)} \phi \mathrm{d}V. \tag{3.1.2}$$

We are not able to carry out the integration directly as we do not know how $V(t)$ evolves in time. Therefore, we consider the integral when $\Delta t \to 0$ so that we have

$$\frac{\mathrm{d}\Phi(t)}{\mathrm{d}t} = \lim_{\Delta t\to 0}\frac{1}{\Delta t}\left\{\int_{V_0+\Delta V} \phi(t+\Delta t)\mathrm{d}V - \int_{V_0}\phi(t)\mathrm{d}V\right\}, \tag{3.1.3}$$

which can be rearranged to give

$$\frac{\mathrm{d}\Phi(t)}{\mathrm{d}t} = \lim_{\Delta t\to 0}\frac{1}{\Delta t}\left\{\int_{V_0} \left[\phi(t+\Delta t) - \phi(t)\right]\mathrm{d}V + \int_{\Delta V}\phi(t+\Delta t)\mathrm{d}V\right\}. \tag{3.1.4}$$

We can use a Taylor-series expansion for $\phi(t+\Delta t)$ about $t+\Delta t$ for which we have

$$\phi(t+\Delta t) = \phi(t) + \frac{\partial \phi}{\partial t}\frac{\Delta t}{1!} + \mathcal{O}(\Delta t)^2. \tag{3.1.5}$$

Inserting Eq.(3.1.5) into Eq.(3.1.4) and rearranging the terms yields

$$\frac{\mathrm{d}\Phi(t)}{\mathrm{d}t} = \int_{V_0}\lim_{\Delta t\to 0}\frac{\phi(t+\Delta t)-\phi(t)}{\Delta t}\mathrm{d}V + \lim_{\Delta t\to 0}\frac{1}{\Delta t}\int_{\Delta V}\left[\phi(t) + \frac{\partial\phi}{\partial t}\frac{\Delta t}{1!} + \mathcal{O}(\Delta t)^3\right]\mathrm{d}V. \tag{3.1.6}$$

The first term in Eq.(3.1.6) becomes the time derivative for a vanishing Δt while all terms including Δt vanish for the second term. Thus, the equation can be rewritten as

$$\frac{\mathrm{d}\Phi(t)}{\mathrm{d}t} = \int_{V_0}\frac{\partial\phi(t)}{\partial t}\mathrm{d}V + \lim_{\Delta t\to 0}\frac{1}{\Delta t}\int_{\Delta V}\phi(t)\mathrm{d}V. \tag{3.1.7}$$

The volume can be transformed as

$$\mathrm{d}V = \mathrm{d}A\cdot\mathbf{u}\mathrm{d}t, \tag{3.1.8}$$

where A is a surface area and $\mathbf{u}$ to local velocity vector. Inserting Eq.(3.1.8) into Eq.(3.1.7) yields

$$\frac{\mathrm{d}\Phi(t)}{\mathrm{d}t} = \int_{V_0}\frac{\partial\phi(t)}{\partial t}\mathrm{d}V + \int_A \phi\mathbf{u}\mathrm{d}A. \tag{3.1.9}$$

Using Gauss' Theorem, we can rewrite Eq.(3.1.9) as

$$\frac{\mathrm{d}\Phi(t)}{\mathrm{d}t} = \int_{V_0}\frac{\partial\phi(t)}{\partial t}\mathrm{d}V + \int_V \nabla\cdot\phi\mathbf{u}\mathrm{d}V. \tag{3.1.10}$$

Both forms of the equation are known as the Reynolds transport theorem and are presented in integral form. A differential form can be obtained by requiring that the volume vanishes so that for $V\to 0$ we obtain from Eq.(3.1.10)

$$\frac{\mathrm{d}\Phi(t)}{\mathrm{d}t} = \frac{\partial\phi(t)}{\partial t} + \nabla\cdot\phi\mathbf{u}. \tag{3.1.11}$$

The conservation of mass is now found by setting Φ to be the mass. Since mass is conserved its time derivative is equal to zero. Furthermore, we already saw that the corresponding relation of ϕ is the flow density so that we can write

$$0 = \frac{\partial\rho}{\partial t} + \nabla\cdot(\rho\mathbf{u}). \tag{3.1.12}$$

For incompressible flows, we further require that the density does not change. From this constraint it follows that the time derivative of the density is zero and since ρ is constant, we can divide the remaining equation by it so that we finally end up with

$$\nabla\cdot\mathbf{u} = 0. \tag{3.1.13}$$

Eq.(3.1.13) represents the conservation of mass, or continuity equation, for an incompressible flow.

The conservation of momentum is derived from Newton's second law which is given as

$$\mathbf{F} = m\mathbf{a}, \tag{3.1.14}$$

where $\mathbf{F}$ is the sum of the internal and external forces acting on the system and $\mathbf{a}$ the acceleration. Cauchy stated that the rate of change of shear stresses (σ) acting upon a fluid control surface represents the internal forces for a fluid. The external forces can be regarded as gravitational ($\mathbf{g}$) or body forces ($\mathbf{f}_{body}$). Thus, the force vector becomes

$$\mathbf{F} = \mathbf{F}_{internal} + \mathbf{F}_{gravity} + \mathbf{F}_{body} = \int_V \nabla\cdot\sigma\mathrm{d}V + \int_V \rho\mathbf{g}\mathrm{d}V + \frac{1}{V}\int_V \rho\mathbf{f}_{body}\mathrm{d}V. \tag{3.1.15}$$

The right-hand side of Eq.(3.1.14) can be integrated over a control volume to give

$$\int_V m\mathbf{a}\mathrm{d}V = \int_V \frac{\partial\rho\mathbf{u}}{\partial t}\mathrm{d}V. \tag{3.1.16}$$

Inserting Eq.(3.1.15) and Eq.(3.1.16) into Eq.(3.1.14) and applying Reynold's Transport Theorem to the right-hand side of Eq.(3.1.16), to allow the system to evolve over time, results in

$$\int_V \frac{\partial\rho\mathbf{u}}{\partial t}\mathrm{d}V + \rho\int_V (\mathbf{u}\cdot\nabla)\mathbf{u}\mathrm{d}V = \int_V \nabla\cdot\sigma\mathrm{d}V + \int_V \rho\mathbf{g}\mathrm{d}V + \frac{1}{V}\int_V \rho\mathbf{f}_{body}\mathrm{d}V. \tag{3.1.17}$$

We can neglect the gravitational and body forces as they only have a minor influence and carry out the integration over all control volumes to get

$$\frac{\partial\rho\mathbf{u}}{\partial t} + \rho(\mathbf{u}\cdot\nabla)\mathbf{u} = \nabla\cdot\sigma. \tag{3.1.18}$$

This is a simplified form of Cauchy's momentum equation but generally used for the study of fluid dynamics. For a frictionless fluid where $\sigma = -p\mathbf{I}$, the Euler equations are recovered where p is the hydrodynamic pressure and $\mathbf{I}$ is the identity matrix. Those equations were long accepted in the 19^{th} century but the role of friction was not properly understood. Louis Marie Henri Navier, Jean Claude Barre de Saint-Venant and George Gabriel Stokes all presented different approaches to extend Euler's equations to be applicable to any fluid. In his 1822 paper titled "Memoire sur les lois du mouvement des fluides", Navier presented his hypothesis about diffusion to the Académie des Sciences in Paris which was published five years later. His work was based on molecular considerations and Anderson [112, p.12] highlighted that "Navier's equations were of the correct form, his theoretical reasoning was greatly flawed, and it is almost a fluke that he obtained the correct terms". It was not until the year 1843, seven years after the death of Navier, that Saint-Venant re-derived Navier's hypothesis from a macroscopic point of view, completely ignoring the molecular considerations given by Navier. Around the same time, in 1845, Stokes published his hypothesis on diffusion in his paper titled "On the Theories of the Internal Friction of Fluids in Motion, and of the Equilibrium and Motion of Elastic Solids". Stokes was unaware of the work of Navier or Saint-Venant. Despite the more rigorous derivation given by Saint-Venant, the equations became known as the Navier–Stokes equations. The assumption of all three authors can be reduced to the viscous stress tensor τ. The total stress tensor is augmented by the viscous stress tensor which now reads

$$\sigma = -p\mathbf{I} + \tau. \tag{3.1.19}$$

The hypothesis of Navier, Saint-Venant and Stokes in turn is given as

$$\tau = \mu[\nabla\mathbf{u} + (\nabla\mathbf{u})^T] - \frac{2}{3}\mu(\nabla\cdot\mathbf{u}). \tag{3.1.20}$$

Taking the derivative of Eq.(3.1.20), the following result is obtained

$$\nabla\cdot\tau = \mu[\nabla\cdot\nabla\mathbf{u} + \nabla(\nabla\cdot\mathbf{u})] + \frac{1}{3}\mu\nabla(\nabla\cdot\mathbf{u}). \tag{3.1.21}$$

The terms containing $\nabla\cdot\mathbf{u}$ are equal to zero for an incompressible flow due to the continuity equation, Eq.(3.1.13). Thus, the final term for the viscous fluid is reduced to

$$\nabla\cdot\tau = \mu\nabla^2\mathbf{u}. \tag{3.1.22}$$

Inserting Eq.(3.1.19) into Eq.(3.1.18) using Eq.(3.1.22) and dividing by the density, the following equation results

$$\frac{\partial\mathbf{u}}{\partial t} + (\mathbf{u}\cdot\nabla)\mathbf{u} = -\frac{1}{\rho}\nabla p + \nu\nabla^2\mathbf{u}, \tag{3.1.23}$$

where $\nu = \mu/\rho$ is the kinematic viscosity. This is the conservation of momentum, or Navier–Stokes, equation. Eq.(3.1.13) and Eq.(3.1.23) combined are the governing equations of an incompressible flow and sometimes also referred to as conservation laws.

3.2 Classification of the Governing Equations of Incompressible Flows

Before the Navier–Stokes equations can be solved numerically, it is important to first classify the equations according to their mathematical properties. These properties have a real physical meaning and consequence in the way incompressible methods treat their primitive variables. We lay the foundation here to classify any system of equations to help the argumentation later made on the physical properties of the pressure.

3.2.1 Time Independent Flow (Steady State)

The Navier–Stokes equations, as derived in Section 3.1, are governing incompressible flows. By setting the time derivatives to zero, one obtains the time independent from of the Navier–Stokes equations, which are

$$\nabla \cdot \mathbf{u} = 0, \tag{3.2.1}$$

$$(\mathbf{u} \cdot \nabla)\mathbf{u} = -\frac{1}{\rho}\nabla p + \nu \nabla^2 \mathbf{u}. \tag{3.2.2}$$

Expanding Eq.(3.2.1) and Eq.(3.2.2) into a scalar representation, we have for a two-dimensional case

$$\frac{\partial u}{\partial x} + \frac{\partial v}{\partial y} = 0, \tag{3.2.3}$$

$$u\frac{\partial u}{\partial x} + v\frac{\partial u}{\partial y} = -\frac{1}{\rho}\frac{\partial p}{\partial x} + \nu\frac{\partial^2 u}{\partial x^2} + \nu\frac{\partial^2 u}{\partial y^2}, \tag{3.2.4}$$

$$u\frac{\partial v}{\partial x} + v\frac{\partial v}{\partial y} = -\frac{1}{\rho}\frac{\partial p}{\partial y} + \nu\frac{\partial^2 v}{\partial x^2} + \nu\frac{\partial^2 v}{\partial y^2}. \tag{3.2.5}$$

To classify the set of Eq.(3.2.3–3.2.5), the system has to be brought into the following form

$$\mathcal{A}\frac{\partial \mathbf{Q}}{\partial x} + \mathcal{B}\frac{\partial \mathbf{Q}}{\partial y} = 0, \tag{3.2.6}$$

where $\mathbf{Q} = [u, v, p]^T$ is the vector containing the primitive variables and $\mathcal{A}, \mathcal{B}$ are the coefficient matrices of Eq.(3.2.3–3.2.5) and given by

$$\mathcal{A} = \begin{bmatrix} 1 & 0 & 0 \\ u & 0 & -\frac{1}{\rho} \\ 0 & u & 0 \end{bmatrix}, \qquad \mathcal{B} = \begin{bmatrix} 0 & 1 & 0 \\ v & 0 & 0 \\ 0 & v & -\frac{1}{\rho} \end{bmatrix}. \tag{3.2.7}$$

Hellwig [113][1] proposed that matrix $\mathcal{A}$ and $\mathcal{B}$ can be combined into a third matrix $\mathcal{T}$ by adding their components with respect to their normal direction so that

[1] See also Hoffmann [4] for a more detailed description

$$\mathcal{T} = \mathcal{A} \cdot n_x + \mathcal{B} \cdot n_y, \tag{3.2.8}$$

where n_x and n_y are the normal vector components in x and y, respectively. Thus, $\mathcal{T}$ is obtained as

$$\mathcal{T} = \begin{bmatrix} n_x & n_y & 0 \\ un_x + vn_y & 0 & -\frac{n_x}{\rho} \\ 0 & un_x + vn_y & -\frac{n_y}{\rho} \end{bmatrix}. \tag{3.2.9}$$

To determine the mathematical property of $\mathcal{T}$, the determinant is set to zero and the equation solved for the characteristics. If the eigenvalues are all real and distinct, the system is classified as hyperbolic, if they are all real but equal, it is parabolic and if all eigenvalues are complex, then it is classified as an elliptic system. Carrying out the steps outlined above one arrives at

$$\det(\mathcal{T}) = -\frac{n_x^2}{\rho}(un_x + vn_y) - \frac{n_y^2}{\rho}(un_x + vn_y) = 0 \tag{3.2.10}$$

Multiplying Eq.(3.2.10) by $-\rho$ and reordering the terms, the following is obtained

$$un_x^3 + vn_x^2 n_y + un_x n_y^2 + vn_y^3 = 0. \tag{3.2.11}$$

Eq.(3.2.11) is divided by n_x^3 and with the substitution of $x = n_y/n_x$, the following cubic equation is obtained

$$vx^3 + ux^2 + vx + u = 0. \tag{3.2.12}$$

Solving for x yields the following three solutions

$$x_1 = +\sqrt{-1}, \qquad x_2 = -\sqrt{-1}, \qquad x_3 = -\frac{u}{v} \tag{3.2.13}$$

Thus, Eq.(3.2.13) is classified as mixed hyperbolic / elliptic as real (distinct, in this case just one) and complex eigenvalues coexist. Recalling that x has been defined as $x = n_y/n_x$ and noting that an arbitrarily small chosen normal vector component n_i can be written as an infinitesimal increment, the following holds

$$x = \frac{n_y}{n_x} = \frac{\mathrm{d}y}{\mathrm{d}x} \tag{3.2.14}$$

Hence, Eq.(3.2.13) is indeed giving the solutions along the characteristics, where $\mathrm{d}y/\mathrm{d}x$ denote directions in physical space.

3.2.2 Time Dependent Flow (Unsteady State)

The time dependent version of the Navier–Stokes equations are solved in a similar manner as in Section 3.2.1. The starting point is the unsteady system of Eq.(3.2.1–3.2.2) given below

$$\alpha\frac{\partial p}{\partial t} + \nabla\cdot\mathbf{u} = 0, \tag{3.2.15}$$

$$\frac{\partial \mathbf{u}}{\partial t} + (\mathbf{u}\cdot\nabla)\mathbf{u} = -\frac{1}{\rho}\nabla p + \nu\nabla^2\mathbf{u}, \tag{3.2.16}$$

which, in expanded form is

$$\alpha\frac{\partial p}{\partial t} + \frac{\partial u}{\partial x} + \frac{\partial v}{\partial y} = 0, \tag{3.2.17}$$

$$\frac{\partial u}{\partial t} + u\frac{\partial u}{\partial x} + v\frac{\partial u}{\partial y} = -\frac{1}{\rho}\frac{\partial p}{\partial x} + \nu\frac{\partial^2 u}{\partial x^2} + \nu\frac{\partial^2 u}{\partial y^2}, \tag{3.2.18}$$

$$\frac{\partial v}{\partial t} + u\frac{\partial v}{\partial x} + v\frac{\partial v}{\partial y} = -\frac{1}{\rho}\frac{\partial p}{\partial y} + \nu\frac{\partial^2 v}{\partial x^2} + \nu\frac{\partial^2 v}{\partial y^2}. \tag{3.2.19}$$

Here, the time derivative of the density in the continuity equation has been substituted by the pressure through the equation or state or the definition of the speed of sound, i.e. $a = \sqrt{(\partial p/\partial\rho)_s}$ (it is not important which route is chosen), where the remaining terms are collected in the α coefficient. This is done to bring the equations into a form which are commonly employed for incompressible flows. Those equations are now split again as in the time independent form as

$$\mathcal{A}\frac{\partial \mathbf{Q}}{\partial t} + \mathcal{B}\frac{\partial \mathbf{Q}}{\partial x} + \mathcal{C}\frac{\partial \mathbf{Q}}{\partial y} = 0, \tag{3.2.20}$$

with $\mathbf{Q} = [u, v, p]^T$. Here, three matrices are formed which are given as

$$\mathcal{A} = \begin{bmatrix} 0 & 0 & \alpha \\ 1 & 0 & 0 \\ 0 & 1 & 0 \end{bmatrix}, \qquad \mathcal{B} = \begin{bmatrix} 1 & 0 & 0 \\ u & 0 & -\frac{1}{\rho} \\ 0 & u & 0 \end{bmatrix}, \qquad \mathcal{C} = \begin{bmatrix} 0 & 1 & 0 \\ v & 0 & 0 \\ 0 & v & -\frac{1}{\rho} \end{bmatrix}. \tag{3.2.21}$$

The combined matrix $\mathcal{T}$ is formed as

$$\mathcal{T} = \mathcal{A}\cdot n_t + \mathcal{B}\cdot n_x + \mathcal{C}\cdot n_y, \tag{3.2.22}$$

where n_t is now the normal direction in time. The explicit form of $\mathcal{T}$ is given as

$$\mathcal{T} = \begin{bmatrix} n_x & n_y & \alpha n_t \\ n_t + un_x + vn_y & 0 & -\frac{n_x}{\rho} \\ 0 & n_t + un_x + vn_y & -\frac{n_y}{\rho} \end{bmatrix}. \tag{3.2.23}$$

The characteristics are found by setting the determinant to zero

$$\det(\mathcal{T}) = \alpha n_t(n_t+un_x+vn_y)^2 + \frac{n_x^2}{\rho}(n_t+un_x+vn_y) + \frac{n_y^2}{\rho}(n_t+un_x+vn_y) = 0. \tag{3.2.24}$$

Expanding terms, one obtains

$$\rho\alpha(n_t^3 + 2un_t^2 n_x + 2vn_t^2 n_y + 2uvn_x n_y n_t + u^2 n_t n_x^2 + v^2 n_t n_y^2) + n_x^2 n_t + un_x^3 + vn_y n_x^2 + n_y^2 n_t + un_x n_y^2 + vn_y^3 = 0. \quad (3.2.25)$$

At this point, the procedure adopted in Section 3.2.1 is not applicable directly. Eq.(3.2.25) has to be simplified so that only two directions, i.e. either n_t, n_x or n_y remain. This can be achieved by noting that the Navier–Stokes equations are Galilean invariant (in the form considered in Eq.(3.2.15–3.2.16)) so that the equations can be split in the x and y direction. Thus, two equations are obtained from Eq.(3.2.25) by setting n_x or n_y to zero. This leads to, in x ($n_y = 0$)

$$\rho\alpha(n_t^3 + 2un_t^2 n_x + u^2 n_t n_x^2) + n_x^2 n_t + un_x^3 = 0, \quad (3.2.26)$$

and in y ($n_x = 0$)

$$\rho\alpha(n_t^3 + 2vn_t^2 n_y + v^2 n_t n_y^2) + n_y^2 n_t + vn_y^3 = 0. \quad (3.2.27)$$

Eq.(3.2.26–3.2.27) are divided by n_t^3 and the substitutions $x = n_x/n_t$ and $y = n_y/n_t$ are made. Thus, the equations now read

$$\rho\alpha(1 + 2ux + u^2x^2) + x^2 + ux^3 = 0, \quad (3.2.28)$$

$$\frac{u}{\rho\alpha}x^3 + (u^2 + \frac{1}{\rho\alpha})x^2 + 2ux + 1 = 0, \quad (3.2.29)$$

in x and

$$\rho\alpha(1 + 2vy + v^2y^2) + y^2 + vy^3 = 0, \quad (3.2.30)$$

$$\frac{v}{\rho\alpha}y^3 + (v^2 + \frac{1}{\rho\alpha})y^2 + 2vy + 1 = 0, \quad (3.2.31)$$

in y, respectively. Eq.(3.2.29) and Eq.(3.2.31) are cubic equations for which their solution yields the eigenvalues of the system. These are

$$x_1 = -\frac{1}{u}, \qquad x_2 = -\frac{1}{2}u\rho\alpha + \frac{1}{2}\sqrt{u^2\rho^2\alpha^2 - 4\rho\alpha}, \qquad x_3 = -\frac{1}{2}u\rho\alpha - \frac{1}{2}\sqrt{u^2\rho^2\alpha^2 - 4\rho\alpha}, \quad (3.2.32)$$

and

$$y_1 = -\frac{1}{v}, \qquad y_2 = -\frac{1}{2}v\rho\alpha + \frac{1}{2}\sqrt{v^2\rho^2\alpha^2 - 4\rho\alpha}, \qquad y_3 = -\frac{1}{2}v\rho\alpha - \frac{1}{2}\sqrt{v^2\rho^2\alpha^2 - 4\rho\alpha}. \quad (3.2.33)$$

Eq.(3.2.32) and Eq.(3.2.33) have real and distinct eigenvalues, thus the system is classified as hyperbolic. It is not important to what the equations evaluate to. It is reasonable to state that $u^2\rho^2\alpha^2 > 4\rho\alpha$ and $v^2\rho^2\alpha^2 > 4\rho\alpha$ so that the square roots in Eq.(3.2.32–3.2.33) remain real. However, at boundaries, we have $u = v = 0$ and

a complex square root is obtained. Similarly, $1/u$ and $1/v$ are not defined at solid boundaries. However, it is the actual expression which classifies the system of equations, not its potential values. Any hyperbolic system can become locally elliptic by setting $u = v = 0$ or for a low speed, low density case so that either $u^2\rho^2\alpha^2 < 4\rho\alpha$ or $v^2\rho^2\alpha^2 < 4\rho\alpha$ is satisfied[2]. However, in these cases it is redundant to talk about the mathematical properties of the system. Even if a system is classified as being hyperbolic, if the flow is completely at rest and in equilibrium, then there will be no characteristics. The whole domain can then turn locally to be elliptic, but there is no flow to be classified in the first place. In a flow which is not at rest, however, the system can locally become elliptic, especially near boundaries. However, flow velocities here are much smaller than those of the mean flow so that these regions can be neglected. The bulk of the domain remains hyperbolic.
The simple inclusion of a time derivative turned a system which has been previously classified as being mixed elliptic / hyperbolic into a fully hyperbolic system. This is to be expected as there cannot be any elliptic, time dependent system. The inclusion of time will always set a limiting speed at which information can travel which in turn naturally introduces characteristic lines into the flow domain. Thus, elliptic features can only exist where no restriction on the propagation of information exist which can be removed by introducing unsteady effects into the equations.
It has also been shown that the Galilean invariance is preserved. Rotating Eq.(3.2.32) so that it aligns with the y direction, Eq.(3.2.33) would be obtained. Thus, the simplification of setting either $n_x = 0$ or $n_y = 0$ and splitting the equations into different directions is justified. This approach also works for a three-dimensional system of equations (assuming Galilean invariance) but the two-dimensional approach has been chosen for simplicity.

3.3 Numerical Methods for Incompressible Flows

Now that the incompressible Navier–Stokes equations have been derived and their mathematical behaviour has been established, we need to employ a special numerical method to solve the incompressible system of equations in absence of a closure for the pressure. Different methods were proposed in the past and those relevant to the current work discussed below. At the end of this Section, a novel idea based on a velocity projection approach is introduced from which a pressure transport equation is be obtained.

3.3.1 The Method of Artificial Compressibility (1967)

The decoupling of pressure from the Navier–Stokes equations, i.e. Eq.(3.2.1–3.2.2), meant that numerical solutions for incompressible flows were not possible by solving the equations directly. The vorticity-streamfunction formulation removed the pressure from the momentum equation but introduced problems elsewhere, however, it remained the only valid incompressible treatment until Chorin [16] introduced his

[2]It can be assumed that $\alpha = 1$ and $\rho > 0$, while the velocity component u and v are always considered as their absolute value

artificial compressibility method. In his method, Chorin first introduced the time derivative of density back into the continuity equation. Since the density is constant throughout an incompressible flow, Chorin substituted the pressure for the density using the definition of the speed of sound as

$$a = \sqrt{\left.\frac{\partial p}{\partial \rho}\right|_s}. \tag{3.3.1}$$

An alternative approach would be to use the ideal equation of state in the form of

$$p = \rho R T, \tag{3.3.2}$$

where R is the specific gas constant and T the temperature. Using either approach, the equations now read

$$\frac{1}{\beta}\frac{\partial p}{\partial \tau} + \nabla \cdot \mathbf{u} = 0, \tag{3.3.3}$$

$$\frac{\partial \mathbf{u}}{\partial \tau} + \frac{\partial \mathbf{u}}{\partial t} + (\mathbf{u} \cdot \nabla)\mathbf{u} = -\frac{1}{\rho}\nabla p + \nu \nabla^2 \mathbf{u}, \tag{3.3.4}$$

where the time derivative is now plagued with a numerical factor, sometimes also referred to as a convergence parameter, for which no closed form solution exists. Chorin circumvented this problem making all time derivatives non-physical and thus marching the solution in pseudo time. Although the equations lose any physical meaning in a time dependent sense, once the steady state limit in pseudo time is achieved, the time derivative of the pressure in the continuity equation vanishes and the physical, time independent form of the Navier–Stokes equations is recovered. If a time dependent solution is of interest, the dual time-stepping procedure of Jameson [114] needs to be employed for which a real time derivative needs to be added to the momentum equation, as can be seen in Eq.(3.3.4). From Eq.(3.2.15–3.2.16), we can see that Eq.(3.3.3–3.3.4) correspond to the same set of equations and thus the AC method is classified as being fully hyperbolic.

The introduction of the convergence parameter requires some further considerations. The time step is commonly chosen based on the CFL number as

$$\Delta t_{inviscid} = \frac{\mathrm{CFL}\Delta \mathrm{x}}{\lambda_{max}}, \tag{3.3.5}$$

where the maximum permissible CFL number needs to be derived from stability considerations and λ_{max} is the highest eigenvalue. Δx is chosen as the smallest grid spacing that is encountered in the domain. Similar to Section 3.2.2, the eigenvalues for the AC method yields[3] (considering a one-dimensional case for simplicity)

$$\lambda_0 = u, \tag{3.3.6}$$

$$\lambda_1 = u + \sqrt{u^2 + \beta/\rho}, \tag{3.3.7}$$

$$\lambda_2 = u - \sqrt{u^2 + \beta/\rho}. \tag{3.3.8}$$

[3]For more details, the reader is referred to references [50, 72]

It can be seen from the definition of the artificial speed of sound $s = \sqrt{u^2 + \beta/\rho}$, that the convergence parameter enters the calculation of the time step, Eq.(3.3.5), by setting $\lambda_{max} = \max(u + \sqrt{u^2 + \beta/\rho}, u - \sqrt{u^2 + \beta/\rho})$. If the definition for the speed of sound ($a = \sqrt{(\partial p/\partial \rho)_s}$) is used so that $\beta = a^2$, it becomes apparent that when setting β orders of magnitude higher than the highest flow velocity encountered (as is the case for the speed of sound compared to incompressible flow velocities), Δt will decrease so that the choice of β does not influence the stability, but the convergence rate of the solution. Details on the correct time step selection will be given in Section 5.3.3.

3.3.2 The Fractional-Step Pressure Projection Method (1968)

Following the introduction of the AC method, Chorin [18] introduced yet another method to solve incompressible flows. It is based on the Helmholtz-Hodge decomposition (also known as the fundamental theorem of vector calculus), which states that any sufficiently smooth vector field can be expressed as a superposition of a divergence-free (solenoidal) and curl-free (irrotational) vector field. This leads to

$$\mathbf{u} = \mathbf{u}_{solenoidal} + \mathbf{u}_{irrotational} = \mathbf{u}_{solenoidal} + \nabla\phi, \tag{3.3.9}$$

where use of $\nabla \times \nabla\phi = 0$ has been made for an arbitrarily chosen scalar ϕ. Chorin used an operator splitting, or Fractional-Step procedure, in which the Navier–Stokes equations are split into the convective-viscous and pressure part and written in semi-discretised form as

$$\frac{\mathbf{u}^* - \mathbf{u}^n}{\Delta t} = \left[\nu\nabla^2\mathbf{u} - (\mathbf{u}\cdot\nabla)\mathbf{u}\right]^n, \tag{3.3.10}$$

$$\frac{\mathbf{u}^{n+1} - \mathbf{u}^*}{\Delta t} = -\frac{1}{\rho}\nabla p^{n+1}. \tag{3.3.11}$$

In the first Fractional-Step (Eq.(3.3.10)), an intermediate velocity field $\mathbf{u}^*$ is predicted based on the velocity vector at time step n. The second Fractional-Step requires the knowledge of $\mathbf{u}^{n+1}$. Making use of the Helmholtz-Hodge decomposition, a divergence-free vector field can be enforced at the next time step $n+1$ for which $\nabla \cdot \mathbf{u}^{n+1} = 0$. The divergence of the vector field has to become zero for an incompressible flow. Therefore, taking the divergence of Eq.(3.3.11) yields

$$\nabla^2 p^{n+1} = -\frac{\rho}{\Delta t}\nabla \cdot \mathbf{u}^* \tag{3.3.12}$$

This Poisson equation can be solved for the pressure and using Eq.(3.3.11), the corrected velocities at time step $n+1$ can be obtained, once the pressure is known, as

$$\mathbf{u}^{n+1} = \mathbf{u}^* - \frac{\Delta t}{\rho}\nabla p^{n+1}. \tag{3.3.13}$$

Since a Poisson equation has been derived for the pressure, the continuity equation does not need to be solved and is used to judge if a solution has become divergence-free.

3.3.3 The Unified Fractional-Step Artificial Compressibility Method with Pressure Projection (2012)

Könözsy [109] and Könözsy and Drikakis [21] introduced a framework in which the AC and PP method of Chorin were unified into a single procedure. It is termed the Fractional-Step, artificial compressibility with pressure projection, or FSAC-PP, method. In its first Fractional-Step, the system of equations is the same as in the PP method, i.e. the pressure gradient term is dropped, however, the perturbed continuity equation from the AC method is added to the system so that the first Fractional-Step reads, in semi-discretised form

$$\frac{1}{\beta}\frac{\partial p}{\partial \tau} + \nabla \cdot \mathbf{u} = 0, \tag{3.3.14}$$

$$\frac{\mathbf{u}^* - \mathbf{u}^n}{\Delta \tau} + \frac{\partial \mathbf{u}}{\partial t} = \nu \nabla^2 \mathbf{u} - (\mathbf{u} \cdot \nabla)\mathbf{u}. \tag{3.3.15}$$

Since the method inherits the pseudo time-stepping from the AC method, a real time derivative is added to the momentum equation as well to solve unsteady flows through the dual time-stepping procedure. The second Fractional-Step is analogous to the PP method in which a pressure Poisson equation is derived, based on the intermediate velocities u^* and v^* as

$$\nabla^2 p^{n+1} = -\frac{\rho}{\Delta \tau} \nabla \cdot \mathbf{u}^*. \tag{3.3.16}$$

Similarly, the velocities are updated as in the PP method as

$$\mathbf{u}^{n+1} = \mathbf{u}^* - \frac{\Delta \tau}{\rho} \nabla p^{n+1} \tag{3.3.17}$$

The introduction of the perturbed continuity equation in the system of equations (Eq.(3.3.14–3.3.15)) renders the first Fractional-Step hyperbolic through the time derivative of the continuity equation. This allows CB schemes and RS to be used in conjunction with the FSAC-PP method. The elliptic features of the pressure Poisson equation further introduce smoothing effects into the system which is stabilising the calculation of the pressure. Unlike in the PP procedure, where a predefined convergence criterion for the Poisson solver has to be reached (or a maximum number of iterations, whichever comes first), the Poisson solver in the FSAC-PP method does not need to reach a converged solution. The inclusion of the perturbed continuity equation from the AC method means that an initial pressure is already available at the current time level n (in the PP method the initial pressure is available at the previous time level $n-1$). Therefore, only a couple of iterations are required, and it was found that usually ten iterations are a good initial estimate which works for a wide range of applications [21, 22]. This stabilises and improves the predicted pressure field which drastically enhances the convergence rate. Arguably, more calculations per time step are needed compared to the AC or PP method, however, experience has shown that the increase in convergence rate outperforms the increased computational time per time step. Könözsy and Drikakis [22] also highlighted that for unsteady flows, a speed-up is observed where the continuity equation further

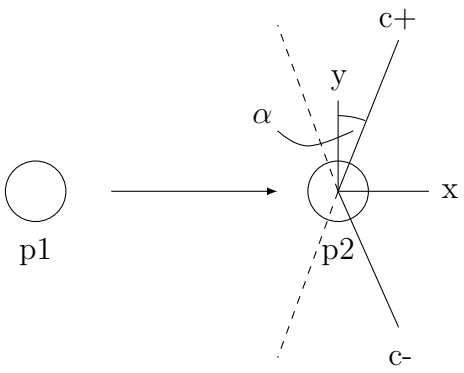

Figure 3.2: Collision of two particles $p1$ and $p2$.

accelerates the convergence of the pressure field. Further calculations are presented herein to support this claim and the role of different CB schemes and RS will also be discussed.

3.3.4 The Fractional-Step Velocity Projection Method (2017)

It was shown in Section 3.2.1, that the incompressible version of the Navier–Stokes equations is mixed elliptic / hyperbolic and in Section 3.3.3, that the FSAC-PP method includes both elliptic and hyperbolic features. As will be shown later, its alignment with the mathematical nature is part of the success of the FSAC-PP method. An alternative approach may be justified in the following way: The system of equations in Eq.(3.2.1–3.2.2) is classified as mixed elliptic / hyperbolic but the only transport equations that are obtained (and thus classified, see Eq.(3.2.3–3.2.5)) depend only upon the velocity. Since there is no transport equation for the pressure, its behaviour is not classified[4]. The following discussion, derived from microscopic and macroscopic considerations, will highlight the issue in more detail.

At solid boundaries, pressure is a measurement of the strength of the impingement of particles[5] onto the boundary. In a more general case, pressure can also be exerted on single particles due to a momentum transfer during a collision. This case is depicted in Figure 3.2.
Two particles are colliding head-on with velocities $\mathbf{u}_{p1} = (u_{p1}, 0, 0)$ and $\mathbf{u}_{p2} = (0, 0, 0)$, respectively, and their initial positions are at $\mathbf{x}_{p1} = (-x_{p1}, 0, 0)$ and $\mathbf{x}_{p2} = (0, 0, 0)$. Assuming an elastic collision, after a time $\Delta t = x_{p1}/u_{p1}$, a collision will occur so that the new velocities will be $\mathbf{u}_{p1} = (0, 0, 0)$ and $\mathbf{u}_{p2} = (u_{p1}, 0, 0)$. The positions are found to be $\mathbf{x}_{p1} = (0, 0, 0)$ and $\mathbf{x}_{p2} = (x_{p2}(\mathbf{u}_{p1}, t), 0, 0)$ so that the direction of travel for particle $p2$ is at an angle of $\alpha = 90°$ with the y-axis, see Figure 3.2. Assuming both particles have the same radius $r_{p1} = r_{p2} = r$, the same thought experiment can be carried out, this time letting the initial position of particle $p1$ be at an offset to the x-axis so that $\mathbf{x}_{p1} = (-x_{p1}, \pm y_{p1}, 0)$. The rest of the

[4]To be precise, the equations are derived for the pressure but only through the substitution of the pressure via the equation of state or speed of sound approach. The underlying conservation of mass, however, is still derived for the density and not pressure.

[5]or atoms, in the following the words atoms and particles are used interchangeably.

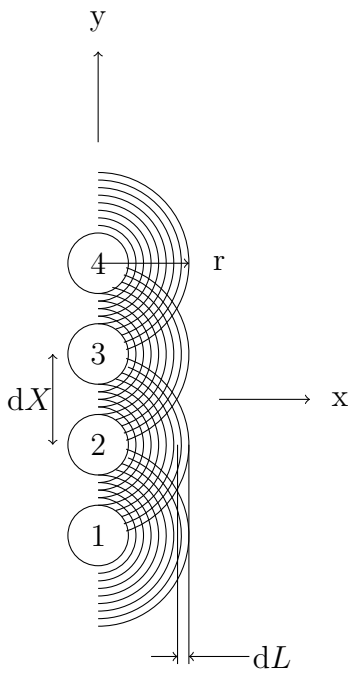

Figure 3.3: Transition from a hyperbolic to a parabolic character from the microscopic to the macroscopic regime.

set up remains the same. For some chosen value of $y_{p1} < r$, the collision of $p1$ with $p2$ will induce a velocity component for both particles in the y-direction for which the direction of travel of both particles is bounded by $0° < \alpha < 180°$. Ignoring the special case considered above for which $y_{p1} = 0$, two characteristics, $c+$ and $c-$, are created which are the possible directions for $p2$ to take post collision. Both $c+$ and $c-$ span the *zone of influence*, which is the region where $p2$ can travel into, i.e. it cannot go beyond $c+$ or $c-$. Note here that both characteristics are functions of the collision angle α so that $c = c \pm f(\alpha)$. These are fed by the *domain of dependence* which are shown as dashed lines in Figure 3.2. No information from outside the *domain of dependence* is able to influence the *zone of influence*. For the limiting case in which $y_{p1} \approx r$ but $y_{p1} < r$ is still satisfied, α will still remain bounded by $0° < \alpha < 180°$ where $0°$ and $180°$ are excluded values from α's range. Thus, two distinct characteristics prevail and the behaviour of pressure from a microscopically, dual-particle system, is found to be hyperbolic, since real and distinct characteristics are found.

The Navier–Stokes equations are, however, valid under the continuum hypothesis and thus the above given considerations have to be scaled-up. This can be achieved by considering now a collection of particles initially all at a position $\mathbf{x}_{p,i} = (0, y_{p,i}, 0)$ which is shown in Figure 3.3.

By analogy, macroscopic pressure waves can be thought to be travelling through space like the ripples of water caused by a droplet. This can be also derived from a microscopic point of view, i.e. in Figure 3.2, if $p2$ is not assumed to be stationary at first. Then, both $p1$ and $p2$ will be moving away from a fixed frame of reference which represents one possible microstate. A macrostate will have a large number of microstates so that the superposition of all possible microstates will produce a radial

wave pattern (all outgoing directions are equally likely) as seen in Figure 3.3. The distance between two particles is denoted by $\mathrm{d}X$ and the difference of the maximum and minimum travelled distance of a single pressure wave in x is denoted by $\mathrm{d}L$. In other words, due to the radial pattern of the pressure waves, there will always be points on the farthest pressure waves which will be, with respect to the x-direction, further away than points travelling at an angle to the x-direction. Considering, for example, $p2$ in Figure 3.3, after a collision with another particle it may travel in the positive x and y direction until a point where it collides with $p3$, which originally got its momentum from a different particle. Since both are restricted to outgoing collision angles $0° < \alpha < 180°$, they both need to travel a certain time $t_{collision}$ until they collide with each other. This can only occur where their *zone of influences* cross each other. However, since the initial collision induced a velocity component in the y-direction, compared to a head-on collision of the same velocity magnitude, there will be always a distance in the x-direction between the point of collision of two particles, here $p2$ and $p3$, compared with a particle whose velocity vector is aligned with the x-axis. This deficit is denoted by $\mathrm{d}L$.
To consider a macroscopic system, use is made of the fact that the inter-particle distance, here denoted by $\mathrm{d}X$, is much smaller than a characteristic length scale so that $\mathrm{d}X \ll L_{characteristics}$. Using Pythagoras' theorem, it is possible to calculate $\mathrm{d}L$ as a function of $\mathrm{d}X$. In the limiting case for $\mathrm{d}X$ going to zero, one arrives at

$$\mathrm{d}L = \lim_{\mathrm{d}X \to 0} r - \sqrt{r^2 - \left(\frac{\mathrm{d}X}{2}\right)^2} = 0. \tag{3.3.18}$$

This is an important result as there can only be a single characteristic front for $\mathrm{d}L$=0, rather than two as seen for the microscopic case. Technically speaking, $c+$ and $c-$ do still exist; however, their effect is not felt by the macroscopic system. Since there is only one characteristic line (pressure front), the considerations given above suggest that the pressure on a macroscopic level should have a parabolic behaviour. This is in contrast with what was found in Section 3.2.1, however, as stated previously, pressure does not have its own transport equation and thus its behaviour is not classified by the procedure presented in the aforementioned Section.
This discussion has, however, highlighted more problems for which currently no solutions exist. The first problem is the lack of an individual transport equation for the pressure in all of the previously discussed methods for incompressible flows. From a physical point it is rather odd that all primitive variables, including passive scalars, have a transport equation except for the pressure, which is a fundamental property of the flow. It could be argued that both the PP and FSAC-PP method do use a Poisson equation for the pressure, however, it is elliptic in nature and does not represent the time evolution of the pressure. It is more of a numerical treatment to close the system. The AC method does include the pseudo time derivative of the pressure in its continuity equation, however, this equation only becomes physical for a steady state flow[6]. SIMPLE-like procedures are purely numerical and are based on a predictor-corrector scheme where the pressure field is guessed and corrected until

[6]For unsteady flows, the dual time-stepping procedure is only affecting the momentum equations and so the continuity equation is still only valid once a steady state has been reached within the current time step.

it converges. The vorticity-streamfunction approach removes the pressure altogether from its equations. The second problem has been already highlighted, those pressure equations which do exist are either not physical transport equations or do not have the expected mathematical behaviour. This has been the motivation to develop the Fractional Step, Velocity Projection (FSVP) method which will be discussed in the following.

The derivation of the FSVP method is based on the FSAC-PP method. Reasons have been given in the above discussion that the FSAC-PP method exhibit both elliptic and hyperbolic traits which are to be expected from the mathematical classification of incompressible flows. A parabolic transport equation for the pressure can be constructed by assuming the system of equations of the FSAC-PP method, i.e. Eq.(3.3.14–3.3.17), however, the divergence free constraint in the continuity equation is now satisfied at time level $n+1$ rather than n as in the FSAC-PP method. The system reads

$$\frac{1}{\beta}\frac{\partial p}{\partial \tau} + \nabla \cdot \mathbf{u}^{n+1} = 0, \tag{3.3.19}$$

$$\frac{\mathbf{u}^* - \mathbf{u}^n}{\Delta\tau} + \frac{\partial \mathbf{u}}{\partial t} = \nu[\nabla^2\mathbf{u} - (\mathbf{u}\cdot\nabla)\mathbf{u}]^n. \tag{3.3.20}$$

As in the FSAC-PP method, the real time derivative is added for unsteady flows. A pressure Poisson equation can be defined as

$$\nabla^2 p^{n+1} = -\frac{\rho}{\Delta\tau}\nabla\cdot\mathbf{u}^*, \tag{3.3.21}$$

and a velocity update by

$$\mathbf{u}^{n+1} = \mathbf{u}^* - \frac{\Delta\tau}{\rho}\nabla p^{n+1}. \tag{3.3.22}$$

This system is not yet closed as there is no information available on $\mathbf{u}^{n+1}$ for the continuity equation, i.e. Eq.(3.3.19). However, Eq.(3.3.22) is presenting a way to calculate the velocity components at the next time level. Inserting Eq.(3.3.22) into Eq.(3.3.19) results in

$$\frac{1}{\beta}\frac{\partial p}{\partial \tau} + \nabla\cdot\left[\mathbf{u}^* - \frac{\Delta\tau}{\rho}\nabla p^{n+1}\right] = 0. \tag{3.3.23}$$

This can be rearranged to

$$\frac{1}{\beta}\frac{\partial p}{\partial \tau} = \frac{\Delta\tau}{\rho}\nabla^2 p^{n+1} - \nabla\cdot\mathbf{u}^*. \tag{3.3.24}$$

Eq.(3.3.24) consist of a time derivative as well as the laplacian of the pressure, which is the canonical form of a parabolic differential equation. Here, $\nabla\cdot\mathbf{u}^*$ is simply a source term. Thus, by assuming the velocity at time level $n+1$ in the perturbed continuity equation, Eq.(3.3.19), a parabolic transport equation for the pressure can be derived. Since the velocity is taken at time level $n+1$, it can be said to be projected into the next time level, similarly to the Pressure Projection concept, where the

pressure is projected into the next time level. Hence, to stick with the current naming convention, the procedure involving the calculation of Eq.(3.3.20), Eq.(3.3.24) and Eq.(3.3.22) is termed the Fractional Step, Velocity Projection (FSVP) method and can be summarised as follows. In the first Fractional-Step, the intermediate velocity is calculated through the momentum equation. This result is used in the second Fractional-Step to obtained the pressure at the next time level $n+1$ and finally, the velocity is updated. The system of equations is summarised below

$$\frac{\mathbf{u}^* - \mathbf{u}^n}{\Delta\tau} + \frac{\partial \mathbf{u}}{\partial t} = [\nu\nabla^2\mathbf{u} - (\mathbf{u}\cdot\nabla)\mathbf{u}]^n, \tag{3.3.25}$$

$$\frac{1}{\beta}\frac{p^{n+1} - p^n}{\partial\tau} = \frac{\Delta\tau}{\rho}\nabla^2 p^{n+1} - \nabla\cdot\mathbf{u}^*, \tag{3.3.26}$$

$$\mathbf{u}^{n+1} = \mathbf{u}^* - \frac{\Delta\tau}{\rho}\nabla p^{n+1}. \tag{3.3.27}$$

Three comments are in order before continuing. Firstly, the Poisson equation has been eliminated from the procedure and does not need to be solved as in the PP and FSAC-PP method. This has the mathematical advantage that the elliptic nature enforced on the pressure is removed, and the numerical advantage, that the Poisson solver does not need to be solved which is time consuming. The parabolic behaviour of the pressure transport equation is putting physical limits on the propagation speed and pressure front into the domain which means that it does not need to be solved iteratively. Rather, it can be solved in a coupled manner where the parabolic nature ensures a correct physical behaviour (this is numerically satisfied by the Poisson equation in the PP and FSAC-PP method which comes at an increased computational cost).
Secondly, due to the inclusion of perturbed continuity equation which in term is coming from the AC method, the time derivatives in Eq.(3.3.25) and Eq.(3.3.26) are non-physical and the system of equations Eq.(3.3.25–3.3.27) is only valid for steady state flows. A dual time-stepping procedure has to be used if an unsteady solution is needed. This is a purely numerical procedure and to remove this from the system (and consequently from the AC and FSAC-PP method as well), the convergence parameter β needs to be defined in terms of a physical quantity. The dual time-stepping procedure is not needed anymore once β takes on a physical meaning. Thirdly, strictly speaking the momentum equation needs to be solved implicitly since the pressure is only available at time level $n+1$. An implicit matrix solver is required to solve the system of equations. Alternatively, as a numerical approximation, the pressure at time level n can be used which is approximately the same as the pressure at the next time level once the solution has converged. This is also sometimes referred to as lagging [4] and used, for example, to linearise the convective flux term. The explicit nature of the continuity equation restricts the time-step so that no computational benefits would be gained by using an implicit solver. On the contrary, the matrix solver would incur only computational costs. The FSAC-PP method decouples the implicit Poisson solver from the explicit continuity-momentum system so that the implicit solver in the FSAC-PP method can be used to speed of the solution. Here, however, since only a couple of iterations are solved,

the need of a sophisticated matrix solver is not required. The FSVP method is also a Fractional-Step type of method, however, the time derivative in the momentum and pressure transport equation is coupling and therefore limiting the possible time-step It is important to stress that by assuming $p^n \simeq p^{n+1}$, especially close to convergence, that it is not expected that the accuracy is affected by the procedure. It may be reasonable, however, that the convergence rate is affected and that even faster convergence can be achieved with an implicit version.

3.3.5 The Fractional-Step, Artificial Compressibility with Velocity Projection Method (2018)

In the FSVP method, the continuity equation is used to derive the parabolic pressure transport equation. Thus, the momentum equation is solved without the continuity equation and therefore the system cannot be classified as hyperbolic due to the absence of the time derivative in the continuity equation. To make the system hyperbolic, the same procedure as in the FSAC-PP method is adopted, where in the first Fractional-Step, the perturbed continuity equation of the AC method is solved along with the reduced momentum equation, in which the pressure gradient is missing. Thus, the first Fractional-Step becomes

$$\frac{1}{\beta}\frac{\partial p}{\partial \tau} + \nabla \cdot \mathbf{u} = 0, \tag{3.3.28}$$

$$\frac{\mathbf{u}^* - \mathbf{u}^n}{\Delta \tau} + \frac{\partial \mathbf{u}}{\partial t} = [\nu \nabla^2 \mathbf{u} - (\mathbf{u} \cdot \nabla)\mathbf{u}]^n. \tag{3.3.29}$$

In the second Fractional-Step, the pressure transport equation is solved analogous to the FSVP method as

$$\frac{1}{\beta}\frac{p^{n+1} - p^n}{\partial \tau} = \frac{\Delta \tau}{\rho}\nabla^2 p^{n+1} - \nabla \cdot \mathbf{u}^*. \tag{3.3.30}$$

Due to the Fractional-Step procedure and the inclusion of the continuity equation, the method is named the Fractional-Step, Artificial Compressibility with Velocity Projection, or FSAC-VP, method. Since the continuity equation is now included and of the form given in Section 3.2.2, the system is classified as mixed hyperbolic / parabolic which is split through the Fractional-Step. Thus, the CB scheme and RS can be applied, just as in the AC and FSAC-PP method, also to the FSAC-VP method.

Chapter 4

The Method of Characteristics and Riemann Problem for Incompressible Flows

In this Section, the method of characteristics for incompressible flows is introduced from a mathematical point of view. Since the novel multi-directional characteristic-based scheme is to be assessed against the single-directional scheme, we present the derivation here for both schemes. The SCB scheme is derived in detail in [15, 72] so that only the necessary steps are derived herein. For a more detailed derivation the reader is referred to the literature. The MCB scheme, on the other hand, has not seen a detailed and documented derivation in the literature and thus a step by step derivation is given with mathematical considerations given along the way. It is put into a generalised form which can be used for any hyperbolic system of equations that solve the incompressible Navier–Stokes equations. Finally, the Section is closed with a discussion of the Riemann problem, its similarity to the method of characteristics and its use within incompressible flows.

4.1 The Method of Characteristics for Incompressible Flows

The literature review revealed that currently two different flavours of the method of characteristics are in use for finite volume schemes. These are the single-direction CB scheme of Drikakis *et al.* [15] and the multi-directional CB scheme of Razavi *et al.* [17] and Zamzamian and Razavi [53]. Before proceeding further with any single- or multi-directional approach, the main idea behind the method of characteristics will be given in the following (applied to fluid mechanics). The textbook definition is that there are lines in the flow along which the derivative may be discontinuous. Along these lines, simplified expressions for the primitive variables (velocity and pressure) are obtained which are then applied to predefined points in the domain (for CFD applications, these are the grid points of the computational mesh). In this way, for each computational (mesh) point, a characteristic solution exists which can be advanced in time. There are two fundamentally different approaches how

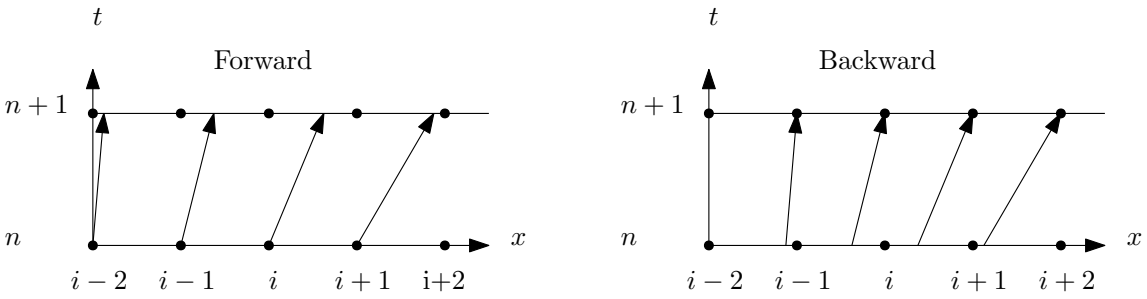

Figure 4.1: Differences in forward and backward characteristic networks.

the characteristics can be computed. Either by considering the characteristics going through the computational points at time level n (forward) or at time level $n+1$ (backward). In the *forward characteristic network*, the solution is defined at all points at time level n through either initial conditions or computations from the previous time step. There are two possibilities to obtain a solution for some $t + \Delta t$. The first possibility is to consider the solution at $n+1$, i.e. by using a fixed Δt for all characteristic lines. These lines would, however, not necessarily coincide with the computational nodes as seen in Figure 4.1 on the left. Interpolation of the characteristic values at $n+1$ would be necessary to obtain solutions at all locations of i. The second solution is to find intersecting characteristic lines which would exist for some $t + \Delta t$, however, Δt would not be constant and a time level $n+1$ cannot be defined. This is referred to as the *unit process* in the literature (see Anderson [23]), in which a domain is mapped out through intersecting characteristics. Where they do intersect, new characteristic lines are formed which then intersect again with other, newly formed characteristics, until the domain is filled with characteristics. This approach was extremely popular when the method of characteristics was first introduced into the field of fluid mechanics as complete nozzle configurations could be dimensioned in this manner. It has, however, the disadvantage of a varying time step which makes its application to CFD not straight forward. Therefore, a second approach exist, the *backward characteristic network*, where the solution at time level $n+1$ is sought through characteristics that emanate from time level n. Since these characteristics do not necessarily pass through computational nodes (see Figure 4.1 on the right), the values for the characteristics at time level n have to be obtained through interpolation. This introduces numerical errors which makes this method less exact compared to the *unit process*. However, it is straight forward to apply this method to CFD solvers. For an excellent overview of characteristic networks, the reader is referred to references [24, 25].

To conclude this top-level description of the method of characteristics, the notion of the compatibility equation has to be introduced. It has been stated that the characteristic lines are those in the flow, along which the derivatives may become discontinuous. These lines have been sketched in Figure 4.1. To obtain a solution at some time $t + \Delta t$, equations along the characteristic lines have to be solved. These equations are derived in Section 4.1.1 for the single-directional characteristic-based scheme and in Section 4.1.2 for the multi-directional characteristic-based scheme. They represent the compatibility equations which are only valid along the characteristics.

A full derivation and a more detailed consideration into the philosophy of the method of characteristics is given in Appendix A for the linear and non-linear advection equation.

4.1.1 Single-Directional Approach

Drikakis *et al.* [15] presented the derivation of the single-directional characteristic-based scheme for the AC method in curve-linear coordinates. This description is adopted here where those terms being zero (due to a Cartesian grid), will be dropped at the end for further investigations. This approach is in accordance with references [51, 53].
The system of equations considered is that of Eq.(3.3.3–3.3.4), however, the crucial simplification is introduced that the following procedure is only developed for a one-dimensional flow. To extend the method to two- or three-dimensions, the same equations are rotated and aligned with the respective flow direction. Hence the equations follow an isotropic viewpoint and are termed single-directional.
In curve-linear (obtained by applying the chain rule with respect to the new coordinate system ξ and η), one-dimensional form, Eq.(3.3.3–3.3.4) become[1]

$$\frac{J}{\beta}\frac{\partial p}{\partial \tau} + \frac{\partial u}{\partial \xi}\frac{\partial \xi}{\partial x} + \frac{\partial v}{\partial \xi}\frac{\partial \xi}{\partial y} = 0, \tag{4.1.1}$$

$$J\frac{\partial u}{\partial \tau} + \frac{\partial u}{\partial \xi}\left(u\frac{\partial \xi}{\partial x} + v\frac{\partial \xi}{\partial y}\right) + u\left(\frac{\partial u}{\partial \xi}\frac{\partial \xi}{\partial x} + \frac{\partial v}{\partial \xi}\frac{\partial \xi}{\partial y}\right) + \frac{\partial p}{\partial \xi}\frac{\partial \xi}{\partial x} = 0, \tag{4.1.2}$$

$$J\frac{\partial v}{\partial \tau} + \frac{\partial v}{\partial \xi}\left(u\frac{\partial \xi}{\partial x} + v\frac{\partial \xi}{\partial y}\right) + v\left(\frac{\partial u}{\partial \xi}\frac{\partial \xi}{\partial x} + \frac{\partial v}{\partial \xi}\frac{\partial \xi}{\partial y}\right) + \frac{\partial p}{\partial \xi}\frac{\partial \xi}{\partial y} = 0. \tag{4.1.3}$$

When deriving the above equations, one would obtain a form without the Jacobian J, as noted also by Neofytou [42]. It is, however, introducing stability into the procedure and hence carried on in this derivation. For legibility, the shorthand notation for partial derivatives is introduced as $\partial\xi/\partial x = \xi_x$ and $\partial\xi/\partial y = \xi_y$. These are also referred to as the metric coefficient of the system and appear due to the curve-linear nature.
A Taylor series backward in time and space is used to obtain the solution at time level $n+1$, as depicted in Figure 4.2, which yields

$$\mathbf{u}_i^{n+1} = \mathbf{u}_j^n + \Delta\tilde{\xi}\frac{\partial \mathbf{u}}{\partial \xi} + \Delta\tau\frac{\partial \mathbf{u}}{\partial \tau} + \mathcal{O}(\Delta x^2, \Delta\tau^2). \tag{4.1.4}$$

Here, $\mathbf{u}$ and $\mathbf{u}_j$ are the vectors containing the primitive variables and the interval $\tilde{\xi}$ is defined by $\tilde{\xi} = \dot{\xi}\Delta\tau$. Location j is the intersection of the characteristic line with the time level n. Real characteristics, in its most general form, are curved, as shown in Figure 4.2. However, since the Taylor series is truncated at $\mathcal{O}(\Delta x^2, \Delta\tau^2)$, the obtained characteristic line can only assume a linear profile. This approach can

[1] The x, y, τ coordinate system is used here unlike in [15], where a x, z, t coordinate system is used.

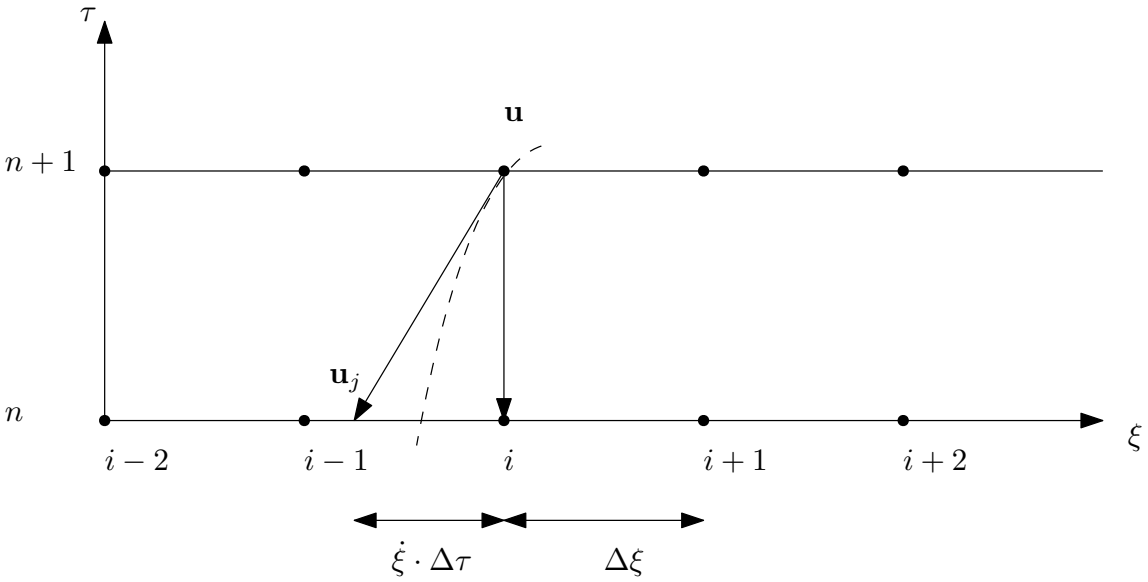

Figure 4.2: One dimensional representation of characteristic lines between time level n and $n+1$. The *real* characteristic is shown as a dashed and curved line while the *numerical* characteristic is a straight line (due to the linear Taylor Series expansion).

be classified as a backward characteristic network. Rearranging Eq.(4.1.4), the time derivative can be expressed as

$$\frac{\partial \mathbf{u}}{\partial \tau} = \frac{\mathbf{u}_i^{n+1} - \mathbf{u}_j^n}{\Delta \tau} - \frac{\partial \mathbf{u}}{\partial \xi} \frac{\Delta \tilde{\xi}}{\Delta \tau}. \tag{4.1.5}$$

The first term is the classical Euler integration scheme whereas the second part is due to the characteristic offset, i.e. $\mathbf{u}_j$ is located between points i and $i-1$. The quantity $\dot{\xi}$ has dimensions of $[s^{-1}]$ since ξ by definition is dimensionless. Eberle [39] suggested one way to introduce the wave speed λ, which has been adopted and modified for incompressible flows by Drikakis to yield

$$\dot{\xi} = \lambda \frac{\sqrt{\xi_x^2 + \xi_y^2}}{J}. \tag{4.1.6}$$

Thus, combining Eq.(4.1.5) and Eq.(4.1.6) yields

$$\frac{\partial \mathbf{u}}{\partial \tau} = \frac{\mathbf{u}_i^{n+1} - \mathbf{u}_j^n}{\Delta \tau} - \lambda \frac{\partial \mathbf{u}}{\partial \xi} \frac{\sqrt{\xi_x^2 + \xi_y^2}}{J}. \tag{4.1.7}$$

Eq.(4.1.7) is an important first step and deserves some more explanation. First of all, the approximate time derivative $(\mathbf{u}_i^{n+1} - \mathbf{u}_j^n)/\Delta\tau$ is not carried out at i from n to $n+1$ but rather at j and i between n and $n+1$, which is the characteristic line. Since the time derivative is not solely evaluated at i, as is the case for non-characteristic time derivatives, a second term in the form of $(\partial \mathbf{u}/\partial \xi)(\Delta\tilde{\xi}/\Delta\tau)$ needs to be introduced to account for the offset at i due to the characteristics. Thus, by applying Eq.(4.1.7) to the system of equation in Eq.(4.1.1–4.1.3), the following system is obtained

$$\frac{1}{\beta}\frac{J}{\sqrt{\xi_x^2+\xi_y^2}\Delta\tau}(p_i^{n+1}-p_j^n)-\frac{\lambda}{\beta}\frac{\partial p}{\partial\xi}+\tilde{x}\frac{\partial u}{\partial\xi}+\tilde{y}\frac{\partial v}{\partial\xi}=0, \tag{4.1.8}$$

$$\frac{J}{\sqrt{\xi_x^2+\xi_y^2}\Delta\tau}(u_i^{n+1}-u_j^n)+\frac{\partial u}{\partial\xi}(\lambda_0-\lambda)+u_i^n\left(\tilde{x}\frac{\partial u}{\partial\xi}+\tilde{y}\frac{\partial v}{\partial\xi}\right)+\tilde{x}\frac{\partial p}{\partial\xi}=0, \tag{4.1.9}$$

$$\frac{J}{\sqrt{\xi_x^2+\xi_y^2}\Delta\tau}(v_i^{n+1}-v_j^n)+\frac{\partial v}{\partial\xi}(\lambda_0-\lambda)+v_i^n\left(\tilde{x}\frac{\partial u}{\partial\xi}+\tilde{y}\frac{\partial v}{\partial\xi}\right)+\tilde{y}\frac{\partial p}{\partial\xi}=0, \tag{4.1.10}$$

where $\lambda_0 = u\tilde{x}+v\tilde{y}$, $\tilde{x}=\xi_x/(\sqrt{\xi_x^2+\xi_y^2})$ and $\tilde{y}=\xi_y/(\sqrt{\xi_x^2+\xi_y^2})$. For Cartesian grids, we set $\tilde{x}=1$ and $\tilde{y}=0$ in the x direction since $\xi_x=1$ but $\xi_y=0$. A similar approach applies to the y direction where $\eta_x=0$ and $\eta_y=1$ so that $\tilde{x}=0$ and $\tilde{y}=1$ results. The compatibility equations can be found from the above system of equations since the time derivative ensured that these equations are on the characteristic pathlines. To obtain these equations, the method of Riemann is used in which Eq.(4.1.8–4.1.10) are all multiplied by a constant coefficient and added together. This can be done as all equations by themselves are all zero. Multiplication of the equations with a constant will not change that and the equations can also be added together. Multiplying Eq.(4.1.8) by a, Eq.(4.1.9) by b and Eq.(4.1.10) by c yields, after rearranging and adding these equations

$$\begin{aligned}&\frac{J}{\sqrt{\xi_x^2+\xi_y^2}\Delta\tau}\left(\frac{a}{\beta}(p_i^{n+1}-p_j^n)+b(u_i^{n+1}-u_j^n)+c(v_i^{n+1}-v_j^n)\right)+\frac{\partial p}{\partial\xi}\left(-\frac{a}{\beta}\lambda+b\tilde{x}+c\tilde{y}\right)\\&+\frac{\partial u}{\partial\xi}(a\tilde{x}+b(\lambda_0-\lambda+u\tilde{x})+cv\tilde{x})+\frac{\partial v}{\partial\xi}(a\tilde{y}+bu\tilde{y}+c(\lambda_0-\lambda+v\tilde{y}))=0.\end{aligned} \tag{4.1.11}$$

Since the equation has to become zero, the partial derivatives $\partial p/\partial\xi$, $\partial u/\partial\xi$ and $\partial v/\partial\xi$ can be set to zero without loss of generality so that

$$\frac{a}{\beta}(p_i^{n+1}-p_j^n)+b(u_i^{n+1}-u_j^n)+c(v_i^{n+1}-v_j^n)=0 \tag{4.1.12}$$

results. Eq.(4.1.12) only results if the derivatives are zero. However, if the derivatives are set to zero, the following is also true

$$-\frac{a}{\beta}\lambda+b\tilde{x}+c\tilde{y}=0, \tag{4.1.13}$$

$$a\tilde{x}+b(\lambda_0-\lambda+u\tilde{x})+cv\tilde{x}=0, \tag{4.1.14}$$

$$a\tilde{y}+bu\tilde{y}+c(\lambda_0-\lambda+v\tilde{y})=0, \tag{4.1.15}$$

which results from the terms inside the brackets from each derivative. The eigenvalues of the system of equations, i.e. $\det(A-\lambda I)=0$ for Eq.(4.1.13–4.1.15) results in

$$\lambda_0 = u\tilde{x} + v\tilde{y}, \tag{4.1.16}$$

$$\lambda_1 = \lambda_0 + \sqrt{\lambda_0^2 + \beta}, \tag{4.1.17}$$

$$\lambda_2 = \lambda_0 - \sqrt{\lambda_0^2 + \beta}, \tag{4.1.18}$$

From Eq.(4.1.16–4.1.18) and Eq.(4.1.13–4.1.15), the characteristic values for the primitive variables can be found in the x-direction, i.e. here denoted by p_i^{n+1}, u_i^{n+1} and v_i^{n+1}. The derivation can be found in [15, 42, 49, 109] and only the final result is stated here as

$$u_i^{n+1} = \tilde{x}R + \tilde{y}(u_0\tilde{y} - v_0\tilde{x}), \tag{4.1.19}$$

$$v_i^{n+1} = \tilde{y}R + \tilde{x}(u_0\tilde{y} - v_0\tilde{x}), \tag{4.1.20}$$

$$p_i^{n+1} = \frac{1}{2\sqrt{\lambda_0^2 + \beta}}(\lambda_1 k_2 - \lambda_2 k_1), \tag{4.1.21}$$

where

$$R = \frac{1}{2\sqrt{\lambda_0^2 + \beta}}[(p_1 - p_2) + \tilde{x}(\lambda_1 u_1 - \lambda_2 u_2) + \tilde{y}(\lambda_1 v_1 - \lambda_2 v_2)], \tag{4.1.22}$$

$$k_1 = p_1 + \lambda_1(u_1\tilde{x} + v_1\tilde{y}), \tag{4.1.23}$$

$$k_2 = p_2 + \lambda_2(u_2\tilde{x} + v_2\tilde{y}). \tag{4.1.24}$$

Here, the subscripts $j = 0, 1, 2$ refer to the primitive variable u_j, v_j and p_j obtained by either considering the zeroth, first or second eigenvalue, i.e. λ_0, λ_1 or λ_2.
To obtain the primitive variables $\mathbf{u}_j$, Godunov's Riemann solver is used in the form

$$\mathbf{u}_{j,i+1/2} = \frac{1}{2}[(1 + \text{sign}\lambda_j)\mathbf{u}_{i+1/2}^L + (1 - \text{sign}\lambda_j)\mathbf{u}_{i+1/2}^R]. \tag{4.1.25}$$

Here, $\mathbf{u}_{i+1/2}^L$ and $\mathbf{u}_{i+1/2}^R$ are the left- and right-sided interpolation of the primitive variables. Drikakis applied a third order reconstruction scheme which has been adopted for the current investigation as well of the form

$$\mathbf{u}_{i+1/2}^L = \frac{1}{6}(5\mathbf{u}_i^n - \mathbf{u}_{i-1}^n + 2\mathbf{u}_{i+1}^n), \tag{4.1.26}$$

$$\mathbf{u}_{i+1/2}^R = \frac{1}{6}(5\mathbf{u}_{i+1}^n - \mathbf{u}_{i+2}^n + 2\mathbf{u}_i^n). \tag{4.1.27}$$

A more detailed derivation of Eq.(4.1.26) and Eq.(4.1.27) will be given in Section 5.3.2. Thus, the characteristic values denoted by u_i^{n+1}, v_i^{n+1} and p_i^{n+1} are found in the x direction at the cell interface located at $i + 1/2, j$. The equations can be used analogously in the y direction for which the coefficients $\tilde{x}$ and $\tilde{y}$ have to be set appropriately. The extension to three-dimensional flows can be found in references [49, 72, 109].

The extension of the single-directional CB scheme, presented here for the AC method, can be extended to the FSAC-PP method by discarding the characteristic pressure. Since the momentum equation in the FSAC-PP method lacks the pressure gradient term, it is not required to obtain a characteristic pressure field for the time integration of the momentum equation and thus is not required. This is in line with the approach taken by Könözsy [109] and Könözsy and Drikakis [21] where the FSAC-PP method was tested in conjunction with the SCB scheme.

4.1.2 Multi-Directional Approach

This Section will give a complete derivation of the multi-directional characteristic-based scheme based on the original introduction in Razavi *et al.* [17]. The basic philosophy is depicted in Figure 4.3 for an unsteady, two-dimensional flow. In such a flow and in analogy to the compressible Euler equations, a pseudo Mach cone[2] exists along which characteristic surfaces reside (shown in orange and green). The characteristic surfaces are tangentially touching the Mach cone where at its center a pseudo pathline, shown in red, exists. The characteristic surfaces and the pseudo pathline meet at the tip of the Mach cone which is precisely at time level n. Therefore, the Mach cone originating from the x, y plane at $\tau = 0$ is for some time $\tau - \Delta\tau$ with respect to the shown state. With the knowledge of the characteristics from the previous time level, a Mach cone can be constructed for some time $\tau + \Delta\tau$, along which bi-characteristics, here shown in blue, exist which define the shape of the Mach cone at some predefined time level $n + 1$, i.e. for a fixed $\Delta\tau$. Emanating from the bi-characteristics are the pseudo acoustic wave fronts shown in violet. In the multi-direction CB scheme, it is thus required to find equations for the bi-characteristics along which compatibility equations are valid. Note also that Figure 4.3 shows a forward characteristic network, while for CFD applications a backward network will be used. In this case, the solution at M is sought (which will be at time level $n + 1$) based on the available data at n, which corresponds to $\tau = 0$ in Figure 4.3. This will be later discussed in more detail.
The derivation starts with the set of equations of the AC method and are repeated below[3]

$$\frac{1}{\beta}\frac{\partial p}{\partial \tau} + \frac{\partial u}{\partial x} + \frac{\partial v}{\partial y} = 0, \tag{4.1.28}$$

$$\frac{\partial u}{\partial \tau} + u\frac{\partial u}{\partial x} + v\frac{\partial u}{\partial y} + \frac{1}{\rho}\frac{\partial p}{\partial x} = 0, \tag{4.1.29}$$

$$\frac{\partial v}{\partial \tau} + u\frac{\partial v}{\partial x} + v\frac{\partial v}{\partial y} + \frac{1}{\rho}\frac{\partial p}{\partial y} = 0. \tag{4.1.30}$$

It has to be mentioned that only the incompressible Euler equations are used, as the inclusion of the second order derivative poses further difficulties. This is commonly omitted in the literature dealing with characteristics and the same approach is

[2]The wording "Mach cone" and "pseudo Mach cone" are used interchangeably.
[3]Here, the dimensional form is considered whereas reference [17] uses a dimensionless system.

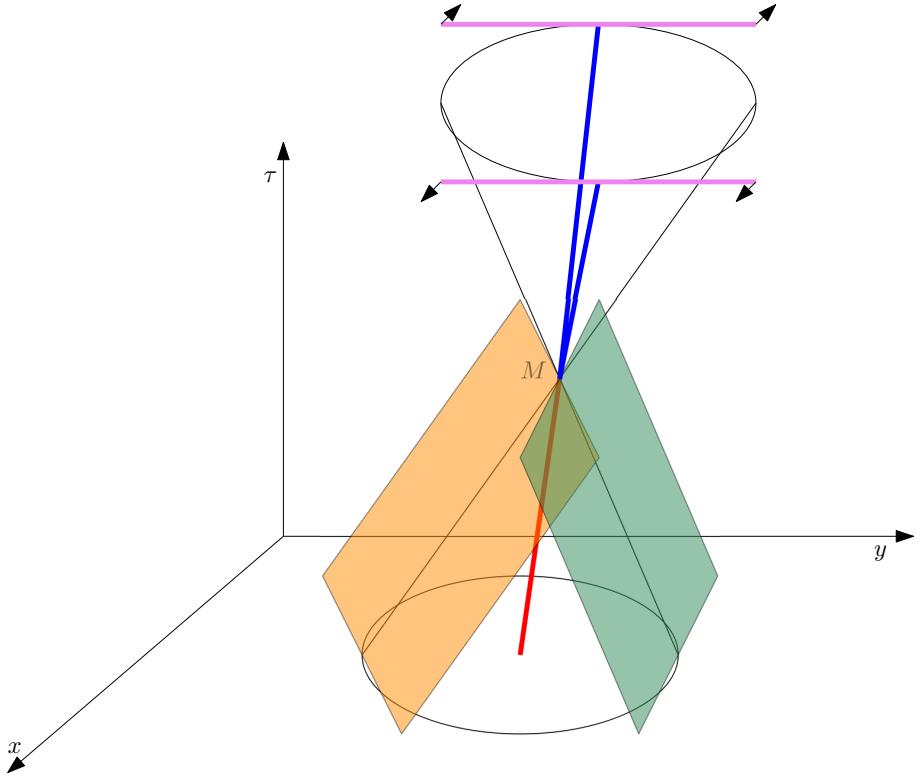

Figure 4.3: Pseudo Mach cone with the pseudo pathline (red) and two characteristic surfaces (orange and green), which all meet at point M. These will dictate how the bi-characteristics (blue) will propagate in time from which pseudo acoustic fronts (violet) emanate.

adopted here. Eq.(4.1.28–4.1.30) are the scalar, Cartesian governing equations into which the characteristic surfaces have to be introduced. For the single-directional approach, it was enough to include the characteristic pathlines through a modified Taylor series, where both space and time were considered so that curved characteristics were resolved. The multi-directional nature of the characteristic surfaces, however, would unnecessarily complicate the situation so that it is easier to simply multiply the characteristic surface into the equation. This is achieved by using the chain rule and deriving the primitive variables along the characteristic surface so that the system becomes

$$\frac{1}{\beta}\frac{\mathrm{d}p}{\mathrm{d}f}\frac{\partial f}{\partial \tau}+\frac{\mathrm{d}u}{\mathrm{d}f}\frac{\partial f}{\partial x}+\frac{\mathrm{d}v}{\mathrm{d}f}\frac{\partial f}{\partial y}=0, \tag{4.1.31}$$

$$\frac{\mathrm{d}u}{\mathrm{d}f}\frac{\partial f}{\partial \tau}+u\frac{\mathrm{d}u}{\mathrm{d}f}\frac{\partial f}{\partial x}+v\frac{\mathrm{d}u}{\mathrm{d}f}\frac{\partial f}{\partial y}+\frac{1}{\rho}\frac{\mathrm{d}p}{\mathrm{d}f}\frac{\partial f}{\partial x}=0, \tag{4.1.32}$$

$$\frac{\mathrm{d}v}{\mathrm{d}f}\frac{\partial f}{\partial \tau}+u\frac{\mathrm{d}v}{\mathrm{d}f}\frac{\partial f}{\partial x}+v\frac{\mathrm{d}v}{\mathrm{d}f}\frac{\partial f}{\partial y}+\frac{1}{\rho}\frac{\mathrm{d}p}{\mathrm{d}f}\frac{\partial f}{\partial y}=0. \tag{4.1.33}$$

Note here that $\mathbf{u}$ is a function of f alone after the transformation and f becomes a function of x, y and τ, hence, a mix of partial and ordinary differentials exists. The metric coefficients shall from now on be expressed as $\partial f/\partial \tau = f_\tau$, $\partial f/\partial x = f_x$ and $\partial f/\partial y = f_y$. Multiplying Eq.(4.1.31–4.1.33) by $\mathrm{d}f$ yields

$$\frac{f_\tau}{\beta}\mathrm{d}p + f_x\mathrm{d}u + f_y\mathrm{d}v = 0, \tag{4.1.34}$$

$$f_\tau\mathrm{d}u + uf_x\mathrm{d}u + vf_y\mathrm{d}u + \frac{f_x}{\rho}\mathrm{d}p = 0, \tag{4.1.35}$$

$$f_\tau\mathrm{d}v + uf_x\mathrm{d}v + vf_y\mathrm{d}v + \frac{f_y}{\rho}\mathrm{d}p = 0, \tag{4.1.36}$$

which can be expressed in matrix form as

$$\begin{bmatrix} f_\tau/\beta & f_x & f_y \\ f_x/\rho & \Psi & 0 \\ f_y/\rho & 0 & \Psi \end{bmatrix} \begin{bmatrix} \mathrm{d}p \\ \mathrm{d}u \\ \mathrm{d}v \end{bmatrix} = \begin{bmatrix} 0 \\ 0 \\ 0 \end{bmatrix}, \tag{4.1.37}$$

where we have defined

$$\Psi = f_\tau + uf_x + vf_y. \tag{4.1.38}$$

It has been mentioned that the definition of the characteristics requires that the derivative along the characteristics may be discontinuous. This is also shown in Appendix A based on physical reasoning which is then mathematically proven. It is also shown that the compatibility equation can be derived by requiring that the determinant of the matrix, holding the coefficients of the system of equations, needs to become zero. Thus, it is found that

$$\det\left(\begin{bmatrix} f_\tau/\beta & f_x & f_y \\ f_x/\rho & \Psi & 0 \\ f_y/\rho & 0 & \Psi \end{bmatrix}\right) = \Psi^2\left(\frac{f_\tau}{\beta}\right) - \Psi\frac{f_y^2}{\rho} - \Psi\frac{f_x^2}{\rho} = 0,$$

$$\Psi^2 - \Psi\frac{\beta}{\rho f_\tau}\left(f_x^2 + f_y^2\right) = 0. \tag{4.1.39}$$

Using the substitution $z = (\beta/(\rho f_\tau))(f_x^2 + f_y^2)$, we can solve the quadratic equation as

$$\Psi^2 - \Psi z = 0,$$

$$\Psi^2 - \Psi z + \left(\frac{z}{2}\right)^2 = \left(\frac{z}{2}\right)^2,$$

$$\left(\Psi - \left(\frac{z}{2}\right)\right)^2 = \left(\frac{z}{2}\right)^2.$$

Taking the positive and negative square root of both sides yields

$$\Psi = \left(\frac{z}{2}\right) \pm \left(\frac{z}{2}\right)$$

so that the final result for Ψ becomes

$$\Psi_1 = 0, \qquad \Psi_2 = \frac{\beta}{\rho f_\tau}\left(f_x^2 + f_y^2\right). \tag{4.1.40}$$

Before continuing, an important relation between the characteristic surface's normal vector and its derivative needs to be determined which will help to understand Eq.(4.1.40). To do so, an arbitrary surface of the form $f(x, y, z) = D$ is considered, where D is a constant[4]. Taking the derivative of the surface with respect to time one finds that

$$\frac{\partial f}{\partial t} = \frac{\mathrm{d}D}{\mathrm{d}t} = 0, \tag{4.1.41}$$

or, using the chain rule,

$$\frac{\partial f}{\partial x}\frac{\mathrm{d}x}{\mathrm{d}t} + \frac{\partial f}{\partial y}\frac{\mathrm{d}y}{\mathrm{d}t} + \frac{\partial f}{\partial z}\frac{\mathrm{d}z}{\mathrm{d}t} = 0. \tag{4.1.42}$$

The ordinary derivatives $\mathrm{d}x/\mathrm{d}t$, $\mathrm{d}y/\mathrm{d}t$ and $\mathrm{d}z/\mathrm{d}t$ are the velocity components u, v and w but also characteristics. Therefore, Eq.(4.1.42) can be rewritten as

$$f_x \cdot u + f_y \cdot v + f_z \cdot w = \nabla f \cdot \mathbf{u} = 0. \tag{4.1.43}$$

Since the velocity vector has to lie on the characteristic surface by definition (see Zucrow and Hoffman [24,37] and their definition of the *interior operator*), it follows that ∇f has to be normal to the characteristic surface itself. Thus, $\nabla f = \vec{N}$. If the z component is considered as the time axis (τ), and recalling that we have defined $\Psi = f_\tau + uf_x + vf_y$, a new definition could be given as

$$\Psi = N_\tau + uN_x + vN_y = \mathbf{u} \cdot \vec{N}, \tag{4.1.44}$$

where the primitive variable vector is now written as $\mathbf{u} = [1, u, v]^T$ with the corresponding normal vector $\vec{N} = [N_\tau, N_x, N_y]^T$. Since the actual length of the normal vector is not important, it can be rescaled to represent the unit normal vector $\mathbf{n}$ so that

$$\Psi = n_\tau + un_x + vn_y = \mathbf{u} \cdot \mathbf{n}, \tag{4.1.45}$$

or

$$\Psi = \mathbf{u} \cdot \mathbf{n} + n_\tau = \nabla f \cdot \mathbf{u}. \tag{4.1.46}$$

Since the velocity vector has to be tangential to the characteristic surface, it follows that its scalar product with the normal vector must be zero. Therefore, Eq.(4.1.44) and Eq.(4.1.45) are indeed valid solutions for the characteristic surface coming from the definition of Eq.(4.1.38). We can further simplify Eq.(4.1.40) by using the fact that $n_x^2 + n_y^2 = 1$ so that we have

$$\Psi_1 = 0, \qquad \Psi_2 = \frac{\beta}{\rho \hat{f}_\tau} = \frac{\beta}{\rho n_\tau}, \tag{4.1.47}$$

[4]This is a simplification, as f_τ in Eq.(4.1.40) for Ψ_2 will be shown to depend on the velocity which changes in time. The common approach in the literature is to set the velocity locally constant so that Ψ_2 becomes a (pseudo) Mach cone, see Figure 4.3. If the velocity is not set to be constant, a (pseudo) Mach conoid would emanate instead.

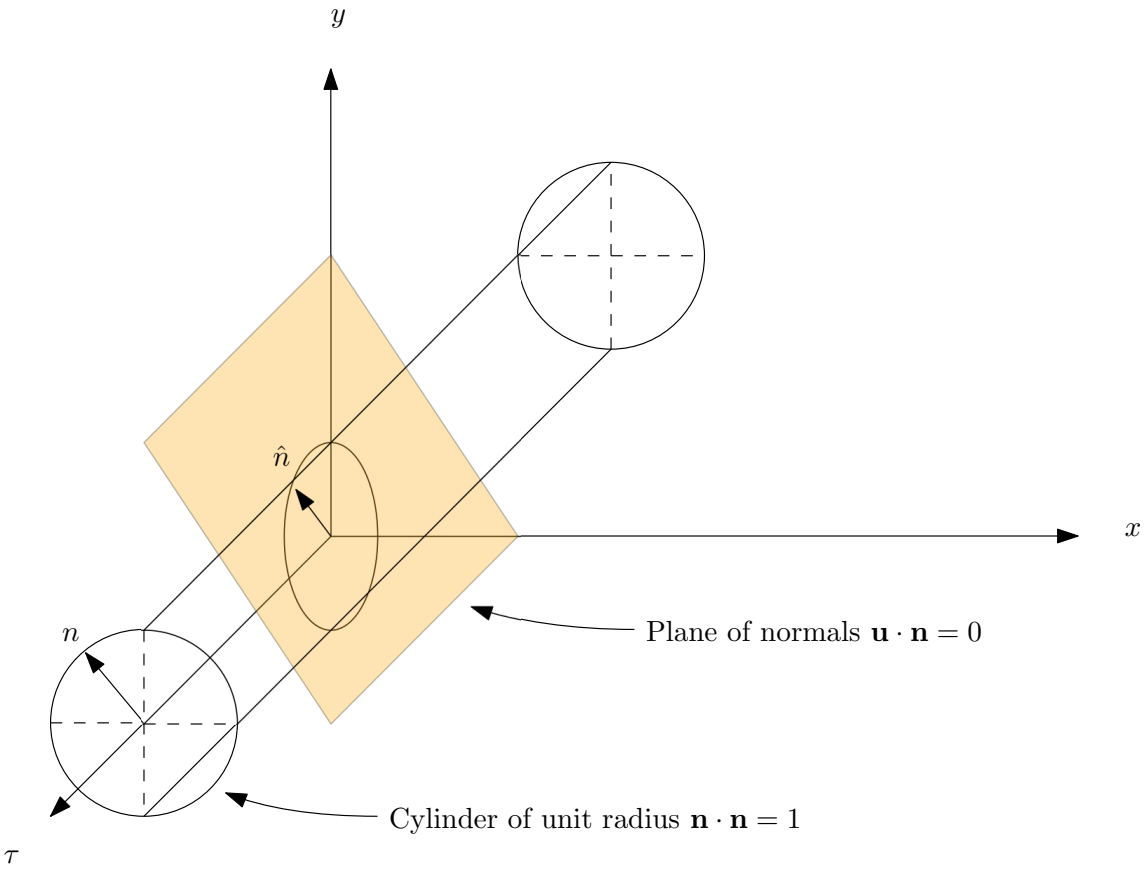

Figure 4.4: Intersection of the plane of normals for the stream surfaces with the unit cylinder projected along the time axis.

with $\hat{f}_\tau = n_\tau = f_\tau / \sqrt{f_x^2 + f_y^2}$. Hence, by equating the solutions of Eq.(4.1.47) to our definition of Ψ in Eq.(4.1.38), we can derive two independent characteristic surfaces which will be done in the following. This is in contrast to the single-directional case where only one characteristic was determined. In-fact, this is also the reason why the single-directional approach cannot be applied to multi-directional characteristics, as it would suppress the presence of a second characteristic surface. Note as well that $\mathbf{u} = (u, v)^T$ and $\mathbf{n} = (n_x, n_y)^T$ are the primitive variable and normal vector, respectively, in space with respect to velocity. The following discussion is dedicated to finding the compatibility equations along those characteristic surfaces and then to determine the characteristic equations which describe the surfaces themselves.

The first case that is considered is $\mathbf{u} \cdot \mathbf{n} = 0$, which results from equating Eq.(4.1.45) to Ψ_1 in Eq.(4.1.47). Since the normal vector of unit length is used, $\mathbf{n} \cdot \mathbf{n} = n_x^2 + n_y^2 = 1$ is always true. These are the only two, linear independent, equations that can be found for the three components of the characteristic surface f_x, f_y and f_τ. Thus, the problem has to be solved from a geometrical viewpoint which is illustrated in Figure 4.4. Let us define the plane of normals as $\mathbf{u} \cdot \mathbf{n} = 0$ and the cylinder of unit radius as $\mathbf{n} \cdot \mathbf{n} = 1$. The cylinder of unit radius is centred on the time axis and can be projected along it. The cylinder will intersect the plane of normals and form an ellipsoid at its intersection. Any arbitrarily chosen normal $\mathbf{n}$ can thus be projected

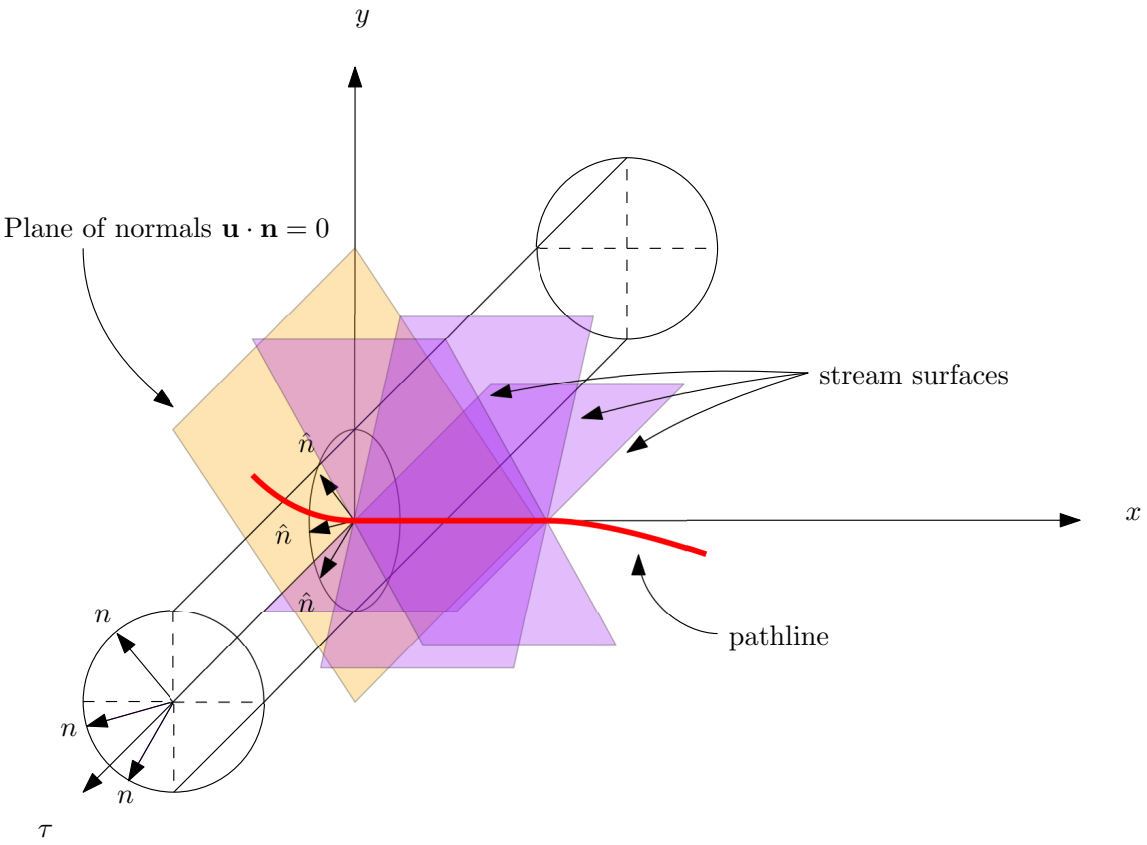

Figure 4.5: Construction of three stream surfaces (purple) and the determination the pseudo pathline (red) as the intersection of all stream surfaces.

into the plane of normals and is denoted by $\hat{n}$. Emanating from each normal vector that is projected in this way is one particular surface that is perpendicular to the projected normal vector. In-fact, this procedure can be carried out for an infinite number of surfaces and is shown for three surfaces in Figure 4.5. The formed surfaces, shown here in purple, are referred to as stream surfaces in the compressible literature and the naming convention is adopted here.

The envelope of all stream surfaces which are found in that manner form an intersecting line which, at its origin, i.e. where it intersects the plane of normals, is tangential to the velocity vector. Therefore, the intersecting line represents the pseudo pathline. This can be also understood from the fact that $\mathbf{u} \cdot \mathbf{n} = 0$. For this equation to be true, the velocity has to be perpendicular to the normal vectors. Since all the normal vectors lie in the plane of normals by definition and the stream surfaces are perpendicular to the plane of normals, it has to follow that the intersecting line of the stream surfaces is tangential to the velocity vector. To find the compatibility equation along the pseudo path line for the primitive variables, the result of $\Psi = 0$ is substituted into Eq.(4.1.37) so that the following system is obtained

$$\begin{bmatrix} f_\tau/\beta & f_x & f_y \\ f_x/\rho & 0 & 0 \\ f_y/\rho & 0 & 0 \end{bmatrix} \begin{bmatrix} \mathrm{d}p \\ \mathrm{d}u \\ \mathrm{d}v \end{bmatrix} = \begin{bmatrix} 0 \\ 0 \\ 0 \end{bmatrix}. \tag{4.1.48}$$

From Eq.(4.1.48), three compatibility equations are obtained as

$$\frac{f_\tau}{\beta}\mathrm{d}p + f_x\mathrm{d}u + f_y\mathrm{d}v = 0, \tag{4.1.49}$$

$$\frac{f_x}{\rho}\mathrm{d}u = 0, \tag{4.1.50}$$

$$\frac{f_y}{\rho}\mathrm{d}v = 0, \tag{4.1.51}$$

After closer examination, however, it becomes apparent that the above obtained compatibility equations are not sufficient to determine the characteristic values of the primitive variables. This can be shown by bringing the coefficient matrix in Eq.(4.1.48) in Row-Echelon form which yields

$$\mathcal{A} = \begin{bmatrix} \frac{f_\tau}{\beta} & f_x & f_y \\ 0 & \frac{-f_x^2\beta}{\rho f_\tau} & \frac{-f_x f_y \beta}{\rho f_\tau} \\ 0 & 0 & 0 \end{bmatrix}. \tag{4.1.52}$$

Since the third row is filled with zeros, matrix $\mathcal{A}$ has $\mathrm{Rank}(\mathcal{A}) = 2$. Since it is a 3×3 matrix, it is rank deficient and thus it is not possible to determine three linear independent compatibility equations from Eq.(4.1.48). Therefore, the second result of Eq.(4.1.47) has to be considered as well.

Recalling that the second characteristic surface was obtained for $\Psi = \beta/(\rho f_\tau)$, the same procedure as before can be applied. A second equation is found again as $\mathbf{n}\cdot\mathbf{n} = n_x^2 + n_y^2 = 1$ but the problem prevails that a third independent equation is absent and geometrical constraints have to be introduced to obtain the compatibility equations.
Figure 4.6 shows the case for $\Psi = \beta/(\rho f_\tau)$, where the plane of normals is now non-homogeneous. This has the consequence that the plane of normals is not passing through the origin of the x, y plane.
This is also illustrated in Figure 4.7, where both cases for $\Psi = 0$ and $\Psi = \beta/(\rho f_\tau)$ are shown. While the solution of $\Psi_1 = 0$ in Eq.(4.1.47) is referred to as the stream surface, the second solution with $\Psi_2 = \beta/(\rho n_\tau)$ is termed the wave surface which is also named in accordance with the compressible literature. Figure 4.7 shows the x, τ plane with the y direction normal to the view so that the plane of normals for both the stream and the wave surface reduce to lines in this representation. The fact that $\mathbf{u}\cdot\mathbf{n} = 0$ passes through the origin while $\mathbf{u}\cdot\mathbf{n} = \beta/(\rho n_\tau)$ is not, can be simply seen by setting the normal vector to zero. Thus, for the stream surface, the left-hand side becomes zero and since it is a homogeneous equation, it passes through the

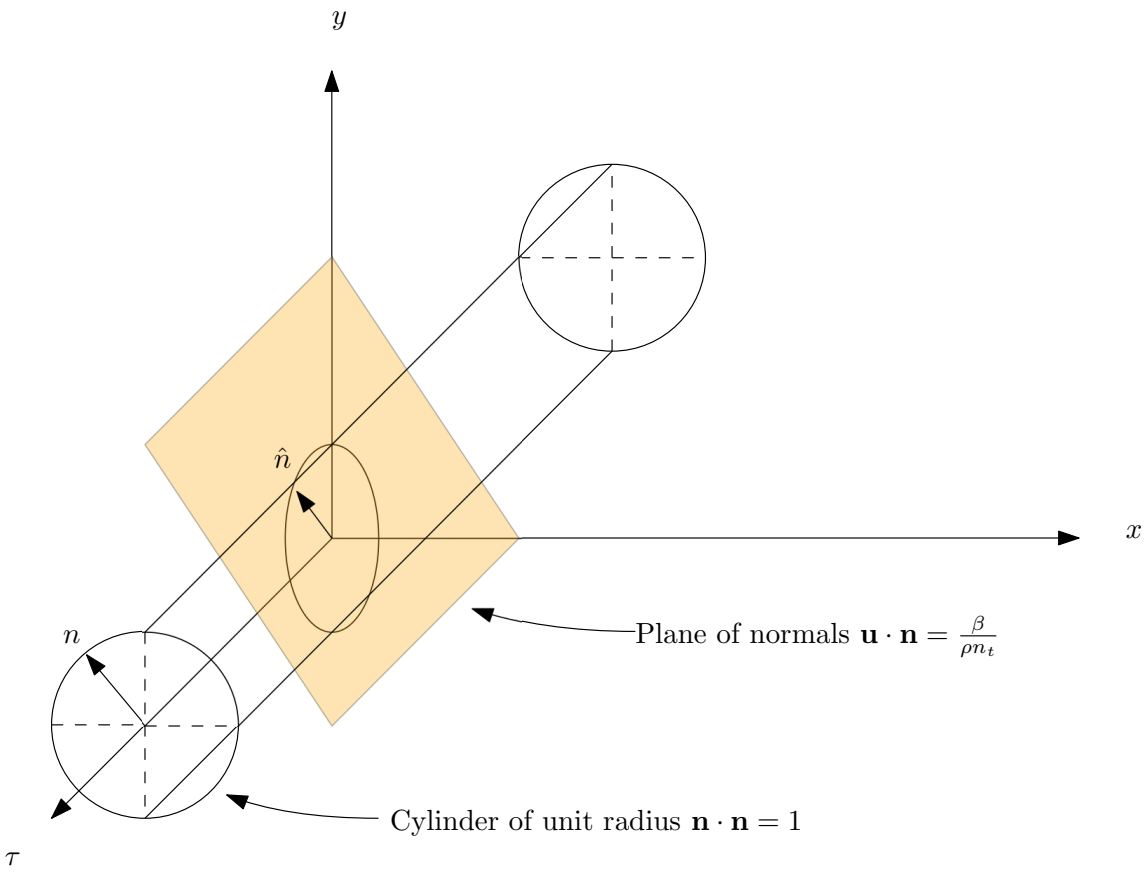

Figure 4.6: Intersection of the plane of normals for the wave surfaces with the unit cylinder projected along the time axis.

origin. However, the wave surface is not equal to zero for a vanishing normal vector and thus cannot pass through the origin. For the stream surface, this means that the envelope of the planes, corresponding to the normal vectors inside the plane of normals, form a pathline, as previously mentioned. This is shown as a dashed line. For the wave surface, however, it means that two characteristic lines emanate from the plane of normals which are subsequently called the bi-characteristics and shown by the dashed lines. By taking an infinite number of planes, these would tangentially touch a pseudo Mach conoid which is also shown in Figure 4.8 for two selected normal vectors $\mathbf{n}$ which are projected into the plane of normals and denoted by $\hat{n}$. These two vectors produce a set of two bi-characteristics so that a total of four wave surfaces are obtained. The first set is obtained by the purple wave surfaces and the bi-characteristics are shown in purple as well. Similarly, the second set corresponding to the red wave surfaces and bi-characteristics are obtained. From Figure 4.7, it can be seen that the Mach conoid can be curved in space. The pseudo Mach cone, on the other hand, is defined as a straight cone, which is tangential to the pseudo Mach conoid at its origin, at M in Figure 4.3. The compatibility equations corresponding to the wave surface are therefore found by inserting $\Psi = \beta/(\rho f_\tau)$ into Eq.(4.1.47) which yields

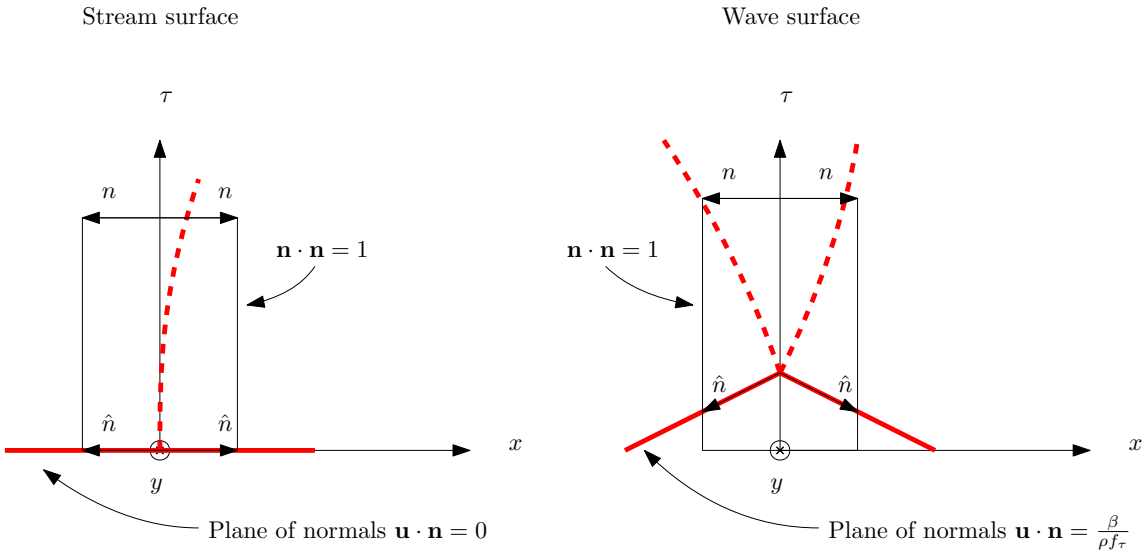

Figure 4.7: Comparison of the plane of normals for the stream and wave surfaces. While all stream surfaces lie in the x, y plane, the wave surfaces intersect the time axis at an instance not equal to zero.

$$\begin{bmatrix} f_\tau/\beta & f_x & f_y \\ f_x/\rho & \frac{\beta}{\rho f_\tau} & 0 \\ f_y/\rho & 0 & \frac{\beta}{\rho f_\tau} \end{bmatrix} \begin{bmatrix} \mathrm{d}p \\ \mathrm{d}u \\ \mathrm{d}v \end{bmatrix} = \begin{bmatrix} 0 \\ 0 \\ 0 \end{bmatrix}. \tag{4.1.53}$$

The corresponding compatibility equations are found as

$$\frac{f_\tau}{\beta}\mathrm{d}p + f_x\mathrm{d}u + f_y\mathrm{d}v = 0, \tag{4.1.54}$$

$$\frac{f_x}{\rho}\mathrm{d}p + \frac{\beta}{\rho f_\tau}\mathrm{d}u = 0, \tag{4.1.55}$$

$$\frac{f_y}{\rho}\mathrm{d}p + \frac{\beta}{\rho f_\tau}\mathrm{d}v = 0. \tag{4.1.56}$$

By considering again the coefficient matrix in Eq.(4.1.53) separately, its Row-Echelon form calculates as

$$\mathcal{A} = \begin{bmatrix} f_\tau & f_x & f_y \\ 0 & \frac{-\beta(f_x^2-1)}{\rho f_\tau} & \frac{-\beta f_x f_y}{\rho f_\tau} \\ 0 & 0 & \frac{\beta(f_x^2+f_y^2-1)}{\rho f_\tau(f_x^2-1)} \end{bmatrix} \tag{4.1.57}$$

and since all rows are filled and are independent of each other, we find that $\mathrm{Rank}(\mathcal{A}) = 3$ which means that three independent compatibility equations have been found. This is, by itself, a remarkable feature of the method of characteristics applied to incompressible flows. Rusanov [14] revisited the method of characteristics for the

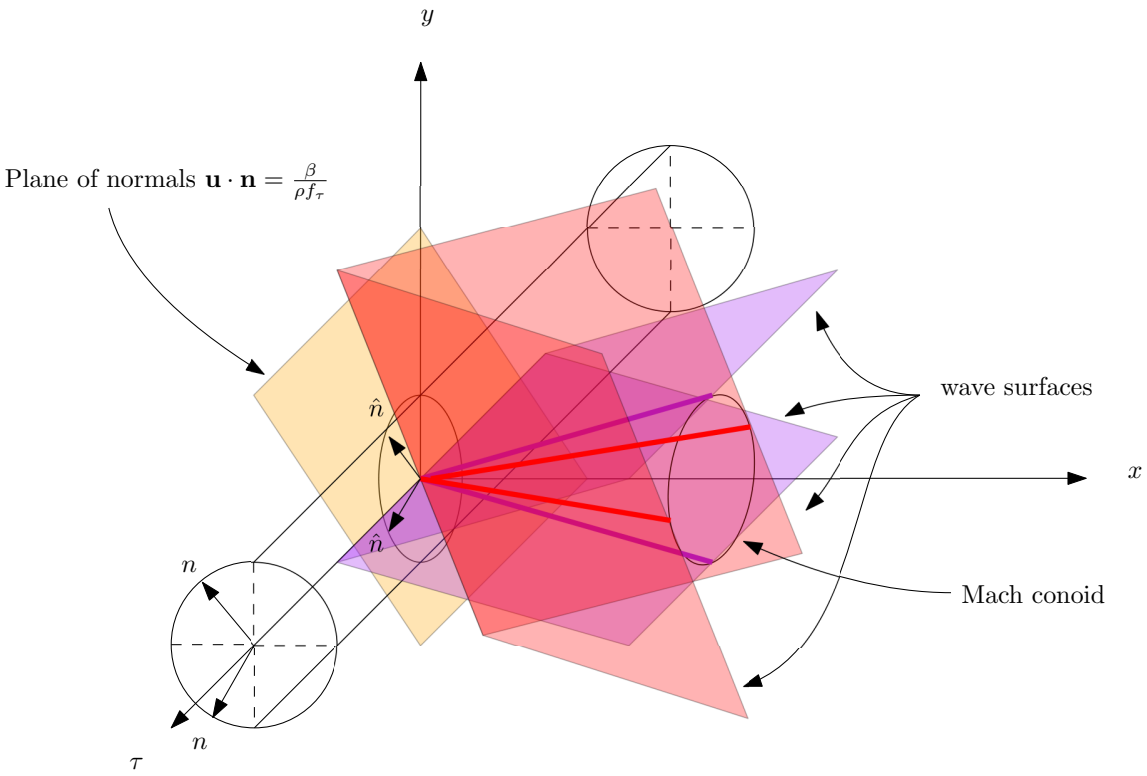

Figure 4.8: Construction of two sets of wave surfaces in red and purple corresponding to its projected normal vector. The formed bi-characteristics are shown here in red and purple, respectively, to show their association to their respective wave surface and correspond to the blue bi-characteristics in Figure 4.3.

Euler equations and gave a general derivation, applicable to any hyperbolic system of equations. However, he also showed that it is not enough to consider only the compatibility equations obtained from either the stream or wave surfaces alone and that a mix of both is needed to arrive at a system of compatibility equations which are linear independent from each other. This can be stated as

Rusanov's Theorem on characteristic wave surfaces[5]:
"*All characteristic stream and wave surfaces obtained from the compressible Euler equations are necessarily rank deficient.*"

This is not surprising, however, since the equation of state is used for the compressible Navier–Stokes and Euler equations to close the system. That means that there are four independent transport equations for a two-dimensional compressible fluid (i.e. for velocity in x and y, density and temperature) while there are five primitive variables (the aforementioned plus the pressure). The lack of a transport equation for the pressure results in rank deficient coefficient matrices for both stream and wave surfaces. For incompressible flows, however, a transport equation for the pressure has to be engineered to close the system of equations, as the equation of states approach does not work. Hence, as seen in the AC method, a third transport

[5]Rusanov did explicitly state this theorem but it can be deducted from his results.

equation for the pressure is constructed so that u, v and p can be computed from their own transport equation. This leads to a non-rank deficient system of compatibility equations, at least for the wave surface. Therefore, the stream surface can be discarded from this point onwards and does not need further considerations.

Eq.(4.1.54–4.1.56) are the compatibility equations and can be discretized to get characteristic expressions for the primitive variables. Before doing so, the surface derivatives are exchanged for the normal component of the surface. The normal vector in space is then given as

$$\mathbf{n} = \begin{bmatrix} n_x \\ n_y \end{bmatrix} = \begin{bmatrix} \cos\phi \\ \sin\phi \end{bmatrix}, \tag{4.1.58}$$

which is taken from Razavi *et al.* [17]. This choice of normal vector components ensures that n_x and n_y are always perpendicular and thus indeed independent of each other. The normal component in time, i.e. n_τ cannot be obtained in the same manner, however, from the stream surface we have $\Psi = \mathbf{u}\cdot\mathbf{n} = n_\tau + u\cdot n_x + v\cdot n_y = n_\tau + u\cdot\cos\phi + v\cdot\sin\phi = \beta/(\rho n_\tau)$. This can be recast as a quadratic equation for which two solutions exist (i.e. along the bi-characteristics). Using the substitution of $z = u\cdot\cos\phi + v\cdot\sin\phi$, the solution for n_τ becomes

$$\begin{aligned}
n_\tau^2 + n_\tau(u\cdot\cos\phi + v\cdot\sin\phi) - \frac{\beta}{\rho} &= 0,\\
n_\tau^2 + n_\tau z + \left(\frac{z}{2}\right)^2 &= \left(\frac{z}{2}\right)^2 + \frac{\beta}{\rho},\\
\left(n_\tau + \left(\frac{z}{2}\right)\right)^2 &= \left(\frac{z}{2}\right)^2 + \frac{\beta}{\rho},\\
n_\tau + \left(\frac{z}{2}\right) &= \pm\sqrt{\left(\frac{z}{2}\right)^2 + \frac{\beta}{\rho}},\\
n_\tau &= \frac{-z \pm \sqrt{z^2 + 4\frac{\beta}{\rho}}}{2},
\end{aligned}$$

and finally, after re-substituting z, the normal direction in time for the bi-characteristics are found as

$$n_{\tau,1,2} = \frac{-(u\cdot\cos\phi + v\cdot\sin\phi) \pm \sqrt{(u\cdot\cos\phi + v\cdot\sin\phi)^2 + 4\frac{\beta}{\rho}}}{2}. \tag{4.1.59}$$

The angle of ϕ can be freely chosen, much in the same manner as the stream and wave surfaces could be freely chosen. In-fact, it was necessary to use an infinite number of stream and wave surfaces to determine the shape of their envelope. However, for computational reasons and practicality, only a few directions will be chosen so that ϕ can be fixed. In almost all the literature on multi-directional CB schemes, four directions are chosen which is adopted here. Only Fathollahi and Zamzamian [57] considered eight directions, or wave angles of ϕ, which showed no significant difference in the accuracy but a favourable increase in convergence rate.

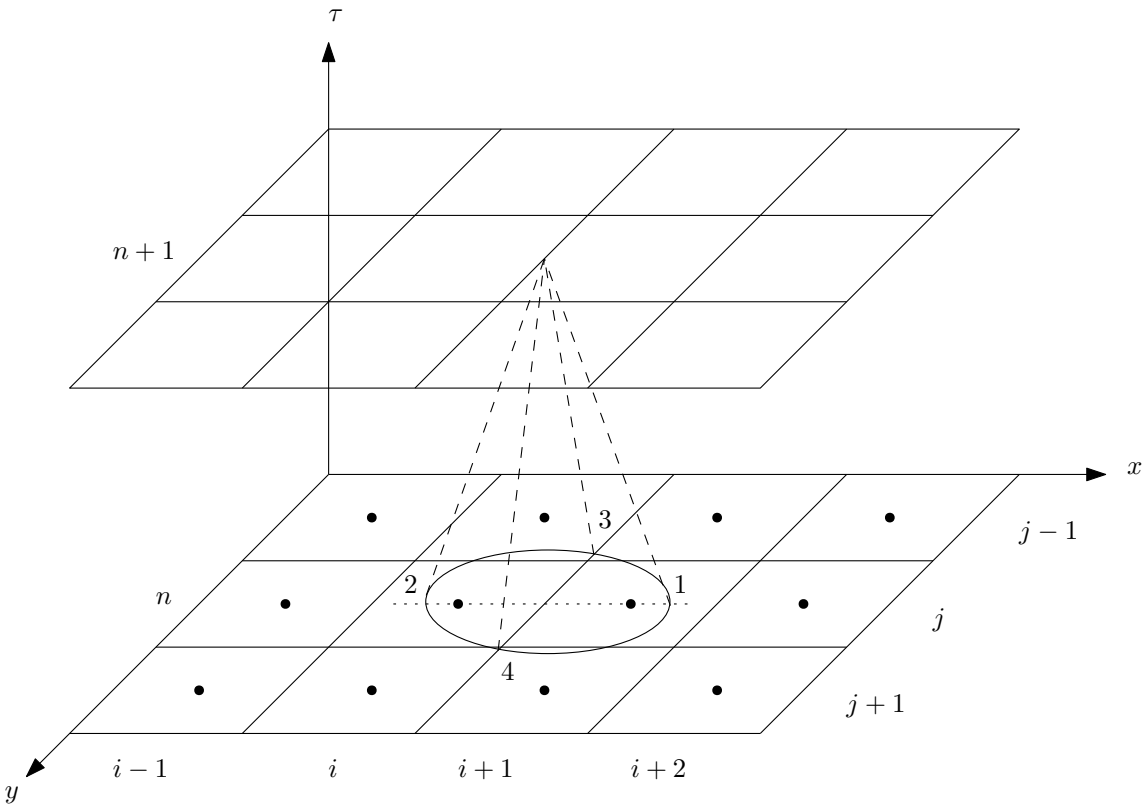

Figure 4.9: The time discretisation procedure for the multi-directional characteristic-based approach. The pseudo Mach cone intersects the time level n where the four characteristic lines are found (1,2,3 and 4). Characteristic line 1 and 2 lie on the intersection of the control volume centroid at i, j and $i+1, j$ while the characteristic lines 3 and 4 emanate from a line that goes through the cell interface at $i + 1/2$.

The discretisation procedure with four selected wave directions on a Cartesian grid is shown in Figure 4.9. Here, the pseudo Mach cone is shown which emanates from the time level $n + 1$ back into the current time level n (which makes it a backward characteristic network of characteristics, just as in the single-directional approach) and the solution is sought for $\mathbf{u}_{i+1/2,j}$, i.e the inter-cell values of the primitive variables. Using the positive x direction as the axis of reference to measure ϕ and going in a counter-clockwise direction, the following values have been selected: $\phi_1 = 0°$, $\phi_2 = 180°$, $\phi_3 = 90°$ and $\phi_4 = 270°$. This ensures that, for Cartesian grids, the line spanned by the cell centroids at i, j and $i + 1, j$ goes through the centre of the cell interface at $i + 1/2, j$ and intersects the first set of bi-characteristics (labelled 1 and 2). This line is shown as a dashed line in Figure 4.9. The second set of bi-characteristics (labelled 3 and 4) pass through the cell interfaces at $i + 1/2$ and along j. To determine the intersection of the characteristics with the plane at time level n, the characteristic equations of the surfaces themselves are needed. The derivation of the characteristic equations along the pseudo Mach conoid is a lengthy procedure and requires knowledge in differential geometry. Razavi *et al* [17], however, introduced a much simpler, shorter and more elegant way to obtain the characteristic equation of the surface which is shown here. Considering the time

derivative of an assumed characteristic surface again, one obtains

$$\frac{\partial f}{\partial \tau} + \frac{\mathrm{d}x}{\mathrm{d}\tau}\frac{\partial f}{\partial x} + \frac{\mathrm{d}y}{\mathrm{d}\tau}\frac{\partial f}{\partial y} = 0. \tag{4.1.60}$$

Rewriting the above yields

$$n_\tau + \frac{\mathrm{d}x}{\mathrm{d}\tau}\cos\phi + \frac{\mathrm{d}y}{\mathrm{d}\tau}\sin\phi = 0 \tag{4.1.61}$$

This is the same equation which was obtain previously for the stream surface, i.e. $\Psi = \mathbf{u} \cdot \nabla f = 0$. Since the time derivative of the assumed characteristic surface should be valid for any characteristic surface, Eq.(4.1.61) should also hold for the wave surface so that two equations are obtained as

$$n_\tau + \frac{\mathrm{d}x}{\mathrm{d}\tau}\cos\phi + \frac{\mathrm{d}y}{\mathrm{d}\tau}\sin\phi = 0, \tag{4.1.62}$$

$$n_\tau + u\cos\phi + v\sin\phi = \frac{\beta}{\rho n_\tau}. \tag{4.1.63}$$

Since $u = \mathrm{d}x/\mathrm{d}\tau$ and $v = \mathrm{d}y/\mathrm{d}\tau$, both versions in Eq.(4.1.62) and Eq.(4.1.63) can be used, which will be useful to determine the characteristic equation itself. Alternatively, it can be argued that the stream surface represents the streamlines and thus the velocity components can be used instead. This is done by subtracting Eq.(4.1.62) from Eq.(4.1.63) so that the following equation is obtained

$$\left(u - \frac{\mathrm{d}x}{\mathrm{d}\tau}\right)\cos\phi + \left(v - \frac{\mathrm{d}y}{\mathrm{d}\tau}\right)\sin\phi = \frac{\beta}{\rho n_\tau}. \tag{4.1.64}$$

Eq.(4.1.64) is indeed the characteristic equation of the system. Figure 4.10 shows this procedure in detail. The stream surface (purple) is subtracted from the wave surface (red) which results in a new surface (green). Considering only the tangents of the stream and wave surface, it can be seen that the corresponding line produced on the new (green) surface is indeed the local characteristic in the time plane which describes the propagation of the Mach cone at time level n. The tangent's directions are indicated by the arrow to show that the subtraction results in the characteristic line (green). It is possible to further simplify Eq.(4.1.64) by splitting it into its x and y direction component. After reordering terms and the splitting, the final two characteristic equations in x and y are thus obtained as

$$\frac{\mathrm{d}x}{\mathrm{d}\tau} = u - \frac{\beta}{\rho n_\tau \cos\phi}, \tag{4.1.65}$$

$$\frac{\mathrm{d}y}{\mathrm{d}\tau} = v - \frac{\beta}{\rho n_\tau \sin\phi}. \tag{4.1.66}$$

The same would be achieved by following the classical approach presented in Zucrow and Hoffman [24, 37] and Delany [25]. Before proceeding with the discretisation of the compatibility and characteristic equations, i.e. Eq.(4.1.54–4.1.56) and Eq.(4.1.65–4.1.66), respectively, it is important to mention that so far it has been

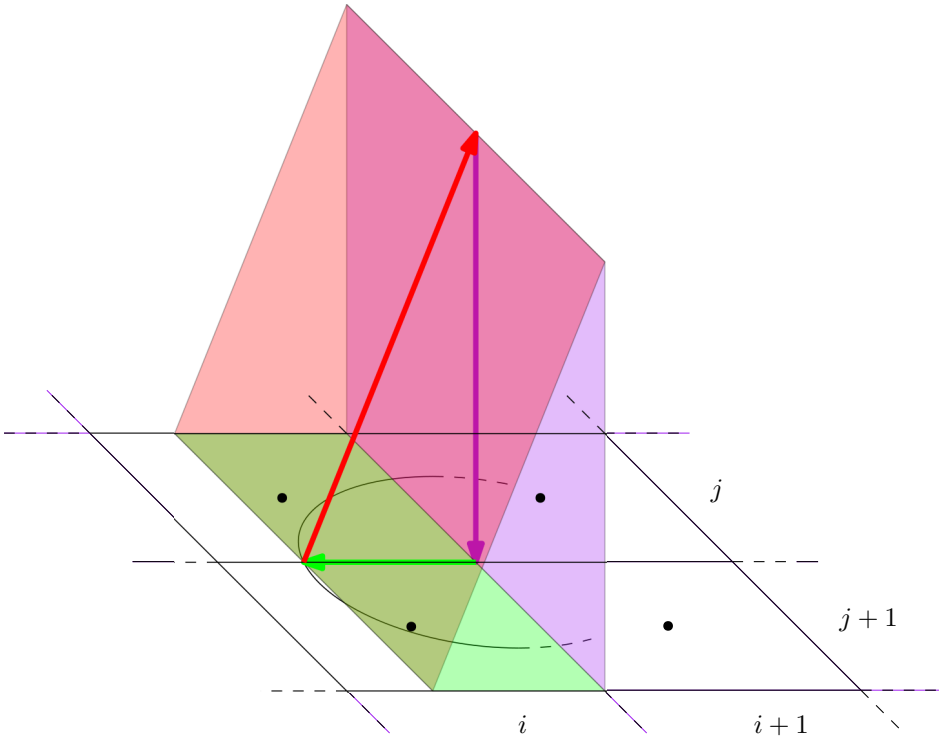

Figure 4.10: The construction of a characteristic surface (green) which represents the propagation of the Mach cone via the subtraction of the stream surface (purple) from the wave surface (red). The tangents of each surface are shown in their respective plane colour.

assumed that the pseudo Mach cone and conoid emanate from point M (Figure 4.3) which is given in the literature to be at time level $n+1$. If that would be the case, then the inter-cell values at time level $n+1$ could be obtained by the method described in this and the previous Section on the single-directional approach. This would imply that the equations of motion do not need to be integrated in time. However, this is not the case and the naming convention of time level $n+1$ is somewhat unfortunate. Rather, it should be referred to as an intermediate time level, say $(n+1)^*$. The characteristic values obtained from either the single- or multi-directional approach are then used in the flux differentiation and time integration procedure which will result in the true value at $n+1$ for the primitive variables.

Returning to the process of discretizing the compatibility equations, Eq.(4.1.54–4.1.56) can be written in expanded form as

$$\frac{f_\tau}{\beta}(p_{i+1/2}^{(n+1)^*} - p_j^n) + (u_{i+1/2}^{(n+1)^*} - u_j^n)\cos\phi + (v_{i+1/2}^{(n+1)^*} - v_j^n)\sin\phi = 0, \tag{4.1.67}$$

$$\frac{\cos\phi}{\rho}(p_{i+1/2}^{(n+1)^*} - p_j^n) + \frac{\beta}{\rho f_\tau}(u_{i+1/2}^{(n+1)^*} - u_j^n) = 0, \tag{4.1.68}$$

$$\frac{\sin\phi}{\rho}(p_{i+1/2}^{(n+1)^*} - p_j^n) + \frac{\beta}{\rho f_\tau}(v_{i+1/2}^{(n+1)^*} - v_j^n) = 0, \tag{4.1.69}$$

where $j = 1, 2, 3, 4$ is associated with the four chosen characteristic wave directions

ϕ. These equations can now be discretized along each wave angle of ϕ which yields

For $\phi = 0°$:

$$\frac{f_\tau}{\beta}(p_{i+1/2}^{(n+1)^*} - p_1^n) + (u_{i+1/2}^{(n+1)^*} - u_1^n) = 0, \tag{4.1.70}$$

$$(p_{i+1/2}^{(n+1)^*} - p_1^n) + \frac{\beta}{f_\tau}(u_{i+1/2}^{(n+1)^*} - u_1^n) = 0. \tag{4.1.71}$$

For $\phi = 90°$:

$$\frac{f_\tau}{\beta}(p_{i+1/2}^{(n+1)^*} - p_3^n) + (v_{i+1/2}^{(n+1)^*} - v_3^n) = 0, \tag{4.1.72}$$

$$(p_{i+1/2}^{(n+1)^*} - p_3^n) + \frac{\beta}{f_\tau}(v_{i+1/2}^{(n+1)^*} - v_3^n) = 0. \tag{4.1.73}$$

For $\phi = 180°$:

$$\frac{f_\tau}{\beta}(p_{i+1/2}^{(n+1)^*} - p_2^n) - (u_{i+1/2}^{(n+1)^*} - u_2^n) = 0, \tag{4.1.74}$$

$$-(p_{i+1/2}^{(n+1)^*} - p_2^n) + \frac{\beta}{f_\tau}(u_{i+1/2}^{(n+1)^*} - u_2^n) = 0. \tag{4.1.75}$$

For $\phi = 270°$:

$$\frac{f_\tau}{\beta}(p_{i+1/2}^{(n+1)^*} - p_4^n) - (v_{i+1/2}^{(n+1)^*} - v_4^n) = 0, \tag{4.1.76}$$

$$-(p_{i+1/2}^{(n+1)^*} - p_4^n) + \frac{\beta}{f_\tau}(v_{i+1/2}^{(n+1)^*} - v_4^n) = 0. \tag{4.1.77}$$

The values of the primitive variables at location $j = 1, 2, 3, 4$ are the intersection of the bi-characteristics and the time level n. Their location can be found by integrating Eq.(4.1.65–4.1.66), i.e.

in the x direction:

$$\int \mathrm{d}x = \int u \mathrm{d}\tau - \int \frac{\beta}{\rho n_\tau \cos\phi} \mathrm{d}\tau, \tag{4.1.78}$$

$$\Delta x = \left(u - \frac{\beta}{\rho n_\tau \cos\phi}\right) \Delta\tau, \tag{4.1.79}$$

and in the y direction:

$$\int \mathrm{d}y = \int v\mathrm{d}\tau - \int \frac{\beta}{\rho n_\tau \sin\phi}\mathrm{d}\tau, \tag{4.1.80}$$

$$\Delta y = \left(v - \frac{\beta}{\rho n_\tau \sin\phi}\right)\Delta\tau. \tag{4.1.81}$$

The integration constants are zero (and omitted here) and the distances are measured in relative terms, i.e. Δx and Δy are the distance from the origin of the pseudo Mach cone, for example $i+1/2, j$ in Figure 4.9, and the intersection of the bi-characteristics at time level n, i.e. $j = 1, 2, 3, 4$, for which the appropriate wave angle of ϕ needs to be inserted. Explicitly stated, these are

For $\phi = 0°$:

$$(x_1 - x_{i+1/2,j}) = \left(u - \frac{\beta}{\rho n_\tau}\right)\Delta\tau. \tag{4.1.82}$$

For $\phi = 90°$:

$$(y_3 - y_{i+1/2,j}) = \left(v - \frac{\beta}{\rho n_\tau}\right)\Delta\tau. \tag{4.1.83}$$

For $\phi = 180°$:

$$(x_{i+1/2,j} - x_2) = \left(u + \frac{\beta}{\rho n_\tau}\right)\Delta\tau. \tag{4.1.84}$$

For $\phi = 270°$:

$$(y_{i+1/2,j} - y_4) = \left(v + \frac{\beta}{\rho n_\tau}\right)\Delta\tau. \tag{4.1.85}$$

The procedure to obtain the characteristic variables p_i^{n+1}, u_i^{n+1} and v_i^{n+1} is as follows. From Eq.(4.1.71) and Eq.(4.1.75), u_i^{n+1} is obtained by eliminating p_i^{n+1}. From Eq.(4.1.73) and Eq.(4.1.77), v_i^{n+1} is obtained in a similar fashion by eliminating p_i^{n+1}. With the knowledge of the characteristic velocities, the characteristic pressure can be obtained as the arithmetic mean value of Eq.(4.1.70,4.1.72,4.1.74,4.1.76). This results in

$$u_{i+1/2}^{(n+1)^*} = \frac{1}{\beta(f_{\tau,1} + f_{\tau,2})}\left[(p_1 - p_2)f_{\tau,1}f_{\tau,2} + (u_1 f_{\tau,2} + u_2 f_{\tau,1})\beta\right], \tag{4.1.86}$$

$$v_{i+1/2}^{(n+1)^*} = \frac{1}{\beta(f_{\tau,1} + f_{\tau,2})}\left[(p_3 - p_4)f_{\tau,3}f_{\tau,4} + (v_3 f_{\tau,4} + v_4 f_{\tau,3})\beta\right], \tag{4.1.87}$$

for the characteristic velocities and

$$\left[p_{i+1/2}^{(n+1)^*}\right]_1 = p_1 - \frac{\beta}{f_{\tau,1}}(u_i^{n+1} - u_1), \tag{4.1.88}$$

$$\left[p_{i+1/2}^{(n+1)^*}\right]_2 = p_2 + \frac{\beta}{f_{\tau,2}}(u_i^{n+1} - u_2), \tag{4.1.89}$$

$$\left[p_{i+1/2}^{(n+1)^*}\right]_3 = p_3 - \frac{\beta}{f_{\tau,3}}(v_i^{n+1} - v_3), \tag{4.1.90}$$

$$\left[p_{i+1/2}^{(n+1)^*}\right]_4 = p_4 + \frac{\beta}{f_{\tau,4}}(v_i^{n+1} - v_4), \tag{4.1.91}$$

for the characteristic pressure. Here, the subscript $f_{\tau,j}$ for $j = 1, 2, 3, 4$ — corresponding to the characteristic variables — indicate along which characteristic path the surface derivative (or normal vector component) is to be evaluated, i.e.

$$f_{\tau,j} = n_{\tau,j} = \frac{-(u_j \cos\phi_j + v_j \sin\phi_j) \pm \sqrt{(u_j \cos\phi_j + v_j \sin\phi_j)^2 + 4\beta/\rho}}{2}, \tag{4.1.92}$$

where ϕ_j, in turn, shows which wave angle is to be taken. See Figure 4.9 for the locations of point $i = 1, 2, 3, 4$. As pointed out by Zucrow and Hoffman [24], it is actually not important which sign is considered in Eq.(4.1.92) for the square root, as long as it is not changed. Therefore, for the rest of the investigation, the positive square root is taken which is in accordance with the classical literature as well [14, 24, 25, 37].
Eq.(4.1.88–4.1.91) further illustrates that the system does not need more than four wave angles to be closed and that the equations are over-constrained for the pressure. Hence, an averaged value is taken in the form of

$$p_{i+1/2}^{(n+1)^*} = \frac{1}{4}\left(\left[p_{i+1/2}^{(n+1)^*}\right]_1 + \left[p_{i+1/2}^{(n+1)^*}\right]_2 + \left[p_{i+1/2}^{(n+1)^*}\right]_3 + \left[p_{i+1/2}^{(n+1)^*}\right]_4\right) \tag{4.1.93}$$

which may also explain why the convergence rate was reported [57] to increase with an increased number of wave angles. The pressure field is stabilised by a greater number of values over which the average is taken but also comes at twice the expense to evaluate the characteristic fluxes.

In the multi-directional CB scheme literature, there exist two schemes which are used: the first- and second-order scheme. In the second-order scheme, the characteristics are evaluated as shown in the above procedure, using the characteristic equations to find the intersection of the bi-characteristics with the time level n at which the values are interpolated to obtain primitive variables values at $j = 1, 2, 3, 4$. In the first-order approach, the characteristic equations are dropped so that the primitive variables values of $j = 1, 2, 3, 4$ are taken to be the reconstructed face value at which the characteristics are currently evaluated at. This is a good approximation for small $\Delta\tau$'s or in quasi homogeneous flows, i.e. those flows where spatial gradient changes are small. Furthermore, this approach is consistent with the single-directional CB scheme. Here, the reconstructed face values are the characteristic values as well. Therefore, the current investigation is concerned with the

first-order approach to have a fair comparison with the single-directional CB scheme.

The above procedure has been presented for the AC method. To extend the procedure to the FSAC-PP method, in which the pressure gradient is dropped from the momentum equation, it is sufficient to discard the characteristic pressure obtained with this procedure and to continue only with the characteristic velocities. The non-characteristic pressure is obtained at a later stage through the Poisson equation. This approach is fully consistent with the single-directional method where the FSAC-PP framework has been extended to include the CB scheme by dropping the characteristic pressure. Similar considerations hold for the FSAC-VP method, which inherits the momentum equation from the FSAC-PP method.

Before continuing, one of the most important features of the multi-directional CB-scheme shall be highlighted. The characteristic equations of the surfaces, i.e. Eq.(4.1.65–4.1.66), and the compatibility equations, i.e. Eq.(4.1.67–4.1.69), all show a dependence on ϕ alone. This means that the method is straight forwardly applicable to structured and unstructured domains. The multi-directional CB-scheme is, therefore, an extension of the Finite Volume Method to naturally include an unstructured flux treatment. In the next Section, a generalised approach of the MCB scheme will be given which is applicable to any hyperbolic system of equations for incompressible flows.

4.1.3 A Generalised Approach

In this Section, the multi-directional procedure to construct a characteristic-based scheme is provided based on the derivation in the previous Section. This is analogous to the generalisation that Rusanov [14] provided for the compressible version of the MCB scheme. The advantage is that the generalised scheme can be applied to any hyperbolic system of equations that governs incompressible flows. The procedure can be summarised in the following points as

1. Multiply the set of governing equations with an unknown surface through the use of the chain rule.
2. Find the local eigenvalues of the system which provides equations to solve for the characteristic surface.
3. Find geometrical constraints so that the system of equations from the previous step can be solved.
4. Once the characteristic surface is known, insert its solution back into the system of equations and solve for the primitive variables which yields the compatibility equations.
5. Solve the compatibility equations along the characteristic surface for each node in the computational domain.

The above procedure is carried out in the following. For that, we consider a system of equations that governs an incompressible flow. We require the system to be

hyperbolic but make no other assumption about the shape or form of the equations. The equation is given as

$$\mathcal{B}_j \frac{\partial \mathbf{u}_j}{\partial t} + \sum_{i=1}^{n} \frac{\partial \mathbf{F}_{ij}}{\partial \mathbf{x}_i} = 0, \tag{4.1.94}$$

where $\mathcal{B}_j$ is preconditioning the system, $\mathbf{u}_j$ is the primitive variables vector and $\mathbf{F}_{ij}$ contains the inviscid fluxes. From step 1, we need to multiply the equations by an assumed characteristic surface. We do so by multiplying it into the system using the chain rule as

$$\mathcal{B}_j \frac{\mathrm{d}\mathbf{u}_j}{\mathrm{d}f} \frac{\partial f}{\partial t} + \sum_{i=1}^{n} \frac{\mathrm{d}\mathbf{F}_{ij}}{\mathrm{d}f} \frac{\partial f}{\partial \mathbf{x}_i} = 0. \tag{4.1.95}$$

Before continuing, we bring Eq.(4.1.95) into a different form that will be useful in the next step. First, we multiply by the preconditioner $\mathcal{B}_j$ and transform the inviscid flux from a conservative form ($\mathbf{F}_{ij}$) to a non conservative form ($a_{ij}\mathrm{d}\mathbf{u}_j$), so as to write the fluxes in primitive variable form. Furthermore, we multiply by $\mathrm{d}f$ and express partial derivatives as $\partial f/\partial t = f_t$ and $\partial f/\partial \mathbf{x}_i = f_{\mathbf{x}_i}$ so that we are left with

$$\mathrm{d}\mathbf{u}_j f_t + \sum_{i=1}^{n} \mathcal{B}_j^{-1} a_{ij} \mathrm{d}\mathbf{u}_j f_{\mathbf{x}_i} = 0. \tag{4.1.96}$$

Zucrow and Hoffman [37] classified the derivation of the method of characteristics into four different categories which are defined as a *physical*, *purely heuristic*, *mathematical* and a *most rigorous mathematical* approach. These different approaches present different level of complexities but all result ultimately in the same equations. Rusanov's derivation is situated under the *most rigorous mathematical* approach, which is different from the route chosen here. While Rusanov used an interior operator of the form $\mathrm{d}_{\mathbf{u}} f = \mathbf{u} \cdot \nabla f$ of which m linear combinations are found to form the compatibility equation, we use a mix of the *physical* and *mathematical* approach here to derive the equations. Here, m represents the number of space and time dimensions combined. Thus, when comparing the results of Rusanov's to the following derivation, differences can be observed which result, however, in the same equations if Rusanov's approach would be used. Returning to Eq.(4.1.96), we factorise the primitive variable as

$$\left(f_t + \sum_{i=1}^{n} \mathcal{B}_j^{-1} a_{ij} f_{\mathbf{x}_i} \right) \mathrm{d}\mathbf{u}_j = 0 \tag{4.1.97}$$

and define

$$\mathcal{T} = f_t + \sum_{i=1}^{n} \mathcal{B}_j^{-1} a_{ij} f_{\mathbf{x}_i} \tag{4.1.98}$$

as the coefficient matrix. We have required that the system of equations we started with is of a hyperbolic type, thus we can find real and distinct eigenvalues for Eq.(4.1.98). A non-trivial solution in the form of $\det(\mathcal{T}) \neq 0$ can thus be written as

$$\det\left(f_t + \sum_{i=1}^{n} \mathcal{B}_j^{-1} a_{ij} f_{\mathbf{x}_i}\right) = \Psi_k, \tag{4.1.99}$$

for Ψ_k, $k = 1, ..., l$ characteristic surfaces. We only require that $\Psi_k = \mathbf{n} \cdot \mathbf{u}$ so that if their product is zero, the vectors are perpendicular and the velocity vector lies inside the characteristic surface. It can, however, also feature an inhomogeneous equation for which the characteristic Mach Cone is constructed. In-fact, there will always be a homogeneous and inhomogeneous solution for Ψ_k which spans the different characteristic surfaces. Since we require that $\Psi_k = \mathbf{n} \cdot \mathbf{u}$, the governing equations can be simplified once the characteristic surface has been multiplied into the system, see Eq.(4.1.38) and Eq.(4.1.45). Next, we compute the rank of Eq.(4.1.98) which results in

$$\text{rank}(\mathcal{T}) = \text{rank}\left(f_t + \sum_{i=1}^{n} \mathcal{B}_j^{-1} a_{ij} f_{\mathbf{x}_i}\right) = p_k(\Psi_k). \tag{4.1.100}$$

We need to express the surface's derivative in terms of the normal vector for which we can define from geometrical considerations. The time evolution of a characteristic surface can be written as

$$\frac{\partial f(\mathbf{x}_i)}{\partial t} = \frac{\partial f}{\partial \mathbf{x}_i}\frac{\mathrm{d}\mathbf{x}_i}{\mathrm{d}t} = f_{\mathbf{x}_i} \cdot \mathbf{u}_i = \nabla f \cdot \mathbf{u} = \mathbf{n} \cdot \mathbf{u} = 0 \tag{4.1.101}$$

from which $\nabla f = \mathbf{n}$ follows. This is always the case, even if $\Psi_k = \mathbf{n} \cdot \mathbf{u} \neq 0$, since the inhomogeneous term will always become zero once the time derivative is invoked on it. We need to compute for each characteristic surface $k = 1, .., l$ the quantity

$$s_k = m - p_k, \tag{4.1.102}$$

where m is taken here as the number of space and time dimensions combined and p_k has been introduced as the rank of $\mathcal{T}$ in Eq.(4.1.100). For $s_k > 0$, the set of compatibility equations result from an rank-deficient system. Thus, only $m - s_k$ linear independent equations can be found for the primitive variables $\mathbf{u}$. For $s_k = 0$, on the other hand, m linear independent compatibility equations can be found on the characteristic surface so that a sufficient amount of information is available on just one characteristic surface. Rusanov [14] stated in his derivation that for all hyperbolic systems following the compressible form of the Navier–Stokes equations, all characteristic surfaces result in a rank-deficient system. Therefore, Rusanov stated that at least a combination of two independent characteristic surfaces are required to sufficiently constrain the compatibility equation. For the case of incompressible flows, however, there exists at least one characteristic surface along which the system is non-rank deficient and all compatibility equations can be found along this surface. The reason — as discussed in Section 4.1.2 — lies in the fact that incompressible systems of equations have to construct an independent transport equation for the pressure, which is simply solved for by the equation of state in the compressible case. The equation of state does not enter the system of equations, i.e. Eq.(4.1.94) so that the rank deficiency necessarily follows. This can be stated mathematically as

$$s_k = \begin{cases} \forall k : s_k > 0, & \text{compressible} \\ \exists k : s_k = 0, & \text{incompressible} \end{cases} \tag{4.1.103}$$

This shows the main difference between the compressible and incompressible version of the CB scheme. For the surface for which we have $s_k = 0$, we insert the corresponding solution of Ψ_k into Eq.(4.1.99) and solve for the primitive variables $\mathbf{u}$. This provides the compatibility equations along the characteristic surface Ψ_k.

As stated in the previous Section, the characteristic equations can be found through differential geometry considerations for which consideration as given by Zucrow and Hoffman [24,37] while Delaney [25] provides a full derivation. We use the approach put forward by Razavi *et al.* [17] which is somewhat more simplistic, yet more intuitively. We start with the material derivative of the characteristic surface. Alternatively, we can use Reynolds transport Theorem, Eq.(3.1.11), and set $\phi = f$ for which one obtains

$$\frac{\partial f}{\partial t} + \sum_{i=1}^{n} \frac{\mathrm{d}\mathbf{x}_i}{\mathrm{d}t} \frac{\partial f}{\partial \mathbf{x}_i} = 0, \tag{4.1.104}$$

where n is the number of spatial dimensions and we made use of the fact that $\mathbf{u} = \mathrm{d}\mathbf{x}_i/\mathrm{d}t$. We have also found previously that

$$\mathbf{u} \cdot \mathbf{n} = \Psi_k. \tag{4.1.105}$$

We introduce the simplification that the characteristic surface does not change in time, rather, we construct a new characteristic surface at each time level which we consider constant during the integration period. This is the same approach taken in the SCB scheme, i.e. see Figure 4.2, where we assumed the characteristic line within the Taylor-series to be linear (a constant line) and not curved. The simplifications also mean that our characteristic surface becomes a pseudo Mach cone, not a pseudo Mach conoid, which is consistent which the classical literature on the CB scheme. If we subtract Eq.(4.1.104) from Eq.(4.1.105), we get

$$\sum_{i=1}^{n} \left(\mathbf{u}_i - \frac{\mathrm{d}\mathbf{x}_i}{\mathrm{d}t} \right) \cdot \mathbf{n} = \Psi_k, \tag{4.1.106}$$

which is the final form of the characteristic surface k. The term in parenthesis may be regarded as the relative velocity of the characteristic surface and a fluid control volume. If the term in parenthesis equates to zero, it means that the characteristic surface has collapsed to the stream surface (or streamline) for which have seen that $\mathbf{u} \cdot \mathbf{n} = \Psi = 0$. The term might, however, equate to a non-zero value. Consider a horizontal flow through a channel without disturbances. A pseudo Mach cone may emanate from any considered point in the flow which will have some vertical direction of travel, while the velocity component of the fluid is the vertical direction is equal to zero. This is the case for the wave surface and we have $\mathbf{u} \cdot \mathbf{n} = \Psi \neq 0$. Constant characteristic lines along the surface over which the compatibility equations are valid are found by inserting the wave angle ϕ into the definition of the unit normal vector, as given in Eq.(4.1.58) and repeated here for convenience

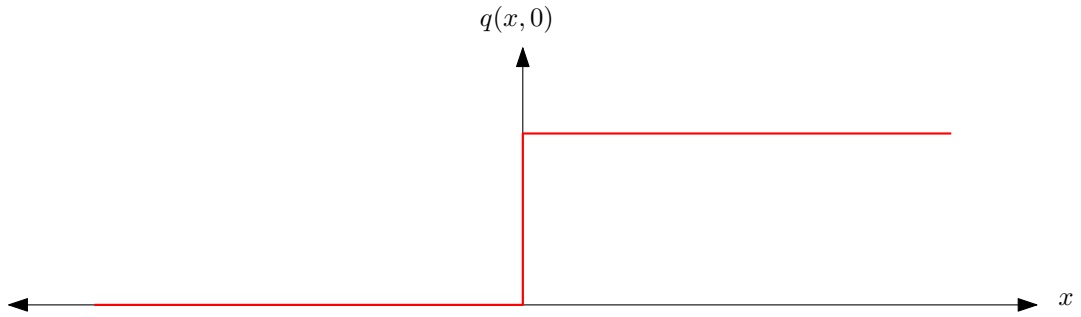

Figure 4.11: The initial value problem of the Riemann. The initial data experiences a discontinuous jump at $x_0 = 0$.

$$\mathbf{n} = \begin{bmatrix} n_x \\ n_y \end{bmatrix} = \begin{bmatrix} \cos\phi \\ \sin\phi \end{bmatrix}.$$

Rusanov [14] did not consider the characteristic equation itself and neither did Drikakis *et al.* [15]. Since explicit numerical integration procedures are usually more restrictive on the time-step based on numerical considerations (CFL number) rather than physical time scales, the computational gain that can be achieved by removing the characteristic equation altogether is justified by the relative small error that is introduced. Razavi *et al.* [17] termed this approach a first order scheme where the inter-cell values which are obtained through interpolation, are used as the primitive variables in the compatibility equation. In-fact, the characteristic equation can be used to determine the start location of the pseudo Mach cone. Once the location is known, the primitive variables can be interpolated to the intersection of the Mach cone with the time level n where the x and y coordinates are determined through the wave angle ϕ. This, using a simple central averaging, has been termed the second-order approach by Razavi *et al.* [17]. In this work, the first-order approach is favoured over the second-order approach to have a fair comparison between the SCB and MCB scheme.

4.2 The Riemann Problem for Incompressible Flows

There are two distinct areas which have to be discussed separately when dealing with the Riemann problem; the Riemann problem itself and the particular Riemann solver used to obtain a solution.

The Riemann problem, for a set of hyperbolic equations, is simply defined as an initial value problem for which the initial data $q(x,0)$ is given by

$$q(x,0) = \begin{cases} q_L & \text{for } x < x_0 \\ q_R & \text{for } x \geq x_0 \end{cases}. \tag{4.2.1}$$

Here we have $q_L \neq q_R$ and x_0 is some location along the x axis, commonly taken as $x_0 = 0$. The initial profile is shown in Figure 4.11. The solution to the Riemann Problem (RP) is obtained by a Riemann Solver (RS). There are exact and

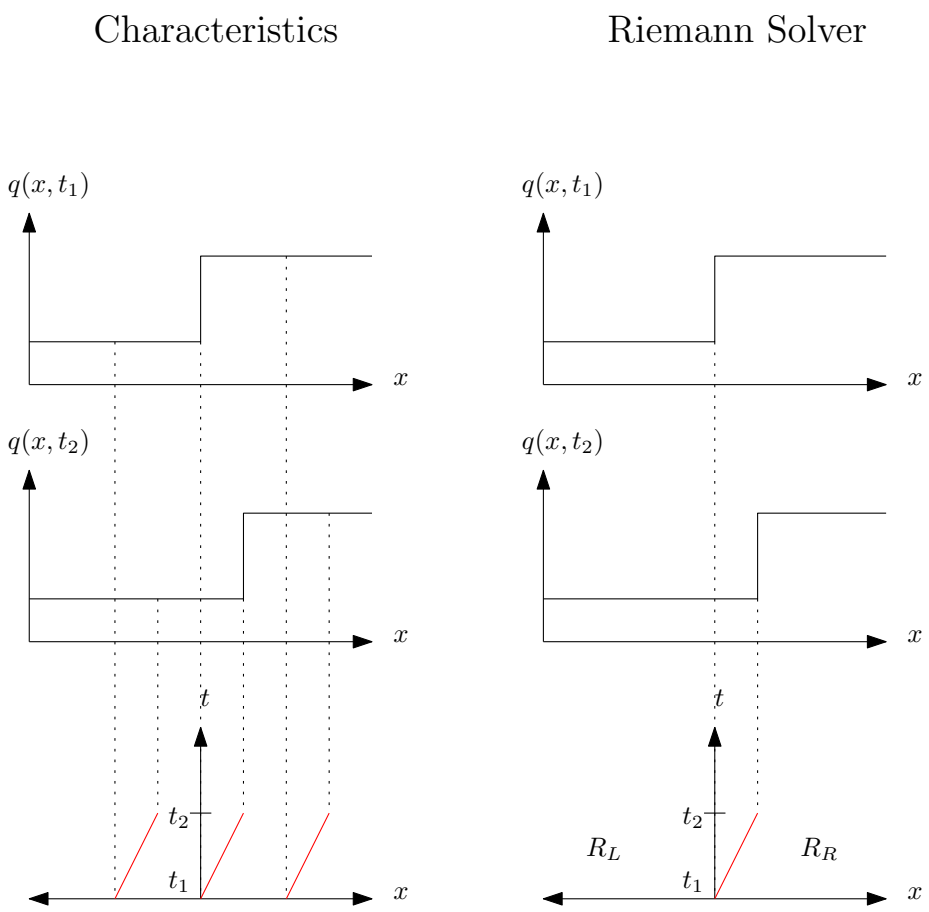

Figure 4.12: The different philosophies behind the Riemann problem/solver and the method of characteristics.

approximate RS, both of which can be applied to linear and non-linear system of hyperbolic equations. As has been stated in Section 2.2, exact RS are not as computational efficient as approximate RS, despite having a higher accuracy. The field of CFD makes almost exclusive use of approximate RS and so the discussion in the following Sections is limited to those. The main idea and philosophy behind the RS, however, shall be reviewed here.

To begin with, the solution to the Riemann problem is not that different to the method of characteristics. This is illustrated in Figure 4.12. Some initial profile $q(x,0) = q(x,t_1)$ is advected along the x axis using the hyperbolic advection equation for a one-dimensional case. At some time t_2, the initial profile of $q(x,t_1)$ has shifted the profile by some distance $\Delta x = \lambda \Delta t$, where λ is the characteristic velocity. This is also shown by transferring values at some predefined locations (which could coincide with the computational mesh) of the initial and advected profile at times t_1 and t_2, respectively, from the x, q into a x, t diagram. The dashed lines indicate which point is tracked and to which time level it corresponds. In the x, t diagram, the characteristics emerge as the trace of those points.
As discussed at length in Section 4.1 and explicitly shown for the advection equation in Appendix A, the method of characteristics seeks those characteristics throughout

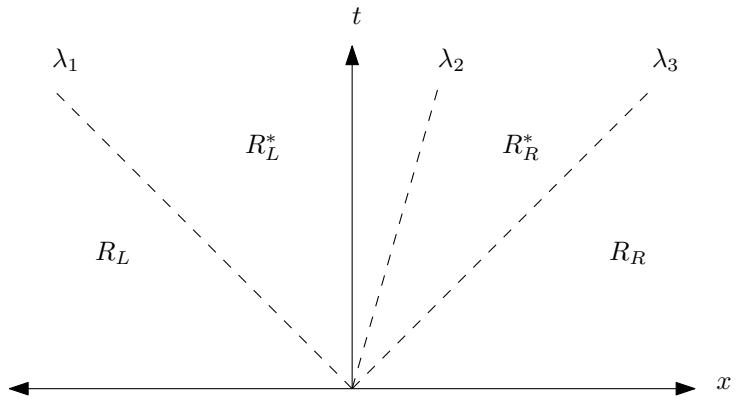

Figure 4.13: The general solution to the Riemann problem.

the domain and tracks them from an initial set of computational nodes through time, either in a forward or backward manner. Compatibility equations are derived which are only valid along those characteristics and so if the solution at a specific point in space is sought, a characteristic line needs to be placed through that point along which its own compatibility equation would result in the desired values for the primitive variables.

The solution to the Riemann problem is a more general case. Returning to Figure 4.12, on the left the above described procedure is shown for the method of characteristics and on the right for the solution of the Riemann problem. By definition, the Riemann problem consists of a discontinuous jump in the initial data and it is this jump which is tracked by a Riemann solver. To obtain values across the jump, two regions are defined as R_L and R_R. There are two regions, or states, which exist in this particular example, left or right of the characteristics. These are indicated by the subscripts. For any given point in time and space, it is thus possible to give a solution to the Riemann problem. Using the x, t diagram shown in Figure 4.12 in the bottom right, it is possible to determine in which region the current pair of x and t is in. For example, if the pair of x, t evaluates to be in region R_L, then the solution is simply q_L which is obtained from the initial data, see Eq.(4.2.1). Analogously, if x, t evaluates to be in R_R, then the solution would be q_R. The basic difference between the method of characteristics and Riemann solvers is thus that for each point where a solution is required, characteristics need to be placed through these points to obtain values through a compatibility equation at that point while the Riemann solver is tracking the discontinuous jump so that it can naturally differentiate between regions left and right of the jump. The method of characteristics does not know where it is in the flow, i.e. if it is left or right of the jump (if in-fact a jump is present), so without that knowledge, each point in the domain needs to be treated explicitly. However, even if there is no jump, the method of characteristics still works.

This discussion has been for a very simplified problem, however, the governing equations for fluid dynamics are more challenging. In-fact, the eigenvalues are immanently linked to the characteristics and have been found in Section 4.1.1, Eq.(4.1.16–4.1.18) for the AC method. These are all distinct and real eigenvalues which renders the system hyperbolic. This is schematically shown in Figure 4.13 for three distinct

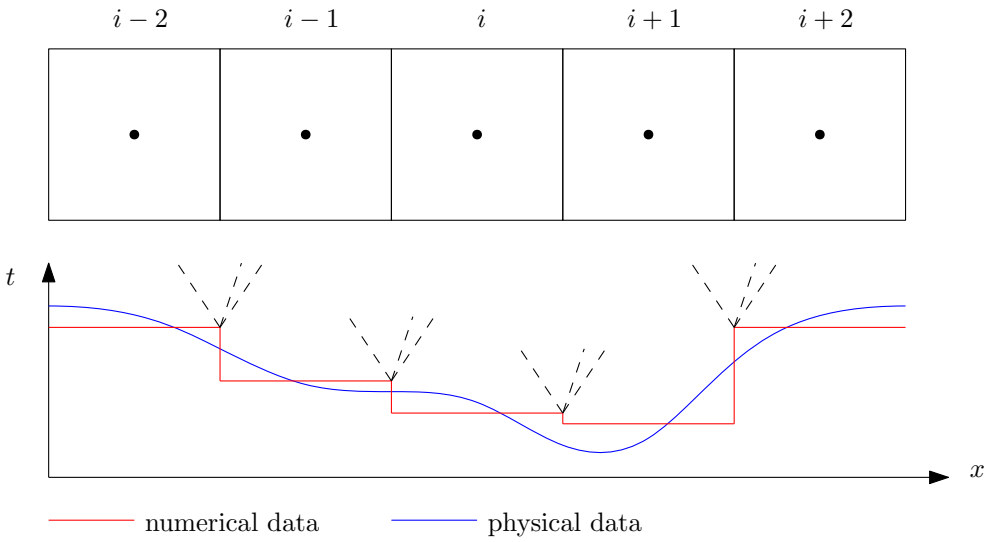

Figure 4.14: A physical smooth profile is represented through discontinuous data in a numerical finite volume framework. The local Riemann Problem can be solved for each cell face to obtain the fluxes across the cell.

characteristics λ_1, λ_2 and λ_3. Since there are more than a single characteristic dividing line, the number of states has also increased. Furthermore, since the governing equations to fluid mechanics are non-linear, the states, or regions, are not necessarily constant anymore. That is, it is not possible to map a value from the initial solution to one of the states for a given pair of x, t, rather, equations for each state have to be developed, much like the compatibility equations along the characteristics, which are only valid inside the region it has been derived for. The challenge in the Riemann Solver now becomes to transform the available data in physical space into the x, t state space so that an appropriate set of equations can be applied to the data to obtain the solution to the Riemann problem.

Godunov [3] introduced the idea that if a set of discretised data (for example the solution obtained through a finite volume procedure) exhibits local discontinuities in its data set (in the context of finite volume methods, this would be at the cell interfaces), then a local Riemann problem can be solved for each discontinuity to obtain a highly accurate solution. This is shown in Figure 4.14, where a physical (blue), continuous signal is computed through a finite volume approach (with a collocated mesh arrangement). The values of the primitive variables inside the control volume are constant and shown in red. At each cell interface, the solution makes a discontinuous jump so that *numerical shock waves* emanate from these locations (shown as dashed lines). The Godunov procedure requires the solution of a Riemann problem (through either an exact or approximate Riemann solver) and higher-order interpolated variables at the cell interfaces from both the left- and right-hand side. The gain of this rather elaborate and complicated procedure is a highly accurate and physical treatment of the convective flux term.

In the next Section, the approximate Riemann solver of Rusanov is introduced and it is shown how it can be combined with the multi-directional CB scheme.

4.2.1 The Method of Rusanov

Rusanov [68] put forward a paper in 1961 presenting a finite difference scheme to capture shock waves in various geometrical domains. He referred to it as the "through" scheme in which the actual discontinuity can be ignored but used to determine changes in physical parameters. Davis [115] later showed that with an appropriate set of characteristic wave speeds, i.e. those that are responsible for the propagation of the characteristic waves, see Figure 4.13, Rusanov's scheme can be shown to be of the simplest, first-order, Riemann solver type. Davis also showed that the Lax-Friedrich scheme can be equivalently transformed into a Riemann solver. The form of the differencing scheme introduced by Rusanov and adopted in this work is

$$\mathbf{F}(\mathbf{u})_{i+1/2} = \frac{1}{2}\left[\mathbf{F}(\mathbf{u})_R + \mathbf{F}(\mathbf{u})_L\right] - \frac{S^+}{2}\left(\mathbf{u}_R - \mathbf{u}_L\right). \tag{4.2.2}$$

This is the one-dimensional representation of the Rusanov flux at the cell interface $i+1/2$ where the fluxes are denoted by $\mathbf{F}(\mathbf{u})_k$, the primitive variables by $\mathbf{u}_k$ and $k = L, R$ indicates the left- or right-sided interpolation of the fluxes and primitive variables. When we compare Eq.(4.2.2) with Eq.(4.1.7), which showed the Taylor-series expansion backwards in time for the SCB scheme, we can see in mathematical form what has been discussed in the previous Section. In the SCB scheme, characteristic lines enter the time derivative (and for that matter characteristic surfaces enter the governing equation using the MCB scheme) which are represented by the second term in Eq.(4.1.7). In the same way, the Riemann solver given in Eq.(4.2.2) consists of a standard flux interpolation at the interface which is given by the first term and then a second term that is multiplied by some characteristic velocity. This velocity is based on the local eigenvalues and bears resemblance to λ as introduced in Section 4.1.1 and 4.2. The discontinuity which can be found at the interface, i.e. $\mathbf{u}_R - \mathbf{u}_L$ is thus scaled by the local eigenvalues through S^+. The particular form of S^+ will be discussed in Section 4.2.2 and 4.2.3. Therefore, the characteristic-based approach consists of tracking characteristic lines through the domain in time while the Riemann solver i simply concerned with the fluxes on the either side of a discontinuous signal. This narrative is in accordance with Figure 4.12 and its discussion. Furthermore, if no discontinuity exists at $i+1/2$, the Riemann solver reverts to a classical second-order flux interpolation scheme.
In order to combine Eq.(4.2.2) with the MCB scheme, the MCB scheme has to be solved twice, once using $\mathbf{u}_R$ and another time for $\mathbf{u}_L$ so to produce two independent left and right characteristic state variables, i.e. Eq.(4.1.86–4.1.87) and Eq.(4.1.93). To do so, the primitive variables $\mathbf{u}_j$ with $j = 1, 2, 3, 4$ are set to either $\mathbf{u}^L_{i+1/2}$ or $\mathbf{u}^R_{i+1/2}$, see Section 5.3.2 for how to obtained the left- and right-sided interpolated values. These characteristic primitive variables can then be used to define two characteristic fluxes and finally to compute the flux based on the Riemann solver using Eq.(4.2.2).

4.2.2 Single-Directional Closure

In this Section, we address the closure of Davis [115] to approximate the signal velocities. Toro [71] argued that these approximations are simple in nature and should not be used for practical computations. However, the critique is aimed at the compressible equations and Drikakis and Rider [72] showed that these are indeed valid and useful approximations for the incompressible case. Based on Davis' suggestions, the signal velocity for the Rusanov RS can be obtained as

$$S^{+} = \max\left\{|A_L^-|, |A_R^-|, |A_L^+|, |A_R^+|\right\}, \tag{4.2.3}$$

with

$$A_L^- = \mathbf{u}_L - \sqrt{\mathbf{u}_L^2 + \beta/\rho}, \tag{4.2.4}$$

$$A_R^- = \mathbf{u}_R - \sqrt{\mathbf{u}_R^2 + \beta/\rho}, \tag{4.2.5}$$

$$A_L^+ = \mathbf{u}_L + \sqrt{\mathbf{u}_L^2 + \beta/\rho}, \tag{4.2.6}$$

$$A_R^+ = \mathbf{u}_R + \sqrt{\mathbf{u}_R^2 + \beta/\rho}. \tag{4.2.7}$$

Here, $\mathbf{u} = (u, v)^T$ is the velocity vector where the indices L, R indicate that the left- or right-sided interpolation of the velocity components is to be taken. Eq.(4.2.3) is valid separately for both the x and y direction. However, no intermediate state, i.e. between the x and y direction is possible. Therefore, it is termed the single-directional closure for the Riemann problem, to be consistent with the naming convention used in the CB schemes.

4.2.3 Multi-Directional Closure

The single-directional closure can be easily extended to the multi-directional closure of the Riemann problem. There are two possible routes that can be taken. The first one consists of extending the definition of the Riemann solver to a multi-directional state, which would be similar to the development of the MCB scheme based on its single-directional counterpart. This development has commenced for Riemann solvers in the compressible literature, see for example [97–99]. The second approach is to extend the Riemann solver in a geometrical sense in which only the wave speeds are considered to be multi-directional while the Riemann solver itself is still single-directional. Since the multi-directional nature is provided through the MCB scheme, it does not need to be provided by the Riemann solver as well. The geometrical extension to the wave speeds is, however, required so that the Riemann solver can be used for any wave directions in conjunction with the MCB scheme.
The definition of the signal velocities, i.e. Eq.(4.2.3) are still valid as these work on vector quantities. The aim is to combine the velocity components into a single expression which, for the limiting case in which the signal velocities propagate along either the x or y axes recover the same result as the single-directional approach but which is also able to detect intermediate states, i.e. those where the signal

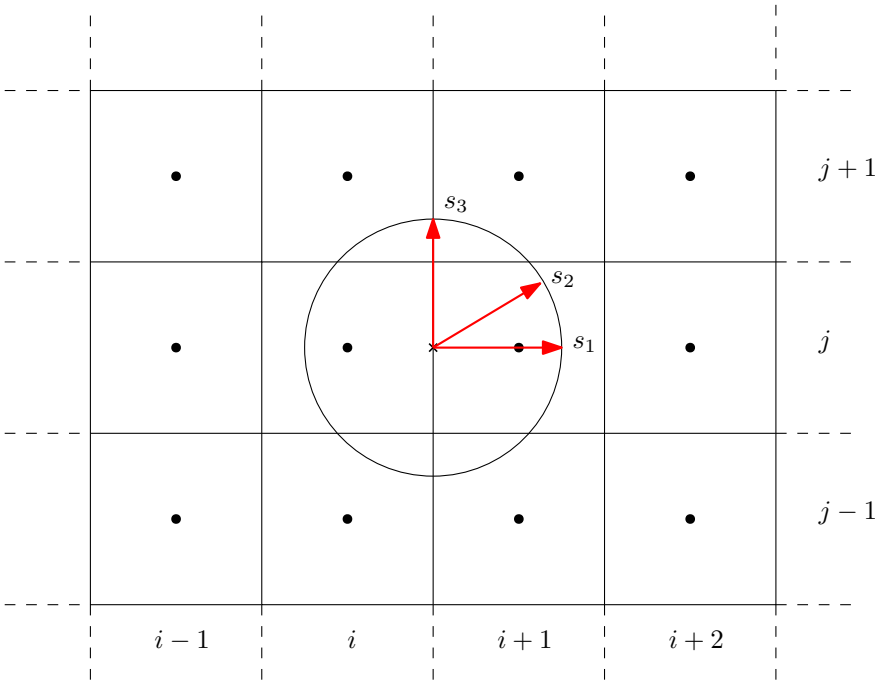

Figure 4.15: The propagation of three arbitrary signal velocities whose locus coincides with the pseudo Mach cone.

velocity is propagating at an angle to the x and y axes. Figure 4.15 presents the case for three, arbitrarily selected signal velocities propagating from the centre of the interface between cell i and $i+1$. The locus of the infinite number of signal velocities, all propagating at the same magnitude, coincide with the pseudo Mach cone, which is indicated in Figure 4.15. The equation for the pseudo Mach cone has been derived in Section 4.1.2 as Eq.(4.1.64) which is repeated below for convenience

$$\left(u - \frac{\mathrm{d}x}{\mathrm{d}\tau}\right)\cos\phi + \left(v - \frac{\mathrm{d}y}{\mathrm{d}\tau}\right)\sin\phi = \frac{\beta}{\rho n_\tau}.$$

The equation was split along the $\mathrm{d}x/\mathrm{d}\tau$ and $\mathrm{d}y/\mathrm{d}\tau$ characteristics which resulted in the two equations for each direction as

$$\frac{\mathrm{d}x}{\mathrm{d}\tau} = u - \frac{\beta}{\rho n_\tau \cos\phi},$$
$$\frac{\mathrm{d}y}{\mathrm{d}\tau} = v - \frac{\beta}{\rho n_\tau \sin\phi}.$$

The selection of ϕ fixes the direction in which the characteristics are considered. However, as was pointed out in Section 4.2, the solution of the Riemann problem is simply the tracking of the initial discontinuity through a characteristic. Due to this close relation of the Riemann problem with the characteristics, it is tempting to extract the multi-directional feature from the characteristics and to feed it into the solution of the Riemann problem. By analysing the process by which the characteristic equations along the pseudo Mach cone were derived, a similar procedure can be used to go from a set of equations for signal velocities in separate equations

to a single equation, containing all possible directions of ϕ. To do so, the velocity vector $\mathbf{u}$ simply needs to be multiplied by the unit normal vector which has been introduced in Eq.(4.1.58). Thus, it is found that

$$\mathbf{u} \cdot \mathbf{n} = \begin{bmatrix} u \\ v \end{bmatrix} \cdot \begin{bmatrix} \cos\phi \\ \sin\phi \end{bmatrix} = u \cdot \cos\phi + v \cdot \sin\phi. \tag{4.2.8}$$

Using Eq.(4.2.8), the coefficients in Eq.(4.2.4–4.2.7) thus become

$$A_L^- = u_L \cos\phi + v_L \sin\phi - \sqrt{(u_L \cos\phi + v_L \sin\phi)^2 + \beta/\rho}, \tag{4.2.9}$$

$$A_R^- = u_R \cos\phi + v_R \sin\phi - \sqrt{(u_R \cos\phi + v_R \sin\phi)^2 + \beta/\rho}, \tag{4.2.10}$$

$$A_L^+ = u_L \cos\phi + v_L \sin\phi + \sqrt{(u_L \cos\phi + v_L \sin\phi)^2 + \beta/\rho}, \tag{4.2.11}$$

$$A_R^+ = u_R \cos\phi + v_R \sin\phi + \sqrt{(u_R \cos\phi + v_R \sin\phi)^2 + \beta/\rho}. \tag{4.2.12}$$

which can be used in Eq.(4.2.3) to obtain the signal velocity S^+. In analogy to the multi-directional CB scheme, this approach is termed the multi-directional closure for the Riemann problem. The inclusion of Eq.(4.2.9–4.2.12) into Rusanov's Riemann solver provides a consistent multi-directional Godunov-type framework in conjunction with the MCB scheme.

Chapter 5

Numerical Discretisation Procedure

The following chapter will outline the numerical discretisation procedures involved in solving the governing equations derived in Chapter 3. Since all equations are discretised using the finite volume method, a brief introduction to the method will be provided along with numerical considerations applicable to the chosen data structure. The numerical approximation and integration schemes are discussed and the Chapter is closed with a review of the boundary conditions that are employed.

5.1 The Finite Volume Method

In their influential 1928 paper, Courant, Friedrich and Levy [116] first used what can now be considered the finite difference method to solve partial differential equations. References exist that show that the method was used even earlier, but the authors were the first to put the method into a computationally useful framework. They used the wave and Laplace equation to solve a 2D domain with a five-point stencil and derived a stability condition — nowadays known as the CFL condition — that showed under which conditions a stable solution can be obtained. From that point on, especially during the advancement of computational power and the need to solve partial differential equations for real world and complex problems, different flavours of the finite difference method were developed which eventually branched off into their own respective framework. Thomée [117] provides an historical account of the development of the finite difference method, starting with the paper of Courant *et al.*, to the development of the finite element method which first appeared under that name in Clough [118] which is based on works of Lord Rayleigh [119, 120] and Ritz [121]. The finite volume method emerged as another alternative alongside collocation, spectral and boundary element methods, however, in the context of computational fluid dynamics, the finite volume method became the preferred choice due to its natural alignment and properties for fluid dynamics. The method has conservative and consistent properties, meaning that a quantity given into a system is conserved and that for a vanished mesh and time step size the truncation error approaches zero and the solution of the original equation is recovered. In essence, the finite volume methods integrate each term inside a differential equation, for

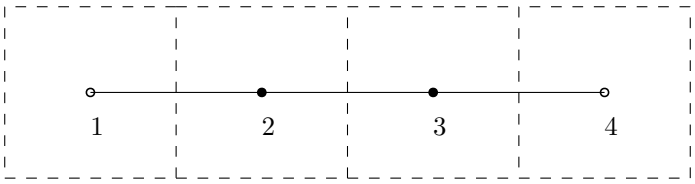

Figure 5.1: A one dimensional domain for a simple finite volume calculation. Open disks represent boundaries and closed circles internal nodes.

example, the term $\partial\phi/\partial x$ could be approximated by

$$\int_V \frac{\partial \phi}{\partial x} \mathrm{d}V = \frac{\partial \phi}{\partial x} V. \tag{5.1.1}$$

Using Gauss' Theorem, we could write the equation in a different form

$$\int_V \frac{\partial \phi}{\partial x} \mathrm{d}V = \int_A \phi \cdot n \mathrm{d}A = \sum_{faces} \phi \cdot n. \tag{5.1.2}$$

Consider Figure 5.1, where a simple one-dimensional domain is shown and consider the approximation of the derivative as above. Applying the derivative to each computational finite volume, i.e. the elements shown with dashed lines, we can write, using Eq.(5.1.2) and noting that the normal vector is positive for element in the right direction and negative in the left

$$\begin{aligned}
\int_{CV_1} \frac{\partial \phi}{\partial x} \mathrm{d}V_{CV_1} + \int_{CV_2} \frac{\partial \phi}{\partial x} \mathrm{d}V_{CV_2} + \int_{CV_3} \frac{\partial \phi}{\partial x} \mathrm{d}V_{CV_3} + \int_{CV_4} \frac{\partial \phi}{\partial x} \mathrm{d}V_{CV_4} = \\
\frac{\partial \phi}{\partial x} V_{CV_1} + \frac{\partial \phi}{\partial x} V_{CV_2} + \frac{\partial \phi}{\partial x} V_{CV_3} + \frac{\partial \phi}{\partial x} V_{CV_4} = \\
\sum_{faces} (\phi \cdot n) A_{CV_1} + \sum_{faces} (\phi \cdot n) A_{CV_2} + \sum_{faces} (\phi \cdot n) A_{CV_3} + \sum_{faces} (\phi \cdot n) A_{CV_4} = \\
(\phi_{+\hat{1}} - \phi_{-\hat{1}}) A_{CV_1} + (\phi_{+\hat{2}} - \phi_{-\hat{2}}) A_{CV_2} + (\phi_{+\hat{3}} - \phi_{-\hat{3}}) A_{CV_3} + (\phi_{+\hat{4}} - \phi_{-\hat{4}}) A_{CV_4}.
\end{aligned} \tag{5.1.3}$$

Here, we assume that the $\hat{i}$ values are interpolated values from the locations at which the variables are stored, i.e. here $i = 1, 2, 3, 4$ and that the sign indicates the left and right hand side interpolated values at the cell interface. Since the area is constant across all elements, we can divide by it. Furthermore, noting that the left- and right-sided interpolation at an interface are equal (assuming no interpolation error), then we have $+\hat{i} = -i \hat{-} 1$. Thus, we can write Eq.(5.1.3) as

$$\begin{aligned}
-\phi_{-\hat{1}} + \phi_{+\hat{1}} + -\phi_{-\hat{2}} + \phi_{+\hat{2}} + -\phi_{-\hat{3}} + \phi_{+\hat{3}} + -\phi_{-\hat{4}} + \phi_{+\hat{4}} = \\
-\phi_{-\hat{1}} + \underbrace{\phi_{+\hat{1}} - \phi_{-\hat{2}}}_{=0} + \underbrace{\phi_{+\hat{2}} - \phi_{-\hat{3}}}_{=0} + \underbrace{\phi_{+\hat{3}} - \phi_{-\hat{4}}}_{=0} + \phi_{+\hat{4}} = \\
\phi_{+\hat{4}} - \phi_{-\hat{1}}.
\end{aligned} \tag{5.1.4}$$

The values of $\phi_{+\hat{4}}$ and $\phi_{-\hat{1}}$ are those that we pass in on the right and left side, respectively. Ignoring for the moment that the boundary conditions are applied at node 1 and 4 (Figure 5.1 can be considered to consist of only internal volumes), we

see that the quantity passed in to the domain on both sides is conserved, i.e. that the numerical discretisation procedure did not add any extra terms. The derivation is similar if node 1 and 4 are considered boundary nodes but the outcome is the same. This is the conservative property of the finite volume method.
The solution to the Euler equation turned out to be particularly difficult to capture using classical finite difference schemes due to the non-linear term that allowed for shock waves, and thus discontinuous profiles to develop. The finite difference method uses approximations to derivatives at discretised points in space and so a discontinuity would result in an infinitely large derivative. The finite volume method, on the other hand, looks at the conservation of physical quantities inside finite control volumes as described above, which may have a discontinuous cell interface. Furthermore, the finite volume method is also directly applicable to unstructured grids, which is not the case for the finite difference method. Thus, its alignment with conservation laws and ease of handling of complex geometries has made it the standard method for computational fluid dynamics applications which is used in this work.

In the following, it is not intended to give a comprehensive overview of the finite volume method, rather the aspects of the methods are highlighted which are used to discretise the equations. An excellent overview of the finite volume method for incompressible flows can be found in the book of Versteeg and Malalsekera [6]. Additional information may be obtained from the book of Ferziger and Peric [122]. The book of Patankar [100] may be used as a general introduction to the finite volume method which, however, focuses only on the SIMPLE algorithm. The lecture script of Murthy [123] provides another excellent reference to the finite volume method focusing on unstructured solver development while the book of Drikakis and Rider provides high-resolution methods for incompressible flows. The advanced reader may wish to consult the books of Hirsch [124, 125] for advanced topics, especially for stability analysis. For compressible flows, the book of Blazek [126] provides an excellent introduction to the finite volume method for structured and unstructured solver development. Advanced topics are covered by Toro [70], focusing on RSs, and LeVeque [127, 128], focusing on high-resolution schemes and methods. For finite volume mesh specific considerations, especially the storage and handling of unstructured grids, the reader is referred to the book of Löhner [129].

5.1.1 Discretisation of First-order Derivatives

The discretisation of the inviscid fluxes of the Navier–Stokes equations contain first-order derivatives. In the previous Section it was stated, that any derivative can be integrated over a finite volume which yields

$$\int_V \frac{\partial \phi}{\partial x} \mathrm{d}V = \frac{\partial \phi}{\partial x} V. \tag{5.1.5}$$

Additionally, using the Gauss Theorem we already saw that the volume integral can be transformed into a surface integral which provides the conservative nature of the method. It is stated below for completeness as

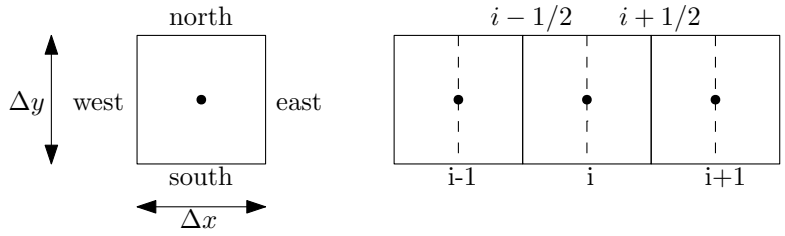

Figure 5.2: A typical computational control volume with its nomenclature (left) and the location of the inter-cell faces (right).

$$\int_V \frac{\partial \phi}{\partial x} \mathrm{d}V = \int_A \phi \cdot n \mathrm{d}A = \sum_{faces} \phi \cdot n. \tag{5.1.6}$$

Here, the normal vector is pointing outward of a control volume and is normal to the inter-cell surface. The quantity ϕ needs to be interpolated to the face which connects control volumes so that it is available on the surface. Appropriate interpolation schemes will be reviewed in Section 5.3. For a two-dimensional flow, the surface area has to be taken per unit length as the surface reduces to a line element. On a Cartesian mesh, Eq.(5.1.6) can be written in an explicit form as

$$\int_V \frac{\partial \phi}{\partial x} \mathrm{d}V = \sum_{faces} \phi \cdot n = \phi_{i+1/2,j} \Delta y - \phi_{i-1/2,j} \Delta y \tag{5.1.7}$$

for the x-direction and

$$\int_V \frac{\partial \phi}{\partial y} \mathrm{d}V = \sum_{faces} \phi \cdot n = \phi_{i,j+1/2} \Delta x - \phi_{i,j-1/2} \Delta x \tag{5.1.8}$$

for the y-direction. Here, Δx and Δy are the line elements representing the surface area and the indices $i \pm 1/2$ and $j \pm 1/2$ represent the east, west, north and south cell interface, respectively. This computational cell is also depicted in Figure 5.2 on the left while the inter-cell interface location is shown on the right for a one-dimensional case. Here, the control volume has been constructed around the node where the primitive variables are stored and the computational mesh, as in Figure 5.1, has been omitted for clarity.

5.1.2 Discretisation of Second-order Derivatives

The discretisation of a second-order derivative is obtained analogous to the first-order case where a derivative of the derivative is taken. In the x-direction, we have

$$\int_V \frac{\partial}{\partial x} \left(\frac{\partial \phi}{\partial x} \right) \mathrm{d}V = \int_V \frac{\left(\frac{\partial \phi}{\partial x}\right)_{i+1/2} - \left(\frac{\partial \phi}{\partial x}\right)_{i-1/2}}{\Delta x} \mathrm{d}V =$$

$$\int_V \frac{\frac{\phi_{i+1} - \phi_i}{\Delta x} - \frac{\phi_i - \phi_{i-1}}{\Delta x}}{\Delta x} \mathrm{d}V = \frac{\phi_{i+1} - 2\phi_i + \phi_{i-1}}{(\Delta x)^2} V. \tag{5.1.9}$$

As can be seen from Eq.(5.1.9), for a Cartesian grid, the classical finite difference form of a second-order derivative is recovered using the finite volume approach. Thus, the second order derivative is discretised for a two-dimensional flow as

$$\int_V \frac{\partial}{\partial x}\left(\frac{\partial \phi}{\partial x}\right) \mathrm{d}V = \frac{\phi_{i+1,j} - 2\phi_{i,j} + \phi_{i-1,j}}{(\Delta x)^2} V \tag{5.1.10}$$

in the x-direction and as

$$\int_V \frac{\partial}{\partial y}\left(\frac{\partial \phi}{\partial y}\right) \mathrm{d}V = \frac{\phi_{i,j+1} - 2\phi_{i,j} + \phi_{i,j-1}}{(\Delta y)^2} V \tag{5.1.11}$$

in the y-direction.

5.1.3 Data Structure for Cartesian Solvers

The particular data structure approach that is chosen dominates the finite volume discretisation procedure, as discussed above, but also how boundary conditions are implemented and data is stored. In the current work, a simplistic multi-block Cartesian solver is developed where multiple blocks can be interfaced with one another to build up more complicated domains. The underlying grid, however, is assumed to be Cartesian and thus the domains are restricted to rectangular shapes. The standard benchmark cases which are considered in this work are, however, all rectangular in nature and thus a simple data structure may even provide a computational advantage. For storing data on a computational mesh, there are two main categories, collocated and staggered grids. In collocated grid arrangements, all primitive variables are stored locally at the same node whereas the staggered approach constructs makeshift grids for each primitive variable, i.e. velocity and pressure, which is stored on their own respective grid. Thus, the flow variables are not stored at the same location and interpolation is required if the information is needed at a specific point. The advantage of the staggered approach is that the velocity and pressure are available at the locations where the equations are discretised. Thus, the velocity-pressure decoupling problem is removed and a stable solution obtained. The decoupling usually results in a smooth velocity but oscillating pressure field. Staggered grids are cumbersome to implement due to their multiple mesh level structure. Simple textbook examples are, however, usually provided using a staggered approach in conjunction with the SIMPLE algorithm, see [6, 100, 122]. The collocated approach did initially introduce the pressure-velocity decoupling effect, which is however not a property of collocated mesh themselves. Around the time when the SIMPLE algorithm was introduced, in 1972 [20], the central scheme was still a popular and easy to implement scheme of second-order. The numerical scheme revolution driven by Harten was still a decade away. Rather than changing the numerical schemes, researchers opted to change the discretisation procedure and so the staggered grid was born. In 1983, Rhie and Chow [130] introduced a correction to their numerical scheme, by considering a central like scheme which further introduced one additional upwind node in their scheme. Thus, the scheme gained transportiveness through the scheme and the pressure-velocity decoupling could be avoided. Essentially, their scheme represented a third-order accurate reconstruction procedure and over time it became

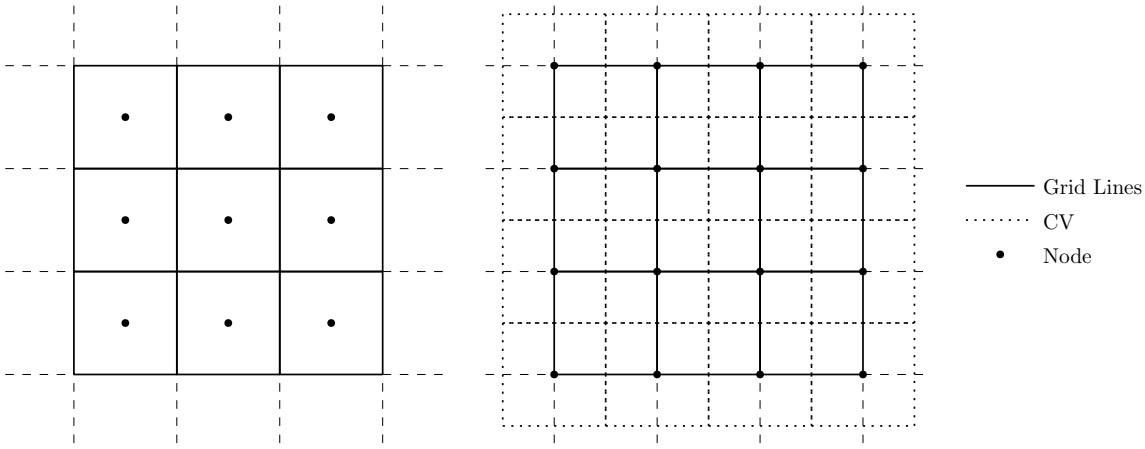

Figure 5.3: Computational mesh arrangements for a collocated cell centred grid (left) and vertex centred grid (right).

accepted knowledge that the convective flux term in the Navier–Stokes equations require interpolation schemes with an odd-order ($1^{st}, 3^{rd}, 5^{th}$... order). In-fact, the first-order upwind scheme did not show the same numerical induced issues which was, however, discarded due to its dissipative nature and first-order of accuracy.
With the emergence of the Rhie–Chow correction and higher-order schemes, collocated grids gained popularity again due to their simplicity. There are two ways in which collocated grids can be arranged on a computational mesh which are shown in Figure 5.3. On the left side, the classical finite volume approach is shown in which the control volume is identical to the grid cell. The primitive variables are stored at the cell centre and thus is sometimes also known as a cell centred or node centred grid. In this approach, the cell centre needs to be constructed since it is not provided by the computational mesh. The vertex centred approach shown on the right stores the primitive variables at the intersection of grid lines. The advantage is that no additional nodes need to be created but the control volume is not defined. In either approach, some additional quantities need to be calculated. The vertex centred approach offers some computational advantages for unstructured mesh approaches [126] and furthermore allows the imposition of Dirichlet boundary conditions directly. Since no information of the primitive variables on the boundaries are available in the cell centred approach, boundary conditions can only be imposed implicitly. Therefore, the vertex centred approach is chosen for the solver's data structure.
The implementation of boundary conditions in particular is shown in Figure 5.4. Here, the storage location of the primitive variables coincides with the physical boundary. Thus, to impose Dirichlet boundary condition at node i, we have

$$\phi_i = \phi_{BC}. \tag{5.1.12}$$

Similarly, the Neumann condition can be directly satisfied on the boundary as

$$\frac{\partial \phi_i}{\partial n} = \phi_{BC}. \tag{5.1.13}$$

In Figure 5.4, the domain extends in the positive x-direction so that all cells shown

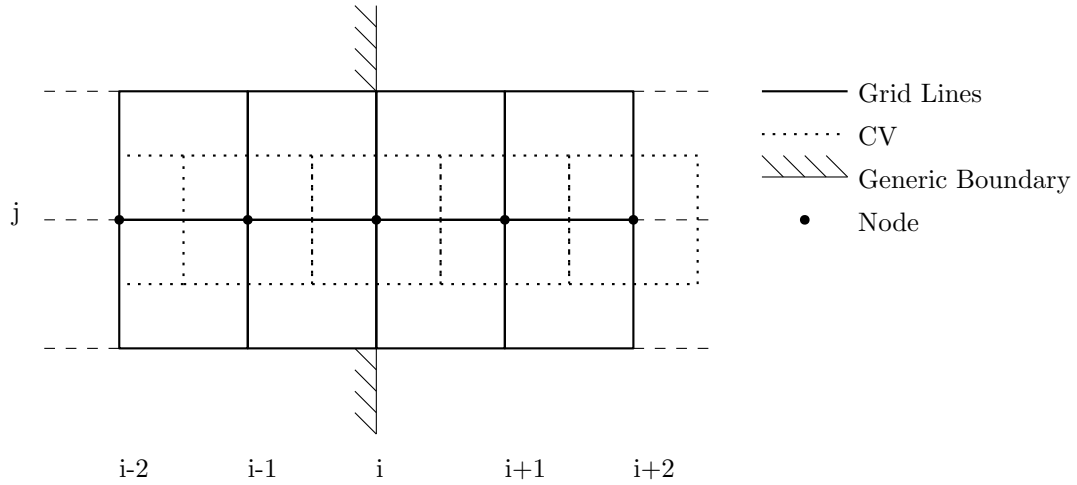

Figure 5.4: Grid arrangement for the implementation of boundary conditions.

to the left of the physical boundary are fictitious, or ghost cells. The cells are populated based on constraints to ensure that the boundary conditions are satisfied. In this way, the spatial loop inside the solver does not need to take special care of the boundaries and a simplified data structure is obtained. Furthermore, the spatial accuracy of the numerical scheme is retained at the boundaries and only limited by the order of accuracy by which the ghost cell values were obtained.
If the boundary condition is a Dirichlet type, then the ghost cells to the left are obtained through extrapolation as

$$\begin{aligned} \phi_i = \phi_{BC} = \frac{\phi_{i+1} + \phi_{i-1}}{2} \Rightarrow \\ \phi_{i-1} = 2\phi_{BC} - \phi_{i+1}. \end{aligned} \tag{5.1.14}$$

If the boundary condition, on the other hand, is of a Neumann type, then the ghost cells are populated as

$$\begin{aligned} \phi_{BC} = \frac{\partial \phi_i}{\partial n} = \frac{\phi_{i+1} - \phi_{i-1}}{2\Delta n} \Rightarrow \\ \phi_{i-1} = \phi_{i+1} + 2\phi_{BC}\Delta n. \end{aligned} \tag{5.1.15}$$

In the special case that $\phi_{BC} = 0$, Eq.(5.1.15) further reduces to

$$\phi_{i-1} = \phi_{i+1}. \tag{5.1.16}$$

For cases where more than one ghost cell is involved, the procedure can be generalised, for example, the Neumann condition for the second ghost cell becomes $\phi_{i-2} = \phi_{i+2}$ and in a similar manner, the Dirichlet condition is adjusted to a higher number of ghost cells.

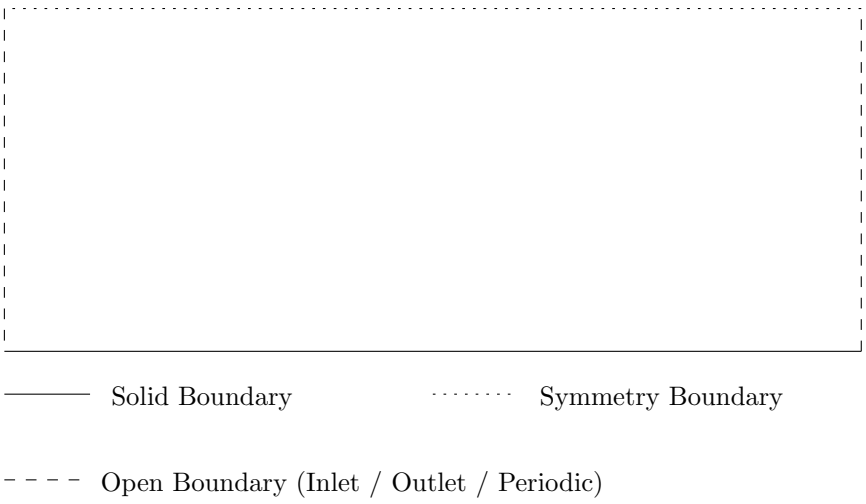

Figure 5.5: Possible boundary conditions in domain.

5.2 Boundary Conditions

In this Section, the most common boundary conditions are briefly reviewed which are implemented into the solver. It may be seen as stating the obvious, however, the author feels that boundary conditions in general are poorly covered in reference books and thus require full documentation to remove ambiguity. These boundaries are shown illustrative in Figure 5.5 and will be elaborated on in the following.

5.2.1 Solid Boundaries (Walls)

Solid boundary conditions are impermeable walls which the flow cannot penetrate. Due to the slip condition at the wall, the velocity components taken at the wall are equal to the wall velocity. For a stationary wall, the velocity is set to zero. The pressure is usually not known but not equal to zero, thus, a Neumann type boundary condition is imposed at the wall. In Figure 5.5, the solid wall is shown on the bottom as a solid line. The velocity boundary conditions thus become

$$u = \phi_{wall,u}, \tag{5.2.1}$$
$$v = \phi_{wall,v}. \tag{5.2.2}$$

The pressure boundary conditions, for simplicity considering a one-dimensional flow, can be derived from the scalar momentum equation as

$$\underbrace{\frac{\partial u}{\partial t}}_{=0} + \underbrace{u\frac{\partial u}{\partial x}}_{=0} = -\frac{1}{\rho}\frac{\partial p}{\partial x} + \underbrace{\nu\frac{\partial^2 u}{\partial x^2}}_{\neq 0}. \tag{5.2.3}$$

The unsteady term is zero as the velocity is specified on the boundary as a Dirichlet type as in Eq.(5.2.1) and Eq.(5.2.2). The convective term is multiplied by the velocity and thus turns to be zero. The diffusive term, however, does not vanish and so the pressure Neumann boundary condition becomes

$$\frac{1}{\rho}\frac{\partial p}{\partial x} = \nu\frac{\partial^2 u}{\partial x^2} \tag{5.2.4}$$

Comparing Eq.(5.2.4) with Eq.(5.1.13), we can see that $\phi_{BC} = \nu(\partial^2 u/\partial x^2)$. For flows outside the Stokes regime, i.e. where convection dominates, it is usually appropriate to neglect the diffusive fluxes at the solid boundary and thus it is common to set $\phi_{BC} = 0$. The same approach has been adopted in the current work.

5.2.2 Open Boundaries (Inflow / Outflow)

Open boundaries are probably one of the most underestimated and still open challenges in the field of fluid dynamics. In 1994, a mini-symposium on open questions and challenges for open boundary conditions was held at the *sixth* and *seventh international conference on numerical methods for laminar and turbulent flow* and is summarised by Sani and Gresho [131]. They provided four test cases, the backward facing step with and without heat transfer, vortex shedding past a circular cylinder and a Poiseuille–Benard channel flow. All flows were considered to be laminar and the both steady and unsteady simulations were of interest. Furthermore, two configurations were given for the domain in question, the first placed the outflow boundary sufficiently far away so as to not disturb the flow while the second domain was made intentionally much shorter. For example, the short domain for the cylinder saw the outflow boundary only four diameters downstream of the cylinder itself. In this region, the von Karman vortex street is still developing. The results were best summarised by Sani and Gresho saying that "it has been an exercise in frustration and we are not thrilled with the results obtained" [131, p. 1007]. In-fact, the very problem with open boundaries is that they simply do not exist in real life. Each system is connected through some form with any other system. To study a singular system numerically, though, it becomes necessary to truncate the system's boundaries from the reservoir it is connected to. In practical terms that means that we have to specify boundary conditions at the interface with the reservoir.
At the macro-scale, an ill-posed open boundary, especially at the outlet, may distort the flow and convergence issues are encountered. At a much smaller scale, however, the problems become more dominant and the physical consequence of truncating the domain becomes apparent. In molecular dynamics simulations, one solves Newton's second law for each atom for which their statistical movement may be evaluated. For a channel flow, it is common to impose periodic boundary conditions so that atoms leaving the domain enter them at the inflow and vice versa. The flow may be left to itself or imposed with an external force to initiate movement. If, however, one wishes to impose true inflow and outflow boundaries, one is faced with two main problems. At the inflow, the atoms that are entering the domain do not have the same number of neighbour atoms as in the centre of the domain since there is no interaction beyond the truncated domain to evaluated inter-atomistic forces. This can amount for up to 30–40% of inter-atomistic forces [132]. Secondly, each atom that enters the domain will change the energy level and so should ideally be placed at an energy level which is required to conserve the overall energy. The former problem can be circumvented by using a feedback loop where a controller is inserting atoms

which in turn is driven by a sensor. The sensor is measuring the flow properties and feeds that information to the controller which is then inserting particles in a way to conserve overall energy, momentum and mass [133]. The latter is especially problematic in multi-scale simulations, where molecular dynamics is coupled with the Navier–Stokes equations to resolve much larger domains. Here, the so-called USHER algorithm [134] may be used to insert particles only at portions so as to not violate the conservation of energy. Further development is also highlighted by Delgado-Buscalioni [135].

This excursion to the micro-scale showed that there are much deeper and fundamental issues associated to imposing open boundaries. This serves as a reminder that our current boundary conditions may only work if they are placed sufficiently far away from anything of interest. That being said, an open boundary condition where flow enters the domain (inflow) is usually not difficult to impose. In Figure 5.5, the primitive variables for the inflow are set as

$$u = \phi_{IN}, \tag{5.2.5}$$
$$v = 0, \tag{5.2.6}$$
$$\frac{\partial p}{\partial n} = 0. \tag{5.2.7}$$

For open boundaries where flow exists the domain (outflow), there is an array of options available to choose from. The particular set of boundary conditions chosen in this work is given as

$$\frac{\partial u}{\partial n} = 0, \tag{5.2.8}$$
$$\frac{\partial v}{\partial n} = 0, \tag{5.2.9}$$
$$p = 0. \tag{5.2.10}$$

A word of caution is in order here. For the velocity component which is tangential to the outflow, a Neumann-type boundary condition is usually sufficient. Specifying an absolute value, i.e. a Dirichlet-type boundary condition, is, according to Sani and Gresho, a poor choice. The reason the pressure uses a Dirichlet condition here is that a fully Neumann-type boundary condition has been observed to dissipate energy for some portion of the domain. Furthermore, if the pressure is not prescribed in at least one cell, the fully Neumann problem is ill-posed and leads to a singular matrix. Imposing the pressure in one cell has been proven to be also not successful as it can, depending on the location of the reference cell, cause the flow to severely change its flow pattern. For example, for the lid driven cavity problem placing the reference cell in one of the bottom corners results in a singular outflow at the corner which removes the vortical structure. Thus, prescribing the pressure over the entirety of the outflow domain removes the problems with the pressure but introduces another issue; it introduces pressure wave reflections at the boundaries. This is especially a problem with elliptic-type methods where the pressure waves are propagated through

the entire domain instantly. Sani and Gresho also discussed the role of the normal velocity component at the outflow and stated that neither a Dirichlet, Neumann (regardless if the pressure is prescribed entirely or just through a reference cell) nor an advection equation-like boundary condition are valid choices. In essence their argumentation highlights that there are no valid outflow boundary conditions but some conditions are still required to be able to simulate the governing equations. It has been found that the above given boundary conditions work best for all cases that are tested in this work but it should be noted that more advanced boundary conditions can be imposed.

5.2.3 Periodic Boundaries

Periodic boundary conditions are the simplest of all and it is probably even confusing to label them as boundary conditions as their very intention is to mimic a flow where no boundaries are present. To impose periodic boundaries in Figure 5.5, consider the east and west face, i.e. the two dashed lines on the left and right. The primitive variables are simply copied from the respective face to the other so that we have

$$u_{east} = u_{west}, \tag{5.2.11}$$
$$v_{east} = v_{west}, \tag{5.2.12}$$
$$p_{east} = p_{west}, \tag{5.2.13}$$

and similarly for the west face. If the boundaries are set apart far enough, the influence of the periodicity on the flow is not felt. At the same time, the periodicity also implies that the flow pattern prevails for the entirety of an infinite domain, which is also non-physical. This assumption would hold only for a homogeneous domain which is rarely, if ever, the case. To study simplistic domains, or the decay of turbulence, though, this particular set of boundary conditions has proven to be an effective tool to investigate fluid dynamics without the need to resolve physical boundaries, which usually induce anisotropic patterns and thus simple models, for example analytical solution, which are used to describe such flows are no longer valid. Periodic boundaries have a right of existence but need to be used with caution.

5.2.4 Symmetry Boundaries

Symmetry boundary conditions are, like periodic boundaries, an example of numerical boundary conditions that simply exist to reduce computational complexity but have no real counterpart in the physical world. Symmetrical boundary conditions approach solid boundary conditions in the limit of an infinitely smooth surface. Therefore, the normal velocity component is still equal to zero while the tangential velocity component, in absence of surface roughness, is unknown and thus turns to be a Neumann type boundary condition. The pressure is untouched and can be solved in the same way as the solid boundary case. The primitive variables thus become, for the symmetry condition given in Figure 5.5

$$u = \frac{\partial u}{\partial y}, \tag{5.2.14}$$

$$v = 0, \tag{5.2.15}$$

$$p = \frac{\partial p}{\partial y}. \tag{5.2.16}$$

5.3 Numerical Schemes

The final part of the numerical discretisation procedure concerns the numerical schemes that are being used. We will show the two schemes which are employed through the study, a third-order polynomial discretisation scheme which does not contain any high-resolution scheme properties such as transportiveness or conservativeness, and a simple second order scheme with artificial dissipation. The latter scheme is merely given as a reference solution as it has been widely used in the literature and it is possible to benchmark the different CB schemes and RS approaches against a classical, well documented scheme. The scheme is modified to handle velocities close to the machine accuracy, where the pressure sensor may treat numerical oscillations as discontinuities which cause numerical oscillations.

5.3.1 Central Scheme with Artificial Dissipation

We first focus on the central scheme with artificial dissipation and show the modifications necessary to treat low velocity flows. The scheme was introduced by Jameson *et al.* [10] where the authors presented a simple extension to the central scheme. We consider here the east face of the control volume for which the scheme is written as

$$\phi_{i+1/2,j}\Delta y = \frac{\phi_{i,j} + \phi_{i+1,j}}{2} - D_{i+1/2,j}. \tag{5.3.1}$$

Here, $D_{i+1/2,j}$ represents the necessary artificial dissipation which is added to the central scheme and given by

$$D_{i+1/2,j} = \Lambda^S_{i+1/2,j}\left[\epsilon^{(2)}_{i+1/2,j}(\phi_{i+1} - \phi_i) - \epsilon^{(4)}_{i+1/2,j}(\phi_{i+2} - 3\phi_{i+1} + 3\phi_i - \phi_{i-1})\right]. \tag{5.3.2}$$

The property Λ is the sum of spectral radii of the convective flux Jacobians [126] which is given for two-dimensions as

$$\Lambda^S_{i+1/2,j} = \Lambda^I_{i+1/2,j} + \Lambda^J_{i+1/2,j}. \tag{5.3.3}$$

The individual components are interpolated to the cell face as

$$\Lambda^{I,J}_{i+1/2,j} = \frac{1}{2}\left(\Lambda^{I,J}_{i,j} + \Lambda^{I,J}_{i+1,j}\right) \tag{5.3.4}$$

while they are solved as

$$\Lambda^{I,J}_{i,j} = (\mathbf{u}^{\perp} + s)\Delta A. \tag{5.3.5}$$

Here, $\mathbf{u}^{\perp}$ is the normal velocity component to the inter-cell face which has a surface area of ΔA, while the artificial speed of sound is given by $s = \sqrt{\mathbf{u}^2 + \beta/\rho}$. See also Section 3.3.1 for more details. The coefficients $\epsilon^{(2)}_{i+1/2,j}$ and $\epsilon^{(4)}_{i+1/2,j}$ are found, in turn, as

$$\epsilon^{(2)}_{i+1/2,j} = k^{(2)} \max\left(\Psi_{i,j}, \Psi_{i+1,j}\right), \tag{5.3.6}$$

$$\epsilon^{(4)}_{i+1/2,j} = \max\left[0, \left(k^{(4)} - \epsilon^{(2)}_{i+1/2,j}\right)\right]. \tag{5.3.7}$$

The property Ψ is referred to as the pressure sensor which is defined as

$$\Psi_{i,j} = \frac{|p_{i+1,j} - 2p_{i,j} + p_{i-1,j}|}{p_{i+1,j} - 2p_{i,j} + p_{i-1,j}}, \tag{5.3.8}$$

which has been introduced so that the scheme can distinguish between smooth and discontinuous parts of the flow. For incompressible flows, discontinuities are not as much of a problem as for compressible flows, however, discontinuities can still arise, for example, in multiphase flows at the phase-separating interface. The pressure sensor is used to drive the scaling factors $\epsilon^{(2)}_{i+1/2,j}$ and $\epsilon^{(4)}_{i+1/2,j}$. These, in turn, determine the amount of artificial dissipation given to the numerical scheme through the addition of a second- and forth-order derivative. The constants $k^{(2)}$ and $k^{(4)}$ are given as

$$k^{(2)} = \frac{1}{2}, \tag{5.3.9}$$

$$\frac{1}{128} < k^{(4)} < \frac{1}{64}. \tag{5.3.10}$$

These are default parameters which have been proven to work for a range of cases. That does not imply, however, that these values work universally.

For flows in which the absolute values approaches the machine accuracy, the pressure sensor, i.e. Eq.(5.3.8), may not be able to distinguish between physical and numerical oscillations. Numerical oscillations may appear at random and introduce numerical shock waves for which the artificial dissipation term may introduce oscillations. To prevent these oscillation, it has been found that setting

$$k^{(2)} = \epsilon^{(2)}_{i+1/2,j} \tag{5.3.11}$$

$$k^{(4)} = \epsilon^{(4)}_{i+1/2,j} \tag{5.3.12}$$

provides a stable, yet still sufficiently dissipative approach where the local dissipation is now only scaled by the sum of the spectral radii of the flux Jacobians. The pressure sensor is effectively removed and therefore numerical oscillations near the machine accuracy do not pose any numerical challenges.

5.3.2 Polynomial Reconstruction Schemes

In this Section, a general procedure is presented which can be used to construct polynomial reconstruction schemes of arbitrary order of accuracy. We consider here a one-dimensional case which can be used in the x- and y-direction and where the spacing in each direction is constant and equal to unity. During the discretisation procedure, the scheme will be scaled by the mesh spacing so that it is also applicable to cases with spacings which are not equal to one. The general reconstruction scheme is given as

$$\phi^L_{i+1/2} = a\phi_i - b\phi_{i-1} + c\phi_{i+1} + d\phi_{i+2} \tag{5.3.13}$$

for a left-sided interpolation and

$$\phi^R_{i+1/2} = a\phi_{i+1} - b\phi_{i+2} + c\phi_i + d\phi_{i-1} \tag{5.3.14}$$

for a right-sided interpolation. The coefficients a, b, c and d are unknowns and are to be determined. In the following we will use the left-sided interpolation, the same results are, however, obtained with the right-sided interpolation scheme. A derivative may be written as an approximation as

$$\left(\frac{\partial\phi}{\partial x}\right)_i = \phi^L_{i+1/2} - \phi^L_{i-1/2}. \tag{5.3.15}$$

Inserting Eq.(5.3.13) into Eq.(5.3.15) yields

$$\left(\frac{\partial\phi}{\partial x}\right)_i = (a\phi_i - b\phi_{i-1} + c\phi_{i+1} + d\phi_{i+2}) - (a\phi_{i-1} - b\phi_{i-2} + c\phi_i + d\phi_{i+1})\,. \tag{5.3.16}$$

This may be rearranged in terms of ϕ which results in

$$\left(\frac{\partial\phi}{\partial x}\right)_i = d\phi_{i+2} + (c-d)\phi_{i+1} + (a-c)\phi_i - (a+b)\phi_{i-1} + b\phi_{i-2}. \tag{5.3.17}$$

The values at $i \pm 1$ and $i \pm 2$ are obtained through a Taylor series in the form of

$$\phi_{i+2}(x) = \phi_i(x) + \frac{\partial\phi}{\partial x}(2\Delta x) + \frac{\partial^2\phi}{\partial x^2}\frac{(2\Delta x)^2}{2!} + \frac{\partial^3\phi}{\partial x^3}\frac{(2\Delta x)^3}{3!} + \frac{\partial^4\phi}{\partial x^4}\frac{(2\Delta x)^4}{4!} + \mathcal{O}(\Delta x)^5, \tag{5.3.18}$$

$$\phi_{i+1}(x) = \phi_i(x) + \frac{\partial\phi}{\partial x}(\Delta x) + \frac{\partial^2\phi}{\partial x^2}\frac{(\Delta x)^2}{2!} + \frac{\partial^3\phi}{\partial x^3}\frac{(\Delta x)^3}{3!} + \frac{\partial^4\phi}{\partial x^4}\frac{(\Delta x)^4}{4!} + \mathcal{O}(\Delta x)^5, \tag{5.3.19}$$

$$\phi_{i-1}(x) = \phi_i(x) - \frac{\partial\phi}{\partial x}(\Delta x) + \frac{\partial^2\phi}{\partial x^2}\frac{(\Delta x)^2}{2!} - \frac{\partial^3\phi}{\partial x^3}\frac{(\Delta x)^3}{3!} + \frac{\partial^4\phi}{\partial x^4}\frac{(\Delta x)^4}{4!} + \mathcal{O}(\Delta x)^5, \tag{5.3.20}$$

$$\phi_{i+2}(x) = \phi_i(x) - \frac{\partial\phi}{\partial x}(2\Delta x) + \frac{\partial^2\phi}{\partial x^2}\frac{(2\Delta x)^2}{2!} - \frac{\partial^3\phi}{\partial x^3}\frac{(2\Delta x)^3}{3!} + \frac{\partial^4\phi}{\partial x^4}\frac{(2\Delta x)^4}{4!} + \mathcal{O}(\Delta x)^4. \tag{5.3.21}$$

Substituting Eq.(5.3.18–5.3.21) back into Eq.(5.3.17), making the denominators part of the unknowns a, b, c, d and recalling that Δx has been assumed to be equal to one, we have

$$\begin{aligned}\left(\frac{\partial\phi}{\partial x}\right)_i = \\ & d\left[\phi_i + 2\frac{\partial\phi}{\partial x} + 4\frac{\partial^2\phi}{\partial x^2} + 8\frac{\partial^3\phi}{\partial x^3} + 16\frac{\partial^4\phi}{\partial x^4}\right] + \\ & (c-d)\left[\phi_i + \frac{\partial\phi}{\partial x} + \frac{\partial^2\phi}{\partial x^2} + \frac{\partial^3\phi}{\partial x^3} + \frac{\partial^4\phi}{\partial x^4}\right] + \\ & (a-c)\phi_i - \\ & (a+b)\left[\phi_i - \frac{\partial\phi}{\partial x} + \frac{\partial^2\phi}{\partial x^2} - \frac{\partial^3\phi}{\partial x^3} + \frac{\partial^4\phi}{\partial x^4}\right] + \\ & b\left[\phi_i - 2\frac{\partial\phi}{\partial x} + 4\frac{\partial^2\phi}{\partial x^2} - 8\frac{\partial^3\phi}{\partial x^3} + 16\frac{\partial^4\phi}{\partial x^4}\right]. \end{aligned} \tag{5.3.22}$$

Eq.(5.3.22) may be rearranged as

$$\left(\frac{\partial\phi}{\partial x}\right)_i = (a-b+c+d)\frac{\partial\phi}{\partial x} + [c-a+3(b+d)]\frac{\partial^2\phi}{\partial x^2} + [c+a+7(d-b)]\frac{\partial^3\phi}{\partial x^3} + [c-a+15(b+d)]\frac{\partial^4\phi}{\partial x^4}. \tag{5.3.23}$$

Using Eq.(5.3.23), schemes with different order of accuracy can be constructed for appropriately chosen values of a, b, c and d. To satisfy a CFL-like constraint, the coefficients of the first-order derivative should add up to one [72]. Setting arbitrarily $b = c = d = 0$, it follows that $a = 1$. Inserting those values back into Eq.(5.3.13) and Eq.(5.3.14), we obtain

$$\phi^L_{i+1/2} = \phi_i, \tag{5.3.24}$$

$$\phi^R_{i+1/2} = \phi_{i+1}, \tag{5.3.25}$$

which is indeed a first-order scheme. To construct higher order schemes, the derivatives are set to zero and the corresponding system of equations for the coefficients is solved. For example, a second-order scheme is obtained by setting $c = d = 0$ so that we have $a - b = 1$ from the first-order derivative (CFL-like constraint) and $3b - a = 0$ so that the second-order derivative in Eq.(5.3.23) vanishes. The values are found as $a = 3/2$ and $b = 1/2$ so that Eq.(5.3.13) and Eq.(5.3.14) yield

$$\phi^L_{i+1/2} = \frac{3}{2}\phi_i - \frac{1}{2}\phi_{i-1}, \tag{5.3.26}$$

$$\phi^R_{i+1/2} = \frac{3}{2}\phi_{i+1} - \frac{1}{2}\phi_{i+2}. \tag{5.3.27}$$

A third-order scheme is found analogously, where we set $d = 0$ and require that the first-order derivative's coefficients equate to unity while eliminating the second-

and third-order derivatives. We obtain the following system of equations for the coefficients

$$\begin{aligned} a - b + c &= 1, \\ 3b - a + c &= 0, \\ a - 7b + c &= 0. \end{aligned} \tag{5.3.28}$$

The coefficient result in $a = 5/6$, $b = 1/6$ and $c = 1/3$ so that Eq.(5.3.13) and Eq.(5.3.14) take the form of

$$\phi^L_{i+1/2} = \frac{5}{6}\phi_i - \frac{1}{6}\phi_{i-1} + \frac{1}{3}\phi_{i+1}, \tag{5.3.29}$$

$$\phi^R_{i+1/2} = \frac{5}{6}\phi_{i+1} - \frac{1}{6}\phi_{i+2} + \frac{1}{3}\phi_i. \tag{5.3.30}$$

Eq.(5.3.29) and Eq.(5.3.29) will be used through the rest of this work and is referred to as the third-order scheme. Once again it is important to note that the simple polynomial reconstruction scheme is a simplistic interpolation, that does not consist of any properties that high-resolution scheme poses. The scheme has its advantages, though, namely that it is relatively easy to implement, requires little computational effort and is easily extended to higher-orders of accuracy.

5.3.3 Time Integration Procedures

The final Section in this numerical discretisation process is concerned with the time integration. Throughout Section 3.3, a case has been made to use explicit time integration schemes so as to preserve the non-linear behaviour of the Navier–Stokes equations. For explicit systems, the Runge–Kutta methods are commonly used due to their compactness, i.e. the integration range is from t to $t + \Delta t$ whereas other higher-order integration methods require time information from previous time levels. Furthermore, higher-order schemes can be easily constructed. In this work, the third-order Runge–Kutta version of Jiang and Shu [136] is used for pseudo time derivatives, which also provides the TVD property in time. It is given as

$$\begin{aligned} \mathbf{u}^* &= \mathbf{u}^n + \Delta\tau \mathrm{RHS}(\mathbf{u}^n), \\ \mathbf{u}^{**} &= \frac{3}{4}\mathbf{u}^n + \frac{1}{4}\mathbf{u}^* + \frac{1}{4}\Delta\tau \mathrm{RHS}(\mathbf{u}^*), \\ \mathbf{u}^{n+1} &= \frac{1}{3}\mathbf{u}^n + \frac{2}{3}\mathbf{u}^{**} + \frac{2}{3}\Delta\tau \mathrm{RHS}(\mathbf{u}^{**}). \end{aligned} \tag{5.3.31}$$

Here, the RHS is the respective right-hand side of the continuity or momentum equation of the incompressible methods listed in Section 3.3. For real time-derivatives, a second-order scheme is used and given as

$$\frac{\partial \mathbf{u}}{\partial t} = \frac{3\mathbf{u}_i^{m+1,n} - 4\mathbf{u}_i^m + \mathbf{u}_i^{m-1}}{2\Delta t}. \tag{5.3.32}$$

At this stage it might be useful to highlight that only the term $3\mathbf{u}_i^{m+1,n}$ is updated during the inner cycle of the Runge–Kutta integration in pseudo time while the remaining terms, i.e. $4\mathbf{u}_i^m$ and $\mathbf{u}_i^{m-1}$ are updated once the Runge–Kutta cycle has converged to a steady state solution.
Theoretically, the Runge–Kutta procedure could be applied to both pseudo and real time derivatives. The reason to opt for a more simplistic second-order scheme is that it does not require any inner iterations. For each stage in the Runge–Kutta cycle, the RHS has to be constructed and integrated. Doing so for the real time-derivative would result in a system that requires two inner iteration loops for the time alone which would result in rather large computational times for unsteady systems. Therefore, the computational much less expensive second-order scheme is used for the real time derivatives.

The time step has to be defined in such a way that it does not introduce oscillations, since explicit schemes are bounded by a stability criterion. The time step is usually based on the inviscid fluxes but for stagnant flows a time step based on the viscous fluxes may be required. The inviscid time step restriction has been already given in Section 3.3.1 and is repeated below for completeness

$$\Delta t_{inviscid} = \frac{\mathrm{CFL}\Delta \mathrm{x}}{\lambda_{max}}, \tag{5.3.33}$$

where λ_{max} is the maximum local eigenvalue. This is a problematic definition for non-hyperbolic system of equations where the eigenvalues could be imaginary. This is usually circumvented by using the maximum local velocity u_{max} for parabolic or elliptic equations. The hyperbolic definition of the local eigenvalue is, however, rather conservative through the introduction of the β parameter so that $\lambda_{max} < u_{max}$ is always satisfied. Thus, even non-hyperbolic systems may use the inviscid time step as defined by Eq.(5.3.33). Furthermore, this has the advantage that the time step is always chosen in the same way for hyperbolic, parabolic and elliptic system of equations. Thus, the inviscid time step is chosen in the same manner for all methods so as to have a fair comparison in terms of residuals and computational cost.
To complete the discussion on the appropriate time step, we need to define the viscous contribution of the Navier–Stokes equations to the time step which is defined as

$$\Delta t_{viscous} = \frac{\mathrm{CFL}(\Delta x)^2}{4\nu}. \tag{5.3.34}$$

The final time step is found by taking

$$\Delta t = \min(\Delta t_{inviscid}, \Delta t_{viscous}). \tag{5.3.35}$$

Further details and considerations to obtain a suitable time step can be found in [21, 123, 126].

Chapter 6

Results and Discussion

The aim of this Section is to first validate the different CB schemes along with the different incompressible methods and to judge their performance for classical benchmark problems. They were selected to investigate different aspects of the Navier–Stokes equations which help to understand the strengths and limitations of each presented method. It is important to stress here that not all simulations will be favourable for one and only one particular method and/or scheme. Rather, the collective behaviour of all simulations needs to be assessed which, by themselves, may not provide the full picture. The following test cases were selected with a brief comment given as to why this particular test case is helpful in understanding the behaviour of each method and scheme.
First, we investigate the flow inside a square cavity in Section 6.1, where the top lid is set in motion and maintains a constant displacement velocity. This causes a vortex to appear in the centre of the cavity which produces secondary and tertiary vortices in the corner. In particular, we are interested in how well each scheme and method performs for high Reynolds number flows. Therefore, Reynolds numbers ranging from Re=100 to Re=5000 are investigated and compared against computational data.
The second test case is concerned with forced separated flows over a backward facing step. This test case has been mainly selected as published results comparing the SCB and MCB scheme have to be judged with scepticism. This work provides results in much better agreement with the experimental data but also highlights issues with the imposition of boundary conditions, open boundary conditions for elliptic equations and the reference data itself against which the results have been compared against in the literature. In order to provide a better comparison, another set of experimental reference data is selected, and simulations were performed to match those data. The Reynolds numbers can be considered to be within a moderate range where the maximum Reynolds number is Re=389.
The third example is similar to the aforementioned example, only that it purposefully stays within the laminar regime. Here, the Reynolds number ranges from Re=10 to Re=100. Especially near the lower end of the Reynolds number spectrum, some methods do have convergence problems and so a comparison at these scales provides inisght to the Reynolds number dependence. Furthermore, the geometry is modified so that the domain does not simply feature a step on one side

but the same step also on the opposite side, i.e. making the domain symmetrical about the centreline. The flow in such suddenly expanding channels exhibit an interesting flow phenomenon called bifurcation, which is the symmetry breaking effect of the Navier–Stokes equations due to the non-linear term. This breaking of symmetry produces an unexpected flow pattern and capturing this behaviour correctly is highly scheme dependent. As we will see, not just the CB scheme or interpolation scheme have an effect but also the incompressible method that is being used.
The final test case is the two-dimensional Taylor–Green vortex problem, in which a vortical flow is given as an initial problem with periodical boundary conditions for which then an analytical solution exists. The flow is inherently unsteady and thus we can investigate the behaviour of each method and scheme for long time integration periods as the kinetic energy decays. The method is traditionally studied as a three-dimensional problem; however we can still investigate the two-dimensional evolution. Comparisons with the three-dimensional case may be difficult to do in a meaningful way but we can still compare the data against the analytic solution.

These four test cases were selected to study a common theme, vortical — or turbulent — flows. If we consider turbulence for the moment, we know from classical text books, see for example Pope [137], Davidson [138] or Tennekes and Lumley [139], that turbulence is inherently three-dimensional and therefore two-dimensional turbulence does not exist. Vortex stretching is a process in which a vortex filament is continuously sheared and strained so that it loses its size and energy and ultimately, at some small scale, dissipates all its remaining energy into heat. Vortex stretching only occurs for three-dimensional flows and is absent when the equations are considered in a two-dimensional form. Therefore, studies investigating two-dimensional turbulent-like structures are usually dismissed based on these grounds. There are, however, plenty examples where the flow can be approximated as a two-dimensional flow while still being governed by turbulence. Take the atmosphere of the earth as an example, its height compared to the radius of the earth is diminishingly small. Yet the turbulence and thus non-linear effects make the weather difficult to predict accurately. In-fact, Kuksin and Shirikyan [140] highlight in their book that there is a wealth of research available on two-dimensional turbulent-like flows. It is not claimed that this is equivalent to real three-dimensional turbulence, but that it can be used to study the effect of turbulence and that it provides a somewhat simplified, model-like, equation environment to study aspects of turbulence. With that in mind, it might be striking with what certainty two-dimensional results are dismissed, while three-dimensional, homogeneous and isotropic turbulent flows are commonly investigated and accepted. Turbulent flows are inherently anisotropic and non-homogeneous and it is here where the multi-directional nature of the developed framework comes into the picture. The scheme provides a framework which is developed with an anisotropic picture of the Navier–Stokes equations in mind. The test cases where selected in a way that we can investigated different aspects of turbulence in an isolated way, rather than to investigate all aspects at once. By dissecting and separating each problem into its own test case, we can make a clear statement about each method and scheme about its applicability to a certain situation. Combining all simulations into one grand picture will reveal the strength and shortcomings of

each tested scheme and method. In particular, the square cavity has been selected to investigate high Reynolds numbers flows, as is characteristic of turbulent flows. Here, the inertia-forces are dominating the viscous forces. The backward-facing step geometry provides further insight into the energy balance of vortical flows. Here, a recirculation area is formed and maintained for which the flow will eventually reattach to the wall. Discrepancies in the reattachment point will highlight a deficit or surplus of kinetic energy contained within the recirculation area. Since it is those vortical structure that provide turbulent kinetic energy to smaller eddies [141], the degree of agreement of different methods and schemes may shed further inside on the applicability of those methods to turbulent flows. The bifurcation phenomenon studied in the suddenly expanding channel geometry is of particular interest as it investigates the sudden change in flow pattern at some critical Reynolds number. To capture these effects requires sophisticated methods and schemes and it will be shown which surprising influence each scheme and method has on the final result. It can be also used to study the onset of the bifurcation from which conclusions can be drawn as to which scheme may be suitable to predict the onset of turbulence correctly. Finally, all turbulent flows are unsteady and so the Taylor–Green vortex flow is a prime candidate to capture this behaviour. Furthermore, the analytical solution allows to compute the expected total kinetic energy of the domain which can be compared against the numerically resolved kinetic energy. The difference in these two values gives information about the numerical dissipation which is inherent to each scheme.

It is important to stress here that it is not claimed that the two-dimensional results are a perfectly suitable replacement for three-dimensional simulations. Rather, it is justified here why those two-dimensional simulations should not be disregarded from the outset. To understand the true value of these schemes and methods, it is still mandatory to investigate actual turbulent and three-dimensional flows. However, as an initial step, we investigate each component of turbulent flows individually as described above to provide a first insight into the scheme and method.

For reproducibility, the simulation parameters that are being used for all simulations and which are kept constant for each test case are summarised in Table 6.1.

6.1 High-Reynolds Number Flow Inside a Square Cavity

The lid driven cavity flow is a classical test case against which new methods and solvers are commonly benchmarked. In a recent publication, Erturk [142] reviewed the literature available on two-dimensional lid driven cavity flows and categorised the research into three categories; those which are concerned with the steady state solution, those which are using stability analysis to determine the critical Reynolds number at which the flow changes from a steady to an unsteady behaviour and those where direct numerical simulations are used to predict the bifurcation to an unsteady

Table 6.1: Simulation parameters for all test cases where test case 1 = lid driven cavity, test case 2 = backward facing step (based on Denham and Patrick), test case 3 = backward facing step (based on Armaley *et al.*), test case 4 = sudden expansion and test case 5 = Taylor–Green vortex problem. β refers to the numerical convergence parameter in the continuity equation of the AC, FSAC-PP and FSAC-VP method, ϵ is the convergence criterion, ω^{PP} is the relaxation factor for the Poisson solver (FSAC-PP only) and it^{PP} the corresponding number of iterations, CFL_{p-t} and CFL_{r-t} the pseudo- and real-time based CFL number and $\alpha_{u,v,p}$ the under-relaxation factors for the primitive variables.

	β	ϵ	ω^{PP}	it^{PP}	CFL_{p-t}	CFL_{r-t}	α_u	α_v	α_p
Test case 1	1.0	10^{-8}	1.0	10	0.7	-	0.7	0.7	0.5
Test case 2	1.0	10^{-8}	1.0	10	0.7	-	0.7	0.7	0.5
Test case 3	1.0	10^{-8}	0.7	10	0.5	-	0.7	0.7	0.5
Test case 4	1.0	10^{-12}	0.7	10	0.8	-	1.0	1.0	1.0
Test case 5	1.0	10^{-4}	1.0	10	0.4	0.7	0.7	0.7	0.7

state numerically. Prasad and Koseff [143] provided experimental data and revealed flow structures that are present in the lid driven cavity problem. As pointed out by Erturk, these flow structures are inherently three-dimensional and thus any two-dimensional simulation can only be approximative of the real flow. This is similar to the argumentation on two-dimensional turbulence. In such cases, it is correct to state that three-dimensional effects — like the Taylor–Görtler vortices — can not be resolved by the two-dimensional simulation. However, we can approximate the bulk of the flow to a high degree of certainty and so these two-dimensional validation cases are invaluable in establishing the validity of numerical schemes and methods. In references [144–147], the steady state simulation was superimposed with a perturbation so as to establish through eigenvalue analysis of the system, at which Reynolds number the flow would become unsteady. Their results suggest that this Reynolds number should be around Re=8000. The studies found in [148–151] considered the flow from a direct numerical simulation point of view, even though the flow was two-dimensional, and gave a range of critical Reynolds numbers which were around $7400 < Re < 8400$, after which the flow would turn to be unsteady. Both approaches agree well with each other and state that for Reynolds numbers above these critical values, no steady state solution can exist. We are faced with a dilemma here in which the work of Ghia *et al.* [152], for example, presents widely accepted reference data for the lid driven cavity from a numerical point of view where steady state results are available up to Re=10000. There are several ways how a steady state solution can be forced. The simplest form is to provide a sufficient amount of numerical dissipation, or modelled physical dissipation. The former can be achieved through low-order interpolation schemes while the latter may be realised through turbulence models. In fact, the central scheme with artificial dissipation offers user-defined parameters through which the amount of numerical dissipation

can be fine tuned, see Eq.(5.3.9) and Eq.(5.3.10) on how the parameter $k^{(2)}$ and $k^{(4)}$ enter the scheme and tune the dissipation. For the polynomial reconstruction scheme in Eq.(5.3.29) and Eq.(5.3.30), however, no such scaling is available so that its numerical dissipation is solely a function the its Taylor-series truncation error which leads to

$$\nu_{\text{num}} \propto \begin{cases} \mathcal{O}(\Delta x^2) + f(k^{(2)}, k^{(4)}), & \text{central scheme} \\ \mathcal{O}(\Delta x^3). & \text{polynomial scheme} \end{cases} \tag{6.1.1}$$

For a vanishingly small Δx, therefore, the numerical dissipation will vanish while the physical dissipation is recovered. Erturk [142] suggested and provided numerical evidence that if the mesh is refined sufficiently, so as to resolve smaller and smaller scales, a steady state solution can be achieved under these circumstances even for Re=10000. Although it contradicts the above cited literature, it is indeed possible that the numerical dissipation provided by a scheme may stabilise the solution of a given problem far above the critical Reynolds number. This highlights the important role of numerical dissipation and the way it can, albeit in the small details, influence the outcome of a simulation significantly. The amount of numerical dissipation within a simulation is notoriously difficult to establish but first attempts to do so have been presented by El Rafei *et al.* [153] in a recent study. We can, however, look at the tell-tale signs that numerical dissipation leaves behind. For example, if we consider the lid driven cavity as an example where we keep the mesh size constant but increase the Reynolds number, we would expect low-dissipative numerical schemes to fail to predict the flow correctly after some critical Reynolds number which is scheme dependent. From Eq.(6.1.1), we can see that the numerical dissipation diminishes faster for the polynomial scheme than for the central scheme with artificial dissipation, due to its higher Taylor-series truncation and the absence of user-defined dissipation. Therefore, it is quite reasonable to assume that the polynomial reconstruction may fail before the central scheme. One may argue that this would make the scheme less applicable to practical situations, however, that would not be entirely correct. It has long been believed that numerical dissipation is a property of the numerical scheme; the very fact that we have a central scheme with artificial dissipation should be evidence enough. In this work, our approach to the problem is different. We make use of the polynomial reconstruction, in this case of third-order, and provide the numerical dissipation through a RS. This approach offers the possibility that an arbitrary high-order of interpolation can be used, without having to consider the amount of dissipation that is added by the scheme. That, in turn, is provided by Rusanov's RS [68] which has been reported to be one of the more dissipative RS [96]. This approach has gained traction in the compressible literature where higher order schemes are used in conjunction with Rusanov's RS to provide stability. See the work of Dumbser and co-workers for more information on this recent development [154–156]. This approach offers the advantage that dissipation is not just added through the RS but also that additional transportiveness and conservativeness is added to the interpolation procedure, a property which is inherent to the SCB scheme due to the inclusion of Godunov's RS but absent in the MCB framework. As has been reviewed in Section 4.2, a RS consolidates numerical discontinuities at cell interfaces through a local eigenvalue analysis. Thus, the

numerical dissipation coming from the RS can be understood to be locally scaled by the eigenvalues, in a sense. Therefore, although we still have to treat the added dissipation as purely numerical, it is based on the local eigenstructure and may be regarded to mimic the physical dissipation much closer than the purely heuristic central scheme with artificial dissipation.

Razavi *et al.* [17] presented results using the SCB and MCB scheme for the lid driven cavity problem up to Re=10000 and reported converged and steady state results for all simulations, which may be attributed to their central scheme with artificial dissipation. In their study, however, the results were obtained at different CFL numbers, claiming that the MCB scheme could be operated at much higher CFL numbers than the SCB scheme and therefore outperform it. Although not explicitly shown here, the same observations could not be made with within the present investigation. Both schemes exhibited the same CFL restrictions and were becoming unstable at around the same critical CFL number which corresponded to the expected stability limit for the explicit Runge–Kutta time integration scheme. We use a third-order version with TVD properties while Razavi *et al.* [17] made use of a forth-order Runge–Kutta scheme. The differences in the maximum permissible CFL number was a factor of two. This, however, did not always show a speed up of equal order. For some simulations, the SCB scheme performed only moderately slower than the MCB scheme in terms of iterations, while the MCB scheme was still operated with a higher CFL number. This makes the presented data difficult to compare for which we have adopted here constant parameters for all test cases, so as to make them directly comparable in a fair manner. Furthermore, due to the onset of an unsteady behaviour at around $7400 < \mathrm{Re} < 8400$, results only up to Re=5000 are presented here. At such Reynolds numbers, turbulent effects are already present which allows to investigate the role of numerical dissipation here. Although higher Reynolds number results could have been obtained, those were dropped due to the divergence in opinions about how the flow should behave.

The geometry along with its boundary conditions is shown in Figure 6.1. The top wall is in a constant horizontal motion with velocity u_{lid} while all remaining walls are stationary. The Reynolds number is adjusted by tuning the viscosity and the reference length is equal to the length of the top wall.

Figures 6.2–6.5 are showing the velocity profiles obtained with the AC, FSAC-PP, FSAC-VP and FSVP method, respectively. For each method, the simulations show the velocity profiles for Re=100, Re=400, Re=1000, Re=3200 and Re=5000. All simulations were obtained using a $n_x \times n_y = 128^2$ computational grid except for Re=5000, where simulations were also carried out for $n_x \times n_y = 256^2$. All simulations were performed using the central scheme with artificial dissipation as well as the polynomial third-order scheme as a reference. The schemes are referred to as AD for artificial dissipation and no CB, or non CB, to indicated that no characteristic-based scheme was used. Furthermore, the SCB and MCB scheme are shown by themselves as well as the Rusanov RS with and without the MCB scheme. These schemes all use the polynomial interpolation scheme for their inter-cell flux reconstruction.

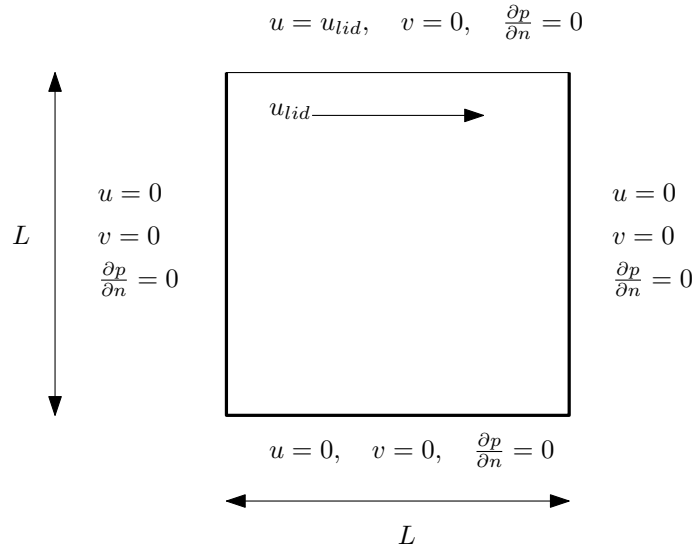

Figure 6.1: Geometrical and boundary condition set up for the lid driven cavity example.

All simulations up to Re=1000 do not show any noticeable difference in the results and agree well with the reference data of Ghia *et al.* [152]. At Re=3200, however, we can see differences among the various schemes which may be attributed to the onset of turbulence. In Figure 6.2d, we can see the velocity profile for the AC method at Re=3200. Here, the AD and MCB scheme do match each other and show no visual qualitative difference. Both Rusanov approaches along with the SCB scheme start to struggle to match the reference data, unlike the AD and MCB scheme. Looking at Figure 6.3d and 6.4d, which depicts the same flow scenario for the FSAC-PP and FSAC-VP method, they show the exact opposite. Here, for both methods, the RS-based approaches perform better than the AD and MCB scheme by themselves. The polynomial reconstruction scheme by itself (no CB) fails to develop the flow at all. As hypothesised above, this scheme is the first to incorrectly predict the flow, once a turbulent-like state is reached in which the numerical dissipation cannot match the removed physical dissipation on the smallest unresolved scales. In-fact, in a flow with vanishing viscosity it would be expected that the lid would just slide over the fluid without it reacting to the top lid movement. In absence of viscous diffusion, the flow would not be able to be dragged along and start to form the main vortex core. Thus, by analogy, the absence of numerical dissipation results in the inability of the flow to develop the primary vortex structures. The AD scheme performs marginally better but still struggles to capture the velocity profiles confidently. From a purely qualitative point of view, the AC method seems to perform the best and even though the RS-based approaches are not as accurate as the AD, non CB and MCB approach, they too show a good agreement with the reference data. It is interesting to note here that the AC method shows much better agreement of the AD and non CB scheme compared to the other methods. However, it is also true that once the multi-directional Godunov-type framework is introduced and use is made of the MCB scheme together with a RS, all the other methods start to perform better while the AC method decreases its accuracy. Looking at

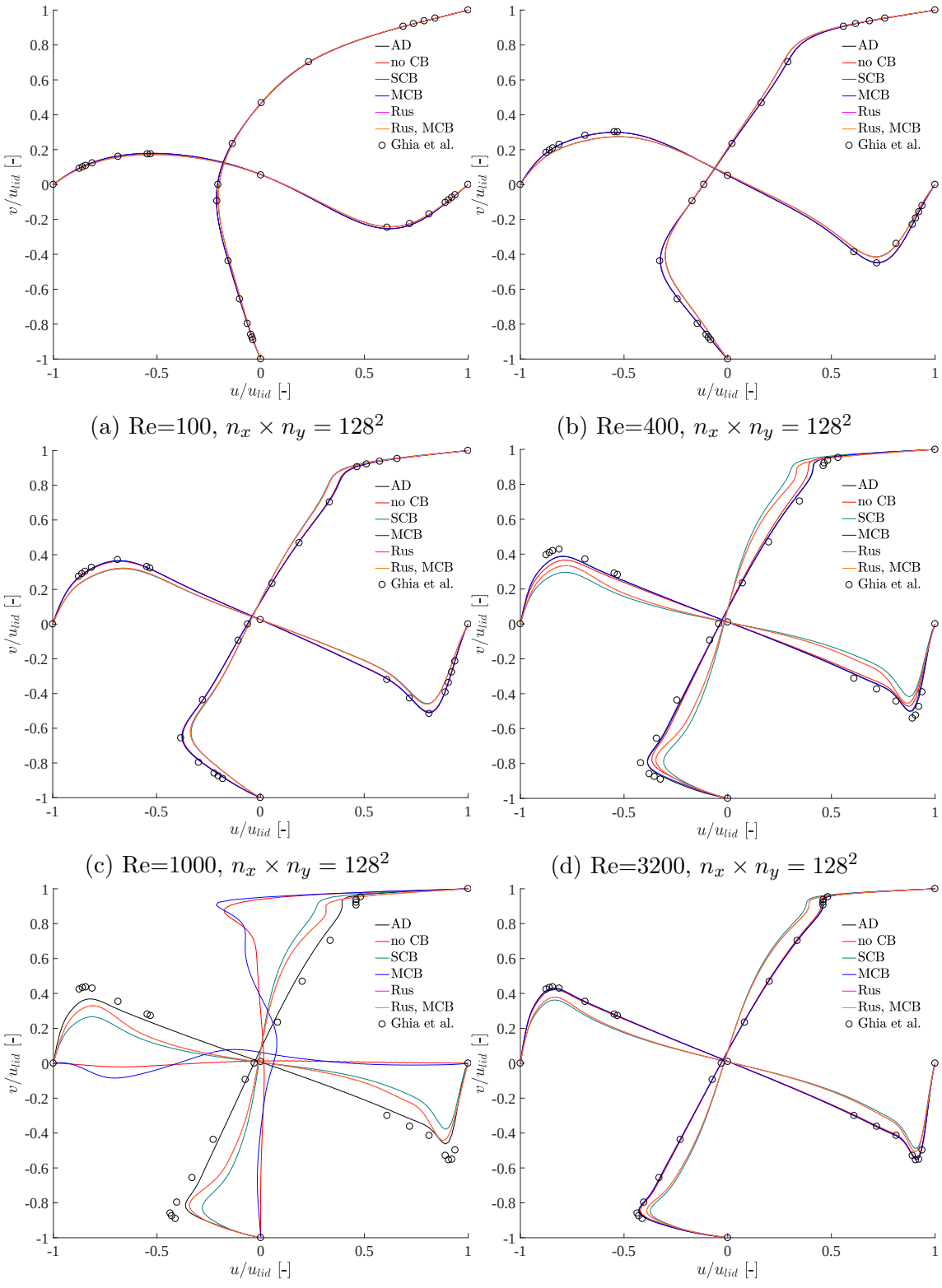

(a) Re=100, $n_x \times n_y = 128^2$

(b) Re=400, $n_x \times n_y = 128^2$

(c) Re=1000, $n_x \times n_y = 128^2$

(d) Re=3200, $n_x \times n_y = 128^2$

(e) Re=5000, $n_x \times n_y = 128^2$

(f) Re=5000, $n_x \times n_y = 256^2$

Figure 6.2: Velocity profiles for different Reynolds numbers along the centreline of the cavity. Results are shown for the AC method.

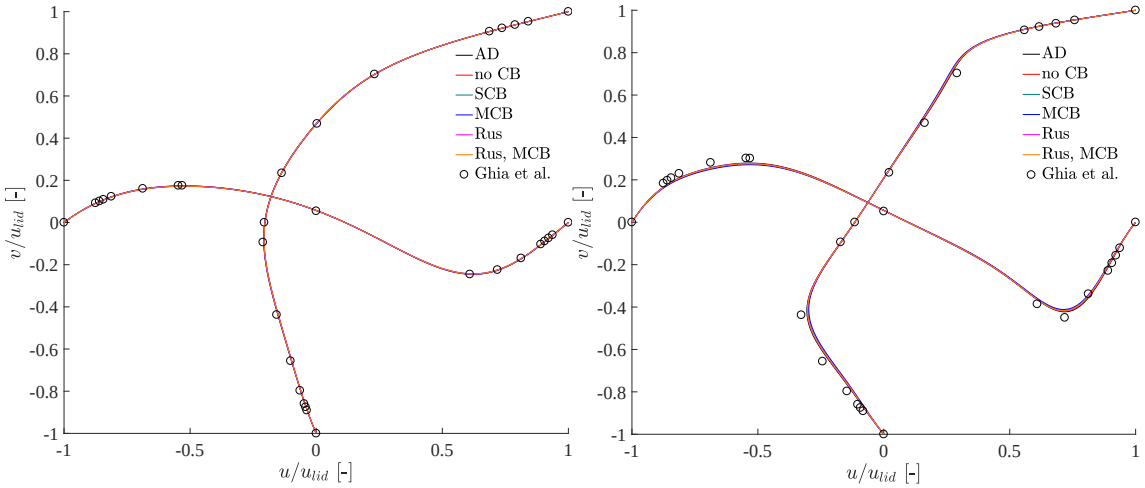

(a) Re=100, $n_x \times n_y = 128^2$ (b) Re=400, $n_x \times n_y = 128^2$

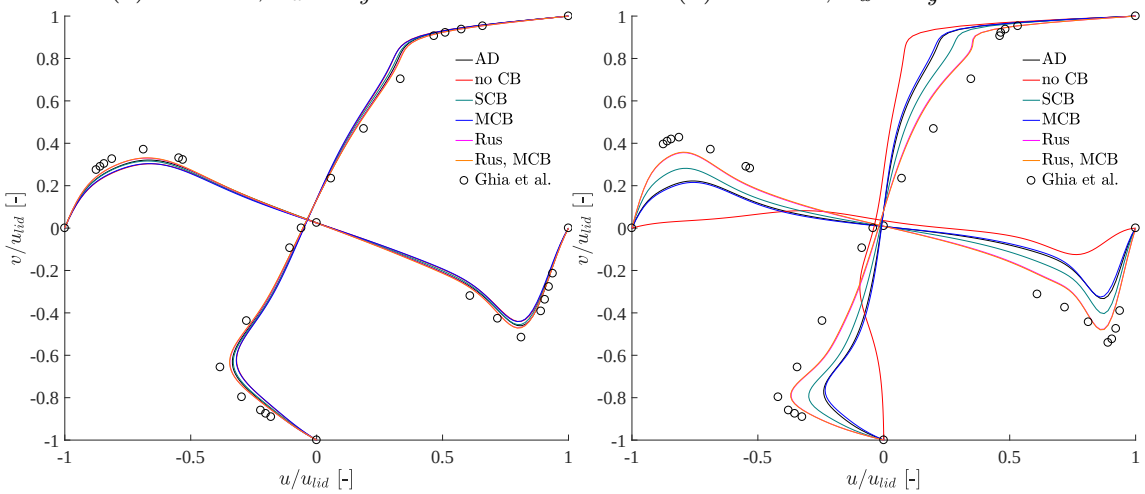

(c) Re=1000, $n_x \times n_y = 128^2$ (d) Re=3200, $n_x \times n_y = 128^2$

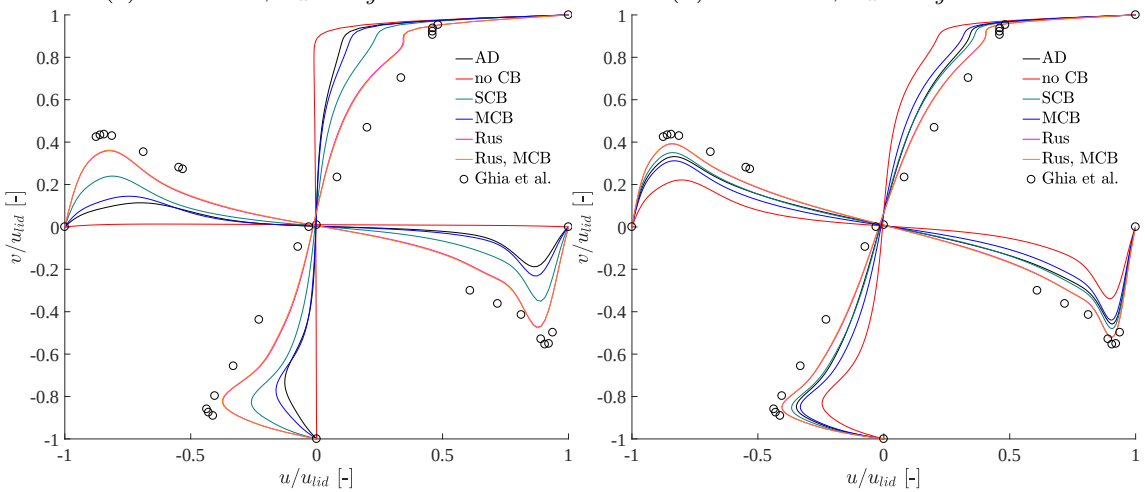

(e) Re=5000, $n_x \times n_y = 128^2$ (f) Re=5000, $n_x \times n_y = 256^2$

Figure 6.3: Velocity profiles for different Reynolds numbers along the centreline of the cavity. Results are shown for the FSAC-PP method.

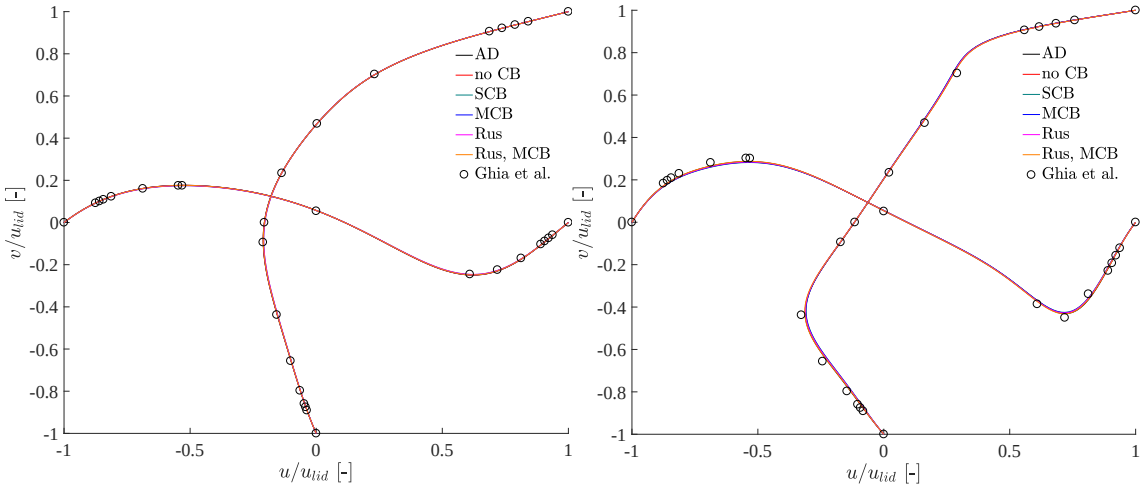

(a) Re=100, $n_x \times n_y = 128^2$ (b) Re=400, $n_x \times n_y = 128^2$

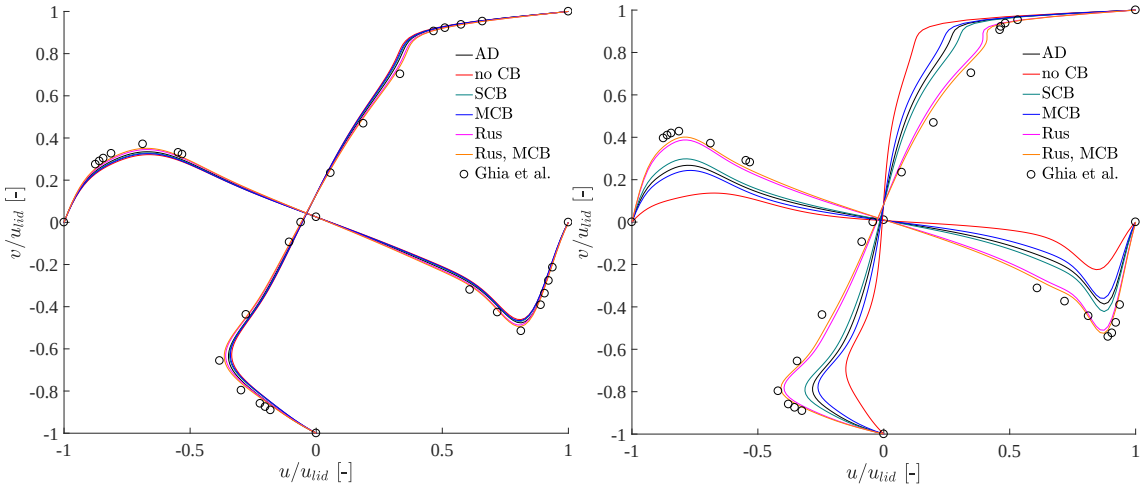

(c) Re=1000, $n_x \times n_y = 128^2$ (d) Re=3200, $n_x \times n_y = 128^2$

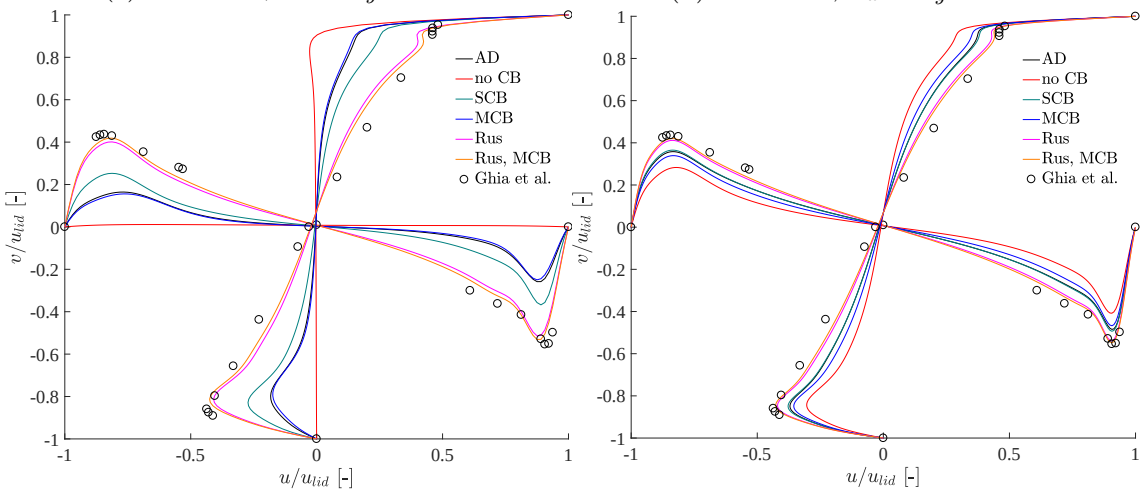

(e) Re=5000, $n_x \times n_y = 128^2$ (f) Re=5000, $n_x \times n_y = 256^2$

Figure 6.4: Velocity profiles for different Reynolds numbers along the centreline of the cavity. Results are shown for the FSAC-VP method.

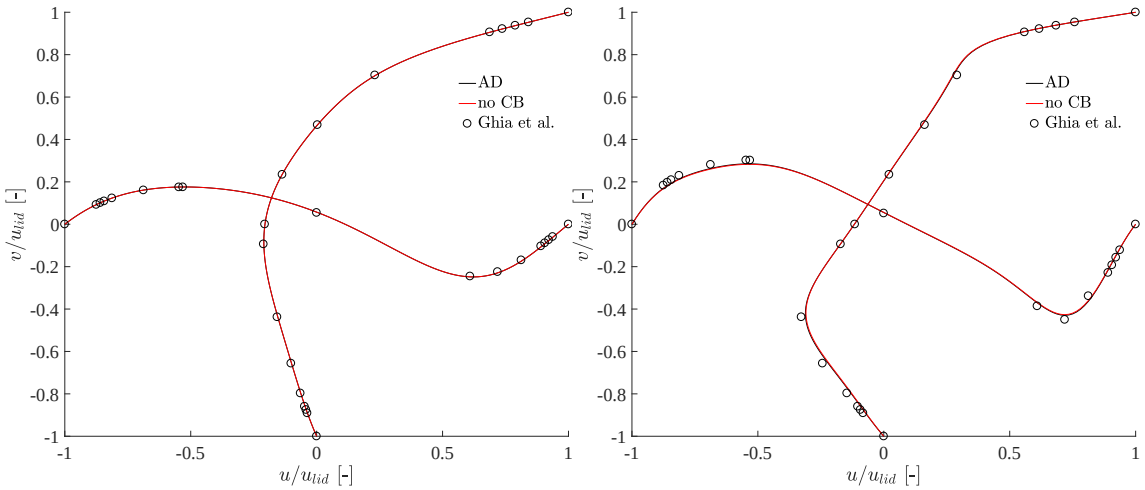

(a) Re=100, $n_x \times n_y = 128^2$ (b) Re=400, $n_x \times n_y = 128^2$

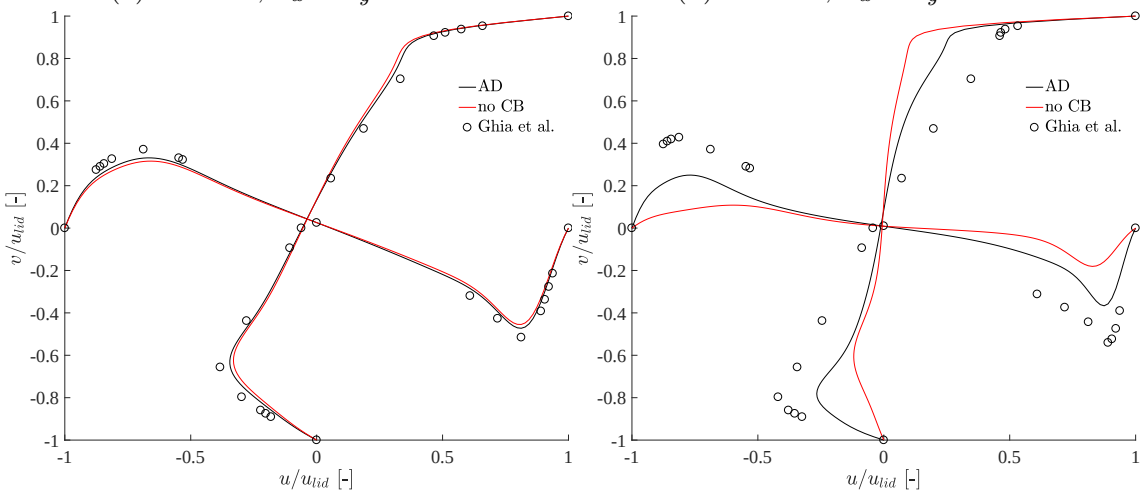

(c) Re=1000, $n_x \times n_y = 128^2$ (d) Re=3200, $n_x \times n_y = 128^2$

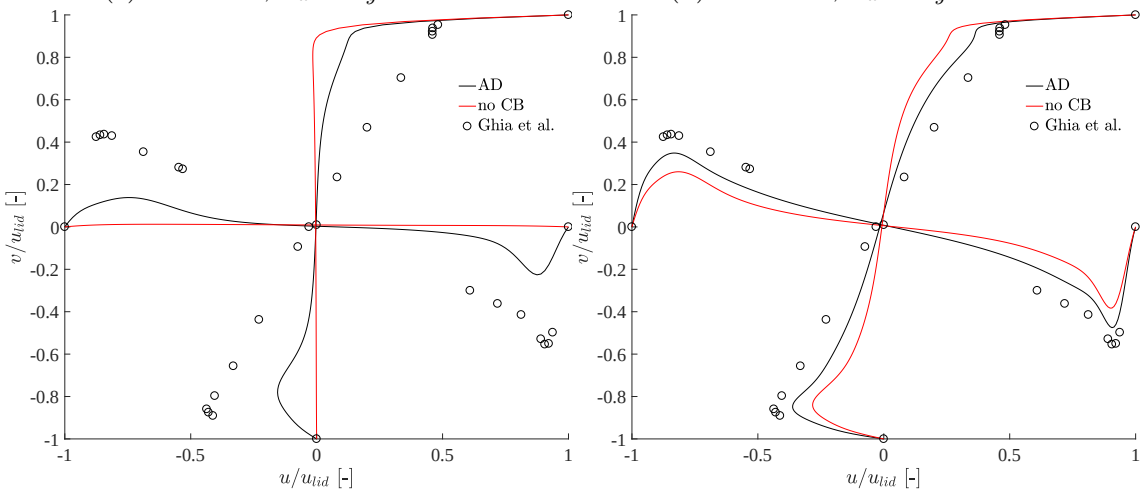

(e) Re=5000, $n_x \times n_y = 128^2$ (f) Re=5000, $n_x \times n_y = 256^2$

Figure 6.5: Velocity profiles for different Reynolds numbers along the centreline of the cavity. Results are shown for the FSVP method.

Re=5000, this becomes even clearer when comparing the results obtained on the $n_x \times n_y = 128^2$ and $n_x \times n_y = 256^2$ mesh. Figure 6.2e shows the coarse grid results where the non CB and MCB scheme both fail to predict the correct behaviour of the flow. Equipping them with a Riemann solver (which makes them the Rus and Rus, MCB scheme), makes them match the numerical reference data more closely. The AD scheme provides itself with enough dissipation so that it performs the best in a case, where the physical dissipation has been filtered by the coarse grid. In Figure 6.2f, however, the same flow is shown only this time using the finer mesh. Here, the non CB and MCB scheme take the extra resolved physical dissipation through the smaller mesh size and are able to match the AD scheme much closer. The RS-based approaches, i.e. the SCB scheme, Rusanov RS and its combination with the MCB scheme, do show some improvements but by far not as drastic as the non CB and MCB scheme. This picture is, again, opposite for the FSAC-PP, FSAC-VP and FSVP method. Specifically, for the FSAC-PP method in Figure 6.3e and 6.3f as well as the FSAC-VP method in Figure 6.4e and 6.4f, the RS-based approaches still perform better than those without a RS. However, increasing the mesh size, the non RS-based approaches do gain in accuracy. Moreover, in this case we can see that introducing physical dissipation alone is sufficient to make the polynomial reconstruction scheme by itself to resolve the main vortical flow structure, whereas on the coarser mesh it is unable to develop the flow at all. This is true for all three methods, i.e. FSAC-PP, FSAC-VP and FSVP. We will also see numerical evidence of this discussion in the form of tabulated data to support these claims.

Figures 6.6–6.9 show the contour plots for the velocity for all tested schemes at a Reynolds number of Re=3200 superimposed by the streamlines. At this Reynolds number, a critical shift in the flow can be observed where the numerical dissipation is just enough for some schemes to develop the main vortex while other schemes struggle to match the reference data in good agreement. These Figures are of particular interest as we can judge the vortex structures from a qualitative point of view. It would have been interesting to extract vortex core locations and compare those to data provided by Ghia *et al.* [152], however, vortex core detection algorithms only work for three-dimensional flows and no information was provided as to how the vortex cores were extracted. One of the more prominent algorithms is known as the lambda-2 method, where the local eigenvalues of the summed square of the symmetric and antisymmetric part of the velocity gradient tensor are found. A vortex core is found if at least two of their eigenvalues are negative. For more information see also Jeong and Hussain [157] but in absence of a reliable method to establish two-dimensional vortex locations, a reproducible comparison cannot be conducted. In these Figures, it can be observed that the AC method does indeed produce a correct vortical behaviour for all schemes tested. There are no qualitative discrepancies in vortex size and location among the schemes. Moving to the FSAC-PP method in Figure 6.7, we start to see differences matching those discussed previously; the non CB scheme is not able to predict the flow structure correctly. Here, the main vortex does start to develop but the secondary vortices in the bottom left and right corner are absent. Interestingly, the MCB scheme by itself is able to predict both the primary and secondary vortices correctly. This is an important

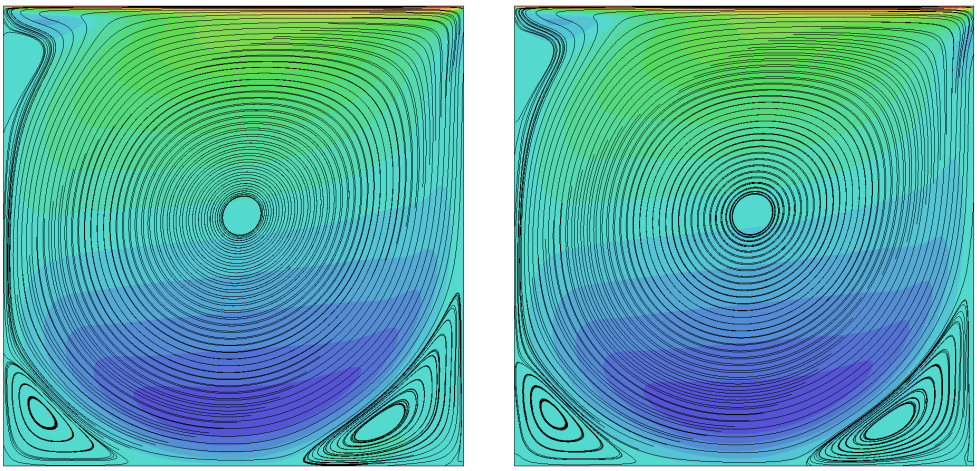

(a) Re=3200, AD

(b) Re=3200, no CB

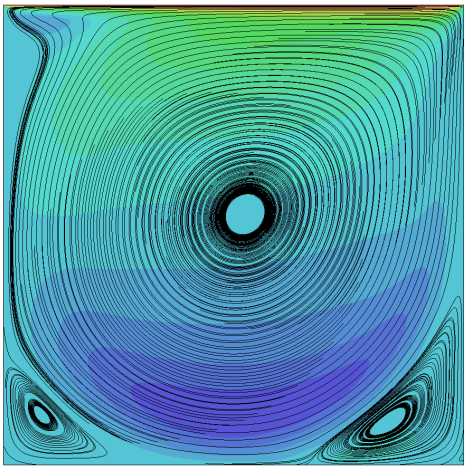

(c) Re=32000, SCB

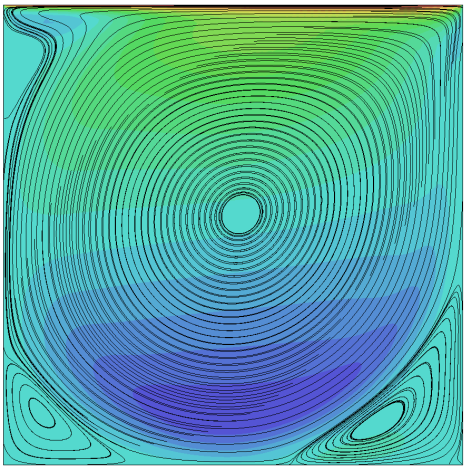

(d) Re=3200, MCB

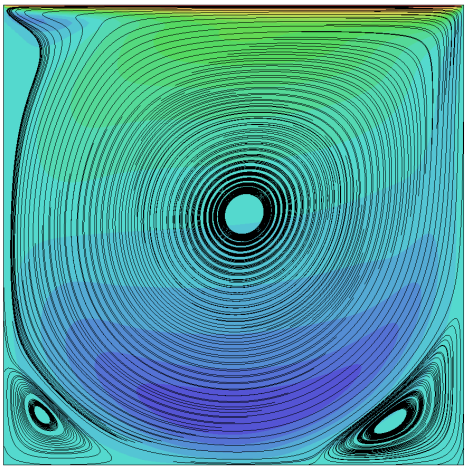

(e) Re=3200, Rusanov

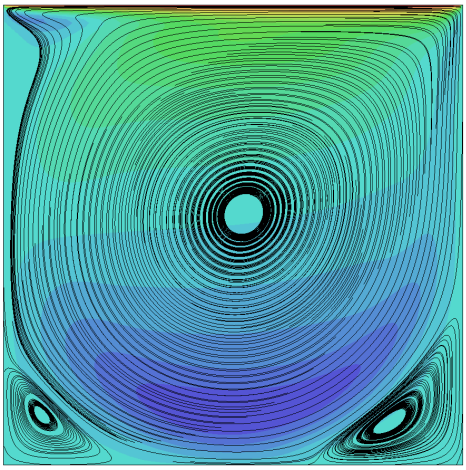

(f) Re=3200, Rusanov+MCB

Figure 6.6: Contour plots of velocity with streamlines for different numerical schemes at a Reynolds number of Re=3200. The results are shown for the AC method.

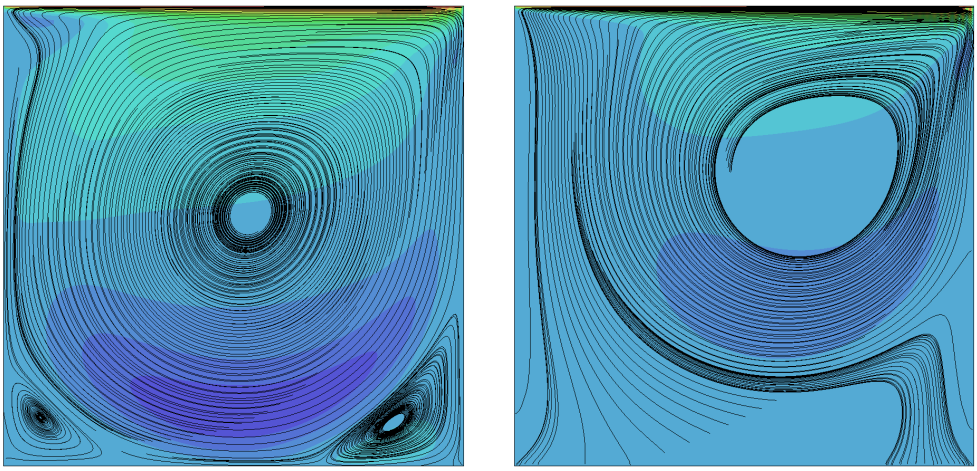

(a) Re=3200, AD

(b) Re=3200, no CB

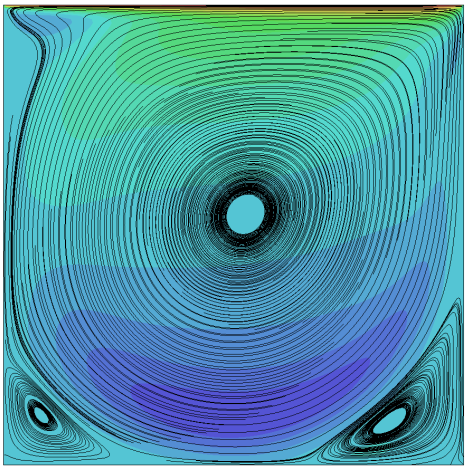

(c) Re=32000, SCB

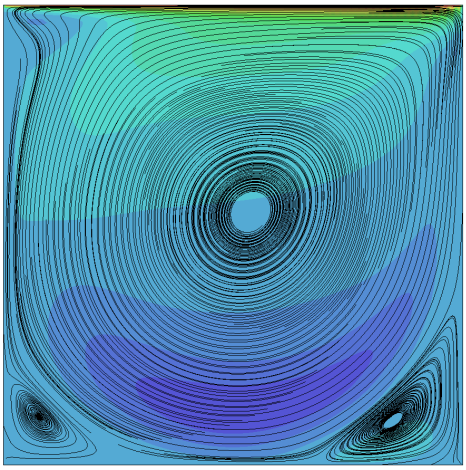

(d) Re=3200, MCB

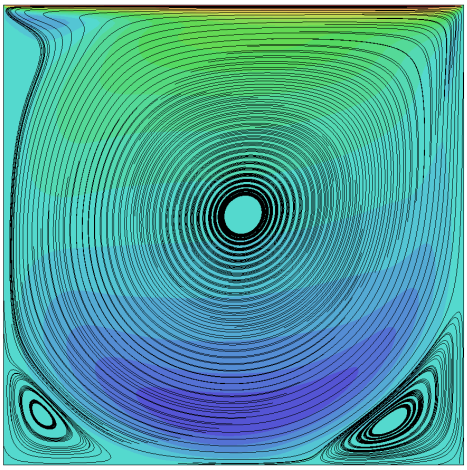

(e) Re=3200, Rusanov

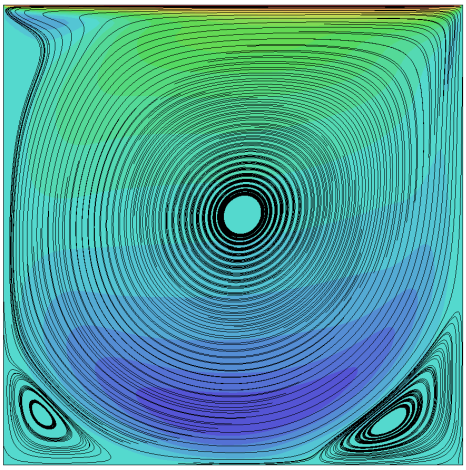

(f) Re=3200, Rusanov+MCB

Figure 6.7: Contour plots of velocity with streamlines for different numerical schemes at a Reynolds number of Re=3200. The results are shown for the FSAC-PP method.

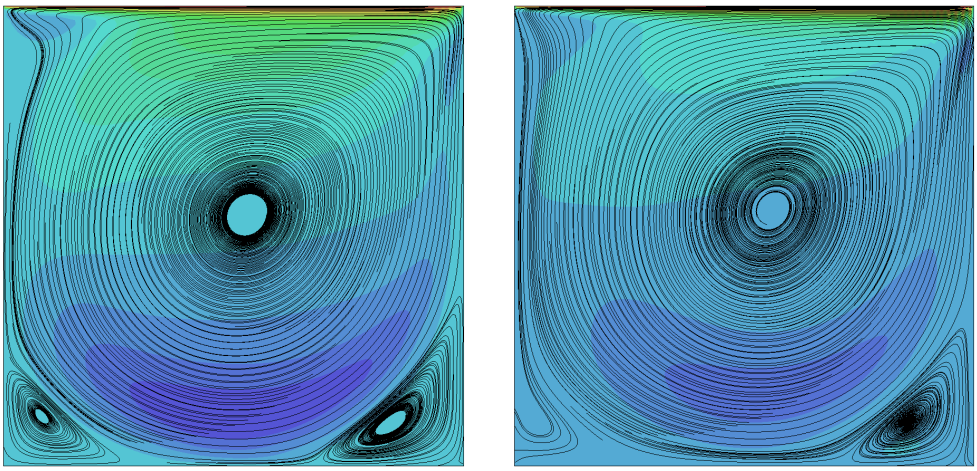

(a) Re=3200, AD

(b) Re=3200, no CB

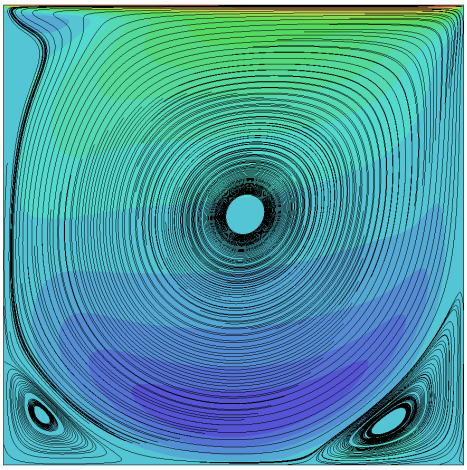

(c) Re=32000, SCB

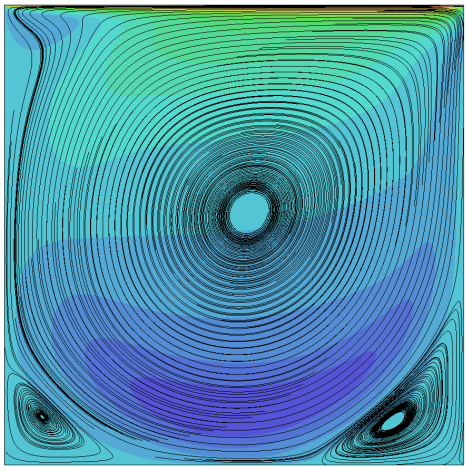

(d) Re=3200, MCB

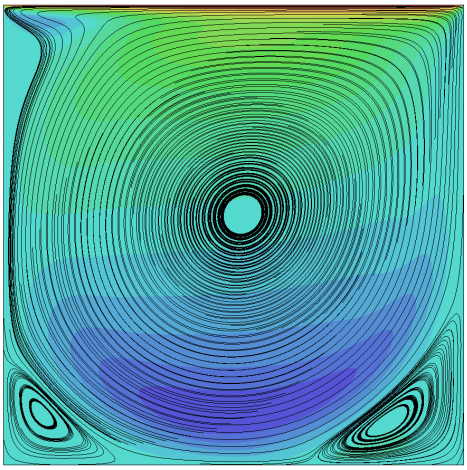

(e) Re=3200, Rusanov

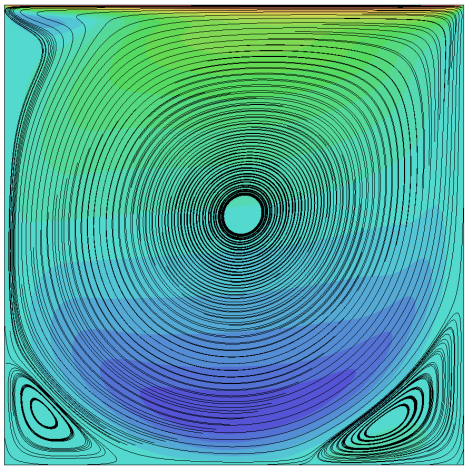

(f) Re=3200, Rusanov+MCB

Figure 6.8: Contour plots of velocity with streamlines for different numerical schemes at a Reynolds number of Re=3200. The results are shown for the FSAC-VP method.

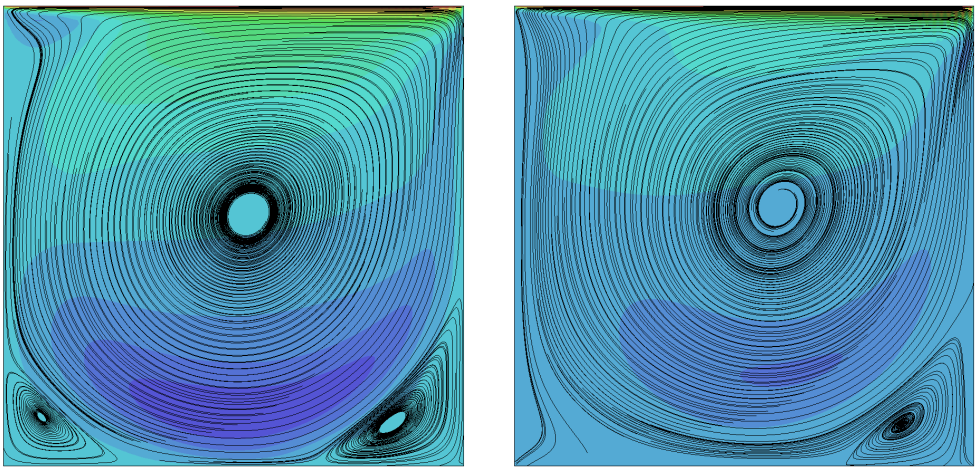

(a) Re=3200, AD (b) Re=3200, no CB

Figure 6.9: Contour plots of velocity with streamlines for different numerical schemes at a Reynolds number of Re=3200. The results are shown for the FSVP method.

finding as it has the same level of numerical dissipation provided by the scheme and does not benefit from the same transportiveness property inherent to the SCB scheme due to its Godunov RS. In-fact, there is very little difference between the SCB and MCB scheme. It would be wrong to conclude that this makes the MCB scheme superior. For such a conclusion, the SCB scheme would need to be operated without its RS. This, however, is not possible as the SCB scheme relies by definition on the RS. It calculates three distinct eigenvalues which, without the RS, would not be able to be reduced to a single set of characteristic variables. However, we can conclude that the MCB scheme is capable of producing vortical structures that are absent from a non CB treatment. This is an important finding for turbulent flows, as we are primarily interested in capturing vortical-dominant flows. The FSAC-VP method in Figure 6.8, on the other hand, does correctly predict the primary vortex structure. The bottom right vortex is predicted as well while the bottom left vortex is not fully resolved. The streamline hints the existence of a vortex but the it is not quite captured. Again, the MCB scheme is able to perform well in this respect and resolves all secondary flow structures correctly. The same is true for the FSVP method in Figure 6.9.

One particular point about this discussion is particularly noteworthy; the FSVP and FSAC-VP method both take as their basis the equations of the FSAC-PP method. The only difference among those methods is that the FSAC-PP method uses an elliptic Poisson equation to predict the pressure while both the FSVP and FSAC-VP method use a parabolic pressure transport equation. It was shown how the set of equations for the FSAC-PP method in Section 3.3.3 can be transformed into those of the FSVP and FSAC-VP method in Section 3.3.4 and 3.3.5, respectively. Thus, we solve the same equations in a different mathematical form which differ in their mathematical behaviour, i.e. in this case, being elliptic or parabolic. This difference alone can have a significant impact on the development of primary vortex structures, as can be seen in Figure 6.7b, 6.8b and 6.9b for the FSAC-PP, FSAC-VP and

FSVP method, respectively. This may be taken as a first sign of evidence that the pressure treatment does matter for incompressible flows and that not every method performs equally well. It is important whether we treat the pressure in a parabolic or elliptic manner and if we allow the pressure to evolve in time through its own transport equation. The latter fact is subtle but rather important. We know from fluid mechanics that the pressure (or rather, a pressure difference) is driving the flow, not the other way around. The common approach on incompressible computational fluid dynamics is, however, to develop the flow and deduct the pressure from the velocity field. This contradiction between physical and numerical reality is exactly what the FSVP and FSAC-VP method have been designed for to address. We are now able to predict the pressure first and deduct the velocity field as a result which is in line with physical expectations. The difference can be clearly seen as discussed above.

Figures 6.10–6.13 show the same contour plots with superimposed stream lines for the AC, FSAC-PP, FSAC-VP and FSVP method, only this time for Re=5000. From Figures 6.2–6.5, we remember that some schemes and methods were not able to predict even the primary vortex structure. This is now also shown in form of the streamlines. In particular, Figure 6.10b shows that even the AC method is not able to predict the correct flow at Re=5000 using only a polynomial reconstruction. Furthermore, the MCB scheme in Figure 6.10d fails to predict the correct flow as well, albeit that some more vortical structures are resolved. For the FSAC-PP method, again, the non CB approach fails to predict any physical vortical motion at all (Figure 6.11b), while the MCB scheme introduces again physically correct flow structures (Figure 6.11d). Interestingly, while the AC method does not provide a correct flow using the MCB scheme, it is enough for the FSAC-PP method to resolve the correct flow structures. The bottom left corner vortex, however, shows only a weakly resolved vortex. Still, it is present, and we can see a clear difference to the AC method. For the FSAC-VP method, the non CB treatment depicts the same scenario as for the FSAC-PP method (Figure 6.12b) but shows a qualitatively better resolved bottom left corner vortex using the MCB scheme (Figure 6.12d). Results for the non CB scheme are similar in the case of the FSVP method compared to its related FSAC-VP method.
In all cases, the RS-based approaches, do not show any significant differences. In-fact, all these schemes predict correctly the primary and secondary vortex structures. This is also true for the results shown at Re=3200. The central scheme with artificial dissipation (AD), on the other-hand, starts to lose its accuracy at Re=5000. While it still produced correct results for all methods at Re=3200, at the higher Reynolds number the FSAC-PP method starts to show that the inherent dissipation in the scheme is not sufficient to predict the bottom left corner vortex correctly. The FSAC-VP and FSVP method do not show the same constrains. This can, of course, be resolved by adjusting the $k^{(2)}$ and $k^{(4)}$ parameter in the scheme but would result in results obtained at different levels of numerical dissipation. Thus, we keep the level constant for all simulations. This, however, highlights an important fact, where the same scheme gives different results for different incompressible methods. Numerical methods are usually not thought of containing numerical dissipation —

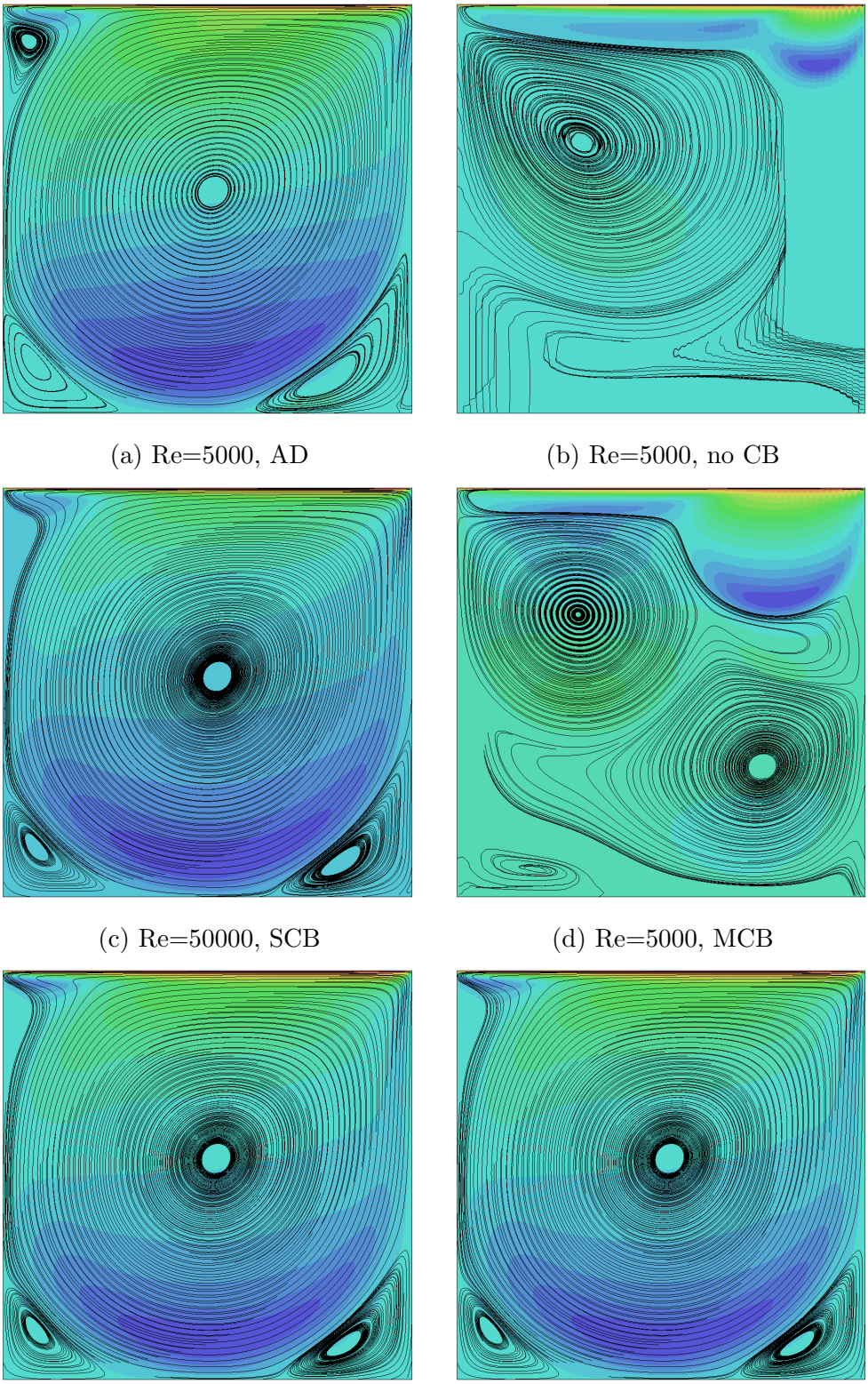

(a) Re=5000, AD

(b) Re=5000, no CB

(c) Re=50000, SCB

(d) Re=5000, MCB

(e) Re=5000, Rusanov

(f) Re=5000, Rusanov+MCB

Figure 6.10: Contour plots of velocity with streamlines for different numerical schemes at a Reynolds number of Re=5000. The results are shown for the AC method.

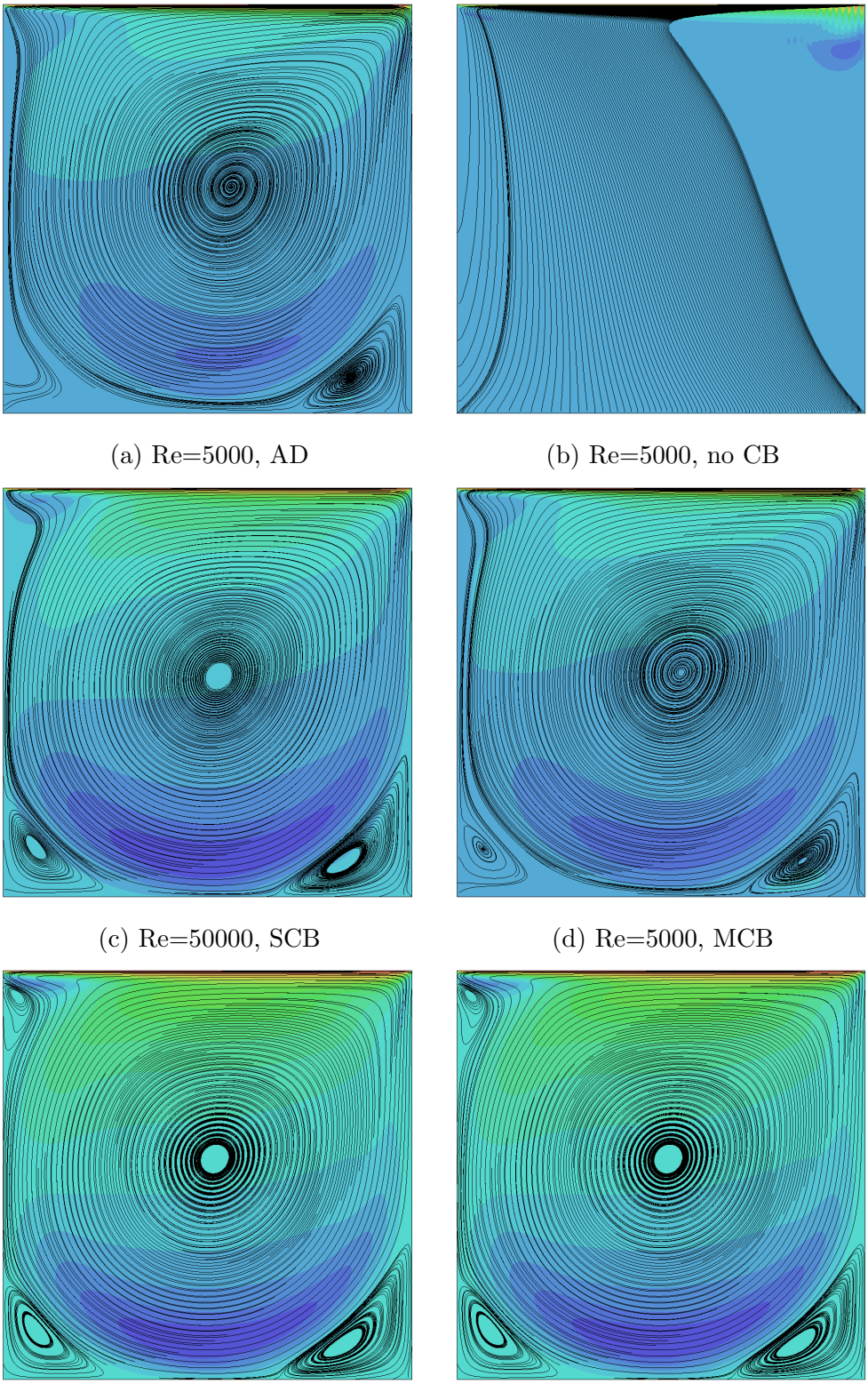

(a) Re=5000, AD

(b) Re=5000, no CB

(c) Re=50000, SCB

(d) Re=5000, MCB

(e) Re=5000, Rusanov

(f) Re=5000, Rusanov+MCB

Figure 6.11: Contour plots of velocity with streamlines for different numerical schemes at a Reynolds number of Re=5000. The results are shown for the FSAC-PP method.

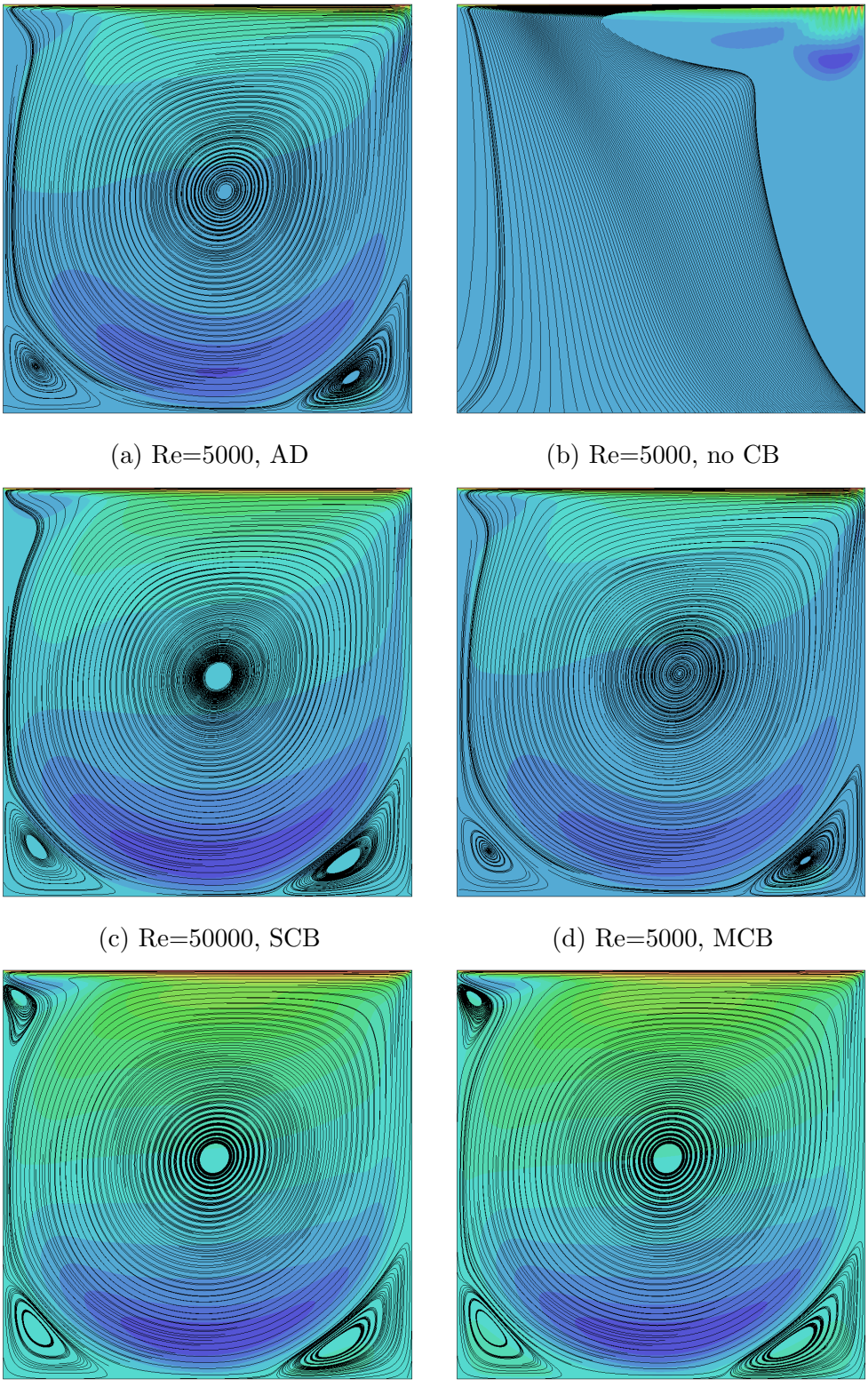

(a) Re=5000, AD

(b) Re=5000, no CB

(c) Re=50000, SCB

(d) Re=5000, MCB

(e) Re=5000, Rusanov

(f) Re=5000, Rusanov+MCB

Figure 6.12: Contour plots of velocity with streamlines for different numerical schemes at a Reynolds number of Re=5000. The results are shown for the FSAC-VP method.

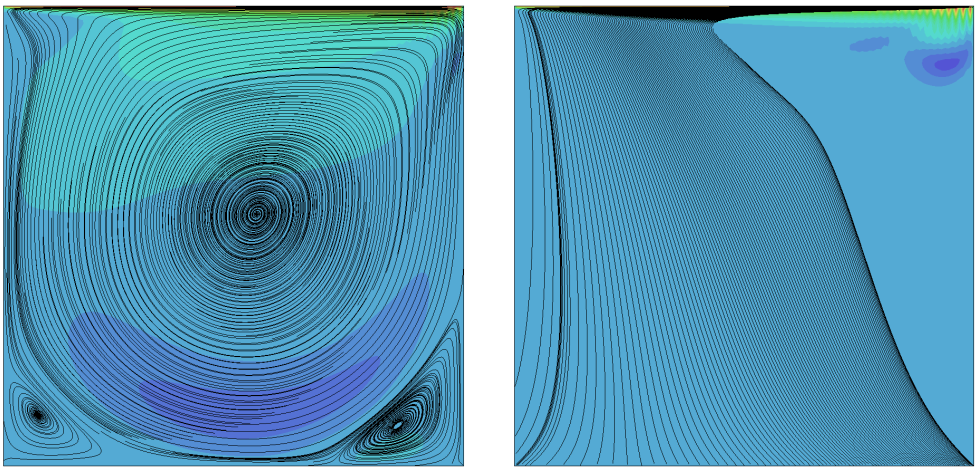

(a) Re=5000, AD (b) Re=5000, no CB

Figure 6.13: Contour plots of velocity with streamlines for different numerical schemes at a Reynolds number of Re=5000. The results are shown for the FSVP method.

and it would be wrong to do so — but we can see that even the choice how different methods treat the Navier–Stokes equations has an influence on the numerical dissipation behaviour of the scheme that is used.

Apart from the numerical dissipation, another important aspect of incompressible flows will be highlighted in the following. The pressure-velocity decoupling is a phenomenon usually encountered when using a central scheme on a collocated mesh, or at least this is the definition given by most textbooks on incompressible flows. For this reason, the staggered grid arrangement was proposed so as to solve the primitive variables at nodes where they need to be available for other equations. Rhie and Chow [130] showed, however, that the inclusion of an additional upwind node in the discretisation removes the need of a staggered grid all together. The pressure-velocity decoupling is highly scheme dependent and so it is worthwhile to investigate here using the different schemes and methods.

In Figure 6.14, the pressure profiles along the diagonal starting in the bottom left and going to the top right corner are shown for each method with each scheme at Re=1000. For this Reynolds number in particular, reference data is provided by Leroy *et al.* [158] who made use of an widely validated open source and finite volume-based solver by the name of *code saturne* [159]. All four methods follow the reference data where, again, the AC method shows the most variation between the different schemes. The FSAC-PP, FSAC-VP and FSVP method match the reference data with an excellent agreement and show almost indistinguishable results for all schemes. In the AC method, however, we start to see spurious oscillation near the top right corner of the cavity which is shown on the right side of the plot. Specifically, the non CB and MCB scheme, as well as the central scheme with artificial dissipation show an oscillatory behaviour. All these schemes have in common that they don't use a RS. The other, RS-based approaches, do provide smooth data

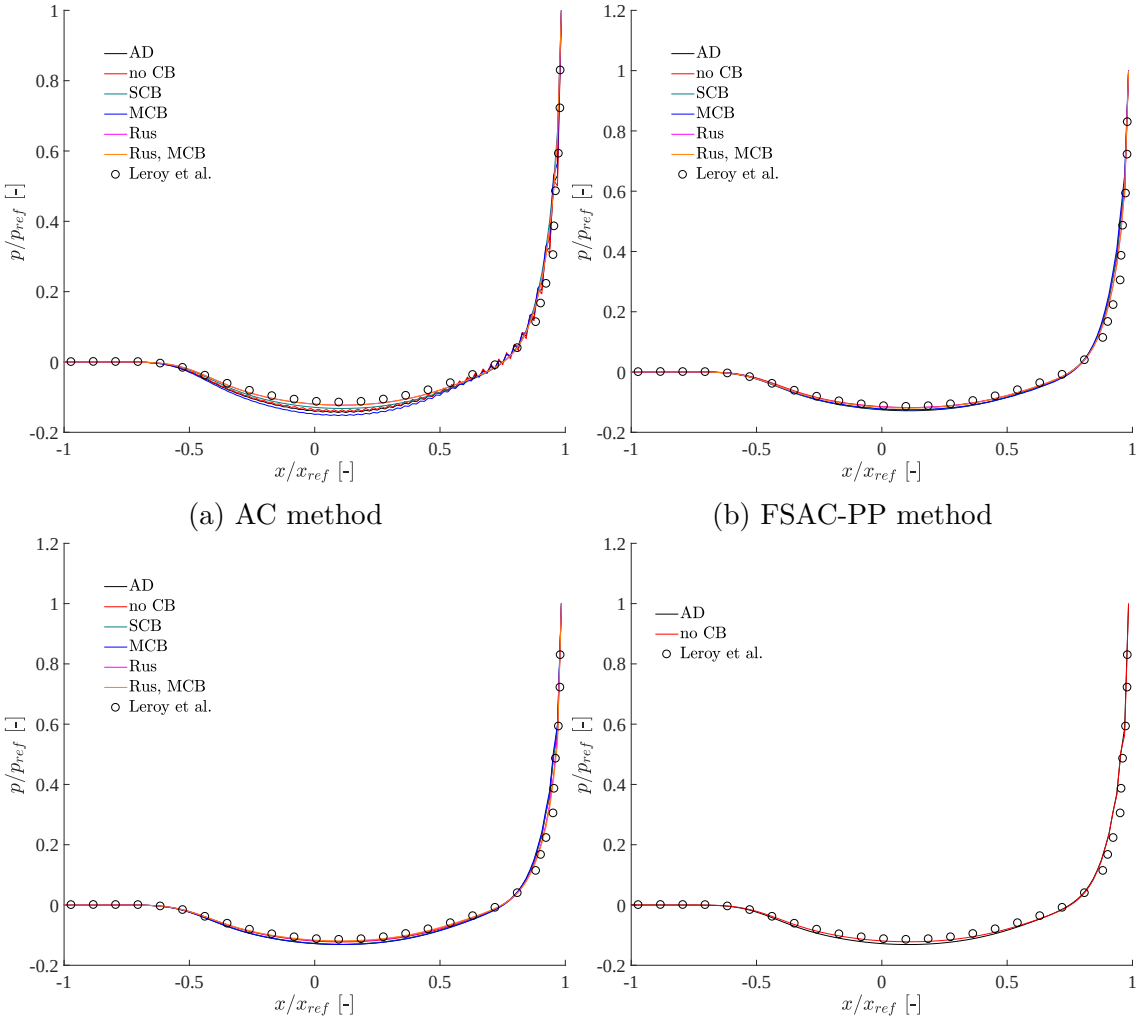

(a) AC method

(b) FSAC-PP method

(c) FSAC-VP method

(d) FSVP method

Figure 6.14: Pressure profile along the diagonal from the bottom left to top right of the cavity for different methods at Re=1000.

on the other hand. Thus, we can see first evidence that the RS treatment does not only provide transportiveness and conservativeness, but also helps to circumvent the pressure-velocity decoupling problem. Referring back to Figure 6.2c in which we plot the velocity profiles for the AC method at Re=1000, no such spurious oscillations are present for any of the given schemes. It is in-fact the central scheme with artificial dissipation which is seemingly agreeing the best with the reference data. Unsurprisingly, the reference data provided by Ghia *et al.* [152] used a second-order central scheme for its derivatives (although in finite difference form) while the convective term was discretised using a first-order scheme with a deferred correction approach of second-order. At convergence, the simulations recover a second-order accuracy while the first-order discretisation of the convective term provides the necessary numerical dissipation. Thus, it is very similar to the second-order central scheme with artificial dissipation used in this study. That also means that the observed difference between the numerical results obtained in this study and the reference data given by Ghia *et al.* does not indicate that one scheme performs better than the other, it

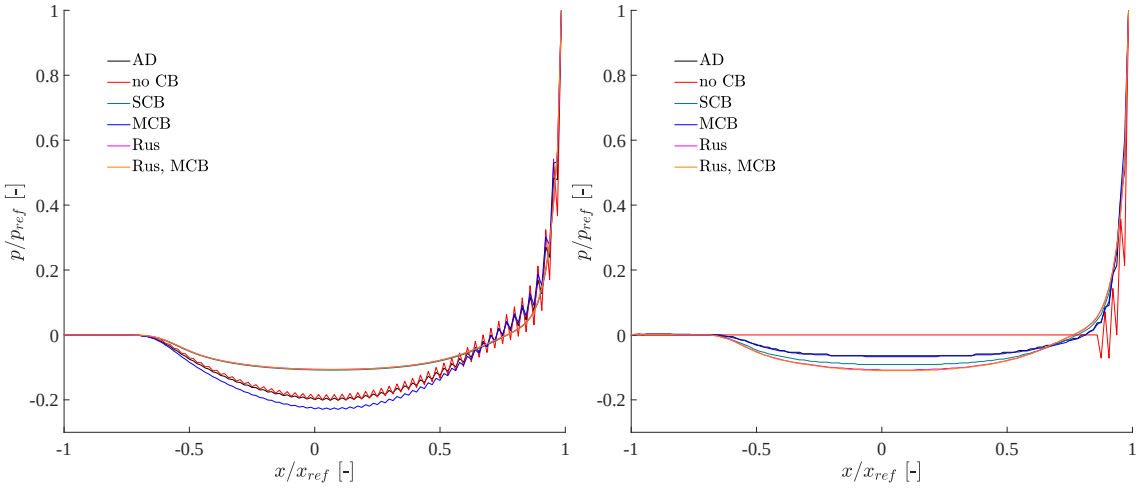

(a) AC method (b) FSAC-PP method

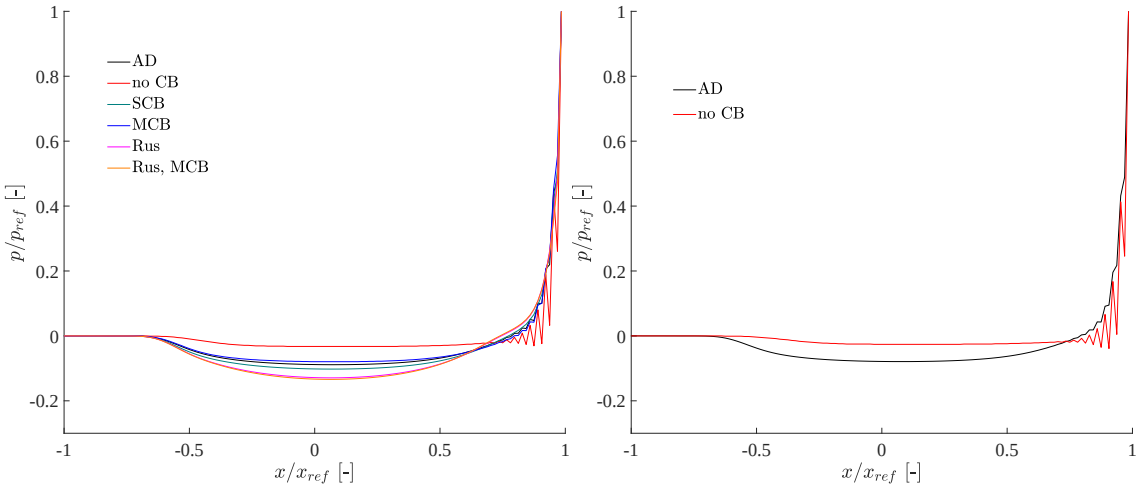

(c) FSAC-VP method (d) FSVP method

Figure 6.15: Pressure profile along the diagonal from the bottom left to top right of the cavity for different methods at Re=3200.

could also be argued that excessive numerical dissipation is present in the data of Ghia *et al.* which does not allow it to pick up flow features that are recovered with a low dissipative scheme. The fact that Ghia *et al.* provide reference data converged to a steady state at Re=10000 might be seen as an indication for that in light of the discussion provided by Erturk [142] in the introduction to this Section. But we are able to see another important feature here which should not go unnoticed; the inherent stabilisation of the elliptic Poisson solver is able to delay the onset of the pressure-velocity decoupling. This advantageous feature is inherited by the FSVP and FSAC-VP method. All pressure curves are smooth, even for the non RS-based schemes.

Figure 6.15 shows the same pressure profiles only now at Re=3200. For this case there is no reference data provided by Leroy *et al.* but due to the good agreement at Re=1000 and since we are only interested, at this point, in qualitative comparisons

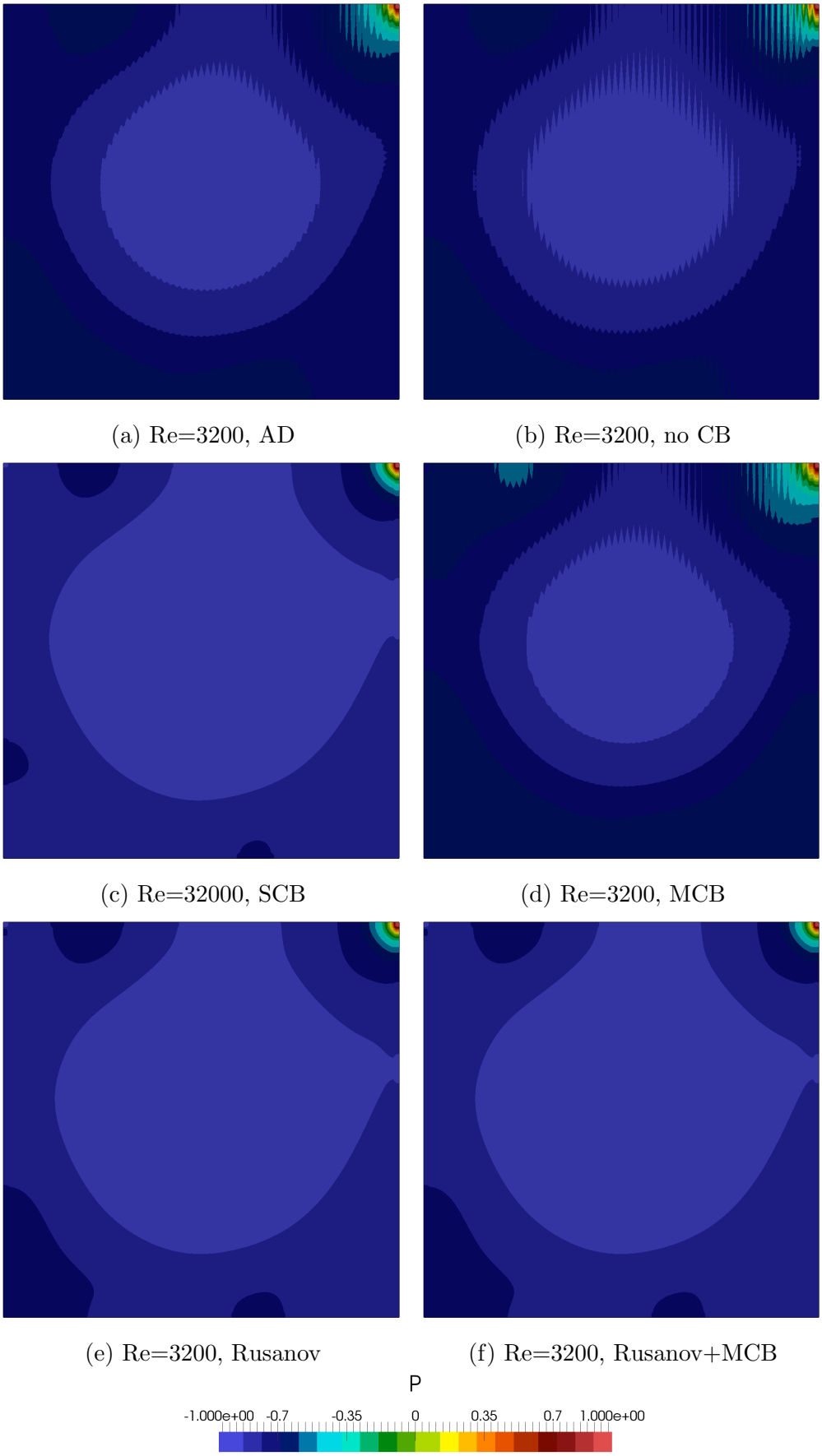

(a) Re=3200, AD

(b) Re=3200, no CB

(c) Re=32000, SCB

(d) Re=3200, MCB

(e) Re=3200, Rusanov

(f) Re=3200, Rusanov+MCB

Figure 6.16: Contour plots of pressure for different numerical schemes at a Reynolds number of Re=3200. The results are shown for the AC method.

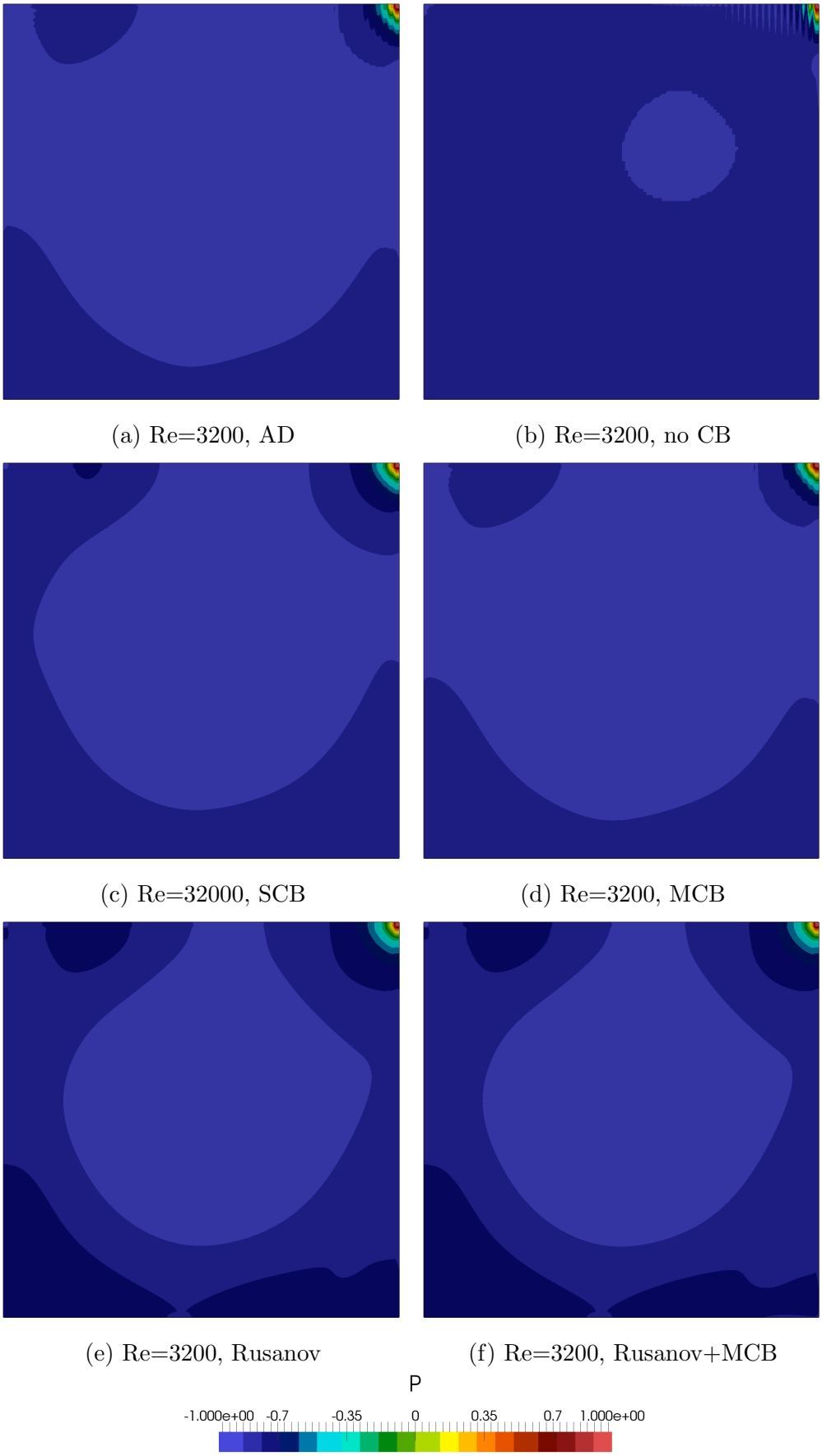

(a) Re=3200, AD

(b) Re=3200, no CB

(c) Re=32000, SCB

(d) Re=3200, MCB

(e) Re=3200, Rusanov

(f) Re=3200, Rusanov+MCB

Figure 6.17: Contour plots of pressure for different numerical schemes at a Reynolds number of Re=3200. The results are shown for the FSAC-PP method.

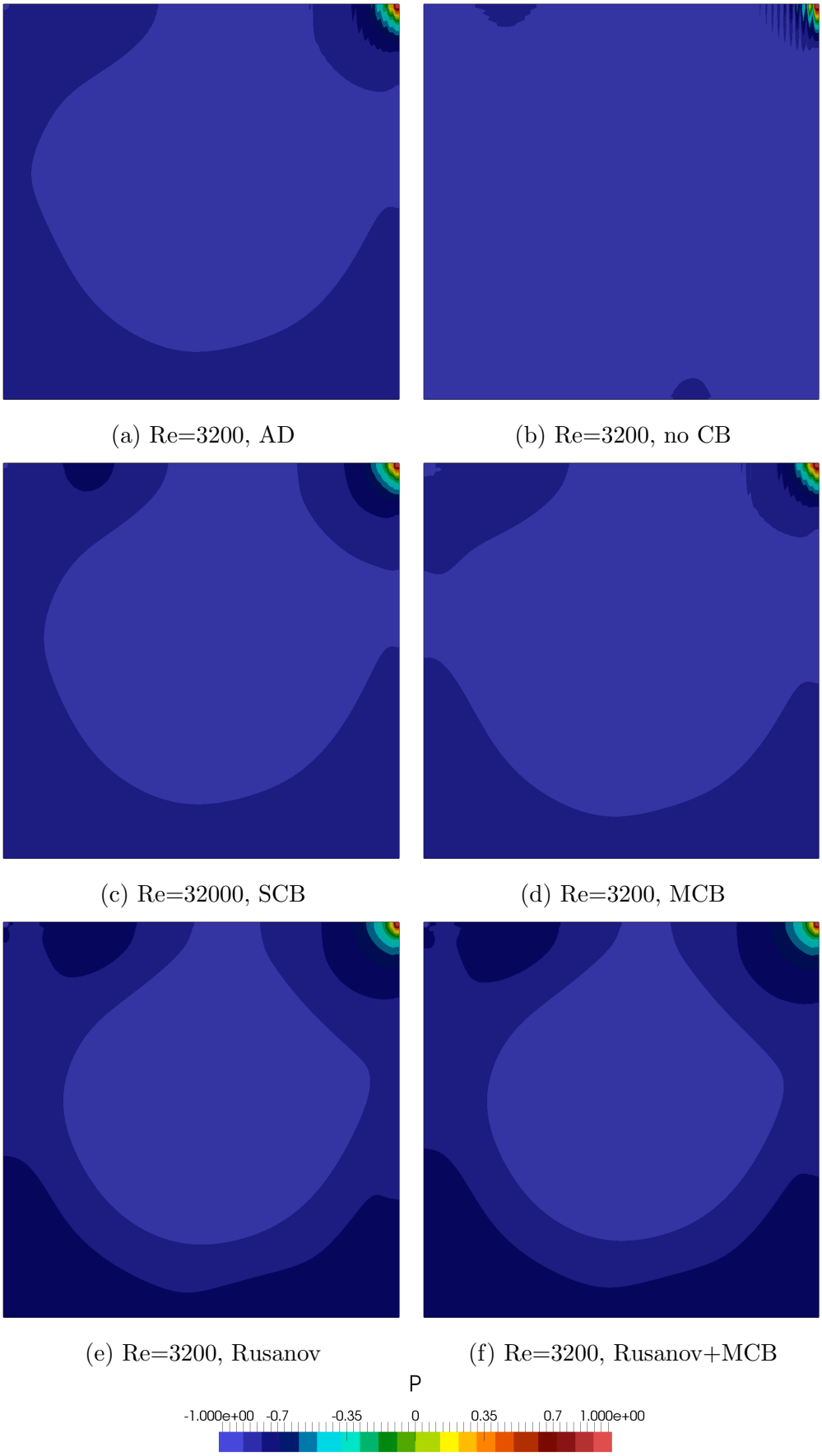

(a) Re=3200, AD

(b) Re=3200, no CB

(c) Re=32000, SCB

(d) Re=3200, MCB

(e) Re=3200, Rusanov

(f) Re=3200, Rusanov+MCB

Figure 6.18: Contour plots of pressure for different numerical schemes at a Reynolds number of Re=3200. The results are shown for the FSAC-VP method.

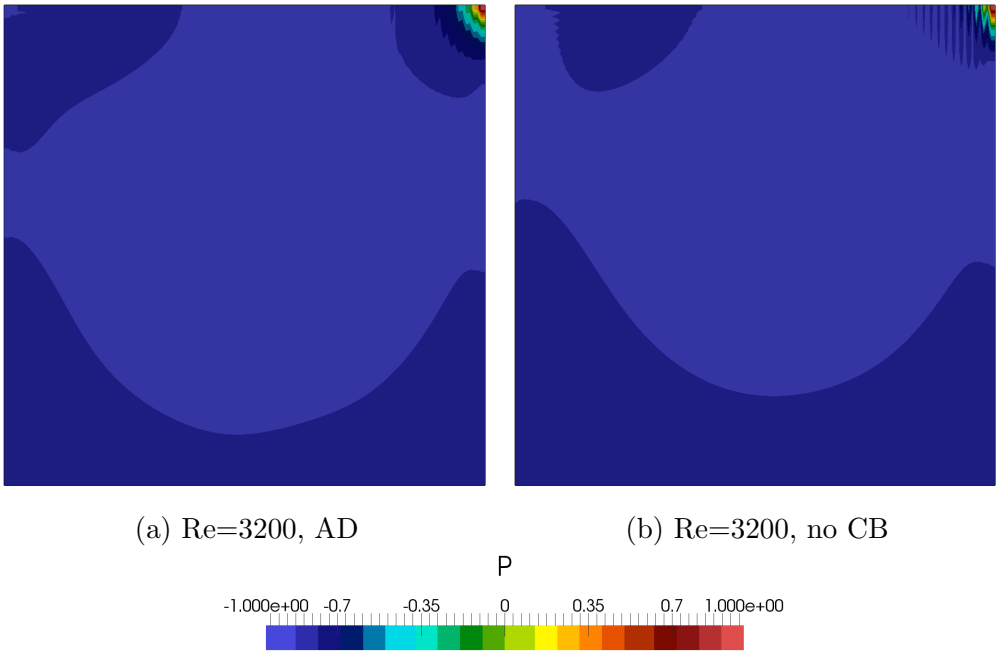

(a) Re=3200, AD (b) Re=3200, no CB

Figure 6.19: Contour plots of pressure for different numerical schemes at a Reynolds number of Re=3200. The results are shown for the FSVP method.

among the different schemes and methods, it is still worthwhile to look at the same behaviour at an increased Reynolds number. Here, the AC method shows considerable oscillations for the non CB, MCB and AD scheme. Applying a RS provides, again, a smooth pressure profile. For the FSAC-PP method, we can observe a weakly decoupled velocity and pressure field for the AD and MCB scheme. The non CB scheme does not develop the flow correctly, as discussed before, and so the pressure profile does not show a physical result either. As for the case at Re=1000, we can see that those results predicting the flow correctly do show less oscillations in the pressure profile than the AC method, which is, again, also present in the FSAC-VP and FSVP method. While the central scheme with artificial dissipation is able to predict the correct velocity profile, it can be seen that it struggles to also provide a smooth pressure field. While the elliptic Poisson solver in the FSAC-PP method does remove those oscillations to some degree, they are still present, especially closer to the top right corner near the moving lid.
This discussion is also shown in Figure 6.16–6.19 for the contours of pressure at Re=3200. The observations made here are applicable to Re=1000 as well as discussed above but more pronounced at Re=3200. Here, we see that again the AD scheme, the non CB and MCB scheme do show most potential to produce a fluctuating pressure field while all RS-based approaches provide a smooth pressure field throughout the domain. The AC method in particular shows most oscillations as was already demonstrated in Figure 6.15. The FSAC-PP method benefits from the elliptic pressure behaviour of the Poisson solver to stabilise the pressure field. Likewise, the FSAC-VP and FSVP method benefit from the parabolic pressure transport equation which also provides further stabilisation of the pressure field. Of course,

it can be argued here that the AC method possesses its own transport equation for the pressure. This is, however, not strictly speaking true. The equation is based on the continuity equation which is purely artificial through the β parameter, which represents the unknown relation between density and pressure. Therefore, the continuity equation only recovers a physical meaning once the equations have converged in pseudo time. In that case, the pressure time derivative is zero and essentially not present in the modified continuity equation. The parabolic transport equation, however, is based on physical reasoning. It might be argued that it too suffers from the pseudo time derivative, but it does not lose physical soundness during the pseudo time stepping. It will always retain its parabolic character which is the assumed correct behaviour of pressure for incompressible flows in this work.

Tables 6.2–6.5 are showing the L_0 and L_1 error norms along with the computational cost, here measured in number of iterations required for all Reynolds numbers and computational grids. It would have been more desirable to measure the computational cost in CPU wall time; however, the simulations were run across several computing facilities with different clock speeds. Even more troublesome, the computational speed was also affected by the load of those facilities which could reduce the computational time by as much as a factor of two. Therefore, any computational timings given for the present case would only distort the analysis and the number of iterations is shown instead. The errors are calculated based on tabulated data provided by Ghia *et al.* [152] and the errors are calculated as

$$L_0 = \max|\phi_{\text{num,i}} - \phi_{\text{Ghia,i}}|, \tag{6.1.2}$$

$$L_1 = \frac{1}{N}\sum_{i=1}^{n}|\phi_{\text{num,i}} - \phi_{\text{Ghia,i}}|, \tag{6.1.3}$$

respectively, where $\phi_{\text{num,i}}$ represents the velocity component u or v obtained from the current simulations and $\phi_{\text{Ghia,i}}$ the tabulated data found in the reference.
Table 6.2 is showing the results obtained from the AC simulations. As shown during the velocity profile discussion, the agreement below and at Re=1000 is excellent with the reference data. The RS-based approaches start to show larger errors at and above Re=1000 which, again, may not necessarily mean that they are less accurate, but that their agreement is less favourable with the second-order scheme with added numerical dissipation used in the reference data. Interestingly though, there is no difference between the Rusanov RS when used with or without the MCB scheme, hinting that the MCB scheme does not improve the situation at all. The first impression might be that this may be due to an implementation error, however, the FSAC-PP and FSAC-VP method do show differences when using this particular combination of numerical schemes, see Table 6.3–6.4. Although not shown here for reasons stated above, the wall time is different for both schemes so that the MCB scheme does indeed get computed when using the AC method, it just does not have any noticeable effect. At Re=5000 and on the fine grid, we can see that the Rusanov RS with and without MCB scheme is about five times faster in terms of iterations than the MCB scheme by itself. In-fact, the MCB scheme was the only scheme to demonstrate convergence problems at Re=5000 on the coarse grid where it reached

Table 6.2: L_0 and L_1 error norm of the velocity profiles on the horizontal and vertical centreline for the v and u velocity component, respectively, for different Reynolds numbers. The results are shown for the AC method.

Re		AD	no RS			Rusanov RS	
$(n_x \times n_y)$		no CB	no CB	SCB	MCB	no CB	MCB
100 (128×128)	iteration	62199	60584	60501	60569	60482	60482
	$L_0(u)$ [%]	0.42	0.41	0.62	0.44	0.67	0.67
	$L_0(v)$ [%]	0.85	0.84	0.34	0.84	0.41	0.41
	$L_1(u)$ [%]	0.14	0.14	0.23	0.15	0.25	0.25
	$L_1(v)$ [%]	0.36	0.36	0.19	0.37	0.21	0.21
400 (128×128)	iteration	63047	61559	59461	61533	57235	57235
	$L_0(u)$ [%]	0.52	0.61	3.51	0.50	3.69	3.69
	$L_0(v)$ [%]	4.45	4.34	3.41	4.38	3.62	3.62
	$L_1(u)$ [%]	0.20	0.25	1.38	0.20	1.38	1.38
	$L_1(v)$ [%]	0.42	0.44	1.88	0.36	1.96	1.96
1000 (128×128)	iteration	132562	128918	118483	127378	111097	111097
	$L_0(u)$ [%]	1.45	1.84	6.53	1.55	6.49	6.49
	$L_0(v)$ [%]	0.69	0.99	6.39	0.62	6.50	6.50
	$L_1(u)$ [%]	0.60	0.80	3.25	0.58	2.86	2.86
	$L_1(v)$ [%]	0.41	0.63	3.98	0.37	3.79	3.79
3200 (128×128)	iteration	239710	218795	211268	231786	202164	202164
	$L_0(u)$ [%]	4.92	7.99	14.75	4.90	11.93	11.93
	$L_0(v)$ [%]	5.25	10.82	14.63	7.20	13.08	13.08
	$L_1(u)$ [%]	2.71	4.33	8.86	2.74	6.48	6.48
	$L_1(v)$ [%]	3.15	5.26	10.66	3.37	8.34	8.34
5000 (128×128)	iteration	249760	306056	264282	500000	229184	229184
	$L_0(u)$ [%]	12.36	60.46	18.83	67.47	14.44	14.44
	$L_0(v)$ [%]	16.85	55.57	22.55	54.63	19.53	19.53
	$L_1(u)$ [%]	4.83	29.76	12.07	32.05	8.38	8.38
	$L_1(v)$ [%]	5.95	35.02	14.35	36.22	10.41	10.41
5000 (256×256)	iteration	1407665	984315	495167	2549952	567608	567608
	$L_0(u)$ [%]	2.07	3.05	9.28	2.07	8.39	8.39
	$L_0(v)$ [%]	1.38	2.73	9.12	1.77	8.40	8.40
	$L_1(u)$ [%]	0.46	0.90	5.72	0.39	4.82	4.82
	$L_1(v)$ [%]	0.43	0.95	6.43	0.37	5.39	5.39

Table 6.3: L_0 and L_1 error norm of the velocity profiles on the horizontal and vertical centreline for the v and u velocity component, respectively, for different Reynolds numbers. The results are shown for the FSAC-PP method.

Re		AD	no RS			Rusanov RS	
$(n_x \times n_y)$		no CB	no CB	SCB	MCB	no CB	MCB
100 (128×128)	iteration	11338	12411	14000	11439	13463	11402
	$L_0(u)$ [%]	0.54	0.47	0.45	0.63	0.49	0.62
	$L_0(v)$ [%]	0.28	0.32	0.30	0.35	0.25	0.34
	$L_1(u)$ [%]	0.19	0.18	0.18	0.22	0.19	0.22
	$L_1(v)$ [%]	0.19	0.17	0.15	0.19	0.16	0.19
400 (128×128)	iteration	16623	17679	21211	18065	20821	17360
	$L_0(u)$ [%]	2.81	3.10	3.31	3.75	3.13	3.20
	$L_0(v)$ [%]	2.73	3.06	3.46	3.85	3.23	3.23
	$L_1(u)$ [%]	1.14	1.27	1.37	1.53	1.22	1.24
	$L_1(v)$ [%]	1.58	1.71	1.84	2.05	1.72	1.75
1000 (128×128)	iteration	26097	36415	47303	40433	41904	25931
	$L_0(u)$ [%]	5.75	7.68	6.30	7.76	5.11	5.12
	$L_0(v)$ [%]	5.49	7.67	6.93	8.44	5.83	5.70
	$L_1(u)$ [%]	3.06	4.11	3.42	4.13	2.45	2.37
	$L_1(v)$ [%]	3.69	5.02	4.22	5.16	3.25	3.16
3200 (128×128)	iteration	133007	235595	176041	147313	123714	83842
	$L_0(u)$ [%]	22.42	41.35	16.52	23.10	10.27	9.95
	$L_0(v)$ [%]	23.17	48.51	17.06	25.47	11.54	11.33
	$L_1(u)$ [%]	13.31	21.72	9.92	13.89	5.24	5.08
	$L_1(v)$ [%]	16.27	29.12	12.10	17.16	6.95	6.76
5000 (128×128)	iteration	191873	48265	269861	216797	182457	128703
	$L_0(u)$ [%]	34.95	44.47	22.06	31.55	12.49	12.17
	$L_0(v)$ [%]	41.72	55.76	26.15	38.16	17.76	17.57
	$L_1(u)$ [%]	20.98	26.48	13.89	19.34	6.73	6.57
	$L_1(v)$ [%]	25.73	34.06	16.71	23.66	8.50	8.29
5000 (256×256)	iteration	138923	330367	355228	282728	174769	143530
	$L_0(u)$ [%]	12.26	24.08	11.57	15.28	7.81	7.65
	$L_0(v)$ [%]	12.18	23.92	11.32	15.19	7.77	7.57
	$L_1(u)$ [%]	7.65	14.83	6.75	9.30	4.03	3.93
	$L_1(v)$ [%]	8.78	17.53	7.65	10.73	4.53	4.42

Table 6.4: L_0 and L_1 error norm of the velocity profiles on the horizontal and vertical centreline for the v and u velocity component, respectively, for different Reynolds numbers. The results are shown for the FSAC-VP method.

Re		AD	no RS			Rusanov RS	
$(n_x \times n_y)$		no CB	no CB	SCB	MCB	no CB	MCB
100 (128×128)	iteration	46141	46142	48967	48972	48935	48942
	$L_0(u)$ [%]	0.34	0.31	0.35	0.33	0.37	0.35
	$L_0(v)$ [%]	0.55	0.54	0.38	0.48	0.36	0.49
	$L_1(u)$ [%]	0.13	0.13	0.16	0.14	0.17	0.14
	$L_1(v)$ [%]	0.21	0.20	0.15	0.17	0.14	0.18
400 (128×128)	iteration	35793	35800	39574	39576	37602	38076
	$L_0(u)$ [%]	2.01	2.30	2.67	2.54	2.43	2.06
	$L_0(v)$ [%]	2.74	2.41	2.48	2.33	2.20	2.50
	$L_1(u)$ [%]	0.79	0.92	1.03	0.98	0.87	0.72
	$L_1(v)$ [%]	1.15	1.28	1.45	1.38	1.30	1.12
1000 (128×128)	iteration	52662	51095	61560	61554	56597	57538
	$L_0(u)$ [%]	4.48	5.98	5.53	5.84	4.21	3.54
	$L_0(v)$ [%]	3.86	5.49	5.30	5.64	4.01	3.27
	$L_1(u)$ [%]	2.28	3.12	2.71	2.90	1.60	1.28
	$L_1(v)$ [%]	2.65	3.69	3.25	3.49	2.13	1.66
3200 (128×128)	iteration	105207	132964	111135	123033	86616	87521
	$L_0(u)$ [%]	17.83	30.67	14.69	20.28	6.25	4.77
	$L_0(v)$ [%]	17.11	35.37	14.57	21.02	8.08	6.60
	$L_1(u)$ [%]	10.55	18.32	8.85	12.18	3.26	2.46
	$L_1(v)$ [%]	12.69	22.77	10.65	14.88	4.22	3.15
5000 (128×128)	iteration	181618	101745	199684	184293	96816	97703
	$L_0(u)$ [%]	29.75	45.77	20.62	30.57	8.36	7.09
	$L_0(v)$ [%]	33.69	55.73	23.78	35.63	14.01	12.38
	$L_1(u)$ [%]	18.08	26.75	13.09	18.66	4.15	3.29
	$L_1(v)$ [%]	21.89	34.12	15.59	22.73	4.85	3.42
5000 (256×256)	iteration	216315	221339	265727	251272	234893	237661
	$L_0(u)$ [%]	9.66	17.29	9.44	12.28	5.00	4.21
	$L_0(v)$ [%]	9.48	17.43	9.32	12.05	5.06	4.04
	$L_1(u)$ [%]	5.96	10.99	5.63	7.44	2.55	1.90
	$L_1(v)$ [%]	6.69	12.72	6.30	8.45	2.71	2.02

Table 6.5: L_0 and L_1 error norm of the velocity profiles on the horizontal and vertical centreline for the v and u velocity component, respectively, for different Reynolds numbers. The results are shown for the FSVP method.

Re		AD	no RS			Rusanov RS	
$(n_x \times n_y)$		no CB	no CB	SCB	MCB	no CB	MCB
100 (128×128)	iteration	47384	47384	-	-	-	-
	$L_0(u)$ [%]	0.33	0.30	-	-	-	-
	$L_0(v)$ [%]	0.51	0.49	-	-	-	-
	$L_1(u)$ [%]	0.13	0.13	-	-	-	-
	$L_1(v)$ [%]	0.18	0.17	-	-	-	-
400 (128×128)	iteration	35509	35518	-	-	-	-
	$L_0(u)$ [%]	2.23	2.55	-	-	-	-
	$L_0(v)$ [%]	2.51	2.35	-	-	-	-
	$L_1(u)$ [%]	0.87	1.00	-	-	-	-
	$L_1(v)$ [%]	1.25	1.39	-	-	-	-
1000 (128×128)	iteration	54978	55443	-	-	-	-
	$L_0(u)$ [%]	5.01	6.69	-	-	-	-
	$L_0(v)$ [%]	4.33	6.19	-	-	-	-
	$L_1(u)$ [%]	2.50	3.42	-	-	-	-
	$L_1(v)$ [%]	2.94	4.10	-	-	-	-
3200 (128×128)	iteration	113304	147396	-	-	-	-
	$L_0(u)$ [%]	19.67	35.03	-	-	-	-
	$L_0(v)$ [%]	19.34	40.37	-	-	-	-
	$L_1(u)$ [%]	11.66	20.04	-	-	-	-
	$L_1(v)$ [%]	14.10	25.18	-	-	-	-
5000 (128×128)	iteration	179470	119219	-	-	-	-
	$L_0(u)$ [%]	32.32	44.83	-	-	-	-
	$L_0(v)$ [%]	37.23	55.73	-	-	-	-
	$L_1(u)$ [%]	19.53	26.58	-	-	-	-
	$L_1(v)$ [%]	23.78	34.07	-	-	-	-
5000 (256×256)	iteration	222903	235792	-	-	-	-
	$L_0(u)$ [%]	10.74	19.84	-	-	-	-
	$L_0(v)$ [%]	10.53	19.76	-	-	-	-
	$L_1(u)$ [%]	6.66	12.45	-	-	-	-
	$L_1(v)$ [%]	7.50	14.52	-	-	-	-

its maximum allowable iterations of 500 000. The residuals were periodically increasing and decreasing and hence this value is somewhat arbitrary and should not be taken as the number of iterations required to reach a converged solution. Furthermore, as can be seen by the L_0 and L_1 norm, as well as the discussion on the velocity profiles before, the MCB scheme was not able to predict the correct flow in the first place and so a discussion on whether it picked up a transient behaviour would be misleading.
Turning to Table 6.3, we can see the errors and computational cost for the FSAC-PP method. The qualitative discussion on the velocity profile is here backed up by the numerical data as well. Basing all of the following discussion on the L_1 norm (unless otherwise stated), we can see that the Rusanov scheme with and without the MCB scheme is matching the errors obtained with the other schemes at lower Reynolds numbers while it outperforms those schemes at higher Reynolds numbers. Since the RS-based approach always produces a correct flow field, we can see accuracy improvements by up to a factor of four. The hybrid Rusanov and MCB scheme does, however, always results in slightly higher errors norms. In a direct comparison, the SCB scheme does always produce slightly better agreement with the reference data, however, the MCB scheme by itself and without a RS converges always faster than the SCB scheme. Using the hybrid Rusanov and MCB scheme together, though, produces better agreement with the reference data (up to a factor of two at high Reynolds number flows) while the residuals are equally halved at higher Reynolds numbers. Thus, the multi-directional nature of MCB scheme coupled with the favourable transportiveness properties of the Rusanov RS shows evidence here that speed-up and gain in computational accuracy can be achieved. The only scheme which is capable to outperform the hybrid scheme is the central scheme with artificial dissipation, in terms of computational cost at least at Re=5000 on the fine grid. However, the computational gain is minimal while the hybrid scheme is twice as accurate. This is remarkable in a way as the reference data also used a central scheme with added dissipation for its discretisation. It would be natural to assume that the same scheme in the context of the FSAC-PP method would perform equally well, as it has done for lower Reynolds numbers. However, at higher Reynolds numbers, the lack of transportiveness starts to show which is not present in the RS-based approach. Furthermore, the central scheme also starts to show an oscillatory profile at higher Reynolds numbers which is, again, absent for the hybrid scheme.
In Table 6.4, the same discussion can be made for the FSAC-VP method. In comparison to the FSAC-PP method, we can see that here too the Rusanov approach produces better accuracy than the other schemes which is improved by coupling it to the MCB scheme. However, the iterations required increases slightly when using the MCB scheme. Furthermore, is cannot be clearly stated that the SCB or MCB scheme by itself is better than the other in terms of accuracy or computational cost. However, once the MCB scheme is paired with the Rusanov RS, the accuracy starts to increase. For example, at Re=3200, the differences in accuracy compared to a non CB scheme are as high as a factor of 6-7. The central scheme with artificial dissipation is able to match the hybrid scheme in terms of iterations — a noticeable exception is presented at Re=3200 and Re=5000 on the coarse grid, where the hybrid scheme performs better — but not in terms of accuracy. The differences on the

coarse grid at Re=5000 are as well a factor of 6-7 for the L_1 norm while reducing to a factor of three on the fine grid at Re=5000. Still, the hybrid scheme performs better than the reference scheme used in Ghia *et al.* [152].
In terms of relative computational times, it is reasonable to compare the FSAC-PP and FSAC-VP against the AC method from which they partly originate. For the FSAC-PP method we can see reduced number of iterations by a factor of 5–6 (Re=100), 3–4 (Re=400), 3–4 (Re=1000), 1–2 (Re=3200), 1–2 (Re=5000, coarse grid) and 2–10 (Re=5000, fine grid), respectively. For the FSAC-VP method, those factors for computational savings become about 1.5 for Re=100 and Re=400, 2–2.5 (Re=1000), 1.5–3 (Re=3200), 1.5–3 (Re=5000, coarse grid) and 2–10 (Re=5000, fine grid), respectively. Thus, by using either of these methods, we can see a significant saving in computational cost. In terms of the FSAC-PP method, this is to be expected and was also highlighted by Könözsy [109] and Könözsy and Drikakis [21] where computational timings where presented along with iterations. They stated that the FSAC-PP method showed a speed up when compared to the AC method in terms of CPU time. At the same time, for Re=3200 and above, we can see that the FSAC-VP method starts to reduce the number of iterations more than the FSAC-PP method is capable of, except for the Rusanov and hybrid scheme consisting of Rusanov and MCB scheme at Re=5000 using the fine grid. Thus, high Reynolds number flows show potential for both methods to significantly decrease the computational time while the FSAC-VP method performs slightly better in this regime.
The results stated above for the FSAC-VP method are equally applicable to the FSVP method. Comparing the results in Table 6.5 with those discussed before in Table 6.4, very little differences can be seen. Thus, the simple inclusion of the perturbed continuity equation in the FSVP method to hyperbolise the system of equations has shown that the accuracy and computational cost can be favourably influenced through the use of RS and CB schemes.

To conclude this Section, a brief summary of the results is given here. From our initial discussion on the numerical dissipation properties of each interpolation scheme, we saw that the polynomial scheme possessed the least amount of numerical dissipation, based on a Taylor-series truncation error argumentation, which was confirmed through the numerical experiments. It was the first scheme to suffer from a lack of dissipation and was unable to resolve the main vortical flow structures as the Reynolds number increased at a constant mesh size. We also saw that the central scheme with artificial dissipation contained, for most cases, enough inherent dissipation to account for the loss in physical dissipation. While that is the case, it was still prone to the pressure-velocity decoupling problem which was especially pronounced at higher Reynolds numbers. The same issues are present for the polynomial reconstruction scheme when used by itself or in conjunction with the MCB scheme. Once it was coupled with a RS-based approach, though, smooth velocity and pressure fields were obtained for all Reynolds numbers. Thus, the RS alone was able to remove the unfavourable decoupling properties while at the same time having the potential of reducing the computational cost and increasing the accuracy. When the Rusanov RS was further coupled with the FSAC-PP and FSAC-VP method, an increase in accuracy was seen for both methods while the computational cost was also

decreased for the FSAC-PP method but not for the FSAC-VP method. The gain in accuracy may be explained by the favourable properties observed of the MCB scheme where it was still able to reproduce vortical structure where the polynomial reconstruction scheme was failing to do so. We also saw that for high Reynolds numbers, there is great potential to reduce the computation cost when using either the FSAC-PP, FSAC-VP or FSVP method when compared to the AC method. That makes these methods computational competitive while the hybrid scheme consisting of the Rusanov RS and the MCB scheme has the potential to accurately predict vortical structures at an even further reduced computational cost.

6.2 Forced Separated Flow over a Backward Facing Step

The last Section highlighted some of the important features of the AC, FSAC-PP method, as well as the newly introduced FSVP and FSAC-VP method for high Reynolds number flows. Furthermore, the different characteristic approaches were tested with different RS-based approaches. In this Section, the focus is shifted towards laminar flows over a step so that at a predefined point the flow separates and has to reattach further downstream. As discussed in the beginning of this Chapter, the reattachment point defines how much kinetic energy is contained within the recirculation bubble. Once the flow becomes turbulent, it is this kinetic energy which is constantly feeding the turbulent eddies with new energy to sustain their energy cascade. The size and shape of the primary vortex is also of importance as it can trigger secondary recirculation areas downstream at the top and bottom wall. This has been investigated by many researchers experimentally and numerically, but in this study, we will focus our attention on the work of Denham and Patrick [160] and Armaley *et al.* [161].
In reference [160], experimental studies over a backward facing step were carried out at Reynolds numbers in the range of $73 < Re < 229$. The experimental apparatus consisted of an inlet channel of length $x/S = 20/3$ in which water was pumped so as to develop a fully laminar velocity profile. The smaller channel was connected to a larger channel which was larger by a step height S over which the flow had to pass. Velocity profiles at different downstream locations in the larger channels were taken and the reattachment point was predicted using laser anemometer measurements. Dye traces were also injected into the flow from which the reattachment point was measured as well. There is one particular problem with the study as it is rather difficult to reproduce numerically. Durst *et al.* [162] provided an overview on different methods to estimate the development length of simple channel flows. They synthesized the information available in the literature into a single equation which is given as

$$\frac{x}{S} = \left[(0.619)^{1.6} + (0.0567\,\mathrm{Re})^{1.6}\right]^{1/1.6}. \tag{6.2.1}$$

Based on the Reynolds number, the non-dimensional development length of the channel can be predicted using this equation. The present case of $x/S = 20/3$ corresponds to a Reynolds number of Re=116, which is far below the maximum

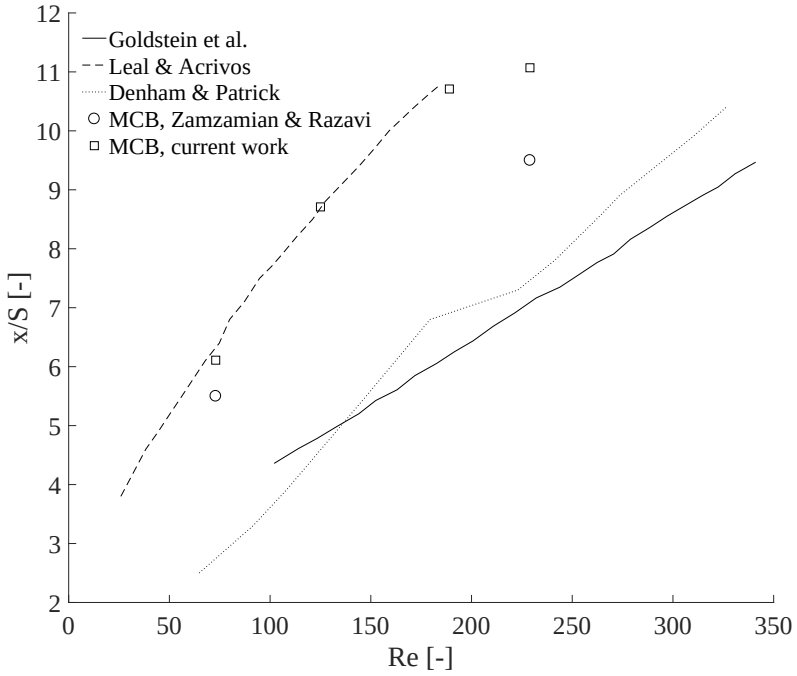

Figure 6.20: Comparison of different experimental studies on the reattachment point x/S for the backward facing step geometry using a expansion ratio of 2:3. Data are shown from Goldstein *et al.* [163], Leal and Acrivos [164] and Denham and Patrick [160]. Further numerical data is shown from Zamzamian and Razavi [53] and from the current work for the multi-directional characteristic-based (MCB) scheme.

number used in the experimental work. The implications are that a non-fully developed velocity profile enters the larger channel which would be difficult to impose in a numerical simulation, so as to match the velocity profiles. But it has further, measurable effects. In their study, Denham and Patrick compared their results against other experimental studies, which is also shown in Figure 6.20. Looking at the length of the recirculation area, their study suggests that the flow reattaches at around $x/S = 7$ for a Reynolds number of Re=200. Goldstein *et al.* [163] predicted that to be closer to $x/S = 6$ while Leal and Acrivos [164] showed results where a ratio of $x/S = 11$ was obtained. In light of the rather large experimental discrepancies, it becomes even more difficult to perform computational comparisons between the experiments and numerical simulations. Yet this is exactly what Zamzamian and Razavi [53] did when they validated their MCB scheme using the AC method. There is no negative judgement implied by the current author on the test case chosen to compare their results; experimental studies do come with a degree of uncertainty, however, at the same time it is felt that the comparison was not carried out with high scientific rigour and that premature conclusions were drawn. Therefore, numerical comparisons between the SCB and MCB scheme are done using only the AC method as this is the same approach Zamzamian and Razavi have chosen to compare their scheme. We use the experimental data provided by Denham and Patrick to validate the results. After the various concerns have been addressed here, we substitute the experimental data for those provided by Armaly *et al.* [161]

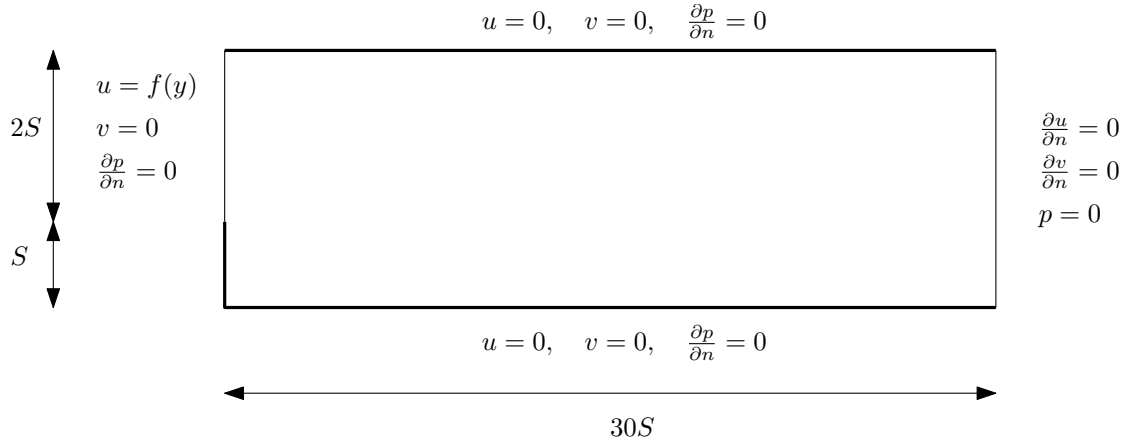

Figure 6.21: Computational domain for the backward facing step problem adapted from Zamzamian and Razavi [53].

and carry out simulations at two different Reynolds numbers for all incompressible methods and numerical schemes.

The geometry chosen to reproduce the experimental data is given in Figure 6.21. In order to impose a velocity profile at the inlet, the smaller channel is removed, and the velocity profile given as a boundary condition, indicated by $u = f(y)$. The velocity profiles from the experiment were digitised and then interpolated using the MatLab environment which was then written to a file and read by the solver. At the step, the velocity was set to zero and the pressure obtained through a Neumann boundary condition. Zamzamian and Razavi used a mesh of $n_x \times n_y = 112 \times 45$, however, it has been found that further refinement is necessary using the present solver as its underlying data structure is based on Cartesian coordinates. The final mesh was selected to contain $n_x \times n_y = 300 \times 120$ elements. The computational results for two different Reynolds numbers are shown in Figure 6.22. The numerical schemes used in the present study are shown by solid lines while those obtained by Zamzamian and Razavi are shown as dashed lines. Inspecting both velocity profiles obtained with either the MCB or SCB scheme in [53], we can see that the velocity is not set to zero at the wall along the step at $x/S = 0$. Thus, an incorrect boundary condition is given at the point at which the flow is supposed to develop from and so it is not surprising to see errors in the developed flow. For example, the MCB scheme of Zamzamian and Razavi does match the experimental data rather well while their SCB implementation seems to produce less accurate results at Re=73. This behaviour is further exaggerated when looking at Re=229, where the SCB scheme initially matches the experimental data in the bulk part of the flow (up to $x/S = 0.8$) but due to the incorrect boundary condition implementation, it fails to produce the correct recirculation areas and thus velocity profiles. The results obtained in this work do over-predict the flow in its bulk for both Reynolds numbers. As Denham and Patrick rightfully pointed out, the downstream flow pattern is largely determined by the upstream flow effects, in this case those occurring in the smaller inlet channel and close to the step itself. By removing such crucial in-

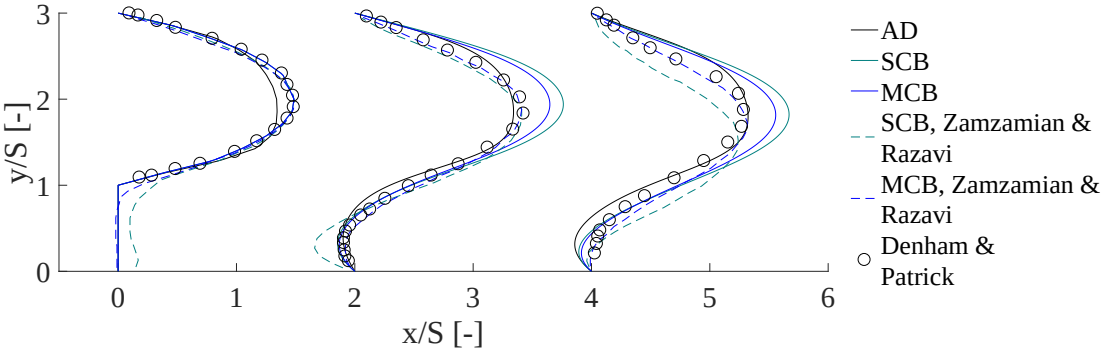

(a) Re=73

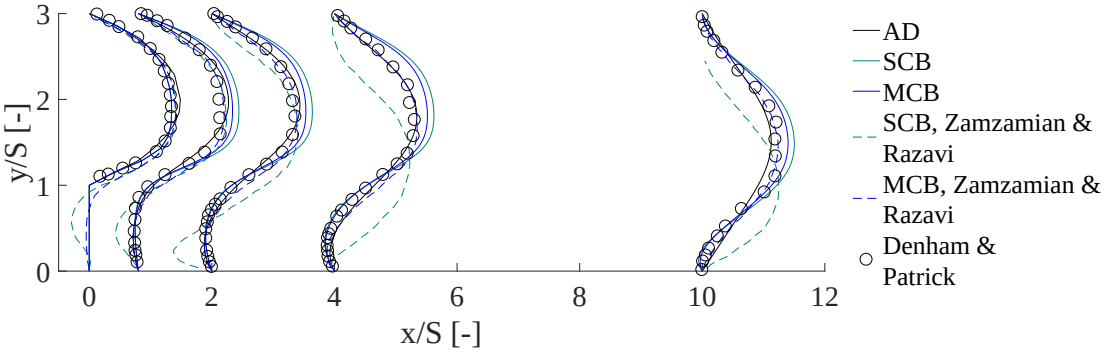

(b) Re=229

Figure 6.22: Comparison of the the CB schemes implemented by Zamzamian and Razavi [53] and the current work for the backward facing step geometry at two different Reynolds numbers.

formation it is impossible to try to match experimental data to a high degree of confidence. Returning back to the boundary condition issue encountered by Zamzamian and Razavi, we can see that the non zero velocity component at the step wall are present for both the SCB and MCB scheme. The MCB scheme seems to be less affected by the ficticious boundary condition but it does not remove the fact that essentially a different flow was modelled. The very fact that fluid was allowed to exit or enter the domain at the step may also explain why the velocity carried more momentum in the present study and thus over-predicting the velocity profiles while those curves that matched the experimental data in Zamzamian and Razavi's study were much closer to the experimental data as momentum had been taken out of the domain. They did, however, also provide further evidence that their results had to be regarded with scepticism. As a validation scheme, they used the central scheme with artificial dissipation, just as in this study and reported that at Re=229 "the central scheme shows remarkable instabilities and comparisons are made only for second-order MCB and (S)CB schemes." [53, p. 8706]. Figure 6.22 shows results obtained with the present solver and the central scheme with artificial dissipation (AD). Contrary to the claims of Zamzamian and Razavi, the results do agree rather well with the experimental data. The extra momentum present in the SCB and

MCB scheme may have been dissipated through the artificial dissipation mechanism to allow the AD scheme to match the experiments in closer agreement. Returning to Figure 6.20, we can also see the reattachment length x/S predicted by Zamzamian and Razavi, the current work and the experimental studies of Goldstein *et al.* [163], Leal and Acrivos [164] and Denham and Patrick [160]. For Zamzamian and Razavi, the reattachment point was not given explicitly and was inferred from streamline plots. For the current work, the reattachment point was obtained from the skin friction coefficient where it has a change in its sign and becomes zero. We can see that the current work agrees much better with the results provided by Leal and Acrivos than those of Denham and Patrick. An important difference between the study of Leal and Acrivos and Denham and Patrick was that in the former study, the top wall in Figure 6.21 was removed and equivalent to a free stream condition. Thus, any interactions of the recirculation area near the step height with potential downstream eddy formations at the top wall is removed. In-fact, no secondary vortex structures could be identified in the present work which may attribute to the close agreement with reference [164]. The study of Zamzamian and Razavi showed reduced reattachment lengths compared to the current work which may indicate the formation of a top wall vortex. Indeed, if such a vortex exists, the reattachment length is expected to increase due to the extra downward momentum transfer. No such evidence was provided by Denham and Patrick, but their lower reattachment length may indicates that a top wall vortex was present but not measured.
Overall, it cannot be concluded that the "second-order MCB provides more accurate results than the second-order (S)CB scheme" [53, p. 8707]. It is furthermore incorrect to state that the central scheme is not capable to predict the correct flow field. At this point, the best guess is that the insufficient description of boundary conditions led to the failure and inaccuracies of the central and SCB scheme, respectively. A further analysis is not possible without inspecting the code which is not publicly available.

Therefore, we do not carry out more analysis using this reference data due to too many uncertainties which ultimately fail to provide any insight into which method or scheme may be working better than the others. For the sake of completeness, however, we carry out a full parametric investigation for the backward facing step problem following the experimental data of Armaly *et al.* [161], where the smaller channel section can be explicitly resolved as the velocity profile entering the larger channel always follows a laminar velocity profile. Furthermore, upstream pressure disturbances may be accounted for as well as its interaction with the downstream pressure and velocity field. The geometry for this particular study is shown in Figure 6.23.

Here, we have $S \neq h$ and specifically $(S + h)/S = 10.1/5.2 \approx 1.94$. Before we perform any numerical investigation, a grid convergence study is carried out and the so-called grid convergence index (GCI) is calculated, which is explained in the following. In his 1994 article, Roache [165] introduced the notion of the GCI which is used to judge if a numerical solution has become grid independent, i.e. it indicates for which mesh level the results would not change further if the mesh would be refined. He paired his analysis with the Richardson extrapolation which can be

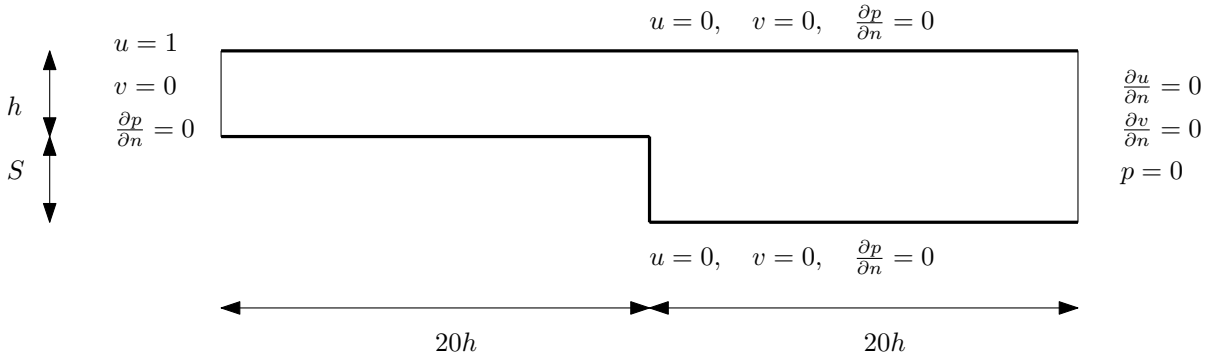

Figure 6.23: Computational domain for the backward facing step problem following the experimental work of Armaly *et al.* [161].

used to extrapolate the results obtained on coarser mesh level to that which would correspond to a fine mesh solution. Later, Celik *et al.* [166] further refined the GCI approach which is adopted for this test case.
In order to perform a GCI study, a minimum of three computational grids are required. For each mesh, a representative grid size has to be established as

$$h = \left[\frac{1}{N} \sum_{i=1}^{N} \Delta A_i \right]^{1/2}, \tag{6.2.2}$$

where ΔA_i is the area of cell i. If we consider three grid levels, we require that $h_1 < h_2 < h_3$. This means that the mesh corresponding to h_1 contains the most elements and thus is the fine grid. Equally, h_2 and h_3 correspond to the medium and coarse mesh solution, respectively. We can define the refinement ratios $r_{21} = h_2/h_1$ and $r_{32} = h_3/h_2$ and the difference in the solution as $\epsilon_{21} = \phi_2 - \phi_1$ and $\epsilon_{32} = \phi_3 - \phi_2$ where ϕ is any suitable integral property, and calculate the apparent order p as

$$p = \frac{1}{\ln(r_{21})} \left| \ln \left| \frac{\epsilon_{32}}{\epsilon_{21}} \right| + q(p) \right|. \tag{6.2.3}$$

Here, $q(p)$ is depending on p itself and defined as

$$q(p) = \ln \left(\frac{r_{21}^p - s}{r_{32}^p - s} \right), \tag{6.2.4}$$

where we have introduced $s = \text{sign}(\epsilon_{32}/\epsilon_{21})$. Eq.(6.2.3) and Eq.(6.2.4) need to be solved iteratively. Once the apparent order p is known, the extrapolated value — corresponding to a grid-independent solution — can be obtained as

$$\phi_{\text{ext}}^{21} = \frac{r_{21}^p \phi_1 - \phi_2}{r_{21}^p - 1}. \tag{6.2.5}$$

Alternatively, the Richardson extrapolation can be used in the form of

$$\phi_{\text{ext}}^{21} = \phi_1 + \frac{\phi_1 - \phi_2}{r_{21}^p - 1}, \tag{6.2.6}$$

where p is now taken as the order of the numerical scheme, corresponding to its Taylor series truncation error. In the same way, an expression for ϕ_{ext}^{32} can be found. The relative error that is made can be calculated as

$$e_{21} = \left| \frac{\phi_1 - \phi_2}{\phi_1} \right| \tag{6.2.7}$$

where again an expression for e_{32} can be found analogously. With this information provided, the GCI can be calculated as

$$GCI_{21} = \frac{1.25 e_{21}}{r_{21}^p - 1}. \tag{6.2.8}$$

The same GCI can be found in Roache [165] where the apparent order p is substituted for the order of the discretisation scheme. The GCI has no absolute meaning, i.e. simply stating the GCI obtained from two grid levels does not bear any meaning. It needs to be compared against other mesh levels (hence the need for at least three grids) from which it can be judged at which point the solution becomes grid independent. That being said, this represents the ideal scenario which is often not applicable for real scientific or industrial problems. Often, the medium mesh solution is chosen rather than the finest grid level, despite the medium grid having a larger error. The mesh size may be restricted by the resources and time available, but for those cases the GCI helps to quantify how much the mesh is influencing the results. The approach described above is applied to the geometry presented in Figure 6.23. The geometry is divided into three blocks and each one meshed using the same number of points along the $x-$ and $y-$direction. In total, five mesh levels are considered where the smallest mesh corresponds to $3(n_x \times n_y) = 3(20 \times 10) = 600$ elements. For each subsequent refinement, the mesh spacing is halved in each direction so that the mesh size quadruples. The reattachment length x/S is chosen here as the integral property ϕ and its change is used to calculate the GCI value. The number of iterations, computational time, extrapolated value and the GCI itself are shown in Table 6.6. On the smallest grid level, the simulations only take seconds to complete, while the finest mesh level requires several hours. In this case, the mesh containing 38400 elements was chosen to be used for all subsequent studies. Although a change in reattachment can still be observed, it is within 2% of the extrapolated value from the fine grid. Similarly, the GCI indicates that the solution is only changing moderately by 1.65%. Despite the lower GCI value for the finest grid, the computational cost increases exponentially. Furthermore, the simulations were carried out with the FSAC-PP method as it has shown to be the fastest method of the four tested in the last Section in most cases. Therefore, in light of a need for a parametric study at different Reynolds numbers, numerical schemes and incompressible methods, the more economical mesh containing only 38400 elements was chosen.

Figure 6.24 and 6.25 show the velocity profiles obtained at different downstream sections x/S of the larger channel with each method and numerical schemes at Re=100 and Re=389, respectively. At the lower Reynolds number, it can be seen that the MCB and non CB approach perform best using the AC method while the

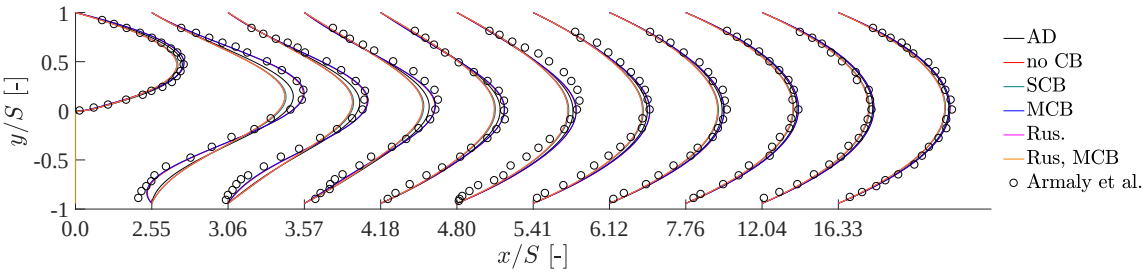

(a) AC

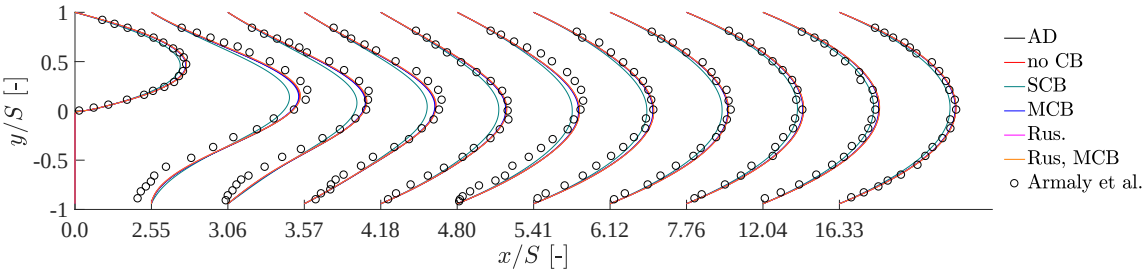

(b) FSAC-PP

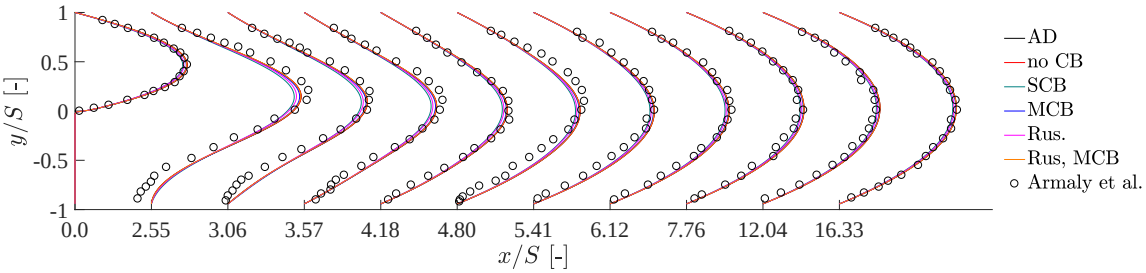

(c) FSAC-VP

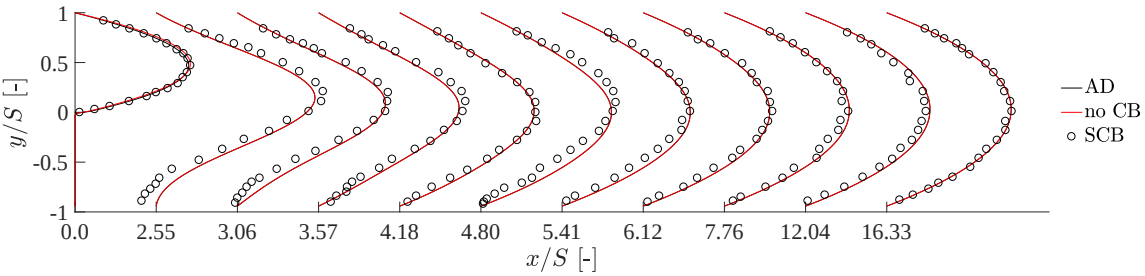

(d) FSVP

Figure 6.24: Comparison of velocity profiles at Re=100 for different incompressible methods for the backward facing step geometry.

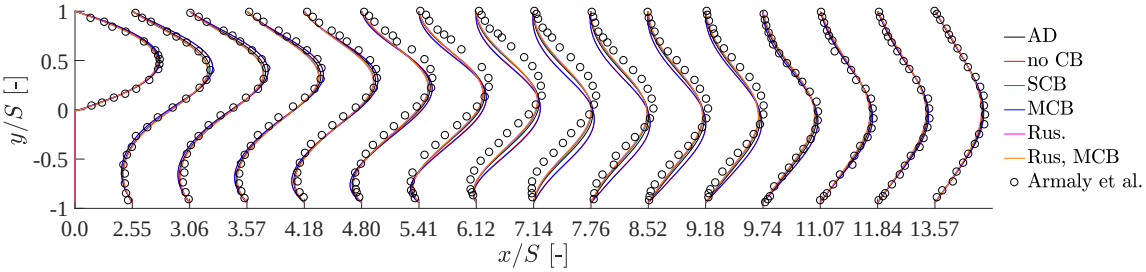

(a) AC

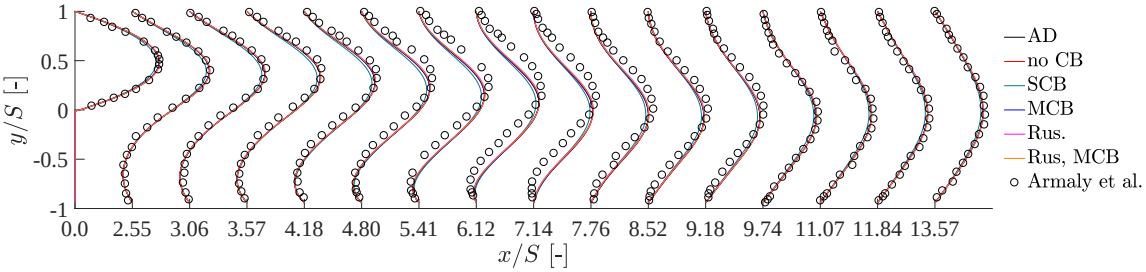

(b) FSAC-PP

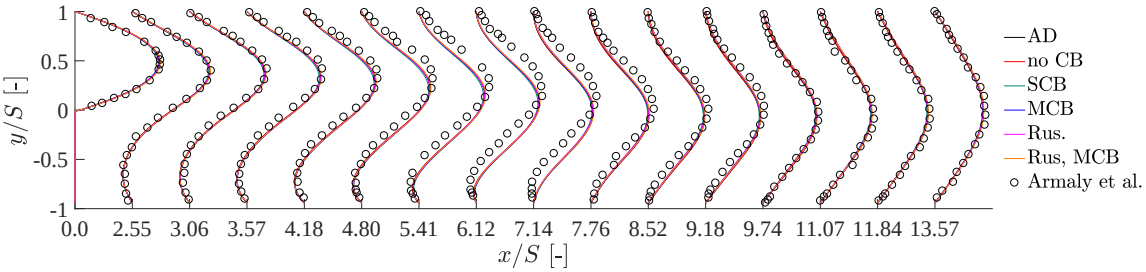

(c) FSAC-VP

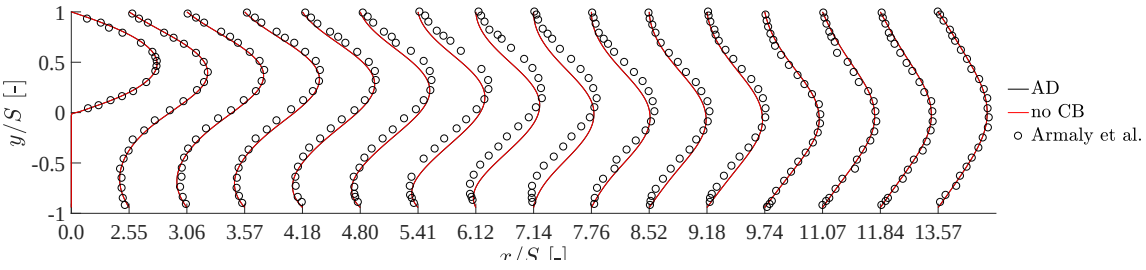

(d) FSVP

Figure 6.25: Comparison of velocity profiles at Re=389 for different incompressible methods for the backward facing step geometry.

Table 6.6: Grid Convergence Index study based on the reattachment length of the lower wall at Re=100 using the FSAC-PP method.

Cells	iterations	CPU time [h]	x/S	ϕ_{ext}	GCI
600	8723	0.0008	2.26534	-	-
2400	18946	0.008	2.48377	2.6053	0.0612
9600	36436	0.059	2.56186	2.6053	0.0212
38400	93465	0.79	2.62402	2.6586	0.0165
153600	237433	9.05	2.66116	2.6818	0.0097

RS-based approaches under-predict the peak velocity initially. Further downstream, there is less of a discrepancy between the two approaches. The central scheme with artificial dissipation lies in the middle of the two extremes, matching the reference data more closely as the flow is advected downstream. At Re=100, it is expected that all physical dissipation is fully resolved. Only once the flow starts to become turbulent do the smallest scales, at which turbulence is dissipated into heat, reduce in size. Thus, for laminar flows, it is expected that all physical dissipation is resolved by the computational grid and there is no need to add further numerical dissipation. This might explain why the central scheme is not matching the reference data as accurately as the MCB or non CB approach which possess less numerical dissipation. An excess of it would only introduce damping of the solution and it can be argued that this is exactly what can be seen for the central scheme. Of course, it has to be kept in mind that the central scheme is only second-order accurate while the polynomial reconstruction has third-order of accuracy, which has an additional influence on the solution. By the same logic, the RS-based approaches all produce more dissipative errors than the central scheme or the MCB and non CB scheme. As has been noted in the literature [96], RS do come with their own inherent numerical dissipation. We can conclude that numerical dissipation is thus useful and required for high Reynolds numbers to stabilise and develop the flow while at low Reynolds numbers, it suggests that an excessive amount of it can have damping properties. This is in-fact in line with the development of numerical schemes in general, as discussed in Chapter 1, where second-order schemes were preferred over their first-order, dissipative, counterparts. Looking at Figure 6.24b, the same flow is shown for the FSAC-PP method. Except for the SCB scheme, there are no noticeable differences between the different numerical schemes. Although the same amount of numerical dissipation is present in the schemes when using the FSAC-PP method instead of the AC method, the former seems to have an in-built feature to equalise any differences in the numerical schemes. This is in-fact the same observations Könözsy [109] made about the FSAC-PP method which showed an indifference towards the numerical interpolation procedures. Features which were only resolved using higher-order interpolations schemes using the AC and FS-PP method were shown to be resolved with the FSAC-PP method even with first order schemes. The FSAC-VP method, on the other hand in Figure 6.24c, shows similar velocity profiles as obtained with the FSAC-PP method but here the Rusanov RS by itself also shows less accurate results than the other schemes. The agreement of those other schemes,

compared to the AC, FSAC-PP method is, however, good and match the reference data equally well. As for the lid driven cavity, there is no noticeable difference between the FSAC-VP and FSVP method.

In Figure 6.25, the same method and schemes are tested at Re=389. In this regime, the flow is still laminar but according to Armaly *et al.* [161], it is close to a critical Reynolds number at which secondary vortices are formed at the top wall. Thus, predicting these secondary vortices correctly is mandatory in order to obtain the correct separation length. Any difference will also have an impact on the velocity profiles. The AC method does separate the flow into two different behaviours based on which scheme is used. The MCB and non CB scheme both predict the peak velocity to be lower than the experiment which is especially pronounced between $6.12 < x/S < 9.18$. The other schemes predict the peak to be at a higher location which could indicate that the MCB and non CB approach are deviated downwards due to a secondary vortex which is not predicted bu the other schemes. A closer look at the separation and reattachment points is required which will be discussed at a later stage. The picture is different for the FSAC-PP method where all velocity profiles are in close agreement. Again, the SCB scheme shows a bit more damping than the other solutions but there is no difference in terms of peak prediction, hinting that no secondary vortex has been detected by any of the numerical schemes. There is, however, the same mismatch with the experimental data approximately in the region of $5.41 < x/S < 7.76$. For the FSAC-VP method, there is even less difference among the various schemes. It suggests that the invariance towards numerical schemes is also passed on from the FSAC-PP method, which can be also confirmed by looking at the FSVP method, which shows the same invariance, although here just for two different schemes. It could be argued that the mesh is fine enough so that differences in numerical schemes are not as pronounced and the false conclusion of scheme invariance can be drawn. After all, in the previous Section on the lid driven cavity, there were large differences in the velocity profile for both the FSAC-PP and FSAC-VP method. This conclusion would be wrong due to several reasons: In the introduction to this Section, a GCI study was carried out which showed that differences are still present in the mesh. Although being small, there is still space for mesh induced errors. It could be further argued that these errors would not be visible in the velocity plots due to the size of the plots and the error range, but then again, the AC method does show visible differences. Compared to the AC method, both the FSAC-PP and FSAC-VP method (and to the same extend the FSVP method) do show less dependency on the numerical scheme and produce results which lie closer together than those predicted with the AC method. Furthermore, the velocity profiles shown for the lid driven cavity in the previous Section were shown for the same mesh size while the Reynolds number increased. Up the Re=1000 the results showed a similar behaviour as in the present Section where the influence of the numerical scheme on the solution was minute. It also needs to be stressed that a low-dissipative polynomial reconstruction scheme has been used on purpose so as to reduce the numerical dissipation error. Once the numerical dissipation is not able to match the physical one, differences are expected but this is due to an under-resolved flow. In cases where the dissipation is balanced, as seen for

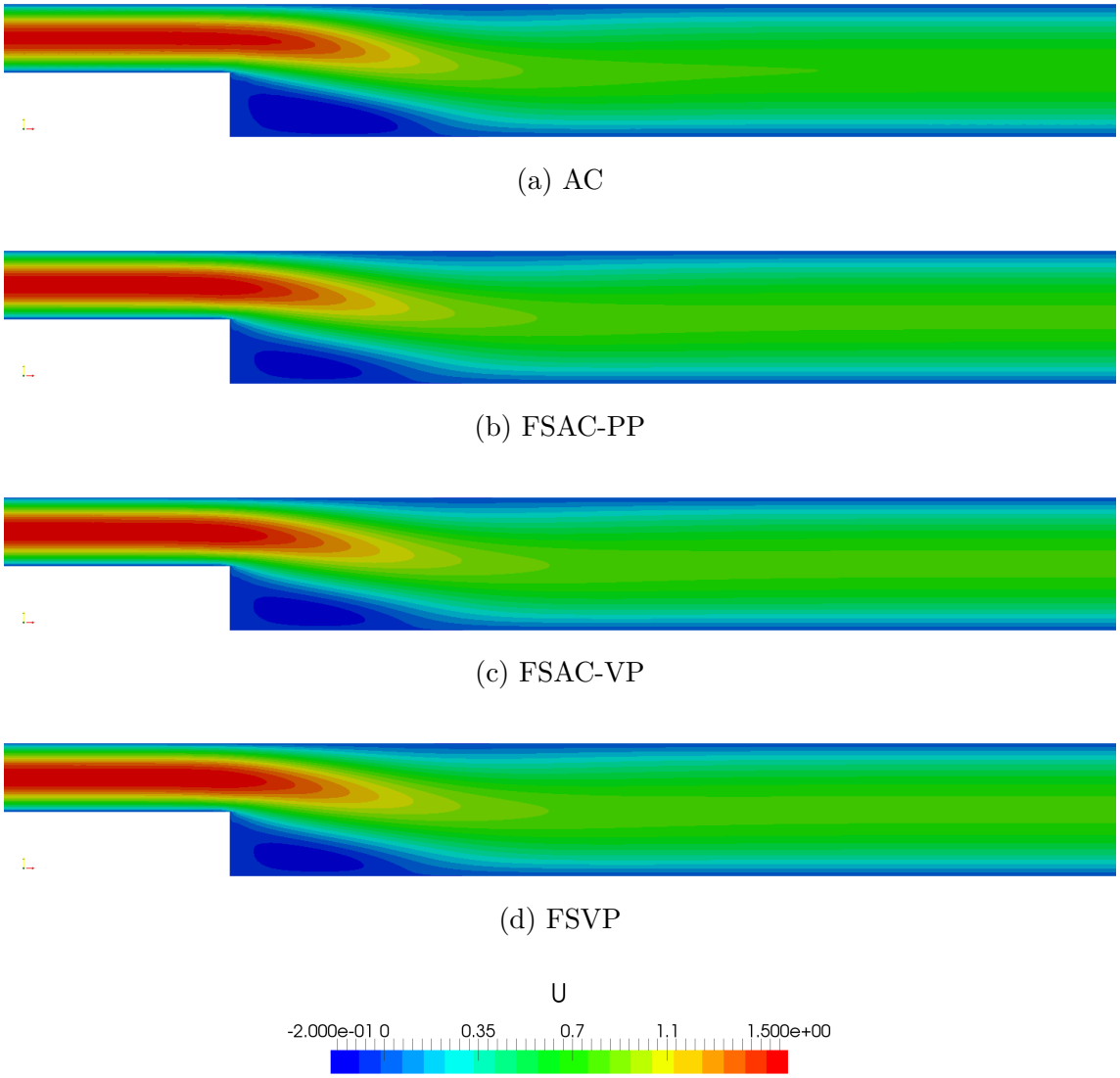

(a) AC

(b) FSAC-PP

(c) FSAC-VP

(d) FSVP

Figure 6.26: Contour plots of the velocity profile for different incompressible methods at Re=100 using a non CB scheme.

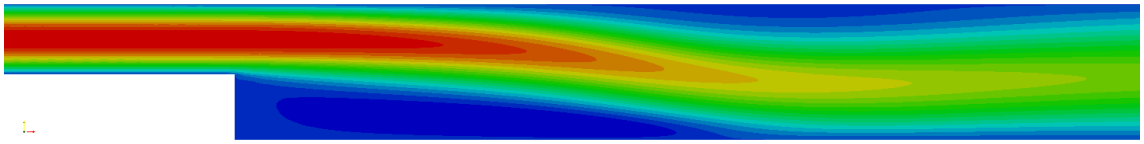

(a) AC

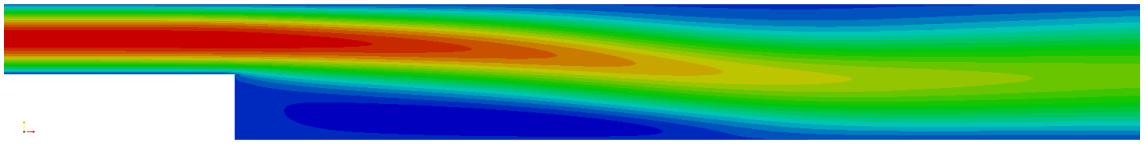

(b) FSAC-PP

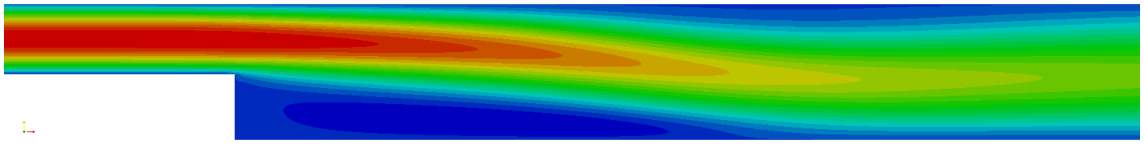

(c) FSAC-VP

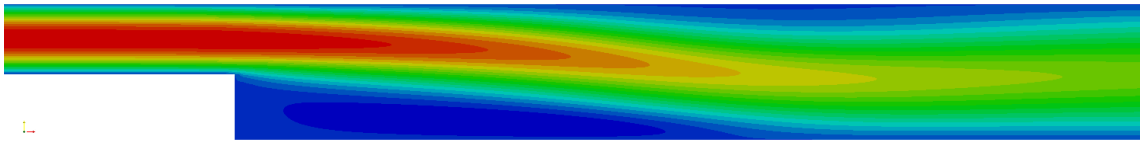

(d) FSVP

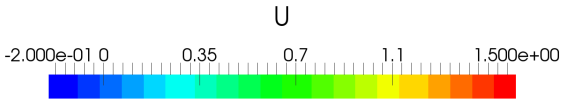

Figure 6.27: Contour plots of the velocity profile for different incompressible methods at Re=389 using a non CB scheme.

cases up to Re=1000 for the lid driven cavity and Re=389 in this Section, the results show little dependence on the numerical scheme when the FSAC-PP, FSAC-VP or FSVP method is used.

Figure 6.26 and 6.27 show the contour plots of velocity at Re=100 and Re=389 for all different incompressible method using the non CB scheme as a reference. From a quantitative point of view, we see that the recirculation area is approximately of the same length and that in general there is little difference in the bulk of the domain, when considering the case for Re=100. For the higher Reynolds number of Re=389, however, it can be confirmed that there is an indication of a secondary recirculation area at the top wall for the AC method, while the other methods do not seem to have produced a vortex similar in size. This creates a difference in downward momentum which has been discussed in conjunction with Figure 6.25a where the mismatch in peak velocity prediction was observed. Judging from a qualitative point of view, however, it does not seem to have affected the reattachment point of the flow to a large degree. The results for the FSAC-PP, FSAC-VP and FSVP method, on the other hand show a consistent picture where at least visually, no differences can be observed.

This discussion can be repeated from a quantitative point of view referring to Table 6.7. Here, the locations x_1, x_4 and x_5 correspond to those in reference [161], where x_1 is the reattachment point of the primary vortex at the bottom wall, x_4 the separation point of the secondary vortex on the top wall and x_5 its corresponding reattachment point. There are several important messages to extract from this Table which will be discussed in turn.
First, consider the accuracy of the different schemes for different methods. At Re=100 and using the AC method, the closest agreement to the experimental data is achieved with the MCB scheme which differs by 1.6%. The largest difference to the experimental data is obtained using either the Rusanov RS or its combination with the MCB scheme, which gives a difference of 19.7%. At Re=389, however, the best agreement is achieved with Rusanov's RS or its combination with the MCB scheme (7.7%) while the MCB scheme by itself produces the largest difference (11.7%), which is exactly the opposite from the lower Reynolds number case. The FSAC-PP method gives its best agreement with the reference data using the Rusanov RS or its combination with the MCB scheme (13.9% for Re=100, 8.0% for Re=389) and its least accurate prediction using the SCB scheme (18.8% for Re=100, 11.0% for Re=389). For the FSAC-VP method, the non CB scheme gives the best agreement (13.2% for Re=100, 8.2% for Re=389) while it too gives the least accurate predictions using the SCB scheme (16.7% for Re=100, 10.2% for Re=389). The Rusanov RS with MCB scheme, however, provides results very close to the non CB scheme. We can calculate the difference between the most and least accurate prediction for each method and see that for the AC method we obtain $19.7\% - 1.6\% = 18.1\%$ and $11.7\% - 7.7\% = 4.0\%$, for Re=100 and Re=389 respectively. The same calculation can be done for the FSAC-PP and FSAC-VP method, for which one obtains 4.9% at Re=100 and 4.0% at Re=389 for the FSAC-PP method and 3.5% at Re=100 and 2% at Re=389 for the FSAC-VP method. This is in-fact consistent with Figure 6.24 and 6.25, although the velocity profiles are shown in these two Figures, where we

Table 6.7: Reattachment length prediction for all methods using two different Reynolds numbers. The nomenclature is in accordance with Armaley *et al.* where x_1/S refers to the reattachment length on the bottom wall while x_4/S and x_5/S refer to the separation and reattachment point on the upper wall, respectively.

			AD	no RS			Rusanov RS		
method	Re		no CB	no CB	SCB	MCB	no CB	MCB	Ref.
AC	100	iterations	338138	339228	326948	337312	330733	330733	-
		x_1/S	2.79	3.17	2.63	3.20	2.61	2.61	3.25
		x_4/S	-	-	-	-	-	-	-
		x_5/S	-	-	-	-	-	-	-
	389	iterations	214563	216806	208100	215619	208142	208142	-
		x_1/S	7.71	7.46	7.72	7.42	7.75	7.75	8.40
		x_4/S	7.11	6.19	7.77	6.11	-	-	-
		x_5/S	9.66	10.74	8.80	10.75	-	-	-
FSAC-PP	100	iterations	93467	93465	128011	111755	125736	108421	-
		x_1/S	2.78	2.78	2.64	2.77	2.80	2.80	3.25
		x_4/S	-	-	-	-	-	-	-
		x_5/S	-	-	-	-	-	-	-
	389	iterations	130247	130288	161031	141330	161449	134110	-
		x_1/S	7.65	7.66	7.48	7.65	7.73	7.71	8.40
		x_4/S	-	-	-	-	-	-	-
		x_5/S	-	-	-	-	-	-	-
FSAC-VP	100	iterations	188164	188280	195342	195670	195455	193571	-
		x_1/S	2.81	2.82	2.71	2.79	2.75	2.81	3.25
		x_4/S	-	-	-	-	-	-	-
		x_5/S	-	-	-	-	-	-	-
	389	iterations	162956	163732	161813	167062	164614	170188	-
		x_1/S	7.70	7.71	7.54	7.62	7.64	7.68	8.40
		x_4/S	7.70	7.70	-	-	-	-	-
		x_5/S	8.87	8.90	-	-	-	-	-
FSVP	100	iterations	190366	190410	-	-	-	-	-
		x_1/S	2.80	2.80	-	-	-	-	3.25
		x_4/S	-	-	-	-	-	-	-
		x_5/S	-	-	-	-	-	-	-
	389	iterations	160928	161636	-	-	-	-	-
		x_1/S	7.66	7.67	-	-	-	-	8.40
		x_4/S	7.95	7.88	-	-	-	-	-
		x_5/S	8.46	8.58	-	-	-	-	-

saw that the largest discrepancies were obtained with the AC method while both the FSAC-PP and FSAC-VP method showed less variation. Thus, we see that the FSAC-PP and FSAC-VP method do not only produce consistently the least and most accurate results using the same scheme but also that the difference among the different methods is lower compared to the AC method, at least for the two Reynolds number tested. Furthermore, while the accuracy in the prediction of the reattachment point deteriorates from 1.6% to 7.7% for the AC method, it increases for both the FSAC-PP and FSAC-VP method from 13.9% to 7.7% and from 13.2% to 8.2%, respectively. As for the cases discussed before, there is very difference between the FSAC-VP and FSVP method.

In terms of iterations, the FSAC-PP method produces, again, the lowest number of required iterations, followed by the FSAC-VP method (requiring about two times more iterations) and the AC method (requiring about three times more iterations). There are, however, fluctuations among the number of iterations required when looking at the FSAC-PP method. The SCB scheme, for example, requires about 37% more iterations than the non CB scheme, which requires the least number of iterations at Re=100. The Rusanov RS also requires more iterations but requires marginally fewer iterations than the SCB scheme. By contrast, the MCB requires only about 4% more iterations at Re=100 compared to scheme with the fastest convergence rate when looking at the FSAC-VP method. This is consistent with the findings on the accuracy, where the least and most accurate scheme only differ by less than 3.5%.

Table 6.7 does also provide information on which scheme predicts secondary vortex structures at the top wall. As a reminder, Armaly *et al.* [161] show that no secondary structure should exist at this Reynolds number. Using the AC method, all but the Rusanov RS-based approaches predict the secondary vortex, where the MCB scheme predicts the largest vortex of non-dimensional size $L = 10.75 - 6.11 = 4.64x/S$. The SCB scheme, on the other hand, although still predicting the presence of a vortex at the top wall, estimates the size to be 1.03, smaller by a factor of four. These findings also explain why the Rusanov RS and its hybridisation with the MCB scheme perform best at this Reynolds number; they do not predict the existence of a secondary vortex. The flow is forced to attach sooner in the case of the MCB scheme (Re=389, AC method) due to the rather large size of the secondary vortex. We saw in the previous Section that the MCB scheme is capable of predicting a vortical flow which may not be physical, see Figure 6.10d. This is not necessarily a failure of the MCB scheme, rather, the MCB scheme is picking up a vortical field and tries to develop it into a physically correct flow but a lack of physical or numerical dissipation is imposing no bounds on the development of the vortical structure. In the present case, dissipation is not an issue as the simulations are still operated well within the laminar flow regime. Something else must be triggering the MCB scheme to develop vortical structures where none should exist. One possible explanation could be the outflow boundary condition, which is imposing a hard boundary condition on the pressure. Here, the pressure is set to zero which automatically allows for pressure waves to be reflected at the outflow. This allows purely numerical pressure waves to travel back and forth and disturb the upstream flow. It is possible that the interaction of those pressure waves and the separation and reattachment point

is causing a fluctuating pressure field upstream that confuses the MCB scheme into thinking that these fluctuations represent turbulence. These turbulent structures may then trigger the development of vortical structures. This claim is, however, not backed-up with data and so should only be taken as a possible explanation among different possibilities[1]. The FSAC-PP method does not show any secondary vortex structures which may be attributed to the Poisson solver. The elliptic properties of it always have a smoothing effect on the pressure field which may help to reduce non-physical pressure oscillations so that no secondary structure is developed in the first place. The FSAC-VP method, on the other hand, does feature secondary vortex structures, however only for the central and non CB scheme. Its size, which is of order one, is small, however. The same is true again for the FSVP method.

Tables 6.8–6.11 show the L_0 and L_1 error norms for all four methods using the different numerical schemes at Re=100 for various locations of x/S. The bigger pictures may be lost by analysing the error norms at each location so that an average error of the form

$$\overline{L_j(u)} = \frac{1}{N}\sum_{i=1}^{N} L_j[u(x/S)|_i], \qquad j = 0, 1 \tag{6.2.9}$$

may be obtained. The discussion carried out in a qualitative way for Figure 6.24 may be repeated quantitatively in the following, based on the average L_1 norm if not stated otherwise. For the AC method, we can see in Table 6.8 that the lowest error is obtained with the MCB (2.94%) scheme closely followed by the non CB approach, which has been found previously as well. The RS-based schemes do all produces errors which are of a similar magnitude and are between 47.7%–54.8% less accurate than the MCB scheme. The central scheme, with a 22.4% higher error, lies in-between the two approaches. For the FSAC-PP method, Table 6.9, the best results are obtained with the Rusanov based approaches at 3.50% difference while the SCB gives the highest error which is 29.1% higher than the results obtained with the Rusanov RS. For the FSAC-VP method in Table 6.10, the best results are obtained using the Rusanov RS together with the MCB scheme (3.52%) while the SCB scheme, again, produces the highest error and differs by only 13.3% to the most accurate scheme. If we compare the central and non CB scheme in the FSAC-VP and FSVP method, we see that their results differs only by 0.02 percent points for each scheme, showing again little difference between the two methods. We can conclude again that the FSAC-PP and FSAC-VP method both produce the best agreement when the Rusanov based scheme is used in conjunction with the MCB scheme while the SCB scheme gives the least agreement. For the AC method, it is actually the MCB scheme by itself which produces best results while its combination with the Rusanov RS gives less favourable agreement. However, the same pattern emerges which was observed in the discussion on the separation and reattachment points. The difference in lowest to highest error is much smaller for the FSAC-VP

[1] An in-depth study on the effect of the boundary conditions was attempted by ultimately dropped due to the complexity involved.

Table 6.8: L_0 and L_1 error norm of the velocity profiles at various locations of x/S for the AC method. Results are given for different characteristic-based approaches including the Rusanov Riemann solver. The central scheme with artificial dissipation is given as a reference solution and the average error, denoted by $\overline{L_0(u)}$ and $\overline{L_1(u)}$, is provided at the bottom of the table.

		AD	no RS			Rusanov RS	
x/S		no CB	no CB	SCB	MCB	no CB	MCB
0.0	$L_0(u)$ [%]	4.91	6.80	9.05	6.59	10.63	10.63
	$L_1(u)$ [%]	1.83	3.80	4.69	3.83	5.58	5.58
2.55	$L_0(u)$ [%]	12.85	6.49	14.53	6.21	14.48	14.48
	$L_1(u)$ [%]	7.18	2.33	8.73	2.13	8.89	8.89
3.06	$L_0(u)$ [%]	11.93	6.92	12.72	6.38	12.62	12.62
	$L_1(u)$ [%]	5.49	3.21	6.51	3.02	6.63	6.63
3.57	$L_0(u)$ [%]	8.15	6.42	11.01	6.10	11.56	11.56
	$L_1(u)$ [%]	4.16	3.29	4.99	3.11	5.12	5.12
4.18	$L_0(u)$ [%]	6.30	5.96	7.54	5.67	8.26	8.26
	$L_1(u)$ [%]	2.60	2.08	3.15	1.91	3.35	3.35
4.80	$L_0(u)$ [%]	11.97	12.47	10.90	12.11	11.20	11.20
	$L_1(u)$ [%]	6.19	6.44	6.20	6.21	6.24	6.24
5.41	$L_0(u)$ [%]	7.25	7.82	6.59	7.49	6.72	6.72
	$L_1(u)$ [%]	3.96	4.14	4.06	3.91	4.14	4.14
6.12	$L_0(u)$ [%]	5.07	5.26	6.27	5.05	6.75	6.75
	$L_1(u)$ [%]	2.67	2.53	3.32	2.35	3.48	3.48
7.76	$L_0(u)$ [%]	4.64	5.14	3.39	5.09	3.93	3.93
	$L_1(u)$ [%]	1.91	1.98	1.98	1.96	2.10	2.10
12.04	$L_0(u)$ [%]	6.22	6.30	5.99	6.30	5.94	5.94
	$L_1(u)$ [%]	2.33	2.86	1.53	2.88	1.60	1.60
16.33	$L_0(u)$ [%]	3.11	2.63	4.56	2.65	5.00	5.00
	$L_1(u)$ [%]	1.28	1.01	2.60	1.02	2.93	2.93
	$\overline{L_0(u)}$ [%]	7.49	6.56	8.41	6.33	8.83	8.83
	$\overline{L_1(u)}$ [%]	3.60	3.06	4.34	2.94	4.55	4.55

Table 6.9: L_0 and L_1 error norm of the velocity profiles at various locations of x/S for the FSAC-PP method. Results are given for different characteristic-based approaches including the Rusanov Riemann solver. The central scheme with artificial dissipation is given as a reference solution and the average error, denoted by $\overline{L_0(u)}$ and $\overline{L_1(u)}$, is provided at the bottom of the table.

		AD	no RS			Rusanov RS	
x/S		no CB	no CB	SCB	MCB	no CB	MCB
0.0	$L_0(u)$ [%]	6.26	6.11	8.41	6.25	5.85	5.87
	$L_1(u)$ [%]	1.68	1.65	4.95	1.61	1.81	1.82
2.55	$L_0(u)$ [%]	13.50	13.42	14.88	13.58	12.94	12.95
	$L_1(u)$ [%]	7.02	7.01	9.27	7.19	6.52	6.51
3.06	$L_0(u)$ [%]	12.07	12.00	12.90	12.06	11.58	11.61
	$L_1(u)$ [%]	5.20	5.19	6.81	5.26	4.82	4.83
3.57	$L_0(u)$ [%]	7.34	7.28	11.48	7.22	6.94	6.97
	$L_1(u)$ [%]	3.67	3.68	5.25	3.74	3.39	3.38
4.18	$L_0(u)$ [%]	6.44	6.40	7.62	6.35	6.30	6.32
	$L_1(u)$ [%]	2.35	2.35	3.25	2.40	2.27	2.27
4.80	$L_0(u)$ [%]	12.79	12.74	11.42	12.61	12.79	12.81
	$L_1(u)$ [%]	6.17	6.18	6.42	6.20	6.12	6.12
5.41	$L_0(u)$ [%]	8.16	8.11	7.00	7.97	8.25	8.28
	$L_1(u)$ [%]	3.94	3.94	4.24	3.96	3.95	3.97
6.12	$L_0(u)$ [%]	5.80	5.75	6.49	5.61	5.94	5.97
	$L_1(u)$ [%]	2.50	2.51	3.46	2.56	2.52	2.53
7.76	$L_0(u)$ [%]	6.02	5.95	3.42	5.70	6.18	6.21
	$L_1(u)$ [%]	2.37	2.33	2.04	2.19	2.46	2.47
12.04	$L_0(u)$ [%]	6.54	6.53	6.17	6.51	6.58	6.59
	$L_1(u)$ [%]	3.57	3.51	1.56	3.33	3.69	3.72
16.33	$L_0(u)$ [%]	2.27	2.20	4.47	2.28	2.41	2.44
	$L_1(u)$ [%]	0.92	0.92	2.47	0.93	0.92	0.93
	$\overline{L_0(u)}$ [%]	7.93	7.86	8.57	7.83	7.80	7.82
	$\overline{L_1(u)}$ [%]	3.58	3.57	4.52	3.58	3.50	3.50

Table 6.10: L_0 and L_1 error norm of the velocity profiles at various locations of x/S for the FSAC-VP method. Results are given for different characteristic-based approaches including the Rusanov Riemann solver. The central scheme with artificial dissipation is given as a reference solution and the average error, denoted by $\overline{L_0(u)}$ and $\overline{L_1(u)}$, is provided at the bottom of the table.

		AD	no RS			Rusanov RS	
x/S		no CB	no CB	SCB	MCB	no CB	MCB
0.0	$L_0(u)$ [%]	6.21	6.08	6.77	6.14	6.12	5.84
	$L_1(u)$ [%]	1.73	1.72	3.45	1.59	2.62	1.71
2.55	$L_0(u)$ [%]	12.99	12.88	14.03	13.32	13.28	12.89
	$L_1(u)$ [%]	6.76	6.71	8.21	7.14	7.38	6.67
3.06	$L_0(u)$ [%]	11.72	11.64	12.37	11.95	11.82	11.62
	$L_1(u)$ [%]	5.05	5.02	5.97	5.27	5.37	4.96
3.57	$L_0(u)$ [%]	7.12	7.07	9.48	7.24	8.20	6.98
	$L_1(u)$ [%]	3.63	3.62	4.54	3.82	4.02	3.55
4.18	$L_0(u)$ [%]	6.40	6.38	5.97	6.38	5.88	6.33
	$L_1(u)$ [%]	2.30	2.29	2.80	2.41	2.60	2.32
4.80	$L_0(u)$ [%]	12.84	12.84	11.38	12.65	11.69	12.77
	$L_1(u)$ [%]	6.24	6.24	6.24	6.27	6.13	6.21
5.41	$L_0(u)$ [%]	8.20	8.20	6.92	7.98	7.06	8.16
	$L_1(u)$ [%]	4.00	4.01	4.06	4.03	3.94	3.98
6.12	$L_0(u)$ [%]	5.83	5.83	5.18	5.59	5.18	5.81
	$L_1(u)$ [%]	2.54	2.55	3.03	2.60	2.79	2.55
7.76	$L_0(u)$ [%]	6.04	6.04	4.25	5.63	4.73	5.96
	$L_1(u)$ [%]	2.37	2.37	1.98	2.16	1.97	2.32
12.04	$L_0(u)$ [%]	6.59	6.59	6.35	6.55	6.43	6.59
	$L_1(u)$ [%]	3.56	3.55	2.01	3.27	2.44	3.52
16.33	$L_0(u)$ [%]	2.24	2.23	3.61	2.35	3.13	2.20
	$L_1(u)$ [%]	0.92	0.92	1.62	0.94	1.27	0.92
	$\overline{L_0(u)}$ [%]	7.84	7.80	7.85	7.80	7.59	7.74
	$\overline{L_1(u)}$ [%]	3.56	3.55	3.99	3.59	3.68	3.52

Table 6.11: L_0 and L_1 error norm of the velocity profiles at various locations of x/S for the FSVP method. The central scheme with artificial dissipation is given as a reference solution and the average error, denoted by $\overline{L_0(u)}$ and $\overline{L_1(u)}$, is provided at the bottom of the table.

		AD	no RS			Rusanov RS	
x/S		no CB	no CB	SCB	MCB	no CB	MCB
0.0	$L_0(u)$ [%]	6.32	6.17	-	-	-	-
	$L_1(u)$ [%]	1.71	1.69	-	-	-	-
2.55	$L_0(u)$ [%]	13.23	13.14	-	-	-	-
	$L_1(u)$ [%]	6.87	6.85	-	-	-	-
3.06	$L_0(u)$ [%]	11.88	11.81	-	-	-	-
	$L_1(u)$ [%]	5.11	5.09	-	-	-	-
3.57	$L_0(u)$ [%]	7.23	7.17	-	-	-	-
	$L_1(u)$ [%]	3.63	3.64	-	-	-	-
4.18	$L_0(u)$ [%]	6.44	6.41	-	-	-	-
	$L_1(u)$ [%]	2.31	2.31	-	-	-	-
4.80	$L_0(u)$ [%]	12.88	12.85	-	-	-	-
	$L_1(u)$ [%]	6.22	6.23	-	-	-	-
5.41	$L_0(u)$ [%]	8.24	8.21	-	-	-	-
	$L_1(u)$ [%]	3.99	3.99	-	-	-	-
6.12	$L_0(u)$ [%]	5.88	5.85	-	-	-	-
	$L_1(u)$ [%]	2.53	2.54	-	-	-	-
7.76	$L_0(u)$ [%]	6.12	6.06	-	-	-	-
	$L_1(u)$ [%]	2.41	2.38	-	-	-	-
12.04	$L_0(u)$ [%]	6.60	6.59	-	-	-	-
	$L_1(u)$ [%]	3.64	3.59	-	-	-	-
16.33	$L_0(u)$ [%]	2.35	2.28	-	-	-	-
	$L_1(u)$ [%]	0.92	0.92	-	-	-	-
	$\overline{L_0(u)}$ [%]	7.93	7.87	-	-	-	-
	$\overline{L_1(u)}$ [%]	3.58	3.57	-	-	-	-

method than for the AC method, with the FSAC-PP method sitting in-between. In-fact, the FSAC-VP method produces about four times less variations than the AC method. This again highlights the increased scheme invariance that the FSAC-VP method seems to have over its competitors.

Looking at Tables 6.12–6.15, we can see the same results obtained at the higher Reynolds number of Re=389. Carrying out the same analysis by looking at the average L_1 error norm, we can see that for the AC method, the best results are now obtained with the Rusanov-based approaches at 7.08% while the largest deviation is obtained with the MCB scheme, which produces differences that are 33.8% higher than the Rusanov-based results. Similarly to the discussion about the separation and reattachment points, we also see here the same flip in schemes, i.e. that for Re=100 the MCB produces the best results while at Re=389 giving the least agreement. For the FSAC-PP method in Table 6.13, we can see that the best result is obtained using Rusanov's RS at 6.67% while the least agreement (using the SCB scheme) deviates from that result by 22.3%. Turning to the FSAC-VP method in Table 6.14, we can see the best results are obtained with the Rusanov RS coupled to the MCB scheme at 6.91% while the scheme with the least agreement is again found to be the SCB scheme, deviating by 11.1% compared to the Rusanov RS with MCB scheme. For the FSVP method, the differences in its average L_1 error norms to the FSAC-VP method differ again by only 0.04 percent points. The same point can be made that here, the FSAC-VP method produces again the least amount of differences between the various numerical schemes. In-fact, the FSAC-PP method has twice as much difference among its schemes while the AC method produces still a difference of a factor of three higher than the FSAC-VP method. This increased scheme invariance for the present test case is actually a remarkable feature and it is worth expanding on it at this stage. It could be argued that all CB and RS-based approach use the same polynomial reconstruction scheme and that this is responsible for the level of accuracy. However, we see in the case of the FSAC-VP method, for both Reynolds numbers, that the central scheme with artificial dissipation produces equal, if not closer, agreement with the reference data. Thus, the argumentation fails to acknowledge the fact that the second-order accurate scheme can predict results equally or more accurate than the third-order scheme. Furthermore, although all approaches feature the same reconstruction scheme, the different characteristic methods and RS are based on different philosophies where differences in the outcome are inevitable. The prevailing metric to judge accuracy in the literature is usually limited to the order of the numerical scheme. This gives, however, only an indication by how much an error reduces when the mesh is refined and does not say anything about the error on the same mesh but for different schemes. Although higher-order schemes give generally better agreement than lower order schemes, it has been demonstrated to this point that not just the numerical reconstruction scheme but also the incompressible method and the underlying pressure treatment itself can have a significant effect on the overall results. Similarly, it is expected that CB schemes derived from single- and multi-directional aspects will have different features that will show some differences in the solution. RS are also expected to have an influence on the overall result but commonly no attempt is made to classify them into groups in which they can be compared based on their accuracy, for example. Rather, RS are classi-

Table 6.12: L_0 and L_1 error norm of the velocity profiles at various locations of x/S for the AC method. Results are given for different characteristic-based approaches including the Rusanov Riemann solver. The central scheme with artificial dissipation is given as a reference solution and the average error, denoted by $\overline{L_0(u)}$ and $\overline{L_1(u)}$, is provided at the bottom of the table.

		AD	no RS			Rusanov RS	
x/S		no CB	no CB	SCB	MCB	no CB	MCB
0.0	$L_0(u)$ [%]	9.57	12.24	7.66	12.66	8.12	8.12
	$L_1(u)$ [%]	3.83	4.81	4.08	4.97	4.46	4.46
2.55	$L_0(u)$ [%]	5.06	11.08	6.46	11.04	6.74	6.74
	$L_1(u)$ [%]	1.87	4.46	2.15	4.50	2.42	2.42
3.06	$L_0(u)$ [%]	9.17	11.53	9.34	11.84	9.76	9.76
	$L_1(u)$ [%]	3.59	3.37	4.66	3.48	4.79	4.79
3.57	$L_0(u)$ [%]	10.30	8.09	13.31	8.34	13.64	13.64
	$L_1(u)$ [%]	5.41	4.40	6.23	4.77	6.25	6.25
4.18	$L_0(u)$ [%]	14.49	13.37	16.04	14.46	15.85	15.85
	$L_1(u)$ [%]	7.14	7.08	7.84	7.66	7.72	7.72
4.80	$L_0(u)$ [%]	21.55	22.54	23.73	23.97	23.61	23.61
	$L_1(u)$ [%]	9.78	11.51	9.98	12.16	9.62	9.62
5.41	$L_0(u)$ [%]	24.66	30.20	24.26	31.36	23.31	23.31
	$L_1(u)$ [%]	11.96	14.96	11.99	15.67	11.58	11.58
6.12	$L_0(u)$ [%]	32.69	41.96	31.69	43.22	30.31	30.31
	$L_1(u)$ [%]	16.70	21.75	15.91	22.50	15.11	15.11
7.14	$L_0(u)$ [%]	29.31	39.80	27.39	40.63	25.74	25.74
	$L_1(u)$ [%]	17.17	23.33	15.70	23.76	14.67	14.67
7.76	$L_0(u)$ [%]	22.85	31.38	21.37	31.69	20.00	20.00
	$L_1(u)$ [%]	11.47	16.93	10.07	17.15	9.24	9.24
8.52	$L_0(u)$ [%]	16.58	23.40	15.34	23.65	14.17	14.17
	$L_1(u)$ [%]	8.84	13.14	7.64	13.22	6.90	6.90
9.18	$L_0(u)$ [%]	16.83	21.34	15.79	21.47	14.78	14.78
	$L_1(u)$ [%]	8.96	12.18	7.94	12.20	7.27	7.27

continued

x/S		AD	no RS			Rusanov RS	
		no CB	no CB	SCB	MCB	no CB	MCB
9.74	$L_0(u)$ [%]	6.62	8.78	7.60	8.87	7.80	7.80
	$L_1(u)$ [%]	2.28	3.89	2.60	3.88	3.03	3.03
11.07	$L_0(u)$ [%]	8.79	6.67	9.58	6.70	10.27	10.27
	$L_1(u)$ [%]	2.64	2.12	3.24	2.09	3.70	3.70
11.84	$L_0(u)$ [%]	5.38	4.38	7.05	4.22	7.86	7.86
	$L_1(u)$ [%]	2.47	1.70	3.12	1.68	3.53	3.53
13.57	$L_0(u)$ [%]	5.69	5.49	7.33	5.48	8.03	8.03
	$L_1(u)$ [%]	2.18	1.87	2.74	1.82	2.94	2.94
	$\overline{L_0(u)}$ [%]	14.97	18.27	15.25	18.73	15.00	15.00
	$\overline{L_1(u)}$ [%]	7.27	9.22	7.24	9.47	7.08	7.08

fied into their capabilities and restrictions, similarly like RANS turbulence models which are suitable for one kind of turbulent flows but not generally for all classes of flows. [2] In this study, the Rusanov's RS was purposefully chosen due to its ability to stabilise the flow using through dissipation [96], equally, the different RS discussed in Section 2.2 may be used for other various properties. For example, Roe's RS provides a linearised version of the convective fluxes which may be useful in highly non-linear flows in which the numerical scheme diverges otherwise. Or the HLL / HLLC RS may be used to increase the resolution of the convective flux and treat it in a non-linear fashion. Due to the work of Smith *et al.* [95], showing the complications arising when using the HLL / HLLC RS in conjunction with the FSAC-PP method — which would also be inherent by the FSAC-VP method — the Rusanov RS was found to be the best choice and further allows to use low-dissipative numerical schemes. It can be argued that the dissipation is then again introduced through the RS, however, as discussed in previous Sections as well, the RS is capable to introduce only the required amount of dissipation which depends on the local eigenvalues of the system. For the FSAC-PP and FSAC-VP method, it is seen that the Rusanov RS is providing constantly the best agreement with reference data while the AC method does not always obtain the most favourable results using a RS-based approach.

[2] This is not strictly speaking true. By providing the correct closure coefficients for a RANS turbulence model, any flow can be simulated in theory. Those closure coefficients may not, however, be easily obtained for all flows and thus calibration is usually limited to flows where the transport properties of the turbulence model are readily available. See Wilcox [167], especially Chapter 3 and 4 for more details on how to obtain the closure coefficients.

Table 6.13: L_0 and L_1 error norm of the velocity profiles at various locations of x/S for the FSACPP method. Results are given for different characteristic-based approaches including the Rusanov Riemann solver. The central scheme with artificial dissipation is given as a reference solution and the average error, denoted by $\overline{L_0(u)}$ and $\overline{L_1(u)}$, is provided at the bottom of the table.

		AD	no RS			Rusanov RS	
x/S		no CB	no CB	SCB	MCB	no CB	MCB
0.0	$L_0(u)$ [%]	9.25	9.11	8.11	9.02	9.46	9.48
	$L_1(u)$ [%]	2.89	3.03	4.70	3.01	2.58	2.58
2.55	$L_0(u)$ [%]	7.27	7.15	7.99	7.29	7.19	7.22
	$L_1(u)$ [%]	2.09	2.04	3.45	2.09	2.11	2.12
3.06	$L_0(u)$ [%]	9.49	9.22	12.90	9.39	9.38	9.45
	$L_1(u)$ [%]	4.59	4.53	6.17	4.61	4.35	4.38
3.57	$L_0(u)$ [%]	12.57	12.60	17.51	12.80	12.07	12.20
	$L_1(u)$ [%]	6.53	6.47	7.95	6.55	6.11	6.16
4.18	$L_0(u)$ [%]	15.90	15.88	19.50	15.93	14.56	14.76
	$L_1(u)$ [%]	8.22	8.15	9.77	8.17	7.59	7.70
4.80	$L_0(u)$ [%]	22.95	23.00	28.76	22.96	20.84	21.14
	$L_1(u)$ [%]	10.52	10.46	11.77	10.41	9.64	9.81
5.41	$L_0(u)$ [%]	24.29	24.30	28.21	24.09	22.43	22.80
	$L_1(u)$ [%]	12.54	12.48	13.98	12.40	11.48	11.70
6.12	$L_0(u)$ [%]	31.15	31.22	34.25	30.91	28.65	29.13
	$L_1(u)$ [%]	16.53	16.48	17.33	16.32	15.31	15.59
7.14	$L_0(u)$ [%]	27.68	27.55	28.05	26.95	25.73	26.28
	$L_1(u)$ [%]	16.01	16.01	15.94	15.69	14.80	15.09
7.76	$L_0(u)$ [%]	19.73	19.95	21.65	19.39	17.49	18.03
	$L_1(u)$ [%]	9.97	10.02	9.99	9.65	8.85	9.16
8.52	$L_0(u)$ [%]	13.33	13.50	14.82	13.21	12.15	12.75
	$L_1(u)$ [%]	7.25	7.31	7.14	7.06	6.46	6.77
9.18	$L_0(u)$ [%]	13.55	13.79	15.12	13.60	12.48	12.98
	$L_1(u)$ [%]	7.35	7.43	7.12	7.32	6.83	7.09

continued

		AD	no RS			Rusanov RS	
x/S		no CB	no CB	SCB	MCB	no CB	MCB
9.74	$L_0(u)$ [%]	5.34	5.36	8.66	5.36	5.81	5.56
	$L_1(u)$ [%]	2.54	2.52	3.71	2.53	2.54	2.50
11.07	$L_0(u)$ [%]	11.09	10.89	11.46	11.21	11.67	11.42
	$L_1(u)$ [%]	3.12	3.09	4.35	3.18	3.17	3.13
11.84	$L_0(u)$ [%]	5.57	5.52	8.69	5.52	5.66	5.43
	$L_1(u)$ [%]	3.07	3.05	4.09	3.03	3.08	2.91
13.57	$L_0(u)$ [%]	4.94	5.09	8.82	5.32	4.82	4.76
	$L_1(u)$ [%]	1.92	1.96	3.19	2.00	1.84	1.81
	$\overline{L_0(u)}$ [%]	14.63	14.63	17.16	14.56	13.77	13.96
	$\overline{L_1(u)}$ [%]	7.20	7.19	8.16	7.13	6.67	6.78

We simply show for this test case that the FSAC-VP method is able to reduce the difference among the different numerical schemes while the AC method shows more reliance on the numerical scheme in terms of accuracy. The same discussion was omitted in the previous Section on the lid driven cavity as the focus was on the effect of numerical dissipation at high Reynolds numbers. We purposefully looked at high Reynolds numbers to see the influence of the various CB schemes and RS in an environment where not enough numerical dissipation is provided by the numerical scheme, with the outcome that RS-based approaches always produced pressure oscillation free results with better agreement to reference data than non RS-based schemes. A quick inspection of Figures 6.2–6.5, especially for Reynolds numbers up to Re=1000, we can see qualitatively that the same observations can be made for the lid driven cavity in a dissipation equilibrium state. Here, the FSAC-PP method also produces the least discrepancies between the schemes while the AC method provides the most, with the FSAC-PP method in-between.

This concludes the current Section for the backward facing step geometry. We first investigated the troublesome geometry based on the experiments of Denham and Patrick [160] to compare the MCB scheme developed in this work with that of Zamzamian and Razavi [53]. We found that the same conclusion drawn in their study could not be repeated in this work and that incorrect boundary conditions are likely the cause for the differences observed. Using the experimental data of Armaly *et al.* [161], it was shown that differences in the predicted velocity profiles and reattachment points were generally low for all schemes and methods. Differences were observed in the prediction of secondary vortical structures in the form of a second

Table 6.14: L_0 and L_1 error norm of the velocity profiles at various locations of x/S for the FSACVP method. Results are given for different characteristic-based approaches including the Rusanov Riemann solver. The central scheme with artificial dissipation is given as a reference solution and the average error, denoted by $\overline{L_0(u)}$ and $\overline{L_1(u)}$, is provided at the bottom of the table.

		AD	no RS			Rusanov RS	
x/S		no CB	no CB	SCB	MCB	no CB	MCB
0.0	$L_0(u)$ [%]	8.80	8.71	7.73	9.11	8.74	9.53
	$L_1(u)$ [%]	3.25	3.35	3.73	3.01	3.21	2.56
2.55	$L_0(u)$ [%]	6.80	6.68	7.95	7.62	7.68	7.46
	$L_1(u)$ [%]	1.96	1.93	2.74	2.23	2.31	2.22
3.06	$L_0(u)$ [%]	8.57	8.53	11.17	9.94	9.61	10.00
	$L_1(u)$ [%]	4.43	4.39	5.54	4.84	4.84	4.61
3.57	$L_0(u)$ [%]	12.45	12.38	15.56	13.37	13.44	12.87
	$L_1(u)$ [%]	6.27	6.19	7.44	6.85	6.73	6.46
4.18	$L_0(u)$ [%]	15.62	15.52	18.11	16.46	16.16	15.29
	$L_1(u)$ [%]	7.84	7.75	9.24	8.53	8.30	8.07
4.80	$L_0(u)$ [%]	22.71	22.61	26.34	23.63	23.34	21.79
	$L_1(u)$ [%]	10.15	10.05	11.37	10.76	10.39	10.19
5.41	$L_0(u)$ [%]	24.17	24.07	25.69	24.40	23.58	23.23
	$L_1(u)$ [%]	12.16	12.06	13.47	12.74	12.33	12.08
6.12	$L_0(u)$ [%]	31.40	31.33	32.59	31.08	29.96	29.51
	$L_1(u)$ [%]	16.32	16.21	17.00	16.56	15.89	15.92
7.14	$L_0(u)$ [%]	27.28	27.10	26.68	27.03	25.68	26.55
	$L_1(u)$ [%]	16.10	16.06	15.67	15.60	14.82	15.13
7.76	$L_0(u)$ [%]	20.58	20.70	19.60	18.57	17.60	17.36
	$L_1(u)$ [%]	10.21	10.23	9.34	9.27	8.58	8.88
8.52	$L_0(u)$ [%]	14.42	14.60	12.79	12.11	11.25	12.16
	$L_1(u)$ [%]	7.64	7.68	6.55	6.51	6.03	6.28
9.18	$L_0(u)$ [%]	14.84	15.05	12.94	12.30	11.65	12.25
	$L_1(u)$ [%]	7.90	7.98	6.54	6.66	6.22	6.50

continued

		AD	no RS			Rusanov RS	
x/S		no CB	no CB	SCB	MCB	no CB	MCB
9.74	$L_0(u)$ [%]	5.84	5.99	7.11	6.61	7.28	6.68
	$L_1(u)$ [%]	2.34	2.31	3.45	2.85	3.21	2.80
11.07	$L_0(u)$ [%]	10.40	10.19	12.75	12.61	13.06	12.80
	$L_1(u)$ [%]	2.99	2.96	4.15	3.56	3.88	3.44
11.84	$L_0(u)$ [%]	5.84	5.84	7.74	6.47	6.86	6.53
	$L_1(u)$ [%]	2.98	2.93	4.06	3.61	3.87	3.47
13.57	$L_0(u)$ [%]	5.73	5.79	7.12	5.47	6.01	4.87
	$L_1(u)$ [%]	2.12	2.15	2.60	2.09	2.28	1.91
	$\overline{L_0(u)}$ [%]	14.72	14.69	15.74	14.80	14.49	14.31
	$\overline{L_1(u)}$ [%]	7.17	7.14	7.68	7.23	7.06	6.91

recirculation area at the top wall, where the AC method consistently predicted the presence of such a region. The FSAC-PP method did not show any secondary recirculation area while the FSAC-VP and FSVP method showed a mix, where CB and RS-based approaches did not predict the second vortex while the non CB and central scheme both did. The experimental study did suggest that a secondary vortex may be formed but only at a slightly higher Reynolds number and thus it can be seen that the FSAC-VP method benefits from the inclusion of CB or RS-based schemes while the FSAC-PP method, possibly due to its smoothing properties in the Poisson solver, contains the innate ability to smooth and reduce any pressure oscillations that may trigger vortical flows. Furthermore, it was discussed that the FSAC-VP method is able to reduce the differences between the various numerical approaches compared the AC and FSAC-PP method. To this point, no explanation for this behaviour was given but since the only difference between the FSAC-PP and FSAC-VP method is its parabolic pressure transport equation — which is derived from the set of equations governing the FSAC-PP method — it may be argued that the representation of the pressure has an important role to play.

In the next Section, the backward facing step geometry is extended to the sudden expansion test case, in essence a mirrored geometry of the one considered here, which furthermore allows the investigation of bifurcation. This phenomenon is crucially depending on the pressure distribution of the flow and may give further insight on how it is affected by the parabolic transport equation.

Table 6.15: L_0 and L_1 error norm of the velocity profiles at various locations of x/S for the FSVP method. Results are given for different characteristic-based approaches including the Rusanov Riemann solver. The central scheme with artificial dissipation is given as a reference solution and the average error, denoted by $\overline{L_0(u)}$ and $\overline{L_1(u)}$, is provided at the bottom of the table.

		AD	no RS			Rusanov RS	
x/S		no CB	no CB	SCB	MCB	no CB	MCB
0.0	$L_0(u)$ [%]	9.67	9.54	-	-	-	-
	$L_1(u)$ [%]	2.69	2.77	-	-	-	-
2.55	$L_0(u)$ [%]	7.32	7.16	-	-	-	-
	$L_1(u)$ [%]	2.18	2.10	-	-	-	-
3.06	$L_0(u)$ [%]	9.86	9.54	-	-	-	-
	$L_1(u)$ [%]	4.61	4.53	-	-	-	-
3.57	$L_0(u)$ [%]	12.83	12.49	-	-	-	-
	$L_1(u)$ [%]	6.51	6.42	-	-	-	-
4.18	$L_0(u)$ [%]	15.63	15.55	-	-	-	-
	$L_1(u)$ [%]	8.22	8.11	-	-	-	-
4.80	$L_0(u)$ [%]	22.33	22.28	-	-	-	-
	$L_1(u)$ [%]	10.47	10.37	-	-	-	-
5.41	$L_0(u)$ [%]	24.05	24.01	-	-	-	-
	$L_1(u)$ [%]	12.44	12.33	-	-	-	-
6.12	$L_0(u)$ [%]	30.77	30.81	-	-	-	-
	$L_1(u)$ [%]	16.51	16.43	-	-	-	-
7.14	$L_0(u)$ [%]	27.60	27.47	-	-	-	-
	$L_1(u)$ [%]	15.85	15.85	-	-	-	-
7.76	$L_0(u)$ [%]	18.63	18.89	-	-	-	-
	$L_1(u)$ [%]	9.57	9.65	-	-	-	-
8.52	$L_0(u)$ [%]	12.97	12.95	-	-	-	-
	$L_1(u)$ [%]	6.82	6.92	-	-	-	-
9.18	$L_0(u)$ [%]	12.81	12.82	-	-	-	-
	$L_1(u)$ [%]	6.92	7.03	-	-	-	-

continued

		AD	no RS			Rusanov RS	
x/S		no CB	no CB	SCB	MCB	no CB	MCB
9.74	$L_0(u)$ [%]	6.03	5.78	-	-	-	-
	$L_1(u)$ [%]	2.59	2.52	-	-	-	-
11.07	$L_0(u)$ [%]	12.35	12.09	-	-	-	-
	$L_1(u)$ [%]	3.31	3.26	-	-	-	-
11.84	$L_0(u)$ [%]	6.25	6.06	-	-	-	-
	$L_1(u)$ [%]	3.43	3.39	-	-	-	-
13.57	$L_0(u)$ [%]	5.18	5.26	-	-	-	-
	$L_1(u)$ [%]	1.90	1.93	-	-	-	-
	$\overline{L_0(u)}$ [%]	14.64	14.54	-	-	-	-
	$\overline{L_1(u)}$ [%]	7.13	7.10	-	-	-	-

6.3 Laminar Bifurcation Phenomena in Suddenly Expanding Channels

As highlighted in the closing comments in the previous Section, the channel geometry which contains a sudden expansion into a larger channel is geometrical similar to the backward facing step problem but contains additional physical flow features that are absent in the previous tested geometry. Specifically, in this case, for some critical Reynolds number, the Navier–Stokes equations bifurcate into a lower energy state at which a non-symmetrical flow pattern is found. This change occurs abruptly and thus presents a challenging case to be predicted correctly. So far, we have seen in the previous two examples that the MCB scheme is capable to predict vortical flows to a better degree than other schemes but can prematurely create vortices which may only exist at higher Reynolds numbers. The latter was especially observed with the AC method while the FSAC-PP, FSAC-VP and FSVP method did not show a similar behaviour for the MCB scheme. On the contrary, the MCB scheme combined with the Rusanov RS showed in most cases the best result or at least results that matched the best scheme to a close degree. The additional numerical dissipation in the Rusanov RS and central scheme may also start to play an important role in predicting the bifurcation phenomena as it occurs at around Re=54, which is still in the laminar regime. Any added numerical dissipation may damp the flow so as to delay the onset of bifurcation. Furthermore — and this is also true for the backward facing step — due to the Cartesian nature of the solver, the mesh cannot be locally refined near the wall. Thus, the velocity gradient near the wall cannot be captured

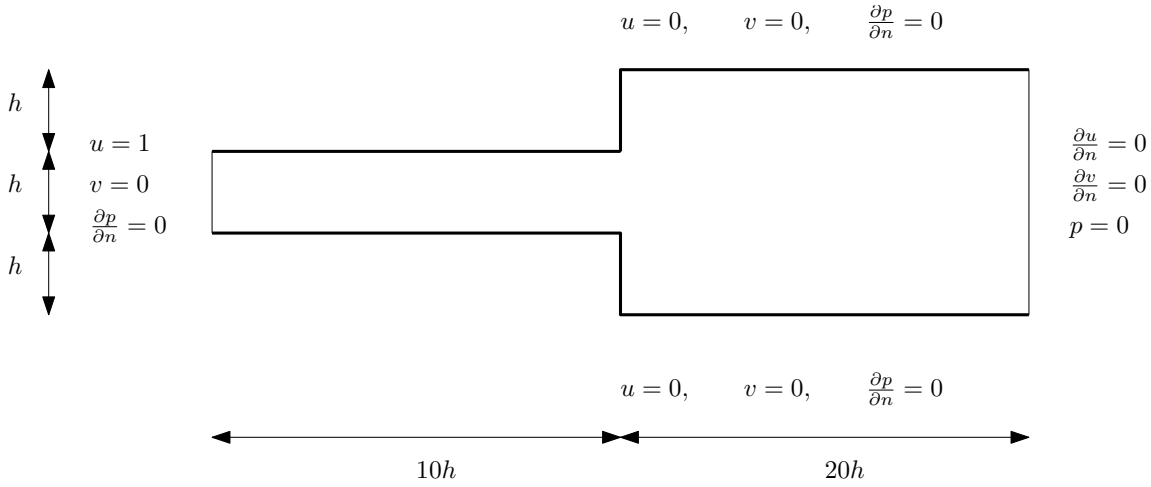

Figure 6.28: Geometry for the sudden expansion geometry with its corresponding boundary conditions and dimensions.

as accurately as on a refined mesh which will have an impact on the reattachment point downstream. Since the sudden expansion features a symmetrical domain, two of those recirculation areas are present and the vortical structures ultimately have an influence on the bifurcation itself. A slight change in reattachment length may trigger the bifurcation incorrectly. Therefore, the case is examined in more detail the possible advantages and disadvantages of each numerical scheme in combination with different incompressible flow methods.

The geometry, along with its boundary conditions and dimensions, is given in Figure 6.28. Here the step height is defined similarly as in the backward facing step case and is valid for both the lower and upper step. Furthermore, the height of the smaller entrance channel is of the same height so that the expansion ration becomes 1:3. Experimental data for the present case is provided by Fearn *et al.* [168] while Oliveira [169] provides a numerical study on Newtonian and non-Newtonian fluids for a sudden expansion geometry of the same geometry. In that study, numerical data for the reattachment point is given so that a direct comparison can be made. Both of these studies focus on low Reynolds number flows as the bifurcation occurs in this regime. Higher Reynolds number studies were conducted by Durst *et al.* [170] using experiments. Akselvoll and Moin [171] used large-eddy simulations for their annular sudden expansion while Friedrich *et al.* [172] provided data for a direct numerical simulation. Hawa and Rusak [173] further presented a bifurcation analysis on their two-dimensional flow in which a perturbation was imposed and its evolution tracked for symmetrical and non-symmetrical flow fields. Further analysis on the bifurcation in general applied to the sudden expansion geometry can be found in Sobey and Drazin [174].

In order to establish grid independent results, a grid convergence study has been conducted and is shown in Table 6.16. Here, the GCI was based on the reattachment length for the upper and lower wall, denoted by X_{r1} and X_{r2}. The results are still changing up to the the finest mesh containing 89600 elements which is likely due to

Table 6.16: Grid dependency study for the FSAC-PP method at a Reynolds number of Re=30.

Cells	X_{r1}	X_{r2}	GCI(r1)	GCI(r2)	time [h]	iterations
1 400	2.78324	2.83458	-	-	0.003	11 534
5 600	2.85779	2.87495	0.1223	0.0658	0.019	22 408
22 400	2.9544	2.96133	0.1533	0.1367	0.22	58 896
89 600	3.03597	3.03854	0.1259	0.1191	3.19	177 801
Richardson Extrapolation	3.0414	3.0437	-	-	-	-

the Cartesian mesh near the wall, but the computational time also increases rather steeply. These results were obtained using the FSAC-PP method which has generally been proving to be the fastest of the four methods tested in this work. In-fact, simulations performed on the finest grid using the AC method at low Reynolds numbers required approximately six days to converge. Since all simulations are carried out at relatively low Reynolds numbers and a total of 420 simulations need to be performed, the more economical grid at 22400 elements was chosen. The number of simulations is rather high since near the bifurcating Reynolds number, several simulations with only slightly increased Reynolds numbers were performed to predict the onset of bifurcation accurately. Due to the critical Reynolds number being located at Re=54, the range of Reynolds numbers simulated for this example were between $10 < Re < 100$. The corresponding GCI value is 13.67% which needs to be kept in mind when comparing the results to the available reference data. Alternatively, we can also compare the results of Oliveira [169] who provided grid independent reattachment points and find that the prediction on the 22400 mesh differ by 4.0% and 3.85% to the predicted value of $x/h = 3.080$.

Figures 6.29–6.32 show the velocity profiles for each incompressible method using different numerical schemes at various downstream locations x/h of the sudden expansion geometry. Similar observations as in the previous Section can be made for the present velocity profiles. In Figure 6.29, the velocity profiles for the AC method are shown. The method shows a high reliance on the numerical scheme that is used and produces either over- or under-predicted values compared to the experimental data of Fearn *et al.* [168]. The non CB and MCB scheme both over-predict the flow while the two Rusanov-based approaches, the SCB and central scheme with artificial dissipation all under-predict the correct velocity profiles. It is possible that the inherent dissipation in these schemes is responsible to amplify the inertia of the flow which slows the convective force. On the other hand, the non CB and MCB scheme by themselves, both relying on the polynomial reconstruction where the numerical dissipation scales with $\mathcal{O}(\Delta x)^3$ from their Taylor-series truncation, show little inherent resistance and as a result over-predict the velocity at the centre of the channel. Due to conservation of mass and momentum, it follows that the velocities inside the recirculation area must be over-predicted as well to slow the flow sufficiently.

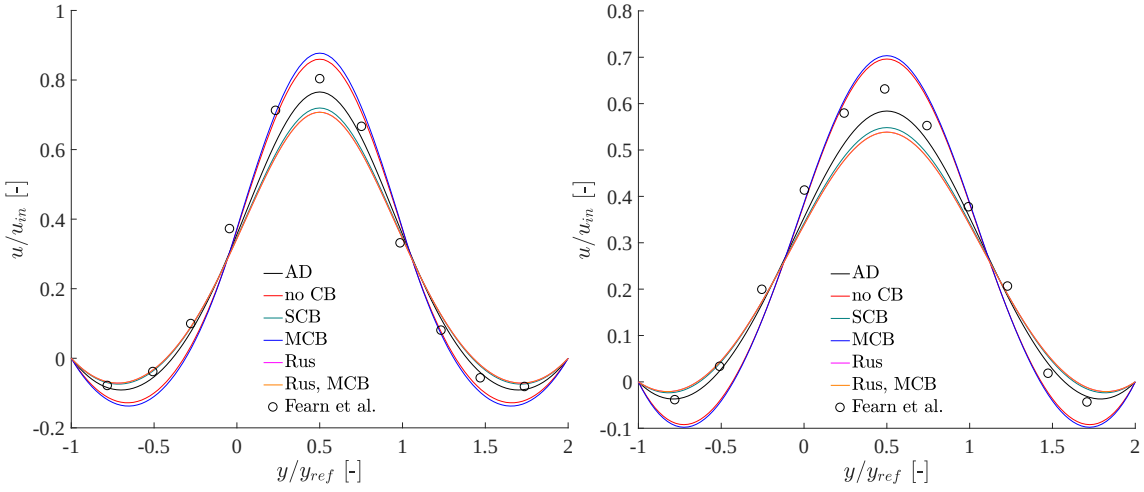

(a) $x/h = 1.25$ (b) $x/h = 2.5$

(c) $x/h = 5.0$ (d) $x/h = 10.0$

Figure 6.29: Velocity profiles at Re=34.6 for various locations of x/h downstream of the sudden expansion. The result are shown for the AC method.

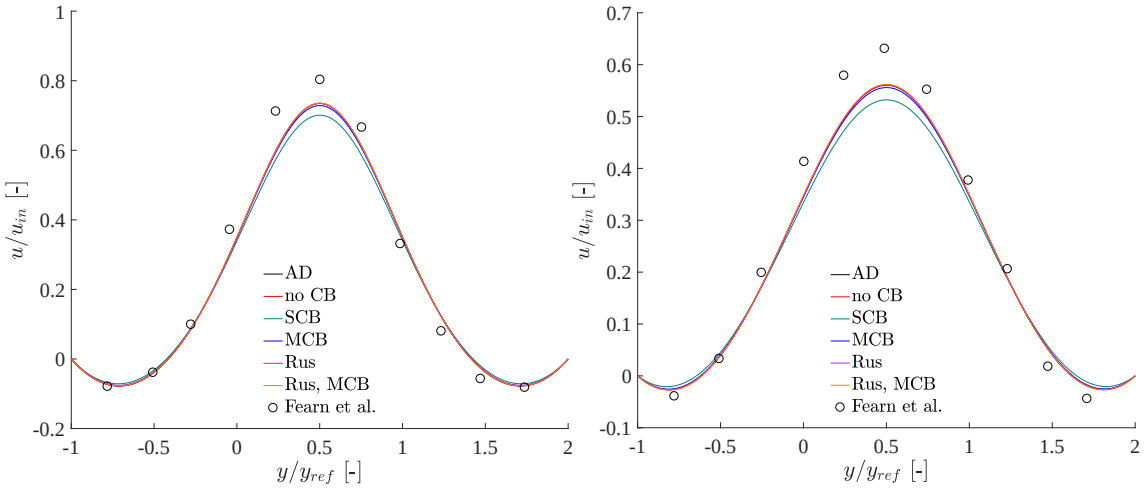

(a) $x/h = 1.25$ (b) $x/h = 2.5$

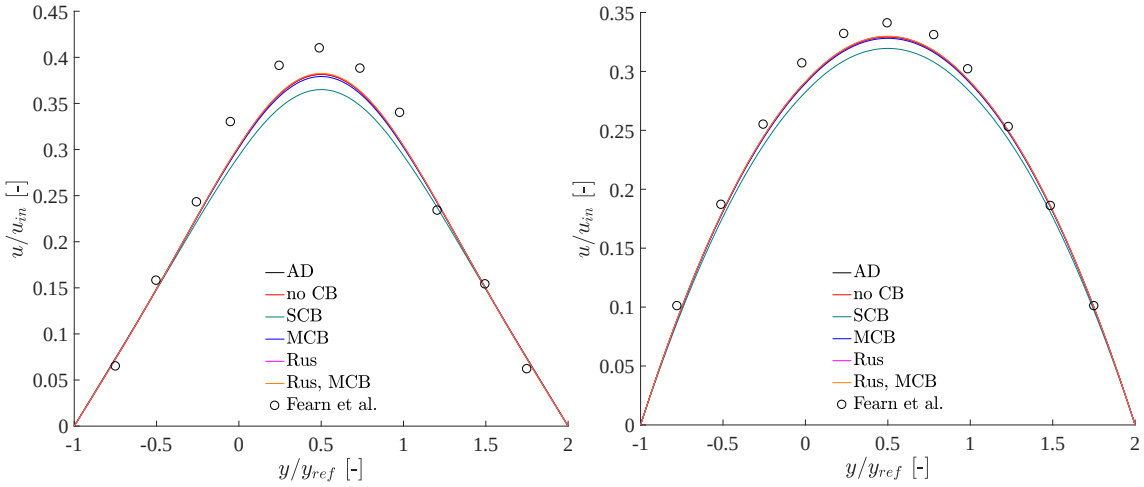

(c) $x/h = 5.0$ (d) $x/h = 10.0$

Figure 6.30: Velocity profiles at Re=34.6 for various locations of x/h downstream of the sudden expansion. The result are shown for the FSAC-PP method.

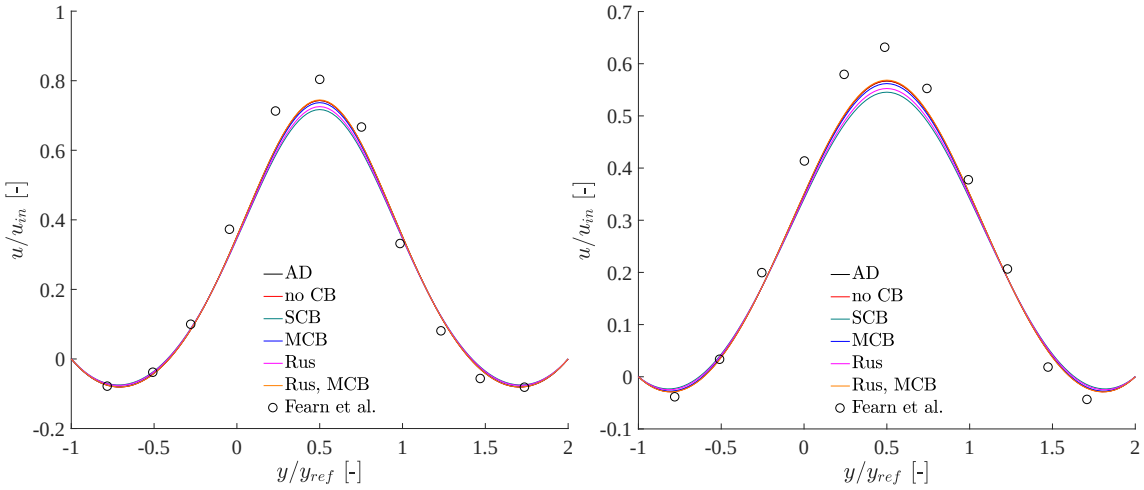

(a) $x/h = 1.25$

(b) $x/h = 2.5$

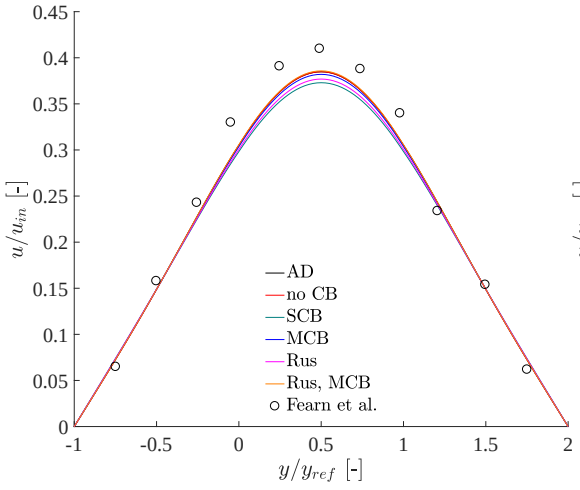

(c) $x/h = 5.0$

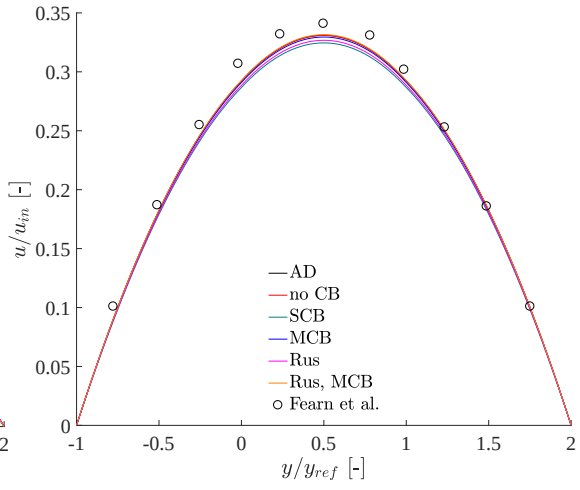

(d) $x/h = 10.0$

Figure 6.31: Velocity profiles at Re=34.6 for various locations of x/h downstream of the sudden expansion. The result are shown for the FSAC-VP method.

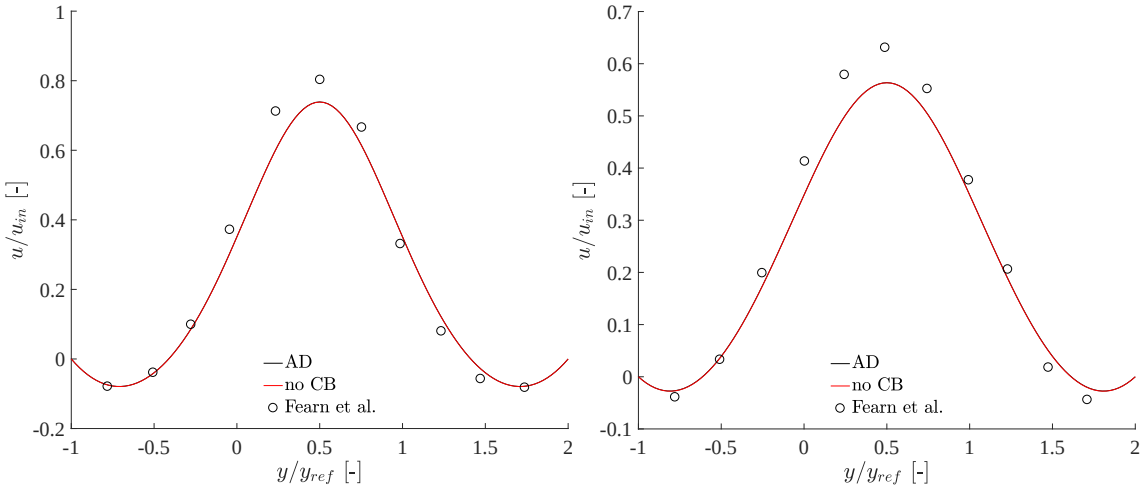

(a) $x/h = 1.25$

(b) $x/h = 2.5$

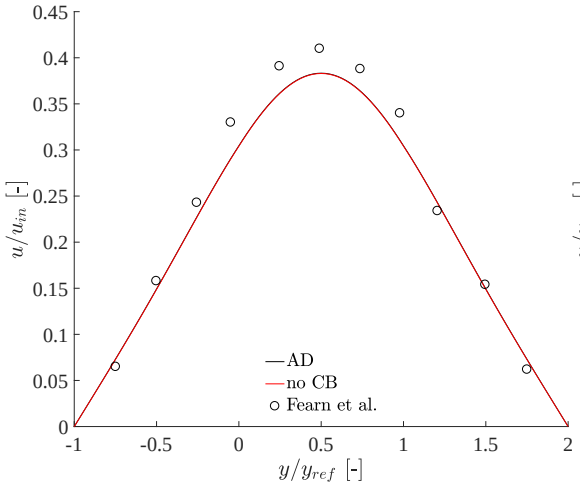

(c) $x/h = 5.0$

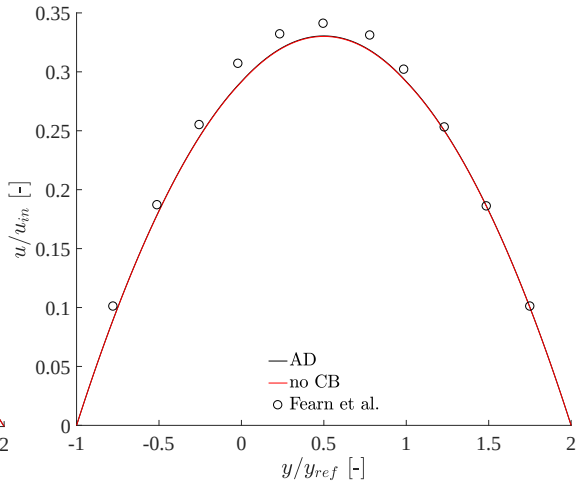

(d) $x/h = 10.0$

Figure 6.32: Velocity profiles at Re=34.6 for various locations of x/h downstream of the sudden expansion. The result are shown for the FSVP method.

Otherwise, a positive mass flux balance would be generated at the outflow boundary which would violate the continuity equation. However, since at a converged state we require that $\nabla \cdot \mathbf{u} = 0$ holds for each computational cell, the continuity equation, and therefore conservation of mass, is automatically satisfied. Thus, the lack of numerical dissipation within the polynomial scheme is responsible for an increased kinetic energy inside the top and bottom recirculation vortices for which we would expect an over-prediction in reattachment point. This will be, indeed, later shown through quantitative data. An increased amount of kinetic energy within those vortices also means that the bifurcation can be triggered before the critical Reynolds number and thus produce a premature anti-symmetrical state. Since the Reynolds number is nothing else than a measure of convective to diffusive inertia forces, where the kinetic energy influences the convective force, it is expected that a change in the structure of the recirculation vortex will have an influence on the bifurcation itself. In Figure 6.30, the same situation is depicted for the FSAC-PP method. Here, all numerical schemes are closely matched with the exception of the SCB scheme again, which shows a slightly less accurate agreement with the experimental data. The agreement with the reference data becomes better the further downstream the flow is which is also true for the AC method. The SCB scheme, however, shows the same under-prediction at all locations compared to the rest of the schemes. For the FSAC-VP method in Figure 6.31, a similar picture emerges where all schemes are closely matched. It is the SCB scheme which shows again the least agreement, although not by much, with the reference data. It is interesting to note there that the Rusanov scheme in conjunction with the MCB scheme outperforms both the Rusanov RS and MCB scheme if they are used separately. At a further downstream location, the flow starts to match the reference data again more closely. The same observations can be made for the FSVP method which shows similar results as the FSAC-VP method when the non CB and central scheme are investigated.

Figures 6.33–6.36 show the same velocity profiles at a Reynolds number of Re=80, which is above the critical Reynolds number of Re=54. For this state, it is expected that the bifurcation has already occurred. In Figure 6.33, the velocity profiles for the AC method are shown. An interesting pattern is observed for the various downstream locations x/h. Both Rusanov RS approaches and the SCB scheme fail to predict the bifurcation while the non CB and MCB scheme, as well as the central scheme, do predict a symmetry breaking of the Navier–Stokes equations. Although it is hypothesised that the excessive numerical dissipation inherent in the central scheme with artificial dissipation and the RS-based approaches could damp the flow so as to prevent the onset of bifurcation, it is shown that only the RS-based approaches prevent the bifurcation while the central scheme still predicts the bifurcation. A possible explanation is found by re-examining Figure 6.29 where it can be seen that the central scheme is matching the reference data closest, especially close to the expansion itself. At $x/h = 1.25$ and $x/h = 2.5$, the peak velocity at the centre is slightly under-predicted but the velocity in the recirculation bubble is matched to a close degree. While the RS-based approaches also provide a good agreement in the recirculation vortices, they still show less accurate agreement with the reference data close to the centreline. Thus, the central scheme with artificial

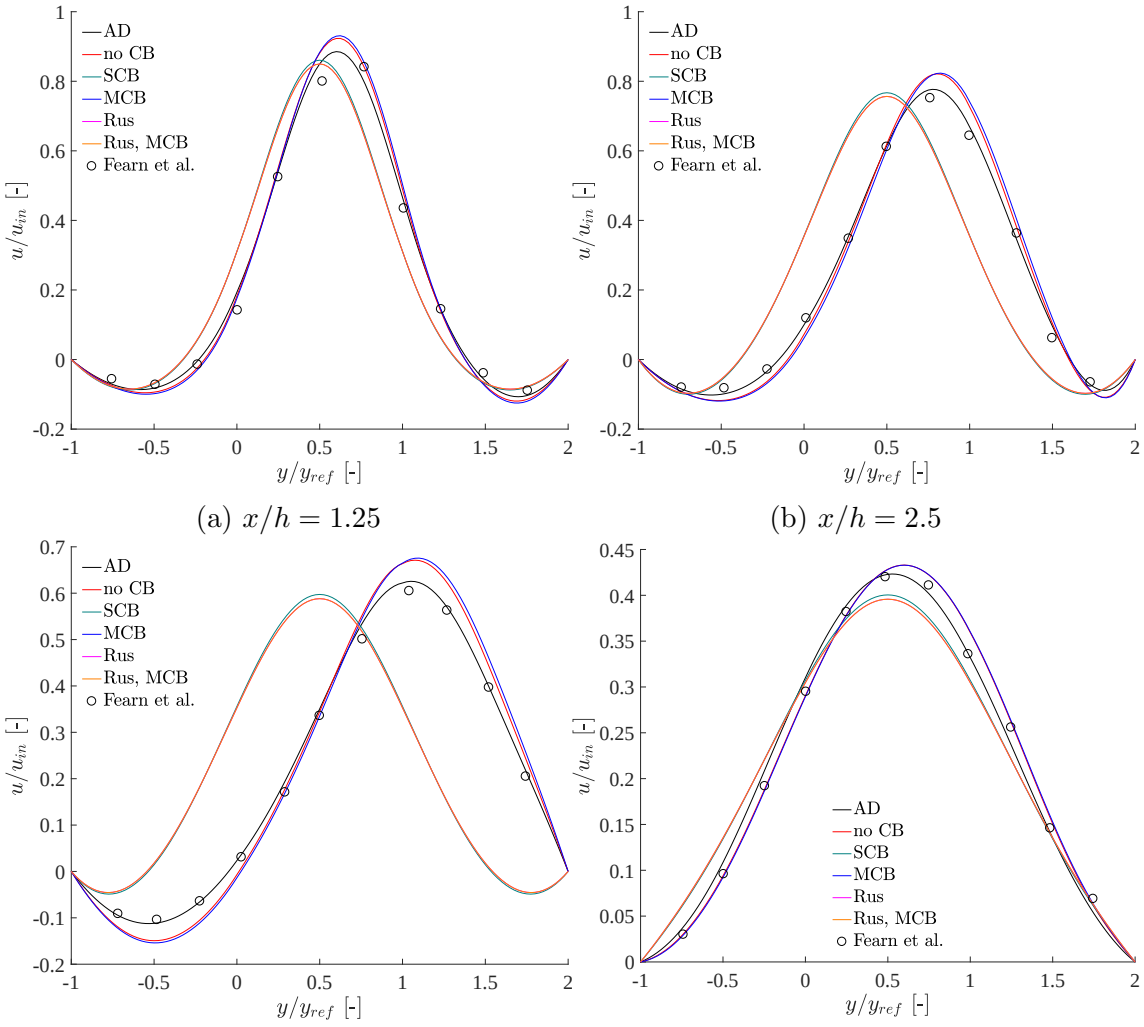

(a) $x/h = 1.25$ (b) $x/h = 2.5$

(c) $x/h = 5.0$ (d) $x/h = 10.0$

Figure 6.33: Velocity profiles at Re=80 for various locations of x/h downstream of the sudden expansion. The result are shown for the AC method.

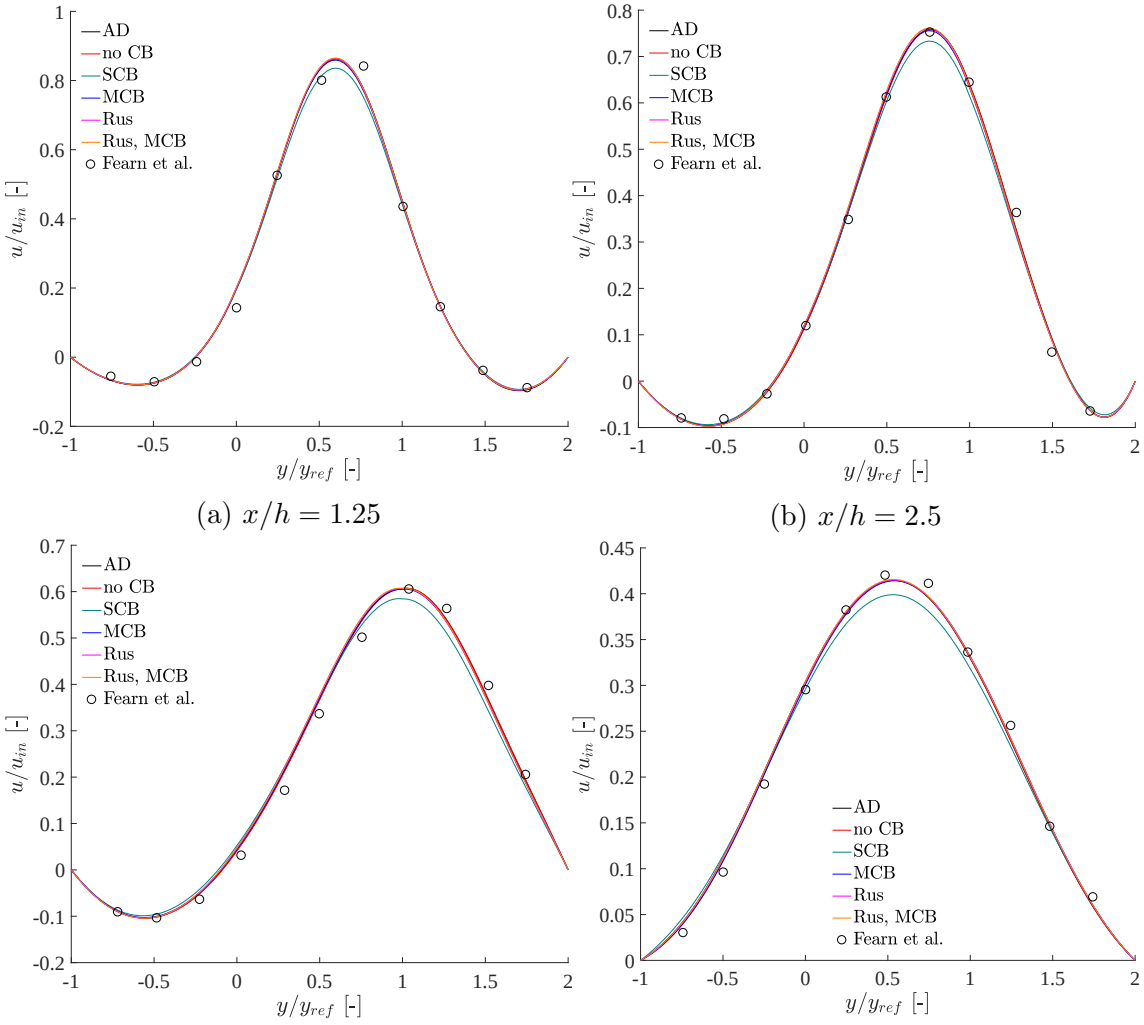

(a) $x/h = 1.25$

(b) $x/h = 2.5$

(c) $x/h = 5.0$

(d) $x/h = 10.0$

Figure 6.34: Velocity profiles at Re=80 for various locations of x/h downstream of the sudden expansion. The result are shown for the FSAC-PP method.

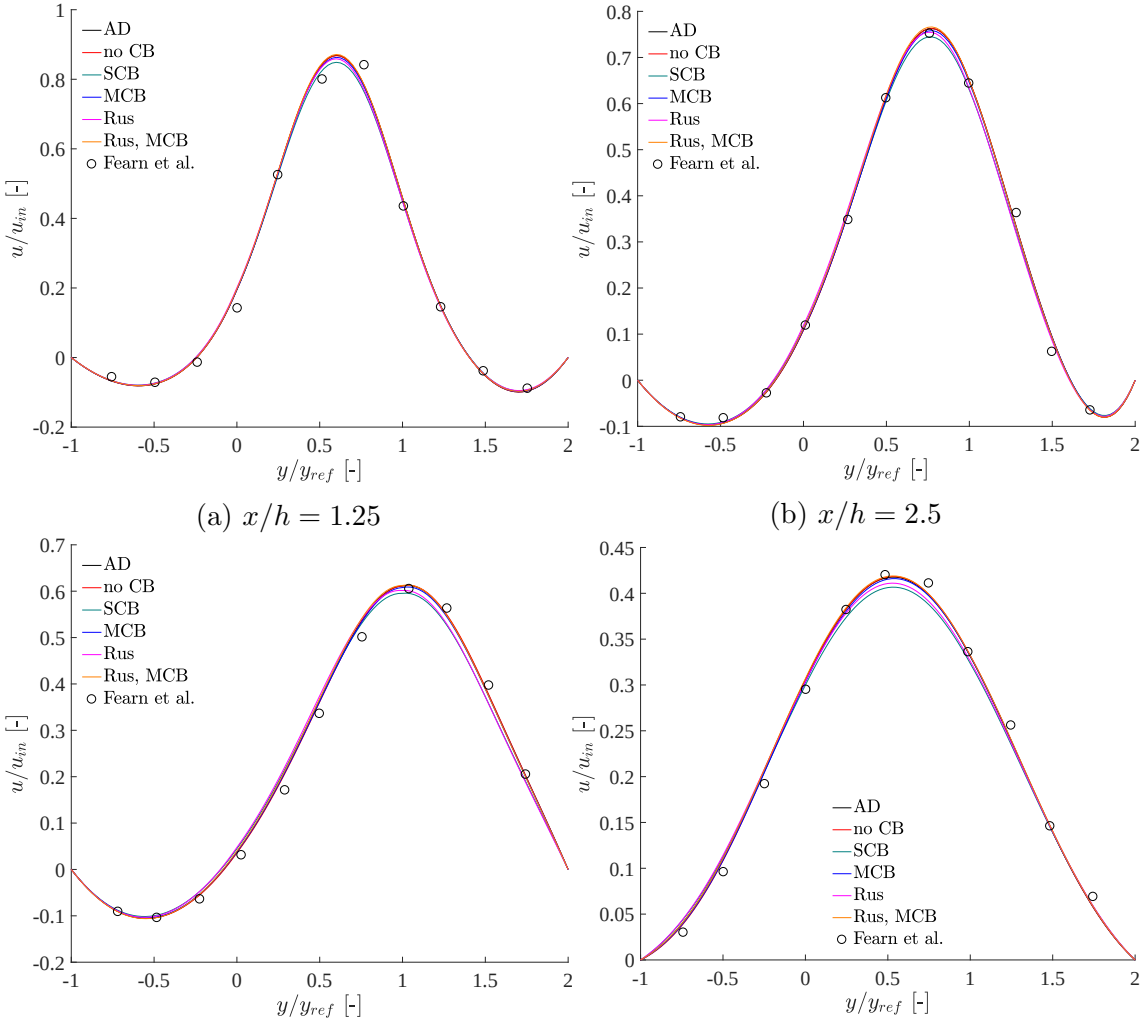

(a) $x/h = 1.25$

(b) $x/h = 2.5$

(c) $x/h = 5.0$

(d) $x/h = 10.0$

Figure 6.35: Velocity profiles at Re=80 for various locations of x/h downstream of the sudden expansion. The result are shown for the FSAC-VP method.

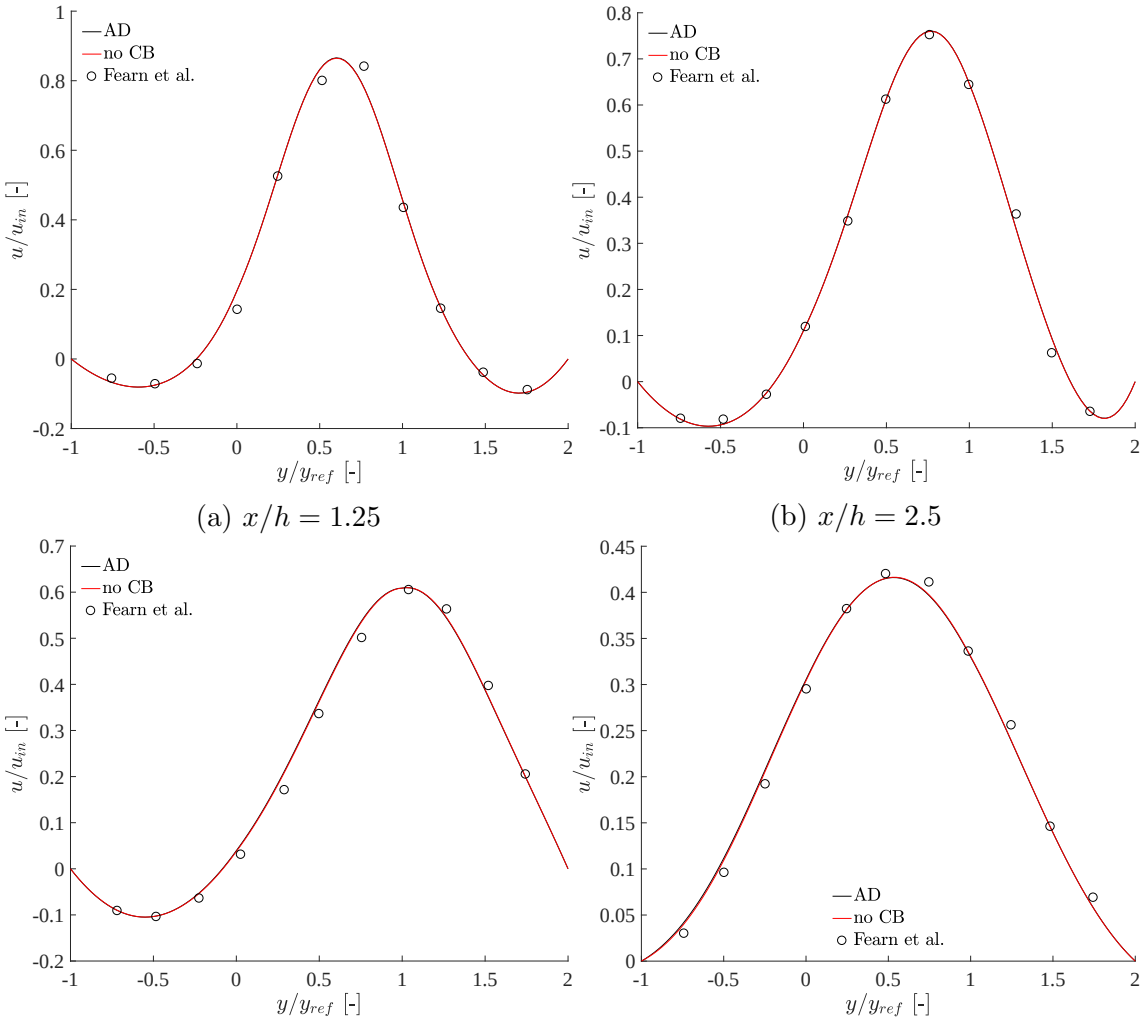

(a) $x/h = 1.25$ (b) $x/h = 2.5$

(c) $x/h = 5.0$ (d) $x/h = 10.0$

Figure 6.36: Velocity profiles at Re=80 for various locations of x/h downstream of the sudden expansion. The result are shown for the FSVP method.

dissipation may just contain enough numerical dissipation which does not prohibit the bifurcated state to occur, while the RS-based approach may contain too much inherent numerical dissipation to adequately capture the bifurcation at all. The FSAC-PP method in Figure 6.34 does not show the same trend and for all velocity profiles, the bifurcation is predicted correctly. The same observations as for the lower Reynolds number can be made where it is only the SCB scheme which shows noticeable differences to the other numerical scheme, which are all closely matched. The same is true for the FSAC-VP method in Figure 6.35, where all but the SCB scheme and Rusanov RS show closely matched profiles. In turn, the same is true for the velocity profiles of the FSVP method in Figure 6.36.

Figure 6.37 further shows the contour plots of velocity for each incompressible method at a Reynolds number of Re=34.6 using the non CB scheme. It can be seen that the recirculation area for the AC method is visibly larger than those obtained using any of the other methods. For the FSAC-PP, FSAC-VP and FSVP method, no noticeable difference in recirculation size can be detected. In Figures 6.38–6.41, the contour plots of velocity at Re=80 are shown for each method and each numerical scheme. It is worth to investigate the bifurcation for each method and scheme combination separately to highlight the random bifurcation phenomenon here. By inspecting these Figures, it becomes apparent that there is no clear trend in which direction the bifurcation will occur, i.e. if the velocity will experience an upward or downward movement off the centreline. This may be different if a gravitational field is considered and included in the governing equations as an external force field but for the present case, no such force term is included. For the AC method we have already discussed that the RS-based approaches, i.e. the two Rusanov RS and the SCB scheme, produce a symmetric velocity field. The central and non CB scheme both generate an upward velocity field while the one predicted using the MCB scheme experiences a downward movement. The FSAC-PP method, on the other hand, is the only method that consistently produces and upward motion of the velocity for all numerical schemes. Using the FSAC-VP method, only the central scheme and Rusanov RS with MCB scheme show an upward motion. Interestingly, both the Rusanov and MCB scheme by themselves produce a downward orientated velocity field while their combination produces and upward moving velocity field. The FSVP method, again, shows a consistent pattern to that of the FSAC-VP method. The reason for this seemingly random behaviour is still not fully settled in the literature. It was found in experimental studies that "the larger separation might attach to either side of the channel without preference" [168, p. 602] which further complicates the situation. No attempt to explain the matter at hand is made and simply note that the numerical scheme as well as the incompressible method that is used play a dominant role in the success of predicting the bifurcation correctly.

The computed error L_0 and L_1 error norms for each velocity profile and numerical scheme for both Reynolds numbers of Re=34.6 and Re=80 are given in Tables 6.17–6.20 for all methods. Comparing all errors against each other may be cumbersome and the bigger picture may be lost. Instead, the average error norms are computed for both norms and summarised at the end of each section of the Table and denoted

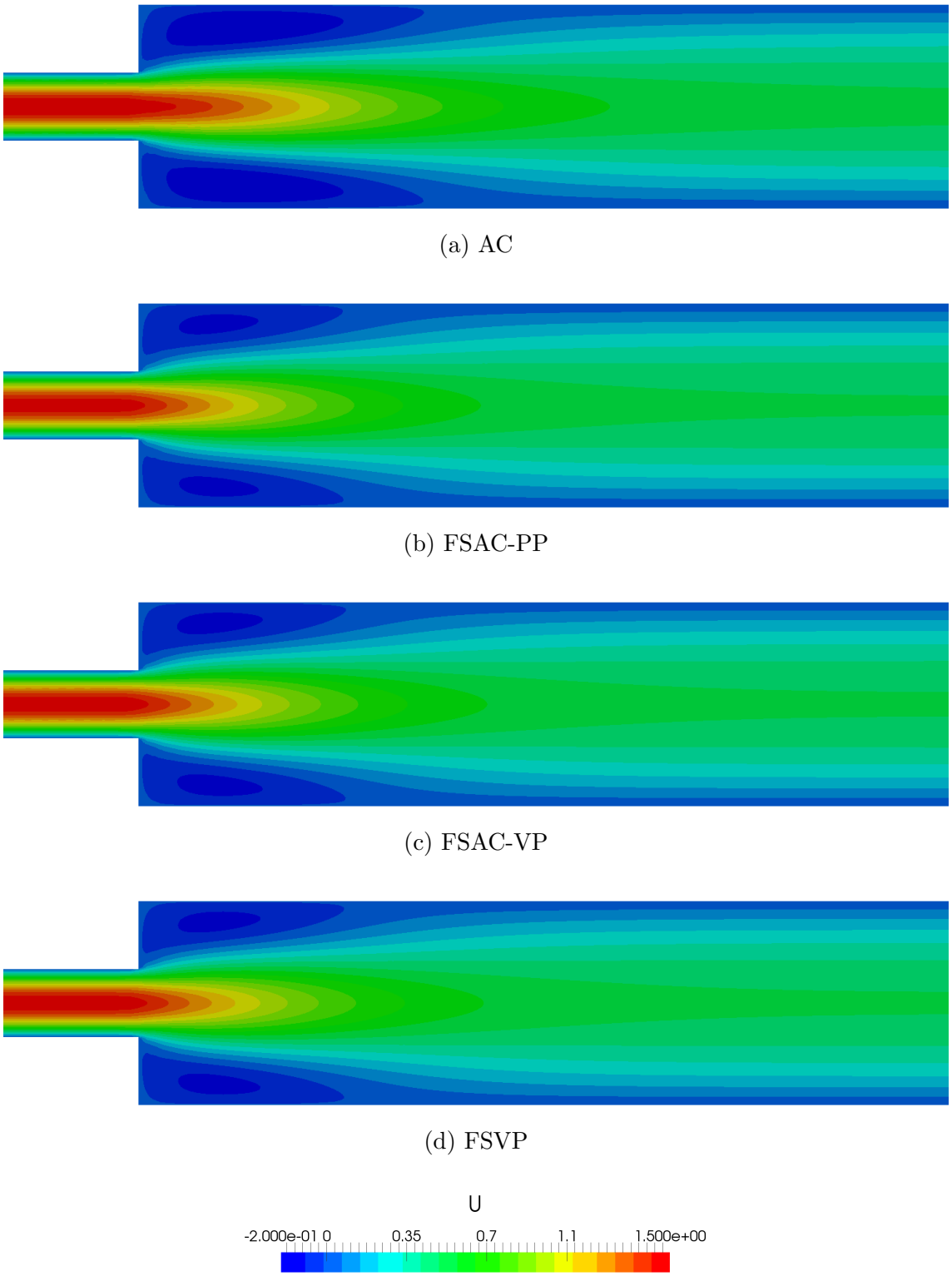

(a) AC

(b) FSAC-PP

(c) FSAC-VP

(d) FSVP

Figure 6.37: Contour plots of the velocity profile for different incompressible methods at Re=34.6 using a non CB scheme.

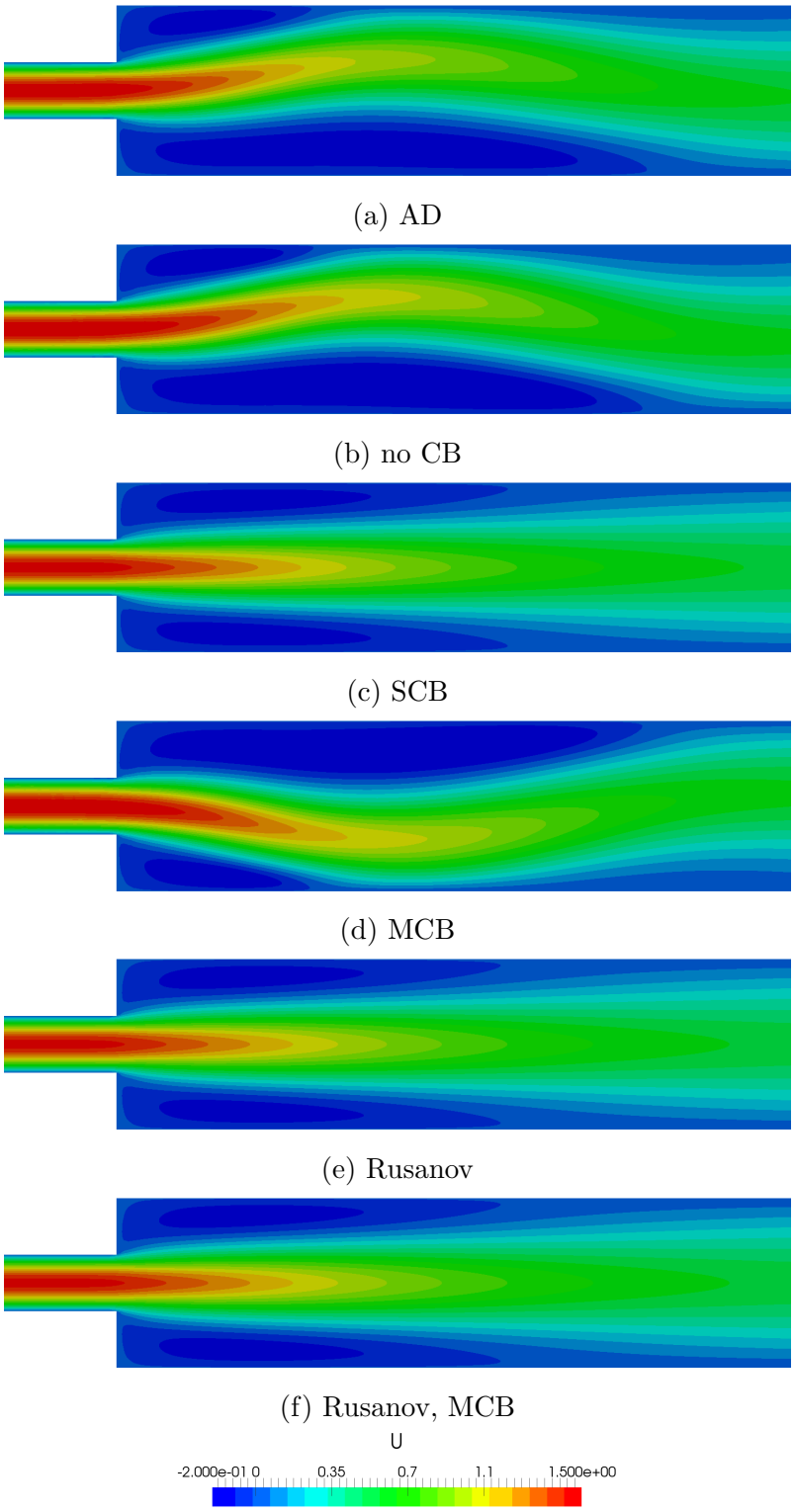

(a) AD

(b) no CB

(c) SCB

(d) MCB

(e) Rusanov

(f) Rusanov, MCB

Figure 6.38: Contour plots of the velocity profile for different numerical schemes at Re=80 for the AC method.

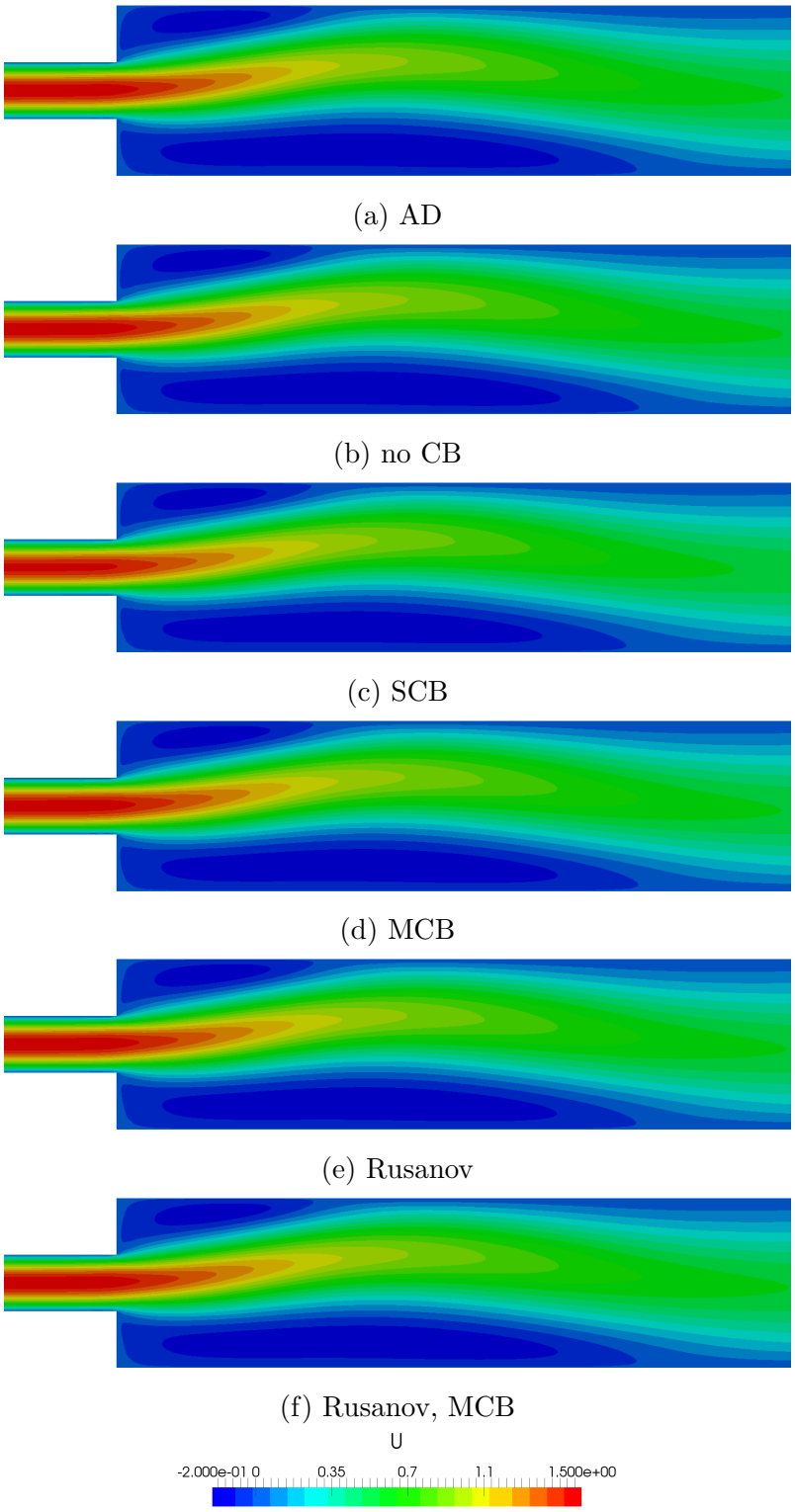

(a) AD

(b) no CB

(c) SCB

(d) MCB

(e) Rusanov

(f) Rusanov, MCB

Figure 6.39: Contour plots of the velocity profile for different numerical schemes at Re=80 for the FSAC-PP method.

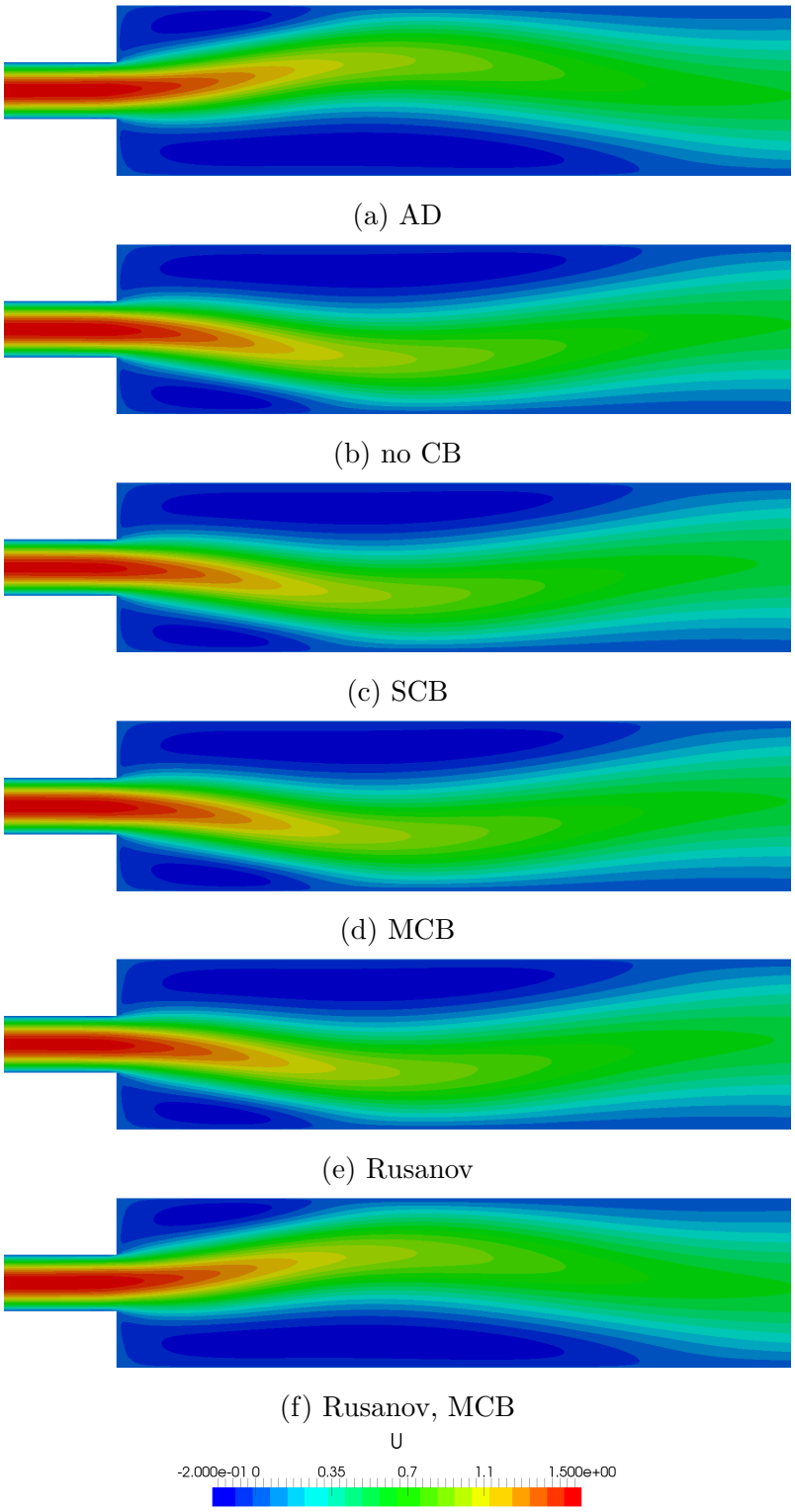

(a) AD

(b) no CB

(c) SCB

(d) MCB

(e) Rusanov

(f) Rusanov, MCB

Figure 6.40: Contour plots of the velocity profile for different numerical schemes at Re=80 for the FSAC-VP method.

Table 6.17: L_0 and L_1 error norms of the velocity profiles for the AC method for two Reynolds numbers. The average errors are given by $\overline{L_0(u)}$ and $\overline{L_1(u)}$, respectively.

			AD	no RS			Rusanov RS	
Re	x/h		no CB	no CB	SCB	MCB	no CB	MCB
	1.25	$L_0(u)$	9.04	6.64	12.37	7.41	13.23	13.23
		$L_1(u)$	3.34	4.32	4.38	4.95	4.74	4.74
	2.5	$L_0(u)$	6.45	7.31	9.28	7.77	10.06	10.06
		$L_1(u)$	2.85	4.69	4.24	5.04	4.65	4.65
34.6	5.0	$L_0(u)$	3.79	5.05	4.38	4.94	4.65	4.65
		$L_1(u)$	1.67	2.97	2.18	2.89	2.36	2.36
	10.0	$L_0(u)$	1.74	1.37	2.20	1.34	2.44	2.44
		$L_1(u)$	0.81	0.59	1.19	0.58	1.37	1.37
		$\overline{L_0(u)}$	5.25	5.09	7.06	5.37	7.59	7.59
		$\overline{L_1(u)}$	2.17	3.14	2.99	3.36	3.28	3.28
	1.25	$L_0(u)$	5.95	9.19	19.20	9.48	19.91	19.91
		$L_1(u)$	2.35	2.86	8.41	3.16	8.30	8.30
	2.5	$L_0(u)$	3.55	8.38	30.51	9.86	29.72	29.72
		$L_1(u)$	1.42	3.31	16.10	4.10	15.94	15.94
	5.0	$L_0(u)$	3.42	6.43	41.31	7.14	41.19	41.19
		$L_1(u)$	1.18	3.75	25.10	4.19	24.87	24.87
80.0	10.0	$L_0(u)$	1.89	2.78	3.91	2.86	4.03	4.03
		$L_1(u)$	1.02	0.75	2.28	0.81	2.39	2.39
	20.0	$L_0(u)$	2.56	3.01	1.85	3.02	1.73	1.73
		$L_1(u)$	1.07	1.34	0.76	1.34	0.64	0.64
	20.0	$\overline{L_0(u)}$	3.47	5.96	19.36	6.47	19.31	19.31
		$\overline{L_1(u)}$	1.41	2.40	10.53	2.72	10.43	10.43

Table 6.18: L_0 and L_1 error norms of the velocity profiles for the FSAC-PP method for two Reynolds numbers. The average errors are given by $\overline{L_0(u)}$ and $\overline{L_1(u)}$, respectively.

			AD	no RS			Rusanov RS	
Re	x/h		no CB	no CB	SCB	MCB	no CB	MCB
	1.25	$L_0(u)$	11.35	11.37	13.82	11.78	11.34	11.28
		$L_1(u)$	3.98	3.98	4.89	4.14	3.98	3.96
	2.5	$L_0(u)$	8.34	8.33	10.65	8.69	8.25	8.20
		$L_1(u)$	3.74	3.73	4.91	3.92	3.70	3.67
34.6	5.0	$L_0(u)$	4.06	4.10	4.98	4.19	4.05	4.03
		$L_1(u)$	1.94	1.96	2.57	2.03	1.93	1.91
	10.0	$L_0(u)$	1.90	1.94	2.75	2.02	1.90	1.88
		$L_1(u)$	0.94	0.97	1.63	1.04	0.93	0.92
		$\overline{L_0(u)}$	6.41	6.44	8.05	6.67	6.38	6.35
		$\overline{L_1(u)}$	2.65	2.66	3.50	2.78	2.63	2.62
	1.25	$L_0(u)$	6.73	6.85	9.18	7.37	6.97	6.88
		$L_1(u)$	2.05	2.01	1.88	2.09	2.12	2.12
	2.5	$L_0(u)$	4.00	4.07	5.33	4.71	4.73	4.65
		$L_1(u)$	1.14	1.10	1.68	1.35	1.48	1.46
	5.0	$L_0(u)$	4.51	4.25	5.62	4.74	5.18	5.13
		$L_1(u)$	2.11	1.99	3.15	2.33	2.51	2.47
80.0	10.0	$L_0(u)$	1.72	1.68	3.05	1.47	1.63	1.61
		$L_1(u)$	0.99	0.92	1.51	0.86	0.95	0.93
	20.0	$L_0(u)$	2.33	2.28	1.71	2.27	2.43	2.45
		$L_1(u)$	0.93	0.87	0.58	0.87	1.00	1.02
	20.0	$\overline{L_0(u)}$	3.86	3.82	4.98	4.11	4.19	4.14
		$\overline{L_1(u)}$	1.44	1.38	1.76	1.50	1.61	1.60

Table 6.19: L_0 and L_1 error norms of the velocity profiles for the FSAC-VP method for two Reynolds numbers. The average errors are given by $\overline{L_0(u)}$ and $\overline{L_1(u)}$, respectively.

			AD	no RS			Rusanov RS	
Re	x/h		no CB	no CB	SCB	MCB	no CB	MCB
	1.25	$L_0(u)$	10.69	10.68	12.56	11.12	11.97	10.58
		$L_1(u)$	3.74	3.73	4.42	3.89	4.19	3.71
	2.5	$L_0(u)$	7.78	7.75	9.51	8.17	8.94	7.63
		$L_1(u)$	3.46	3.44	4.35	3.66	4.06	3.38
34.6	5.0	$L_0(u)$	3.90	3.92	4.51	4.04	4.31	3.86
		$L_1(u)$	1.83	1.83	2.26	1.93	2.12	1.79
	10.0	$L_0(u)$	1.77	1.79	2.32	1.90	2.15	1.74
		$L_1(u)$	0.84	0.85	1.28	0.94	1.13	0.81
		$\overline{L_0(u)}$	6.03	6.03	7.23	6.31	6.84	5.95
		$\overline{L_1(u)}$	2.47	2.46	3.08	2.60	2.88	2.42
	1.25	$L_0(u)$	5.95	5.99	7.83	6.40	7.26	5.89
		$L_1(u)$	2.09	2.06	1.88	2.02	2.06	2.09
	2.5	$L_0(u)$	3.28	3.23	4.34	3.35	4.66	3.35
		$L_1(u)$	1.03	1.01	1.26	0.98	1.32	1.19
	5.0	$L_0(u)$	3.89	3.62	4.52	3.81	5.07	4.22
		$L_1(u)$	1.68	1.55	2.38	1.69	2.54	1.86
80.0	10.0	$L_0(u)$	1.68	1.61	2.33	1.61	1.98	1.68
		$L_1(u)$	0.93	0.84	1.26	0.86	1.18	0.92
	20.0	$L_0(u)$	2.45	2.42	1.99	2.34	2.28	2.59
		$L_1(u)$	1.02	0.98	0.65	0.91	0.87	1.11
	20.0	$\overline{L_0(u)}$	3.45	3.37	4.20	3.50	4.25	3.55
		$\overline{L_1(u)}$	1.35	1.29	1.49	1.29	1.59	1.44

Table 6.20: L_0 and L_1 error norms of the velocity profiles for the FSVP method for two Reynolds numbers. The average errors are given by $\overline{L_0(u)}$ and $\overline{L_1(u)}$, respectively.

			AD	no RS			Rusanov RS	
Re	x/h		no CB	no CB	SCB	MCB	no CB	MCB
	1.25	$L_0(u)$	10.98	11.01	-	-	-	-
		$L_1(u)$	3.84	3.85	-	-	-	-
	2.5	$L_0(u)$	8.03	8.05	-	-	-	-
		$L_1(u)$	3.60	3.61	-	-	-	-
34.6	5.0	$L_0(u)$	3.96	3.99	-	-	-	-
		$L_1(u)$	1.88	1.90	-	-	-	-
	10.0	$L_0(u)$	1.82	1.86	-	-	-	-
		$L_1(u)$	0.87	0.90	-	-	-	-
		$\overline{L_0(u)}$	6.20	6.23	-	-	-	-
		$\overline{L_1(u)}$	2.55	2.56	-	-	-	-
	1.25	$L_0(u)$	6.24	6.34	-	-	-	-
		$L_1(u)$	2.06	2.02	-	-	-	-
	2.5	$L_0(u)$	3.38	3.44	-	-	-	-
		$L_1(u)$	1.01	0.98	-	-	-	-
	5.0	$L_0(u)$	4.09	3.83	-	-	-	-
		$L_1(u)$	1.82	1.70	-	-	-	-
80.0								
	10.0	$L_0(u)$	1.74	1.69	-	-	-	-
		$L_1(u)$	0.97	0.89	-	-	-	-
	20.0	$L_0(u)$	2.40	2.35	-	-	-	-
		$L_1(u)$	0.98	0.92	-	-	-	-
	20.0	$\overline{L_0(u)}$	3.57	3.53	-	-	-	-
		$\overline{L_1(u)}$	1.37	1.30	-	-	-	-

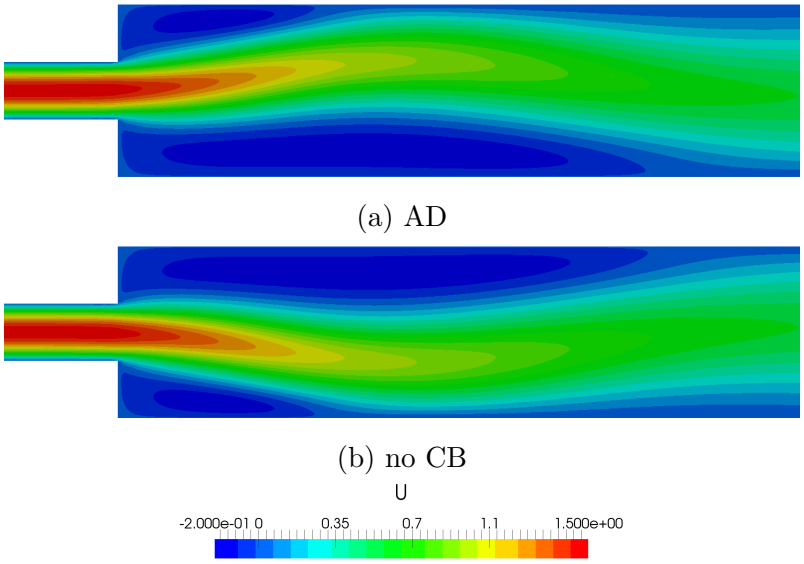

(a) AD

(b) no CB

Figure 6.41: Contour plots of the velocity profile for different numerical schemes at Re=80 for the FSVP method.

by $\overline{L_0(u)}$ and $\overline{L_1(u)}$, respectively. In the following, the comparisons are done based on the averaged L_1 norm, unless otherwise stated.
First, the most and least accurate schemes are found and discussed. For the AC method and for both Reynolds numbers, the central scheme produces the best results while the least accurate results are obtained with the MCB scheme at Re=34.6 and the RS-based approaches for the higher Reynolds number of Re=80. This is not surprising since those were the schemes that failed to predict the bifurcation. For the FSAC-PP method in Table 6.18, the Rusanov scheme with MCB coupling produces the best agreement at the lower Reynolds number while the non CB scheme matched the reference data best at Re=80. As observed from a qualitative point of view, the least agreement was achieved with the SCB scheme for both Reynolds numbers. For the FSAC-VP method in Table 6.19, the best agreement has once again been obtained with the Rusanov and MCB scheme combined while both the non CB and MCB scheme provided the best agreement at Re=80. The SCB scheme provides the least favourable agreement at Re=34.6 and the Rusanov RS, in this case, provides the largest discrepancy at Re=80. For the FSVP method, there is no need to classify which scheme performs best or worst at different Reynolds numbers as only two schemes are investigated. It can be seen, however, that in Table 6.20 both schemes provide very close agreement to one another. In terms of absolute error norms, all methods provide errors which are approximately in same range and can be loosely defined as $1\% < \overline{L_1(u)} < 3.5\%$. There is no large difference between the methods in terms of accuracy. However, as seen in the velocity profiles from Figures 6.29–6.32 at Re=34.6 and Figures 6.33–6.36 at Re=80, there are differences within each method. In-fact, when computing the differences between the most and least accurate result for each method, we get differences of 35.4% (86.7%) for the AC method, 25.1% (21.6%) for the FSAC-PP method and 21.4% (18.9%) for the

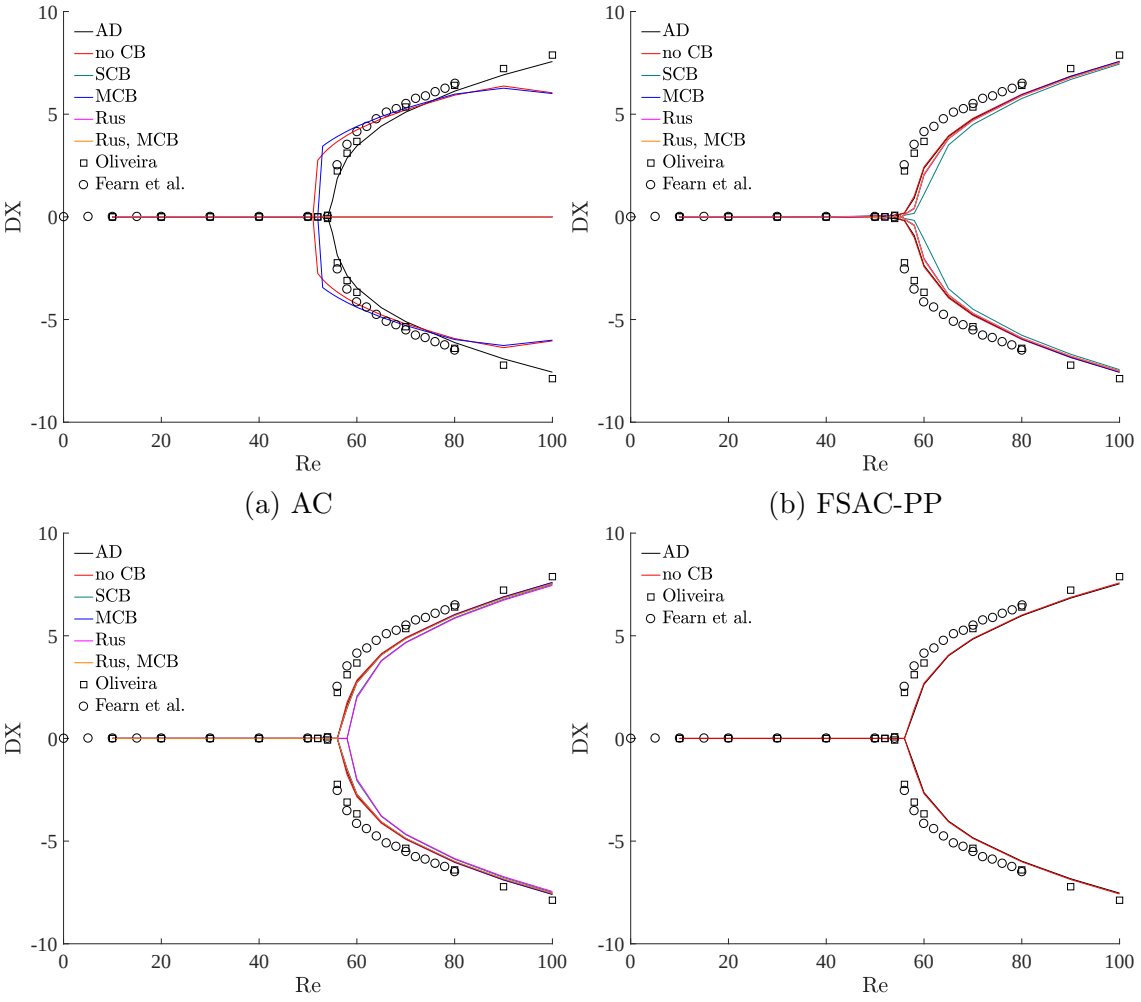

(a) AC (b) FSAC-PP

(c) FSAC-VP (d) FSVP

Figure 6.42: Bifurcation diagram for different incompressible flow methods.

FSAC-VP method, where the first value corresponds to the differences at Re=34.6 and the values given in parenthesis correspond to Re=80. We see a large difference for the AC method at Re=80 which is due to the inability to predict the bifurcation for some numerical schemes. Even if those schemes are removed from the analysis, the difference between the most and least accurate scheme at Re=80 for the AC method becomes 48.2%. Compared to the FSAC-PP and FSAC-VP method, the error increases for the AC method once the bifurcated state is encountered while the other two methods decrease their overall error. At Re=80, the maximum difference is approximately a factor of 2.5 less for both the FSAC-PP and FSAC-VP methods compared to the AC method where the FSAC-VP method shows again the least amount of deviation among the various schemes. The difference at Re=34.6 is lower, however, it is still the FSAC-VP method that provides the most consistent results in terms of differences between the schemes. The same discussion is, again, not sensible to do and would be somewhat misleading for the FSVP method as only two schemes are considered which are matching each other rather well.

In Figure 6.42, the bifurcation diagrams for the different incompressible methods are shown for all their numerical schemes. Here, the property on the y-axis is defined as $DX = |X_{r1} - X_{r2}|$ and we follow the convention of the literature in which DX and $(-1) \cdot DX$ is plotted against the Reynolds number. In the literature, the ratio of v_{ref}/u_0 is sometimes also used to indicated the bifurcation, where v_{ref} is the vertical velocity component at some point x/h downstream on the centreline and u_0 is the freestream velocity. Here, the first definition is used due to the available reference data from the literature [168, 169].
In Figure 6.42a, the bifurcating diagram for the AC method is shown. The reference data indicates that the critical Reynolds number is around Re=54 as stated previously and we can see that the RS-based approaches fail to predict the bifurcation for all Reynolds numbers which is in accordance with the observations made at Re=80 from the contour plots of velocity, see Figure 6.38. Only the central scheme with artificial dissipation is able to predict the bifurcation at the correct Reynolds number and follows the reference data closely. Both the non CB and MCB scheme predict the onset of bifurcation as well, albeit at Re=51 and Re=52, respectively, but ultimately fail to predict the steady increase in the difference of the two reattachment points expressed by DX. Looking at Figure 6.42b, showing the FSAC-PP method, we can see that all schemes predict the bifurcation, although the onset of bifurcation appearing gradually without the sharp transition from the symmetric to the anti-symmetric state and delayed, after the critical Reynolds number of Re=54. The SCB scheme provides the largest delay in onset of bifurcation but close to the largest Reynolds number tested, here Re=100, all schemes are again in close agreement to each other and the reference data. The FSAC-VP method in Figure 6.42c shows a much sharper transition from the symmetric to the anti-symmetric state. Only the Rusanov RS and SCB scheme predict the onset of bifurcation at Re=60 while all the other schemes predict it at Re=58 which is in better agreement with the reference data. Remarkably, though, there is little visible difference between the schemes and the trend of the reference data is matched. The same observations are again valid also for the FSVP method. This shows once again that the inherent parabolic nature of the FSAC-VP method is able to stabilise the differences in the numerical schemes so that their overall behaviour does not show any visible difference, as highlighted already during the discussion in the previous Sections. If we compare the AC method to the FSAC-VP method specifically here, recalling the governing equations of the AC method (Eq.(3.3.3–3.3.4)) and of the FSAC-VP method (Eq.(3.3.28–3.3.30)), we see that the only difference is that the pressure gradient is dropped for the FSAC-VP method from the momentum equation and solved through the newly derived pressure transport equation. However, this simple extension of having a evolution equation for the pressure has a rather large impact on the overall solution. Once again, the results suggest that the treatment of the pressure is of critical importance if the correct physical flow field is concerned and furthermore if a scheme-independent solution is sought. This can be also viewed from a different perspective; what high-resolution schemes are to the non-linear term of the Navier–Stokes equations, are incompressible flow method to treat the pressure. In other words, various incompressible methods will have a different effect on the pressure field, just like high-resolution schemes will have on the velocity field. The analogy

high-resolution methods may be misleading as there is not a Taylor-series truncation error associated with an incompressible flow method, but it helps to highlight that different methods produce a different behaviour in the pressure. Since the pressure is driving the velocity field and not the other way around, it is argued here that such methods are required to accurately predict a pressure field which is then used to capture the velocity field accurately. Although no discontinuities are present in the current case, it needs to be remembered that turbulent flows are driven by the non-linear behaviour of the Navier–Stokes equations and thus an accurate prediction of the pressure field may help to accurately describe the underlying turbulent flows. It is due to this fact that the sudden expansion was investigated here in closer detail which showed that both the FSAC-VP and FSVP method predict a sharp transition from the symmetrical to the anti-symmetrical case which is closely followed by the FSAC-PP method, which however showed a more gradual departure from the symmetrical state. Before assessing the bifurcation from a quantitative point of view, it should be kept in mind that all results were obtained on a medium sized grid with a GCI of 13.67%. Furthermore, the difference in the predicted reattachment point here to those obtained by Oliveira [169] differ by approximately 4%. It is reasonable to assume that mesh independent results would predict the bifurcating Reynolds number much closer to the critical one.

In Tables 6.21–6.24, the reattachment point for each method and numerical scheme is given at each Reynolds number for which reference data is available. Those simulations for which no reference data is available, have been dropped from the tables but used in the bifurcation diagrams in Figure 6.42. The number of required iterations is also given as a reference. Starting with the AC method in Table 6.21, it can be seen that the reattachment point is over-predicted by the non CB and MCB scheme at lower Reynolds numbers. At Re=10, the difference is more than a factor of two while the other schemes match the reference data well. The trend prevails for increasing Reynolds numbers, but the difference becomes smaller. At Re=30, the non CB and MCB scheme still over-predict the reattachment by approximately 25%. In the initial discussion on the velocity profiles in Figures 6.29–6.32, it was stated that the change in recirculation vortices will affect the reattachment length and in turn the bifurcation itself. It was concluded that the non CB and MCB scheme both will prematurely predict the bifurcation which is also evident from Table 6.21, where the non CB scheme bifurcates at Re=52. Interestingly, the MCB scheme bifurcates at Re=54, which is the critical Reynolds number. At sub-critical Reynolds numbers, the reattachment lengths X_{r1} and X_{r2} always correlate perfectly to each other and for those schemes experiencing a bifurcation, it appears suddenly with a sharp departure from the symmetrical case. Those schemes who do not show a breaking from the symmetry allow their recirculation area to grow and in turn, this means that the reattachment points become increasingly larger. The perfect correlation between those two values is retained up to Re=100. It is possible that the bifurcation eventually occurs outside of the tested Reynolds number range, but it is not tested here. Even if it would, the error to the non CB and MCB scheme would be rather large. For those schemes predicting the bifurcation, it can be seen that the number of iterations increases drastically. This is an effect which will be

Table 6.21: Prediction of the reattachment length for different Reynolds numbers using the AC method for various combinations of CB schemes and the Rusanov Riemann solver.

		AD	no RS			Rusanov RS		
Re		no CB	no CB	SCB	MCB	no CB	MCB	Ref [169]
	iteration	696787	3631653	690039	4532716	696382	696476	-
10	X_{r1}	1.304	2.655	1.130	2.634	1.117	1.117	1.211
	X_{r2}	1.304	2.655	1.130	2.634	1.117	1.117	1.211
	iteration	163424	2113766	163702	1547448	166414	166411	-
20	X_{r1}	2.183	3.387	1.968	3.364	1.936	1.936	2.111
	X_{r2}	2.183	3.387	1.968	3.364	1.936	1.936	2.111
	iteration	109341	1221133	107248	785612	106580	106591	-
30	X_{r1}	3.120	4.213	2.879	4.194	2.828	2.828	3.080
	X_{r2}	3.120	4.213	2.879	4.194	2.828	2.828	3.080
	iteration	102533	791709	100955	478125	100464	100460	-
40	X_{r1}	4.083	5.085	3.824	5.070	3.753	3.753	4.075
	X_{r2}	4.083	5.085	3.824	5.070	3.753	3.753	4.075
	iteration	94732	568705	91784	330816	91432	91429	-
50	X_{r1}	5.056	5.990	4.785	5.985	4.697	4.697	5.080
	X_{r2}	5.055	5.990	4.785	5.985	4.697	4.697	5.081
	iteration	95118	858132	91683	318747	90572	90572	-
52	X_{r1}	5.249	4.330	4.978	6.169	4.886	4.886	5.279
	X_{r2}	5.251	7.089	4.978	6.169	4.886	4.886	5.285
	iteration	154541	630303	91897	476622	90803	90803	-
54	X_{r1}	5.448	4.088	5.172	3.838	5.076	5.076	5.445
	X_{r2}	5.444	7.369	5.172	7.452	5.076	5.076	5.523
	iteration	748021	553873	92342	430348	91269	91273	-
56	X_{r1}	4.590	3.939	5.366	3.749	5.266	5.266	4.440
	X_{r2}	6.467	7.604	5.366	7.663	5.266	5.266	6.678
	iteration	356102	533040	97869	403268	96932	96928	-
58	X_{r1}	4.164	3.839	5.561	3.683	5.457	5.457	4.107
	X_{r2}	7.022	7.814	5.561	7.857	5.457	5.457	7.208
	iteration	249418	515231	99678	383592	98563	98556	-
60	X_{r1}	3.956	3.770	5.755	3.635	5.648	5.648	3.935
	X_{r2}	7.409	8.008	5.755	8.040	5.648	5.648	7.609

continued

Re		AD	no RS			Rusanov RS		Ref [169]
		no CB	no CB	SCB	MCB	no CB	MCB	
	iteration	156686	455579	101927	328784	100829	100832	-
70	X_{r1}	3.638	3.629	6.732	3.550	6.605	6.605	3.669
	X_{r2}	8.739	8.843	6.732	8.844	6.605	6.605	9.019
	iteration	149699	411266	104035	304704	104958	104951	-
80	X_{r1}	3.610	3.626	7.713	3.562	7.566	7.566	3.658
	X_{r2}	9.731	9.553	7.713	9.538	7.566	7.566	10.060
	iteration	148799	388146	110098	292355	109346	109341	-
90	X_{r1}	3.652	3.668	8.697	3.610	8.529	8.529	3.708
	X_{r2}	10.567	10.039	8.697	9.876	8.529	8.529	10.930
	iteration	154207	365681	110430	295891	109700	109701	-
100	X_{r1}	3.717	3.730	9.683	3.676	9.493	9.493	3.781
	X_{r2}	11.282	9.771	9.683	9.681	9.493	9.493	11.660

discussed later but it should be noted here that the prediction of the symmetry breaking requires not only a suitable method and numerical scheme combination but also an increased computational time.

In Table 6.22, the same reattachment points and number of required iterations are shown for the FSAC-PP method. As was already seen in Figure 6.42b, all numerical schemes predicted the onset of bifurcation, albeit slightly delayed compared to the reference data. This can also be seen from the table where the predicted reattachment point agrees well with the reference data and differences are within 10%. Below the critical Reynolds number, the agreement is excellent, and differences are much smaller. At Re=10, for example, the highest deviation from the reference data is obtained with the SCB scheme at 4.2% while all the other schemes match the reference data within 1%. The Rusanov scheme even matches the results exactly, although it has to be kept in mind that these results are still obtained on a medium mesh size. A full mesh independent result is likely to change these numbers slightly, but it is expected that the overall agreement will persist. Above the critical Reynolds number, the agreement to Oliveira [169] stays within the 10% differences which is largely due to the delayed prediction of the bifurcation. From Figure 6.42b it can be seen that the overall experimental trend is matched rather well, and all schemes follow the same curve. If the critical Reynolds number would be in closer agreement, it is expected that the predicted reattachment point would be also in closer agreement to the data given by Oliveira [169]. Since the bifurcation is predicted for all schemes, we can also make comments on the number of iterations which was more difficult in the case of the AC method, where the different behaviour of the numerical schemes also produced less consistent data on the iterations. Here, the number of required

Table 6.22: Prediction of the reattachment length for different Reynolds numbers using the FSAC-PP method for various combinations of CB schemes and the Rusanov Riemann solver.

		AD	no RS			Rusanov RS		
Re		no CB	no CB	SCB	MCB	no CB	MCB	Ref [169]
	iteration	68164	68164	88652	77805	85234	76780	-
10	X_{r1}	1.218	1.218	1.160	1.199	1.211	1.212	1.211
	X_{r2}	1.216	1.217	1.161	1.198	1.211	1.211	1.211
	iteration	63564	63567	77596	71278	76451	70299	-
20	X_{r1}	2.050	2.052	1.960	2.030	2.049	2.050	2.111
	X_{r2}	2.046	2.049	1.958	2.028	2.047	2.048	2.111
	iteration	58897	58896	68241	64767	67870	63793	-
30	X_{r1}	2.957	2.961	2.839	2.936	2.958	2.960	3.080
	X_{r2}	2.950	2.954	2.834	2.930	2.953	2.955	3.080
	iteration	54292	54291	61483	58382	61441	58369	-
40	X_{r1}	3.894	3.902	3.747	3.874	3.897	3.901	4.075
	X_{r2}	3.880	3.888	3.758	3.862	3.887	3.891	4.075
	iteration	72662	72955	57272	62362	66594	64421	-
50	X_{r1}	4.854	4.866	4.705	4.836	4.856	4.861	5.080
	X_{r2}	4.817	4.829	4.682	4.807	4.830	4.836	5.081
	iteration	101961	103038	68241	88776	94788	91491	-
52	X_{r1}	5.055	5.068	4.866	4.994	5.054	5.060	5.279
	X_{r2}	5.000	5.013	4.898	5.035	5.017	5.023	5.285
	iteration	157548	160834	98874	134456	143614	139714	-
54	X_{r1}	5.177	5.190	5.094	5.239	5.200	5.207	5.445
	X_{r2}	5.264	5.279	5.048	5.176	5.257	5.262	5.523
	iteration	309091	323916	158368	243044	260922	257718	-
56	X_{r1}	5.322	5.333	5.221	5.342	5.368	5.374	4.440
	X_{r2}	5.503	5.522	5.299	5.461	5.475	5.480	6.678
	iteration	896302	878294	334541	768416	865548	901939	-
58	X_{r1}	5.127	5.084	5.362	5.377	5.415	5.405	4.107
	X_{r2}	6.031	6.095	5.534	5.802	5.805	5.825	7.208
	iteration	370621	355946	888435	481042	514272	486624	-
60	X_{r1}	4.450	4.427	5.051	4.641	4.655	4.628	3.935
	X_{r2}	6.817	6.861	6.149	6.688	6.700	6.726	7.609

continued

Re		AD	no RS			Rusanov RS		Ref [169]
		no CB	no CB	SCB	MCB	no CB	MCB	
	iteration	116122	114816	126413	119971	127121	125149	-
70	X_{r1}	3.733	3.734	3.782	3.779	3.785	3.782	3.669
	X_{r2}	8.497	8.531	8.278	8.499	8.475	8.485	9.019
	iteration	92806	91835	94097	92946	99882	98683	-
80	X_{r1}	3.647	3.653	3.650	3.679	3.681	3.679	3.658
	X_{r2}	9.583	9.622	9.416	9.618	9.572	9.579	10.060
	iteration	100257	96853	95949	97232	114014	105340	-
90	X_{r1}	3.669	3.676	3.656	3.696	3.703	3.702	3.708
	X_{r2}	10.479	10.525	10.346	10.539	10.480	10.486	10.930
	iteration	102456	106408	109105	119534	108770	102731	-
100	X_{r1}	3.740	3.749	3.705	3.762	3.754	3.753	3.781
	X_{r2}	11.256	11.308	11.147	11.336	11.263	11.269	11.660

iterations is uniformly distributed for each Reynolds number, where the non CB and central scheme produce the lowest and very similar number of iterations up to the critical Reynolds number. The predicted reattachment point is in equally good agreement amongst these two schemes while the number of iterations only becomes larger than the other schemes above the critical Reynolds number. Sufficiently far away from the critical Reynolds number, the number of iterations equalise again and are more uniformly distributed. The SCB scheme initially produces smaller iterations around the critical Reynolds number, however, this is due to the fact that the bifurcation itself is delayed the most using the SCB scheme. Thus, while the other schemes start to predict the bifurcation, requiring more iterations, the SCB scheme is still in a symmetrical state and therefore seems to require less iterations. Once the bifurcation is predicted using the SCB scheme, the iterations increase rapidly. There is a strong correlation between the number of iterations and the bifurcating critical Reynolds number, which will be discussed later in more detail.

Turning to Table 6.23, the same data is shown for the FSAC-VP method. Similar observations made for the FSAC-PP can also be done here. At Re=10, the agreement is overall excellent with the reference data and shows only slightly more deviation from the reference data than the FSAC-PP method. The central scheme and non CB scheme also show overall less iterations which holds up to Re=100. The difference compared to Oliveira [169] is also within 10% and would be expected from the close visual agreement of the bifurcating diagrams in Figure 6.42b and 6.42c. The number of required iterations is again equally distributed sufficiently far away from the critical Reynolds number. At Re=10, the lower spectrum of the simulated Reynolds number range, the iterations appear to increase abruptly which can also be seen in

Table 6.23: Prediction of the reattachment length for different Reynolds numbers using the FSAC-VP method for various combinations of CB schemes and the Rusanov Riemann solver.

		AD	no RS			Rusanov RS		
Re		no CB	no CB	SCB	MCB	no CB	MCB	Ref [169]
	iteration	184761	184922	302671	297819	310080	301977	-
10	X_{r1}	1.249	1.254	1.164	1.239	1.171	1.251	1.211
	X_{r2}	1.249	1.254	1.164	1.239	1.171	1.251	1.211
	iteration	102790	102817	104384	104279	103917	103963	-
20	X_{r1}	2.079	2.083	1.988	2.065	2.005	2.083	2.111
	X_{r2}	2.079	2.083	1.988	2.065	2.005	2.083	2.111
	iteration	90622	90639	96830	96645	96454	96398	-
30	X_{r1}	2.987	2.994	2.884	2.967	2.910	2.992	3.080
	X_{r2}	2.987	2.994	2.884	2.967	2.910	2.992	3.080
	iteration	79094	79099	86632	86553	86444	86449	-
40	X_{r1}	3.922	3.933	3.811	3.900	3.845	3.931	4.075
	X_{r2}	3.923	3.933	3.811	3.900	3.845	3.931	4.075
	iteration	73634	73574	79348	82008	76313	77893	-
50	X_{r1}	4.871	4.887	4.755	4.848	4.795	4.884	5.080
	X_{r2}	4.872	4.887	4.755	4.849	4.795	4.884	5.081
	iteration	77585	77532	80567	82248	81251	83123	-
52	X_{r1}	5.065	5.081	4.946	5.042	4.987	5.078	5.279
	X_{r2}	5.066	5.082	4.947	5.042	4.987	5.078	5.285
	iteration	81313	77695	80720	87110	81502	83313	-
54	X_{r1}	5.258	5.275	5.137	5.235	5.179	5.271	5.445
	X_{r2}	5.259	5.276	5.138	5.236	5.179	5.272	5.523
	iteration	197039	216972	109571	209469	81691	88751	-
56	X_{r1}	5.451	5.469	5.329	5.428	5.371	5.466	4.440
	X_{r2}	5.454	5.472	5.330	5.431	5.371	5.466	6.678
	iteration	1154110	1004392	484974	1358168	256720	1605128	-
58	X_{r1}	4.751	4.688	5.518	4.816	5.563	4.830	4.107
	X_{r2}	6.377	6.455	5.524	6.299	5.564	6.345	7.208
	iteration	453449	429991	800466	472976	986158	557505	-
60	X_{r1}	4.240	4.217	4.561	4.261	4.647	4.281	3.935
	X_{r2}	7.006	7.054	6.620	6.971	6.626	6.999	7.609

continued

Re		AD	no RS			Rusanov RS		Ref [169]
		no CB	no CB	SCB	MCB	no CB	MCB	
	iteration	173750	157038	173975	159584	199912	206382	-
70	X_{r1}	3.684	3.685	3.725	3.688	3.761	3.702	3.669
	X_{r2}	8.562	8.601	8.410	8.561	8.420	8.559	9.019
	iteration	124996	129970	137720	135519	184594	151121	-
80	X_{r1}	3.621	3.626	3.632	3.623	3.661	3.632	3.658
	X_{r2}	9.623	9.666	9.513	9.639	9.510	9.617	10.060
	iteration	116331	137315	138234	137822	144780	142072	-
90	X_{r1}	3.651	3.658	3.652	3.653	3.676	3.658	3.708
	X_{r2}	10.505	10.555	10.423	10.537	10.409	10.500	10.930
	iteration	117561	127616	140343	134273	140414	136251	-
100	X_{r1}	3.712	3.721	3.708	3.715	3.729	3.715	3.781
	X_{r2}	11.263	11.318	11.206	11.309	11.184	11.262	11.660

Table 6.21 for the AC method but is absent for the FSAC-PP method in Table 6.22. The FSAC-PP method was introduced to circumvent the shortcomings of the AC method that produced a stiff set of equations at low Reynolds numbers which causes the convergence rate to slow down as the Reynolds number is decreased. It seems that this positive feature of the FSAC-PP method is not necessarily inherited by the FSAC-VP method, although it may only be the case for the present test case and a range of test cases would be required to settle this question. The aim here, however, is not to validate the FSAC-VP method at low Reynolds number — for such flows it has not been specifically designed — but rather to test it where the flow features some complex structures that needs to be resolved, such as the bifurcation in the present case. Similar to the AC method, the FSAC-VP method shows very little to no difference in the difference of the predicted reattachment points up to the critical Reynolds number where a sharp bifurcation occurs, here at Re=58. As discussed previously and can be also seen in Figure 6.42c, the bifurcation for the SCB scheme and Rusanov RS is delayed up to Re=60. Both the AC and FSAC-VP method (as well as the FSVP method by proxy) contain at least one real characteristic which limits the propagation of information in the domain through their hyperbolic and parabolic pressure behaviour, respectively. This barrier on information propagation may ultimately be responsible for the sharp triggering of the bifurcation compared to the FSAC-PP method, where the elliptic pressure behaviour does not impose any propagation restriction of pressure waves.

In Table 6.24, the same information is given for the FSVP method which generally agrees well with the FSAC-VP method as in the previous discussion already highlighted. The bifurcation occurs here at Re=58 as well, while the iterations required

Table 6.24: Prediction of the reattachment length for different Reynolds numbers using the FSVP method for various combinations of CB schemes and the Rusanov Riemann solver.

		AD	no RS			Rusanov RS		
Re		no CB	no CB	SCB	MCB	no CB	MCB	Ref [169]
	iteration	243267	242962	-	-	-	-	-
10	X_{r1}	1.232	1.232	-	-	-	-	1.211
	X_{r2}	1.232	1.232	-	-	-	-	1.211
	iteration	104845	104899	-	-	-	-	-
20	X_{r1}	2.061	2.063	-	-	-	-	2.111
	X_{r2}	2.061	2.063	-	-	-	-	2.111
	iteration	94739	94799	-	-	-	-	-
30	X_{r1}	2.966	2.971	-	-	-	-	3.080
	X_{r2}	2.966	2.971	-	-	-	-	3.080
	iteration	83946	83976	-	-	-	-	-
40	X_{r1}	3.899	3.908	-	-	-	-	4.075
	X_{r2}	3.900	3.908	-	-	-	-	4.075
	iteration	78758	78659	-	-	-	-	-
50	X_{r1}	4.847	4.859	-	-	-	-	5.080
	X_{r2}	4.847	4.860	-	-	-	-	5.081
	iteration	78925	78815	-	-	-	-	-
52	X_{r1}	5.040	5.054	-	-	-	-	5.279
	X_{r2}	5.040	5.054	-	-	-	-	5.285
	iteration	79040	78924	-	-	-	-	-
54	X_{r1}	5.233	5.247	-	-	-	-	5.445
	X_{r2}	5.233	5.247	-	-	-	-	5.523
	iteration	154716	141146	-	-	-	-	-
56	X_{r1}	5.426	5.441	-	-	-	-	4.440
	X_{r2}	5.427	5.443	-	-	-	-	6.678
	iteration	1715983	1501307	-	-	-	-	-
58	X_{r1}	4.920	4.854	-	-	-	-	4.107
	X_{r2}	6.214	6.291	-	-	-	-	7.208
	iteration	507442	496781	-	-	-	-	-
60	X_{r1}	4.299	4.279	-	-	-	-	3.935
	X_{r2}	6.933	6.975	-	-	-	-	7.609

continued

Re		AD	no RS			Rusanov RS		Ref [169]
		no CB	no CB	SCB	MCB	no CB	MCB	
	iteration	170053	164646	-	-	-	-	-
70	X_{r1}	3.693	3.695	-	-	-	-	3.669
	X_{r2}	8.529	8.564	-	-	-	-	9.019
	iteration	135599	134057	-	-	-	-	-
80	X_{r1}	3.624	3.630	-	-	-	-	3.658
	X_{r2}	9.598	9.638	-	-	-	-	10.060
	iteration	123168	134735	-	-	-	-	-
90	X_{r1}	3.652	3.659	-	-	-	-	3.708
	X_{r2}	10.485	10.531	-	-	-	-	10.930
	iteration	120734	137373	-	-	-	-	-
100	X_{r1}	3.712	3.721	-	-	-	-	3.781
	X_{r2}	11.246	11.298	-	-	-	-	11.660

are 32.7% and 33.1% higher for the central and non CB scheme, respectively, at the same Reynolds number. At the sub-critical Reynolds number, the iterations are generally at the same level while above the critical Reynolds number, iterations can be approximately up to 20% higher. Thus, the hyperbolisation through the perturbed continuity equation within the FSAC-VP method does not only allow hyperbolic schemes such as Riemann solvers and the method of characteristics to be used, it also can promote convergence acceleration to some degree which is also reported by Könözsy [109] and Könözsy and Drikakis [21] where the continuity equation of the AC method provides the initial pressure for the FSAC-PP method which is responsible, in parts, for the increased convergence rate of the FSAC-PP method over the AC method.

Figure 6.43 shows the number of iterations from Tables 6.21–6.24 in graphical form for each numerical scheme and method for a direct comparison. For all schemes that showed a bifurcated state previously, a clear peak in iterations can be observed. This appears as all flows initially develop as symmetrical flow field. Once the perturbations within the flow field get strong enough, a bifurcated state can develop. However, the bifurcation develops from the symmetrical flow field and therefore requires more iterations. The reason as to why the iterations drop drastically beyond the critical Reynolds number is due to the perturbation becoming stronger; the bifurcation can occur sooner than for the critical Reynolds number and therefore require less iterations. The total number of iterations, however, is larger than for the symmetrical flow field, i.e. below the critical Reynolds number. Only the AC method shows here that the iterations can be considerably higher even below the

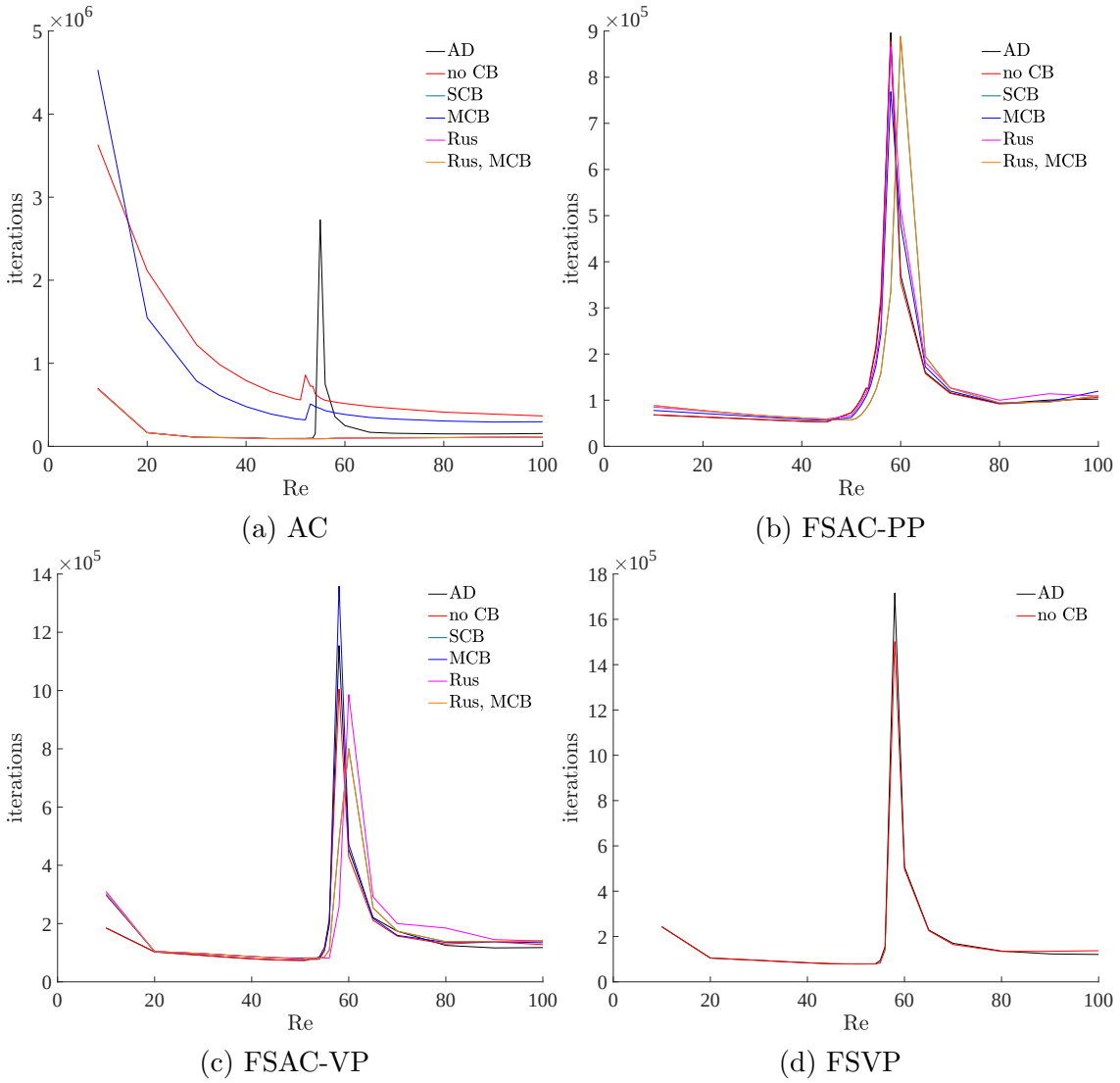

Figure 6.43: Number of iterations required by different incompressible methods for different Reynolds numbers.

critical Reynolds number; this is, however, attributed to stiffness of the AC method when used for low Reynolds number flows. As discussed above, the FSAC-VP and FSVP method show a tendency to increase the residuals as well near low Reynolds numbers, however, not as drastically as the AC method. While the peak structures and total number of iterations is comparable for the FSAC-PP, FSAC-VP and FSVP method, the AC method shows a considerable difference between the non CB and MCB scheme as well as the central scheme, for which the bifurcation was predicted. The other schemes produce a similar level of iterations but ultimately fail to predict the bifurcation. While the non CB and MCB scheme show a similar increase in residuals at the critical Reynolds number, the central scheme with artificial dissipation shows a radical increase in iterations. This peak structure is closer to the one observed in any of the other methods which indicates that the non CB and MCB schemes have little difficulties in changing from a symmetrical to a fully anti-symmetrical state. Comparing the total number of iterations, it can be seen

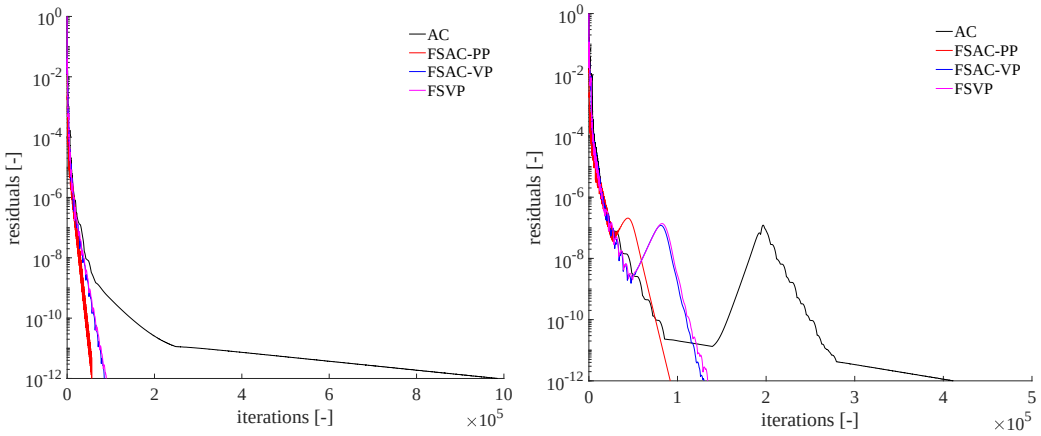

(a) Re=34.6 (b) Re=80

Figure 6.44: Number of iterations required by the non CB scheme for different incompressible methods at Re=34.6 and Re=80.

that it is the AC method again which requires the most iterations, especially near low Reynolds numbers as discussed above.

In Figure 6.44, the residuals for Re=34.6 and Re=80 are shown for all four methods using the non CB scheme. At Re=34.6, it can be seen that the residuals are dropping initially at the same rate up to 10^{-8}. Beyond this point, the AC method reduces its convergence rate and the simulations require substantially more iterations than the FSAC-PP, FSAC-VP and FSVP method. The FSAC-PP method does show the steepest convergence rate, closely followed by the FSAC-VP method which is in accordance with the discussion of previous Sections. For Re=80 in the bifurcated state, a fundamentally different picture is revealed. At first, the residuals drop normally just as if a symmetric state would be obtained. For some critical threshold value, the residual suddenly starts to increase after which the residuals drop again. This is the point where the flow starts to bifurcate from the symmetrical to the anti-symmetrical state. The change in flow pattern causes the residual to rise and once the flow has settled for a new state, the residual drop again. This is in accordance with the numerical behaviour of the simulations of oliveira [169]. Since the residuals are shown for the Re=80 case, it can be assumed that the perturbations are strong enough and should develop sooner than those around the critical Reynolds number. For the FSAC-PP method, those perturbations cause the bifurcation between a residual threshold of 10^{-7}–10^{-8} while the FSAC-VP and FSVP method bifurcate at a slightly lower threshold, here between 10^{-8}–10^{-9}. The AC method, on the other hand, only starts to pick up the bifurcation between 10^{-10}–10^{-11} which is the reason that the convergence criterion was set as low as $\epsilon = 10^{-12}$. It can be seen that a further iteration penalty is given to the AC method due to this late detection in bifurcation, or, seen from another perspective, the early detection of bifurcation by the FSAC-PP method ensures that a lower number of iterations are required. Furthermore, Figure 6.44b may also explain why some schemes may not detect the bifurcation at all. It might be that for the SCB and RS-based approach, all which did not predict the bifurcation, will eventually detect the symmetry breaking but

at a lower residual. This may be problematic as $\epsilon = 10^{-12}$ is already close to the resolution of double precision floating point variables. Although the residual threshold may have been reduced even further to test this hypothesis, it is also clear from Figure 6.44 that a further reduction in the convergence criterion would incur a significantly increased computational time for the AC method. Decreasing the residual from 10^{-11} to 10^{-12} alone requires approximately 60–80% of the total computational time. For Reynolds numbers closer to zero, this time would exponentially increase, see also Figure 6.43a. In light of the need of parametric results for different Reynolds numbers with different numerical scheme, no attempt to carry out simulations at a reduced convergence criterion has been therefore attempted.

This concludes the discussion of the laminar flow through a sudden expansion which develops a bifurcated state for some critical Reynolds number. Due to the amount of computations required, a medium sized grid was chosen based on a GCI study. We saw that the AC method produced the largest difference in velocity profiles and subsequently in the prediction of reattachment point while the FSAC-PP, FSAC-VP and FSVP method all shoed much closer agreement to one another. Those three methods also tended to under-predict the experimental data while the AC method showed that some numerical schemes could result in over-prediction of the velocity field. All this combined resulted in the AC method to produce scheme-dependent results, where for some schemes the bifurcation was observed while others failed to predict it at all. The MCB scheme was able to predict the bifurcation in all cases while the SCB scheme was not. One may find that the results obtained in the literature show converged and bifurcated results for the AC method using the SCB scheme, see Drikakis [175] for example, however in those cases it is important to use a locally refined mesh near boundaries or even higher order schemes, all which the FSAC-PP, FSAC-VP and FSVP method did not show any dependence on. The predicted bifurcation itself appeared randomly and there were no clear preferences whether the flow would deflect upwards or downwards. Experimental evidence supports this observation [168]. It was shown that the elliptic treatment of the pressure in the FSAC-PP method may be responsible for a gradual onset of bifurcation while the hyperbolic and parabolic AC, FSAC-VP and FSVP method all showed a sharp transition from the symmetrical to anti-symmetrical state. Finally, the residuals showed that the FSAC-PP method is once again the most economical method closely followed by the FSAC-VP and FSVP method while the AC method gradually decreased its convergence rate which resulted in substantially more iterations. In terms of accuracy, there is no clear best scheme but from Tables 6.17–6.20 it can be seen that the SCB produces most often the least accurate results while the MCB scheme together with its Rusanov combination, or the Rusanov RS by itself, consistently provided close agreement with the reference data. The central scheme with artificial dissipation also showed overall good agreement, especially for the bifurcation diagram of the AC method. It has to be kept in mind, however, that the used grid is not free of errors and that a finer grid is likely to have some effect on the accuracy.
Overall, the MCB scheme fared well for all cases and, except for the AC method, its combination with the Rusanov RS also showed favourable results. In the next Sec-

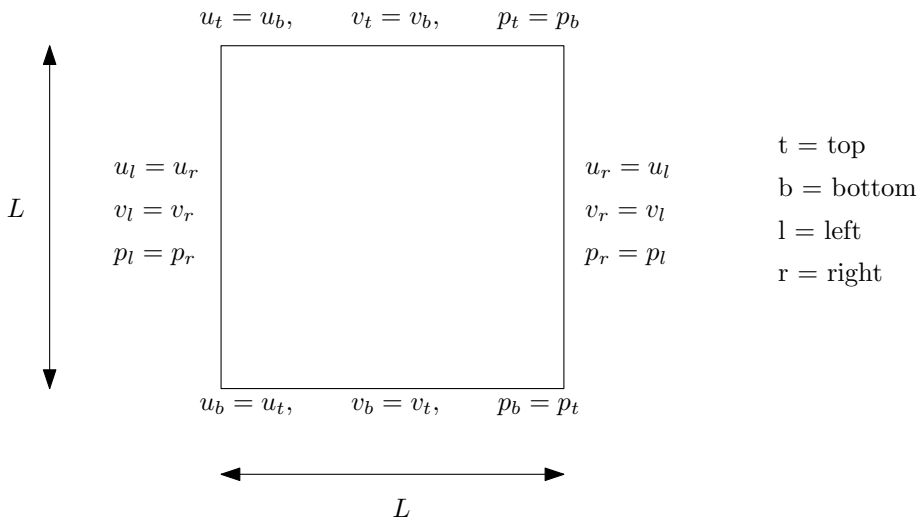

Figure 6.45: Geometry for the Taylor–Green vortex problem with its corresponding periodic boundary conditions and dimensions.

tion, this approach is extended to unsteady flows to examine to long time integration behaviour of each of those schemes and incompressible methods.

6.4 Vortex Evolution for Periodical Domains

In this final Section on the evaluation of the various Godunov-type methods against their benchmark solutions, the Taylor–Green vortex problem is considered to investigate the transient behaviour for each scheme and method. To do so, the governing equations have to be solved using a dual time-stepping procedure for which a real time derivative is added to the momentum equation of each incompressible method, see Section 3.3. The real time derivative is solved using a second-order accurate backwards Euler method given by Eq.(5.3.32). The problem is solved on a square domain with fully periodic boundary conditions as depicted in Figure 6.45. Here, the primitive variables on the boundaries are copied to the opposing side to realise the periodic conditions, as described in Section 5.2.3. The initial values of the flow are given by

$$\begin{aligned} u_0(x,y,0) &= -\cos(2m\pi x)\sin(2m\pi y), \\ v_0(x,y,0) &= \sin(2m\pi x)\cos(2m\pi y), \\ p_0(x,y,0) &= -\frac{1}{4}\left[\cos(4m\pi x) + \cos(4m\pi y)\right], \end{aligned} \tag{6.4.1}$$

where the velocity produces a vortical flow pattern, see Figure 6.46. Here, the contours correspond to normalised velocity values in the range of $-1 < u < 1$ and $-0.5 < p < 0.5$ for the pressure, according to the initial conditions of Eq.(6.4.1). The number and size of vortices is controlled by the parameter m which is set here to unity. A higher value would result in more, but smaller vortices. The advantage of this type of flow is that it produces a well-defined and periodic vortical flow without

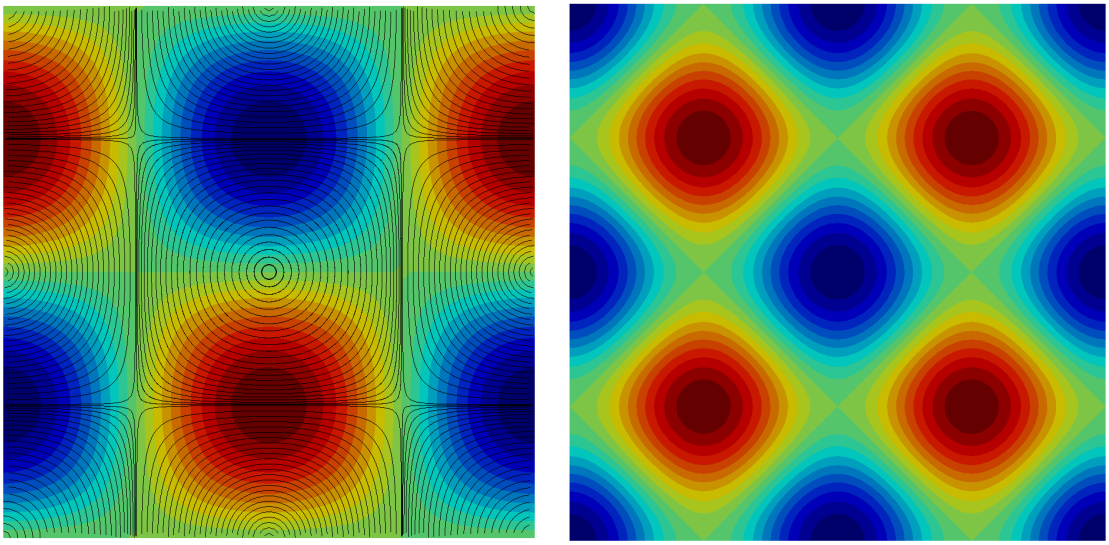

(a) u-velocity (b) pressure

Figure 6.46: Initial velocity and pressure field for the Taylor–Green vortex problem. The streamlines are superimposed onto the velocity field to highlight the symmetrical vortical pattern.

any other flow feature so that each schemes' ability to predict such features can be uniquely tested. For a two-dimensional domain, an analytic solution is found as [72]

$$\begin{aligned} u(x,y,t) &= u_0(x,y,0)\exp\left[-2\nu(2m\pi)^2 t\right], \\ v(x,y,t) &= v_0(x,y,0)\exp\left[-2\nu(2m\pi)^2 t\right], \\ p(x,y,t) &= p_0(x,y,0)\exp\left[-4\nu(2m\pi)^2 t\right], \end{aligned} \tag{6.4.2}$$

which is depending on the physical dissipation ν. The exponential dependence on time hints that the initial vortical structure dissipates over time and thus $u = v = p = 0$ is expected for $t \to \infty$. Since the velocity is analytically known, the kinetic energy and its change over time, i.e. $\partial E_{kin}/\partial t$, can be computed analytically. Since dissipation is the mechanism by which kinetic energy reduces over time, the comparison of the computed and analytic kinetic energy can be used to quantify the numerical dissipation inherent in each scheme. Furthermore, any differences among incompressible methods may indicate an influence on the behaviour of numerical dissipation.

Drikakis *et al.* [176] investigated the Taylor–Green vortex for a weakly compressible and three-dimensional case. They found that after Re=3000, the solutions showed a Reynolds number independence after which there was no noticeable difference in the production of kinetic energy, using a dimensionless time-scale. Brachet *et al.* [177] investigated the transition to turbulence using Reynolds numbers in the range of $100 < Re < 3000$ and investigating the small scale structures in the flow. For that, a mesh size of 256^3 elements was chosen. Their data suggest that the Reynolds number independent solution may indeed exist but also that the structures require

longer development times with increasing Reynolds number, here using a dimensional time-scale. This provides a trade-off problem between the computational cost and highest computable Reynolds number. In this study, a Reynolds number of Re=1000 is chosen as a middle ground at which two-dimensional turbulent structure may develop while keeping the computational cost at a reasonable limit. The time integration period is set to 200 seconds after which the flow is found to have reached a nearly time-independent solution; here, the pressure values are of the order of $\mathcal{O}(10^{-8})$. Three different mesh sizes are investigated using 32^2, 64^2 and 128^2 computational elements. For all but the AC method — on the 128^2 mesh — were solutions obtained up to 200 seconds. Due to the excessive computational cost incurred by the AC method for unsteady flows, the time interval was shortened to 50 seconds of simulated time, which will be discussed in detail below.

Brachet *et al.* [178] performed direct numerical simulations on a 800^2 and 2048^2 computational grid to study two-dimensional turbulent structures. These did, indeed, show qualitative turbulent structures while the quantitative assessment showed differences to the expected three-dimensional state. For example, the spectral index n was slightly higher than Kolmogorov's much celebrated $n = -5/3$ law which he postulated should be constant and present for any turbulent flow. Chapelier *et al.* [179] proposed a novel multiscale approach within the discontinuous Galerkin framework. Compared to LES simulations, which provide the needed truncated physical dissipation through a sub-grid scale model, they showed that only a second-order scheme was capable to provide sufficient numerical dissipation to capture the correct energy transfer mechanism. Higher-order schemes with less inherent numerical dissipation showed a pile-up of energies at the small scales which resulted in a non-physical energy transfer from the largest down to the smallest scales. Bull and Jameson [180] introduced a new flux reconstruction, specifically designed for optimising the wave dissipation and dispersion errors. Their scheme was validated against the Taylor–Green problem where they showed the need of accurate schemes to capture turbulent structures. Using a spectral element method, Shu *et al.* [181] showed that higher-order filtering can have adverse effects on the convergence rate and further found that the enstrophy and kinetic energy may not be necessarily suitable candidates to examine the accuracy of a Taylor–Green solution. Sifounakis *et al.* [182] proposed a new adaptive mesh refinement approach for Cartesian grids and showed slightly increased convergence rates for a refined mesh topology, while Dumbser *et al.* [155] proposed a unified higher-order framework for solid and continuum mechanics where the Taylor–Green vortex was tested at laminar Reynolds numbers where good agreement with the data of Brachet *et al.* [177] was shown. In a recent study, El Rafei *et al.* [153] investigated the Taylor–Green vortex problem under similar conditions as Drikakis *et al.* [176] and gave a modified equation analysis that was capable to predict the shape and structure of the numerical dissipation.

Most of the studies concerned with the Taylor–Green vortex use three-dimensional domains, with the exception of Brachet *et al.* [178] studying two-dimensional turbulent structures. The work of Sifounakis *et al.* [182] and Dumbser *et al.* [155] also showed two-dimensional simulations, among others, however these were purely per-

formed for validation purposes. Those studies concerned with the numerical dissipation and its influence on the simulation are all three-dimensional, but no analytical solution is known for this case, for which then direct numerical simulation data needs to be consulted. For the current case, the accuracy and numerical dissipation behaviour of each scheme in different incompressible framework is of interest. Through the use of the analytic expression, we are able to make a quantitative analysis on the numerical dissipation. It would be also interesting to conduct three-dimensional simulations here to gain further insight on turbulent structures, however, as already stated in previous Sections, the space-time coupling in the MCB scheme does not allow for a trivial expansion to three-dimensional space as this would result in a four-dimensional space-time. Thus, the two-dimensional space is examined here for which further analysis can be done on the behaviour of different schemes in an unsteady regime.

Figure 6.47 and 6.48 show the difference of the computed kinetic energy k_{num} to the analytical kinetic energy k. The results are shown on three different grids with 32^2, 64^2 and 128^2 elements, where the results are scaled by the maximum value of k so as to make them comparable across grid sizes. The results are shown for the first 50 seconds of simulated time. On the left of Figure 6.47, the AC method is shown. Here, the non CB and central scheme both produce the highest deviation from the analytical kinetic energy while the MCB scheme and the RS-based approaches show a similar level of difference. The initial difference of the MCB scheme decays much faster than the Rusanov RS and its hybridisation with the MCB scheme on the coarse and medium grid, while on the fine grid the situation is reversed. Here, however, the SCB and both Rusanov RS approaches produces the highest deviation, making the non CB and central scheme more accurate. Interestingly, going from a coarse to a fine grid, an increase in error can be seen for the SCB scheme and Rusanov-based approaches. The error for the MCB scheme remains largely constant for all grid levels while both the non CB and central scheme show a slight increase as well.
For the same Figure on the right, results obtained with the FSAC-PP method are shown. Compared to the AC method, oscillations in the numerical scheme can be observed for the time interval $10 < t < 20$, which are more pronounced on the coarse level while being almost diminished on the medium grid and absent on the fine grid. All schemes except the Rusanov-based approaches show this tendency. In-fact, as can be seen for the coarse and medium grid, the Rusanov RS by itself shows initially the same error development as its hybrid version combined with the MCB scheme. In the interval of $5 < t < 10$, those two curves part ways and the hybrid scheme consisting of the Rusanov RS and the MCB scheme provide less error than the Rusanov RS by itself. The initial peak is initially better predicted by the MCB scheme than the SCB, central and non CB scheme although the central and non CB scheme provide a steeper reduction in error and provide again more accurate results after $t > 10$ on the coarse and medium mesh. On the fine mesh, all schemes provide similar error curves where the Rusanov-based approach produce the least error initially while providing higher errors in the range of $10 < t < 20$ on all grids. This highlights two things; first, the RS approach does indeed promote accuracy in the FSAC-PP framework while secondly, the dissipative nature of the Rusanov RS

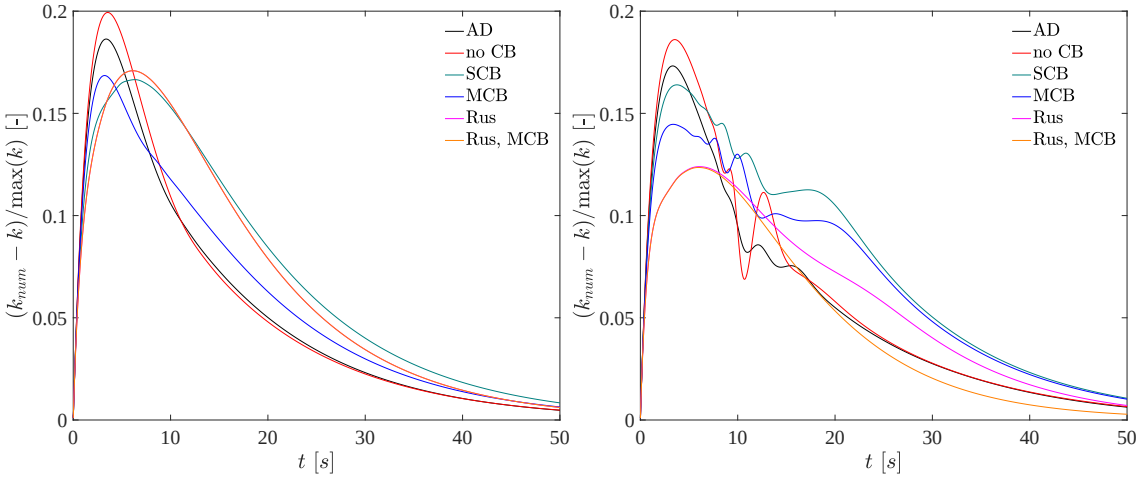

(a) AC, $n_x \times n_y = 32^2$ (b) FSAC-PP, $n_x \times n_y = 32^2$

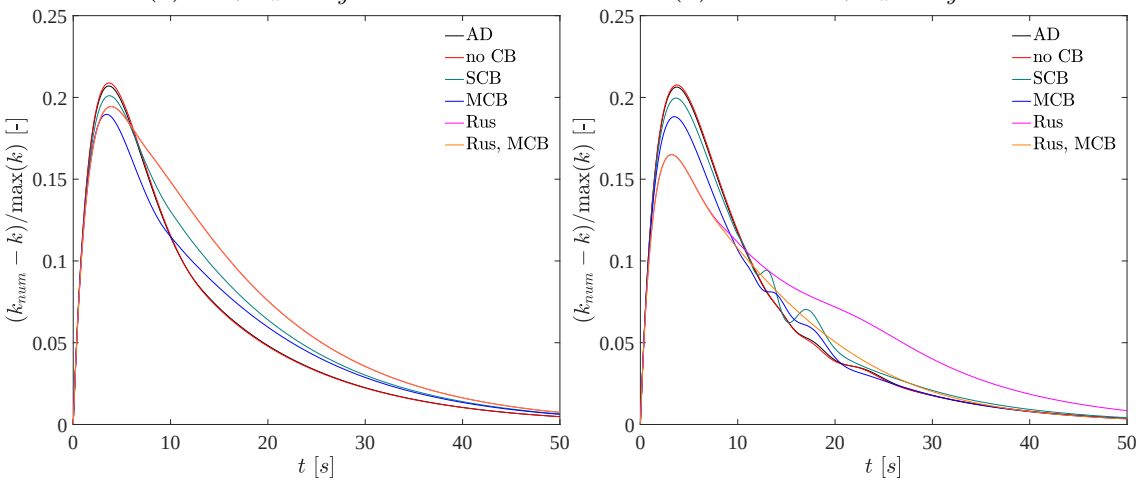

(c) AC, $n_x \times n_y = 64^2$ (d) FSAC-PP, $n_x \times n_y = 64^2$

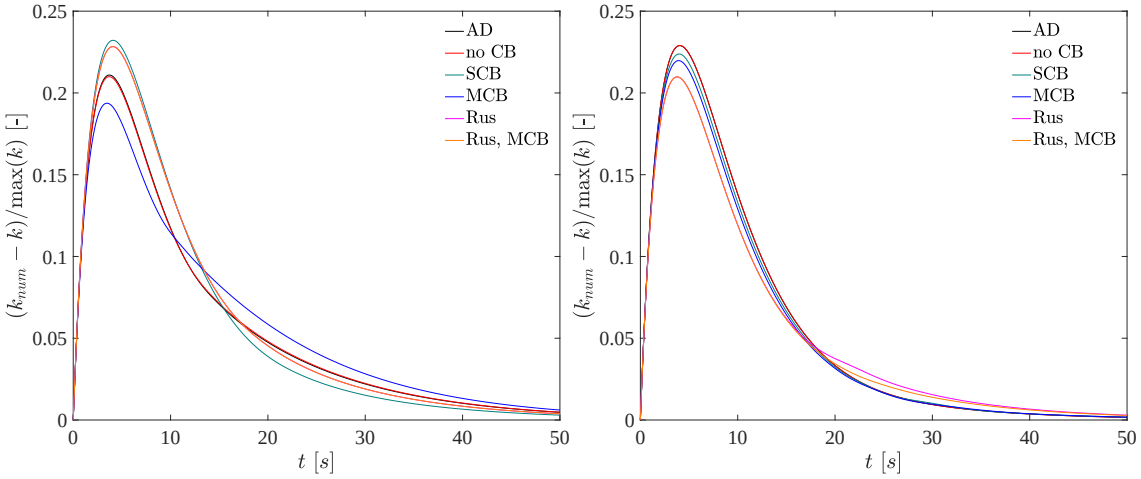

(e) AC, $n_x \times n_y = 128^2$ (f) FSAC-PP, $n_x \times n_y = 128^2$

Figure 6.47: Evolution of the error in the computed kinetic energy compared to the analytic kinetic energy for different grid sizes of $n_x \times n_y = 32^2$, 64^2 and 128^2 using the AC method (left) and FSAC-PP method (right).

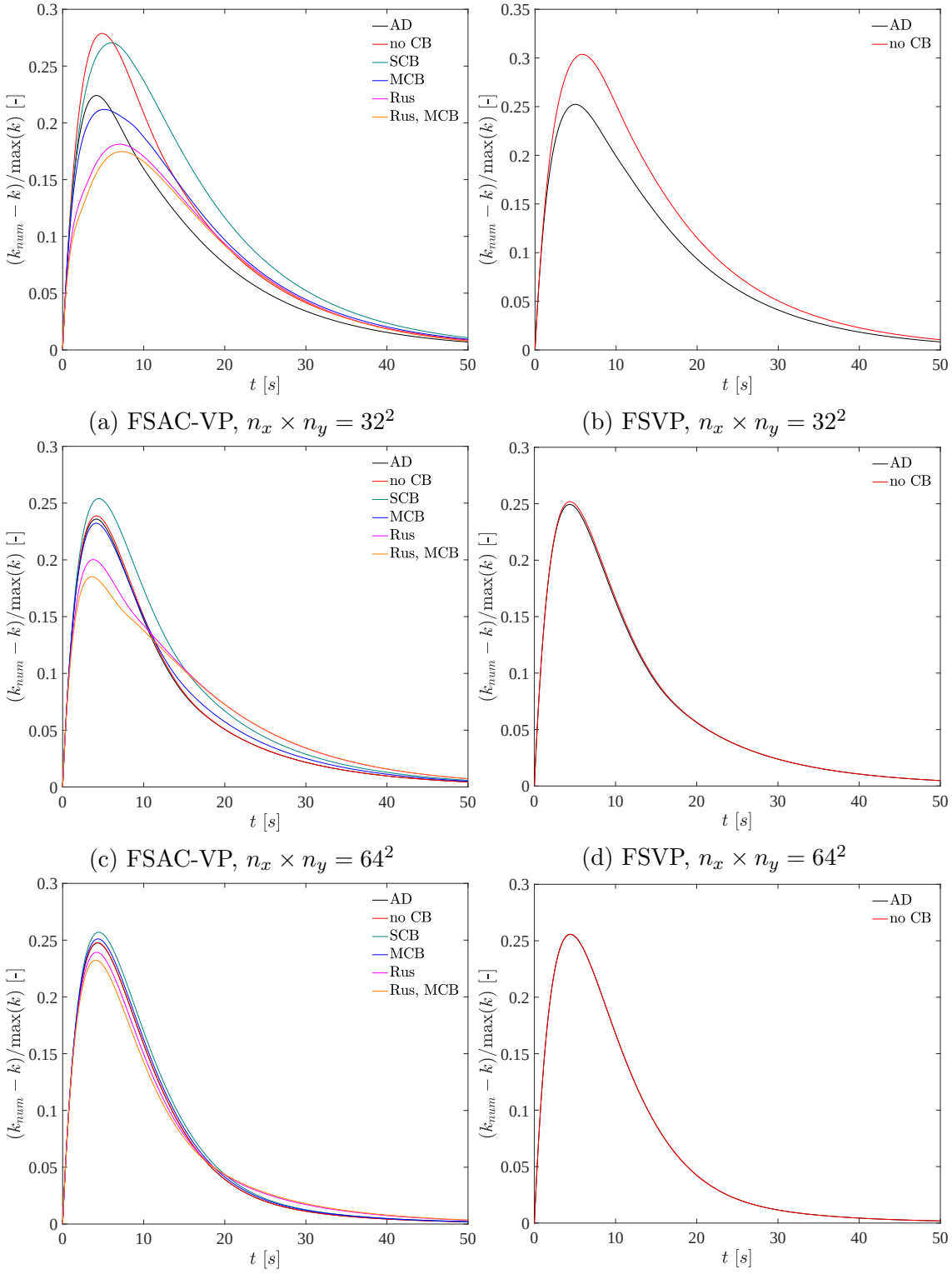

(a) FSAC-VP, $n_x \times n_y = 32^2$

(b) FSVP, $n_x \times n_y = 32^2$

(c) FSAC-VP, $n_x \times n_y = 64^2$

(d) FSVP, $n_x \times n_y = 64^2$

(e) FSAC-VP, $n_x \times n_y = 128^2$

(f) FSVP, $n_x \times n_y = 128^2$

Figure 6.48: Evolution of the error in the computed kinetic energy compared to the analytic kinetic energy for different grid sizes of $n_x \times n_y = 32^2$, 64^2 and 128^2 using the FSAC-VP method (left) and FSVP method (right).

is shown when longer time intervals are considered. Another interesting fact can be observed on the coarse and medium grid, where the MCB scheme provides smaller error curves than the SCB scheme while the shape and structure of the oscillations match each other. The oscillatory behaviour of the central and non CB scheme does not seem to correlate with that of the CB approaches. Similar to the AC method, those schemes also provide the highest error curves, here for all grid sizes.
In Figure 6.48 on the left, the results for the FSAC-VP method are shown. First of all, the oscillations shown in the FSAC-PP method are not present which may be attributed to the parabolic pressure equation, as the pressure is driving the development of the velocity field. This is a reasonable conclusion and is supported by the curves showing the error of the pressure in Figure 6.49 and 6.50, where no oscillations in the pressure are observed for the FSAC-VP method while still being present for the FSAC-PP method. Throughout this work, it has been shown that the elliptic Poisson equation was able to provide a smooth pressure field from which the velocity was developed. This has shown favourable convergence properties of the FSAC-PP method compared to the other incompressible methods. In this case, however, the flow is not considered to be stationary but unsteady. The elliptic Poisson equation of the FSAC-PP method, Eq.(3.3.16) is repeated here for convenience

$$\nabla^2 p^{n+1} = -\frac{\rho}{\Delta\tau}\nabla \cdot \mathbf{u}^*$$

as well as the parabolic pressure transport equation of the FSAC-VP and FSVP method, Eq.(3.3.30)

$$\frac{1}{\beta}\frac{p^{n+1} - p^n}{\partial\tau} = \frac{\Delta\tau}{\rho}\nabla^2 p^{n+1} - \nabla \cdot \mathbf{u}^*.$$

While Eq.(3.3.16) only contains information in space (hence its elliptic behaviour), it is unable to provide a smooth pressure field as time progresses. Eq.(3.3.30), on the other hand, is bounded in time (hence its parabolic behaviour) which means that the equation is able to provide not only a smooth pressure field in space but also in time. Arguably, the time-derivative in Eq.(3.3.16) is in pseudo-time and it may be argued that this cannot be interpreted as real time. However, it is only in pseudo-time because the exact relation between the density and pressure is not known. As discussed in Section 3.3.1, this ill-defined functional relation is expressed by the β parameter and once this expression is known, Eq.(3.3.16) would hold for unsteady flows as well. For the moment, the equation may be seen to be only valid in pseudo-time but that does not remove its inherent ability to possess some form of memory effect of the pressure field for which physical bounds are imposed. Indeed, the parabolic behaviour is imposing a single characteristic line into the flow which provides the natural barrier, for example as a limited information propagation speed or the presence of a domain of dependence and influence separated by the characteristic. The elliptic Poisson equation does not have the same information in time so that subsequent time-steps are not related to each other and oscillations may occur in the pressure, which then form oscillations in the velocity field. Returning back to Figure 6.48, for the FSAC-VP method the non CB and SCB scheme show the least accurate results across different grid levels, while from the medium grid level onwards, the non CB scheme matches the accuracy of the central scheme. It is

again the Rusanov RS with and without the MCB scheme which produces the least amount of error for the initial peak while the error curves increase slightly above the other schemes as time increases. The non CB scheme shows a tendency to reduce the error when increasing the grid size which is matching by the FSVP method on the right side of Figure 6.48. For both the AC and FSAC-PP method, this tendency was reversed. The central scheme does not seem to change its accuracy over different grid levels for the FSAC-VP method while Rusanov-based approaches and MCB scheme do show an increase again in error.
At the finest grid level of 128^2 elements, the error curves equalise and little difference among the numerical schemes can be observed. However, looking across the different grids, we can confirm the observation of Chapelier *et al.* [179] who stated that higher-order schemes produce too little numerical dissipation which results in larger errors. In their case, they observed a pile-up of energy at the small scales which is not investigated here. However, it can be seen that the third-order accurate non CB scheme does produce in most cases the least accurate results. Those schemes that have a sufficient amount of inherent numerical dissipation, provide more accurate dissipation rates and thus smaller errors in the predicted kinetic energy. At the same time, it has to be mentioned, that the MCB scheme without the Rusanov RS seems to be located between the two extremes of having either too much or too little dissipation. For all incompressible methods, it is more accurate than the non CB scheme which uses the same polynomial flux reconstruction while for the FSAC-PP and FSAC-VP method its combination with the Rusanov RS and the Rusanov RS by itself are the only schemes able to produce less errors, at least for the initial peak in error. For all methods, except the FSVP method due to its non-hyperbolic nature, the MCB shows smaller error curves than the SCB scheme which may show its advantage over single-directional treatment of purely vortical flows.

As already highlighted in the discussion above, the pressure plays a dominant role in the current case. Therefore, the computed L_1 error norm at each time-step is plotted in Figure 6.49 and 6.50 for the different incompressible methods. The L_1 error curves for pressure using the AC method are shown in Figure 6.49 on the left-hand side. On all grids, but especially on the coarse one, a double-peak structure can be spotted which is most pronounced for the SCB scheme and Rusanov RS with and without the MCB scheme. They do not present perfect double-peak structure on the medium and fine grid, but it can be still argued that the structures seen on the coarse grid are simply more dissipated on the medium and fine grid. Drikakis *et al.* [176] argued that these structures are likely due to the dispersive properties of their third-order scheme. They used a higher Reynolds number but also a three-dimensional space. It is possible that those two factors alone can produce more pronounced double-peak structures which are less present at the lower Reynolds number in two-dimensional space. In terms of the characteristic approach, the SCB and MCB scheme along with its Godunov-type approach using the Rusanov RS produce the highest errors. On the fine grid, those approaches reduce in error and are more accurate than the central and non CB scheme while the MCB scheme produces an almost constant level of error which on the fine grid becomes the least accurate scheme in terms of the pressure. That is, while the MCB scheme does not decrease in error, all the

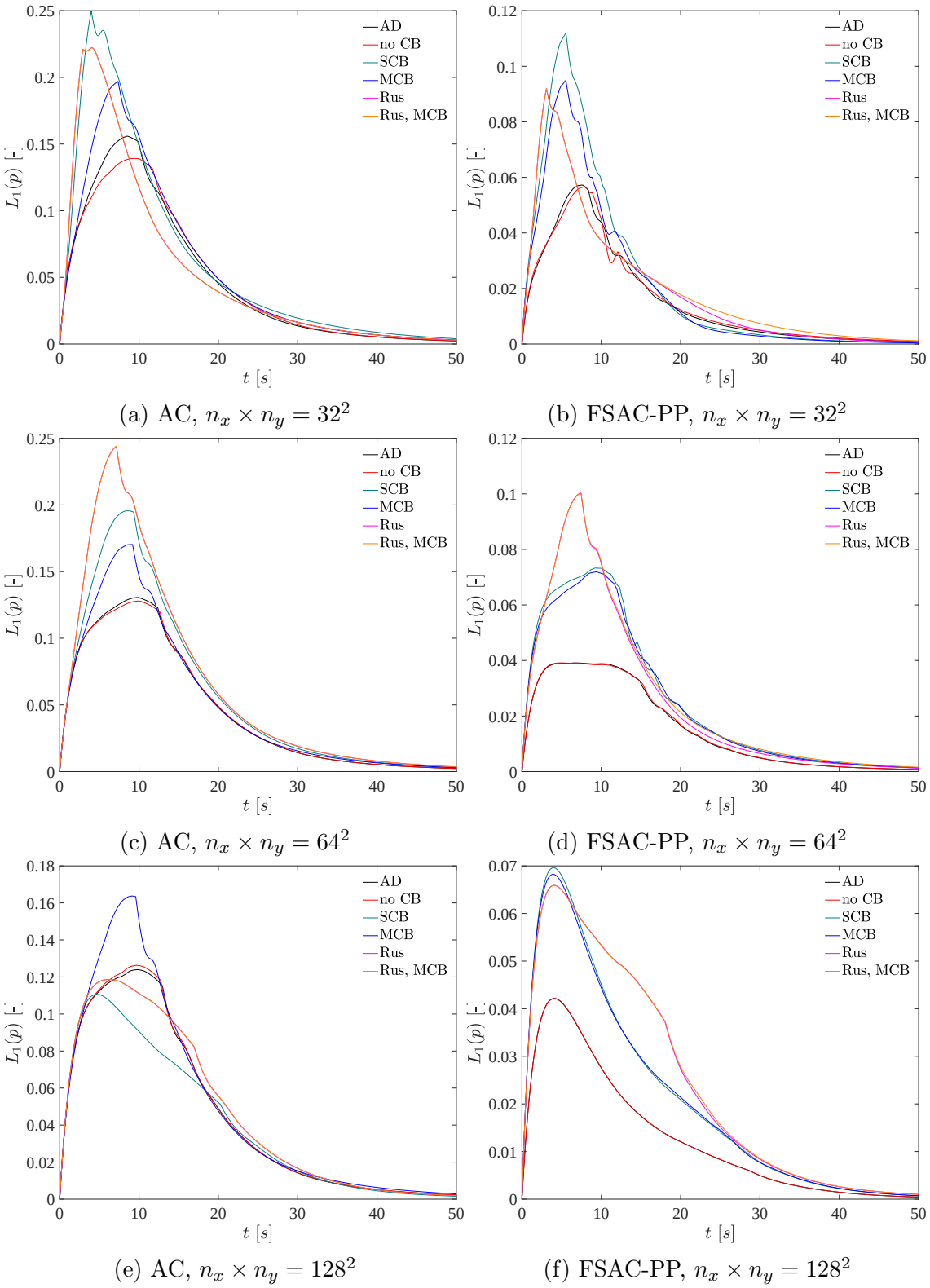

(a) AC, $n_x \times n_y = 32^2$

(b) FSAC-PP, $n_x \times n_y = 32^2$

(c) AC, $n_x \times n_y = 64^2$

(d) FSAC-PP, $n_x \times n_y = 64^2$

(e) AC, $n_x \times n_y = 128^2$

(f) FSAC-PP, $n_x \times n_y = 128^2$

Figure 6.49: Evolution of the L_1 error norm for the pressure for different grid sizes of $n_x \times n_y = 32^2$, 64^2 and 128^2 using the AC method (left) and FSAC-PP method (right).

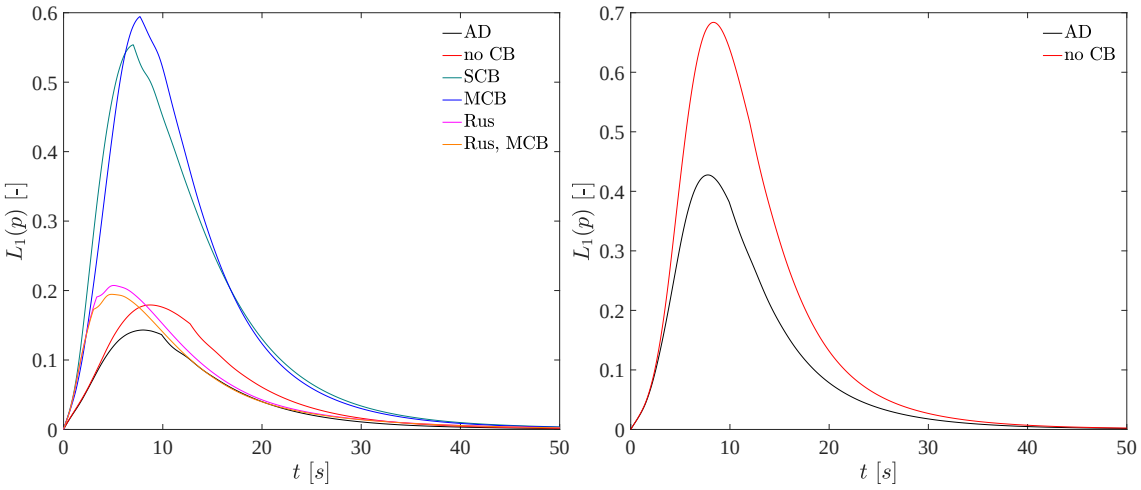

(a) FSAC-VP, $n_x \times n_y = 32^2$

(b) FSVP, $n_x \times n_y = 32^2$

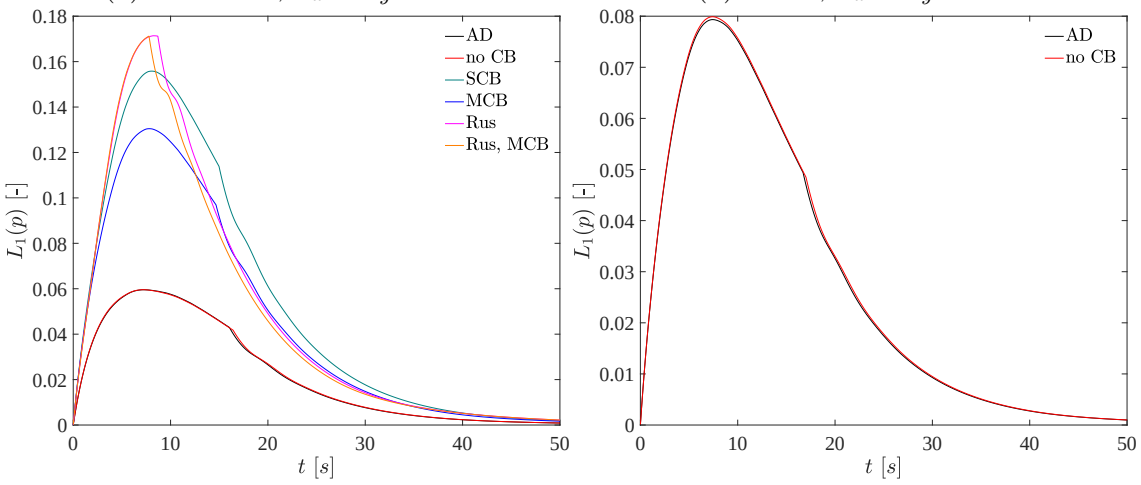

(c) FSAC-VP, $n_x \times n_y = 64^2$

(d) FSVP, $n_x \times n_y = 64^2$

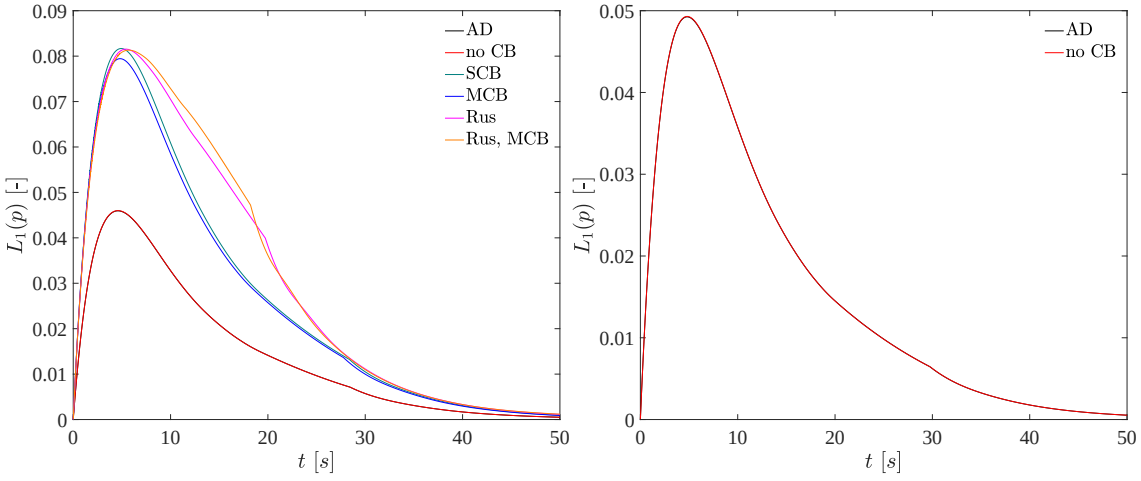

(e) FSAC-VP, $n_x \times n_y = 128^2$

(f) FSVP, $n_x \times n_y = 128^2$

Figure 6.50: Evolution of the L_1 error norm for the pressure for different grid sizes of $n_x \times n_y = 32^2$, 64^2 and 128^2 using the FSAC-VP method (left) and FSVP method (right).

other schemes do.
For the same Figure on the right, the results obtained with the FSAC-PP method are shown. A much weaker double-peak structure can be identified which may be again explained by the smoothing properties of the elliptic Poisson equation. However, the oscillations seen in Figure 6.47 for the difference in kinetic energy are still present, especially on the coarse and medium grid. For the fine grid solution, smooth pressure error curves are obtained. As discussed above, these oscillations are due to the lack of memory of the flow in the Poisson solver who is smoothing the pressure field only locally in time but not with respect to the pressure field from the previous time-step. While the central and non CB scheme show a flat peak on the medium grid, they show again smaller errors than the CB approaches. In terms of total error, however, it can be seen that the error curves for the pressure are approximately a factor of two smaller than those obtained with the AC method.
For the FSAC-VP method in Figure 6.49f on the left, we can see a sharp increase in error on the coarse grid for both characteristic schemes. The errors normalise on the medium and fine grid and approach the same level as that of the FSAC-PP method, showing a reduction in error by a factor of seven, approximately. Similar to the FSAC-PP method, the double-peak structures are more dissipated compared to the AC method but still faintly present. Furthermore, the coarse and medium grid is free from oscillations in the SCB and MCB scheme as seen for the FSAC-PP method. The various Godunov-type approaches, i.e. the SCB scheme and the Rusanov RS with and without the MCB scheme, show smooth curves for all mesh levels but also the largest errors, except for the coarse grid. The central and non CB scheme show again the least error with smooth profiles, free of dispersive errors. Those dispersive errors in the non CB scheme as seen in the FSAC-PP method are not present for the FSAC-VP method which may, again, be attributed to the parabolic pressure transport equation.
For the FSVP method on the right-hand side of the same Figure, the first larger difference between it and the FSAC-VP method can be observed. Here, the central and non CB scheme produce error curves that are a factor of 2–4 higher than those obtained with the FSAC-VP method. The only difference here being that the FSAC-VP method contains the perturbed continuity equation of the AC method while the momentum and pressure transport equation are identical for both methods. The original idea of the FSAC-VP method was to extend the FSVP method by the continuity equation to provide a hyperbolic first Fractional-Step so as to use the developed Godunov-type schemes in this work. However, Figure 6.50 reveals that there is a benefit or predicting an initial pressure field, albeit from a non-physical continuity equation, for which then reduced error curves are obtained. In general, this discussion highlights the dependence of the Navier–Stokes equations on the incompressible method that is used. Although all numerical schemes and other conditions are kept the same, errors in the pressure can still arise due to different pressure treatments of the incompressible methods and their mathematical characteristics.

Tables 6.25–6.28 show the integrated L_0 and L_1 error for each method using the different numerical schemes along with the average iterations that were needed to

Table 6.25: Comparisons of the integrated L_0 and L_1 errors for the AC method on different meshes at a Reynolds number of Re=1000. The average number of iterations per time-step is given to judge the computational cost.

		AD	no RS			Rusanov RS	
$n_x \times n_y$		no CB	no CB	SCB	MCB	no CB	MCB
	iterations	882	947	928	960	946	946
	$L_0(u)$	6.07e-02	6.19e-02	6.91e-02	6.52e-02	6.17e-02	6.17e-02
	$L_0(v)$	6.07e-02	6.19e-02	6.91e-02	6.52e-02	6.17e-02	6.17e-02
32×32	$L_0(p)$	2.34e-02	2.36e-02	2.99e-02	2.57e-02	2.68e-02	2.68e-02
	$L_1(u)$	2.74e-02	2.74e-02	3.56e-02	3.07e-02	3.27e-02	3.27e-02
	$L_1(v)$	2.74e-02	2.74e-02	3.56e-02	3.07e-02	3.27e-02	3.27e-02
	$L_1(p)$	1.23e-02	1.22e-02	1.58e-02	1.40e-02	1.37e-02	1.37e-02
	iterations	2433	2662	2487	2701	2583	2583
	$L_0(u)$	6.21e-02	6.22e-02	6.81e-02	6.47e-02	7.11e-02	7.11e-02
	$L_0(v)$	6.21e-02	6.22e-02	6.81e-02	6.47e-02	7.11e-02	7.11e-02
64×64	$L_0(p)$	2.36e-02	2.36e-02	2.82e-02	2.53e-02	3.10e-02	3.10e-02
	$L_1(u)$	2.81e-02	2.80e-02	3.18e-02	3.09e-02	3.42e-02	3.42e-02
	$L_1(v)$	2.81e-02	2.80e-02	3.18e-02	3.09e-02	3.42e-02	3.42e-02
	$L_1(p)$	1.18e-02	1.18e-02	1.50e-02	1.31e-02	1.69e-02	1.69e-02
	iterations	9378	9397	7612	9578	7975	7974
	$L_0(u)$	2.11e-01	2.11e-01	2.11e-01	2.15e-01	2.19e-01	2.19e-01
	$L_0(v)$	2.11e-01	2.11e-01	2.11e-01	2.15e-01	2.19e-01	2.19e-01
128×128	$L_0(p)$	9.26e-02	9.30e-02	8.94e-02	9.87e-02	9.72e-02	9.71e-02
	$L_1(u)$	8.92e-02	8.97e-02	8.12e-02	9.75e-02	8.65e-02	8.65e-02
	$L_1(v)$	8.92e-02	8.97e-02	8.12e-02	9.75e-02	8.65e-02	8.65e-02
	$L_1(p)$	4.60e-02	4.63e-02	4.09e-02	5.06e-02	4.70e-02	4.70e-02

converge in pseudo time. This measure can be used as an indication as to what the computational cost per time step is. The integral values for the error were obtained as

$$L_j(\phi) = \frac{1}{T}\int_0^T L_j(\phi(t))\mathrm{d}t, \qquad j = 0, 1 \tag{6.4.3}$$

where the L_0 and L_1 norm are defined by Eq.(6.1.2) and Eq.(6.1.3), respectively. In Table 6.25, the errors for the AC method are shown. A sharp increase in error can be seen for all schemes on the 128^2 mesh which is attributed to the shorter simulated time of 50 seconds in total, while the solutions on the 64^2 and 32^2 grid were obtained for the simulation time of 200 seconds, for reasons stated in the introduction to this Section. The error stays largely constant when going from the coarse to medium grid for the L_1 norm for both velocity and pressure. Due to the

Table 6.26: Comparisons of the integrated L_0 and L_1 errors for the FSAC-PP method on different meshes at a Reynolds number of Re=1000. The average number of iterations per time-step is given to judge the computational cost.

		AD	no RS			Rusanov RS	
$n_x \times n_y$		no CB	no CB	SCB	MCB	no CB	MCB
	iterations	22	24	30	29	802	28
	$L_0(u)$	6.31e-02	6.41e-02	7.29e-02	7.11e-02	6.83e-02	5.32e-02
	$L_0(v)$	5.37e-02	6.01e-02	3.28e-02	3.38e-02	3.59e-02	5.31e-02
32×32	$L_0(p)$	8.43e-03	9.06e-03	1.24e-02	1.12e-02	1.10e-02	1.15e-02
	$L_1(u)$	3.04e-02	3.10e-02	3.87e-02	3.79e-02	4.05e-02	3.02e-02
	$L_1(v)$	2.49e-02	2.86e-02	1.45e-02	1.55e-02	1.90e-02	2.98e-02
	$L_1(p)$	3.88e-03	3.93e-03	5.64e-03	4.96e-03	4.97e-03	5.24e-03
	iterations	52	55	90	85	90	84
	$L_0(u)$	5.96e-02	6.00e-02	5.99e-02	5.74e-02	6.73e-02	5.46e-02
	$L_0(v)$	5.95e-02	5.97e-02	6.06e-02	5.95e-02	4.66e-02	6.26e-02
64×64	$L_0(p)$	8.58e-03	8.62e-03	1.46e-02	1.38e-02	1.40e-02	1.43e-02
	$L_1(u)$	2.58e-02	2.59e-02	2.75e-02	2.58e-02	3.43e-02	2.64e-02
	$L_1(v)$	2.58e-02	2.58e-02	2.78e-02	2.73e-02	2.15e-02	3.13e-02
	$L_1(p)$	3.94e-03	3.96e-03	6.45e-03	6.27e-03	6.59e-03	6.85e-03
	iterations	165	179	276	258	288	263
	$L_0(u)$	5.50e-02	5.50e-02	5.50e-02	5.45e-02	5.81e-02	5.69e-02
	$L_0(v)$	5.50e-02	5.50e-02	5.50e-02	5.48e-02	5.62e-02	5.74e-02
128×128	$L_0(p)$	7.73e-03	7.73e-03	1.28e-02	1.26e-02	1.36e-02	1.36e-02
	$L_1(u)$	2.13e-02	2.13e-02	2.15e-02	2.14e-02	2.43e-02	2.36e-02
	$L_1(v)$	2.13e-02	2.13e-02	2.16e-02	2.15e-02	2.33e-02	2.39e-02
	$L_1(p)$	3.22e-03	3.23e-03	5.34e-03	5.31e-03	6.13e-03	6.15e-03

initial conditions, see Figure 6.46, and the analytic solution for the decay in velocity according to Eq.(6.4.2), it is expected that the flow should preserve the symmetric nature and thus the L_0 and L_1 norm should produce the same result for the u- and v-velocity component. This is the case for all schemes on all grid levels for the AC method. The average number of iterations required to converge within one pseudo time-step is increasing by a factor of 3–4 when decreasing the mesh spacing by half, which corresponds to a fourfold increase in number of elements. Thus, the increased resolution comes at the cost of increased computational time.

The results for the FSAC-PP method are shown in Table 6.26. Here, the L_0 and L_1 norm are no longer the same for the velocity components. While large differences are observed on the coarse grid (up to 53% difference for the Rusanov RS), the maximum difference reduces to 37% on the medium and 4% on the fine grid, respectively. Thus, the symmetric nature of the flow is not preserved. The absolute

Table 6.27: Comparisons of the integrated L_0 and L_1 errors for the FSAC-VP method on different meshes at a Reynolds number of Re=1000. The average number of iterations per time-step is given to judge the computational cost.

		AD	no RS			Rusanov RS	
$n_x \times n_y$		no CB	no CB	SCB	MCB	no CB	MCB
	iterations	104	111	143	128	124	122
	$L_0(u)$	7.76e-02	8.95e-02	9.88e-02	9.33e-02	7.29e-02	7.12e-02
	$L_0(v)$	7.76e-02	8.95e-02	9.88e-02	9.33e-02	7.29e-02	7.12e-02
32×32	$L_0(p)$	1.64e-02	2.16e-02	4.99e-02	4.80e-02	2.39e-02	2.29e-02
	$L_1(u)$	3.29e-02	3.64e-02	4.02e-02	3.68e-02	3.57e-02	3.54e-02
	$L_1(v)$	3.29e-02	3.64e-02	4.02e-02	3.68e-02	3.57e-02	3.54e-02
	$L_1(p)$	1.06e-02	1.41e-02	3.69e-02	3.71e-02	1.43e-02	1.35e-02
	iterations	86	87	95	90	102	103
	$L_0(u)$	6.66e-02	6.70e-02	7.53e-02	6.99e-02	7.29e-02	7.17e-02
	$L_0(v)$	6.66e-02	6.70e-02	7.53e-02	6.99e-02	7.29e-02	7.17e-02
64×64	$L_0(p)$	1.10e-02	1.11e-02	2.38e-02	2.05e-02	2.18e-02	2.10e-02
	$L_1(u)$	2.81e-02	2.82e-02	3.17e-02	2.96e-02	3.34e-02	3.34e-02
	$L_1(v)$	2.81e-02	2.82e-02	3.17e-02	2.96e-02	3.34e-02	3.34e-02
	$L_1(p)$	5.70e-03	5.73e-03	1.37e-02	1.16e-02	1.29e-02	1.24e-02
	iterations	43	43	44	43	49	49
	$L_0(u)$	5.84e-02	5.84e-02	6.08e-02	5.97e-02	6.29e-02	6.28e-02
	$L_0(v)$	5.84e-02	5.84e-02	6.08e-02	5.97e-02	6.29e-02	6.28e-02
128×128	$L_0(p)$	8.56e-03	8.57e-03	1.53e-02	1.48e-02	1.60e-02	1.59e-02
	$L_1(u)$	2.31e-02	2.31e-02	2.41e-02	2.37e-02	2.61e-02	2.64e-02
	$L_1(v)$	2.31e-02	2.31e-02	2.41e-02	2.37e-02	2.61e-02	2.64e-02
	$L_1(p)$	3.67e-03	3.67e-03	6.68e-03	6.48e-03	7.69e-03	7.82e-03

values of the error norms on the fine level are much smaller than those for the AC method. Since those error norms could be integrated up to 200 seconds of simulated time, it is expected that the errors are smaller as the kinetic energy, Figure 6.47 and 6.48, shows that most of the error is produced within the first 50 seconds of simulated time. For the coarse and medium grid, the errors are of comparable nature for the AC and FSAC-PP method while the error in pressure is an order of magnitude smaller than the AC method. The required number of iterations show a significant reduction compared to the AC method but also increase from the coarse to fine grid. On the coarse, medium and fine mesh, the speed-up on average compared to the AC method was a factor of 34.6, 33.9 and 36.5, respectively. Here, the result of the Rusanov RS on the coarse level has been discarded for the FSAC-PP method. Including this result produces still a speed-up, on average, of a factor of 6.0. This represents significant gains in terms of computational times while the error

Table 6.28: Comparisons of the integrated L_0 and L_1 errors for the FSVP method on different meshes at a Reynolds number of Re=1000. The average number of iterations per time-step is given to judge the computational cost.

		AD	no RS			Rusanov RS	
$n_x \times n_y$		no CB	no CB	SCB	MCB	no CB	MCB
	iterations	149	167	-	-	-	-
	$L_0(u)$	9.51e-02	1.16e-01	-	-	-	-
	$L_0(v)$	9.51e-02	1.16e-01	-	-	-	-
32×32	$L_0(p)$	3.25e-02	4.91e-02	-	-	-	-
	$L_1(u)$	3.56e-02	3.93e-02	-	-	-	-
	$L_1(v)$	3.56e-02	3.93e-02	-	-	-	-
	$L_1(p)$	2.55e-02	4.06e-02	-	-	-	-
	iterations	106	106	-	-	-	-
	$L_0(u)$	7.03e-02	7.07e-02	-	-	-	-
	$L_0(v)$	7.03e-02	7.07e-02	-	-	-	-
64×64	$L_0(p)$	1.29e-02	1.31e-02	-	-	-	-
	$L_1(u)$	2.93e-02	2.95e-02	-	-	-	-
	$L_1(v)$	2.93e-02	2.95e-02	-	-	-	-
	$L_1(p)$	7.13e-03	7.20e-03	-	-	-	-
	iterations	49	49	-	-	-	-
	$L_0(u)$	5.94e-02	5.95e-02	-	-	-	-
	$L_0(v)$	5.94e-02	5.95e-02	-	-	-	-
128×128	$L_0(p)$	9.06e-03	9.06e-03	-	-	-	-
	$L_1(u)$	2.35e-02	2.35e-02	-	-	-	-
	$L_1(v)$	2.35e-02	2.35e-02	-	-	-	-
	$L_1(p)$	3.90e-03	3.90e-03	-	-	-	-

in pressure is lower than the one obtained with the AC method. The symmetrical nature, however, has not been preserved using the FSAC-PP method.
The results for the FSAC-VP method are shown in Table 6.27. First of all, error norms for both the u- and v-velocity component are both identical for all numerical schemes across different grid levels. In terms of their absolute values, they are located between the AC and FSAC-PP method. In terms of the required number of iterations to obtain a converged solution in pseudo time, however, the opposite trend to that observed with the AC and FSAC-PP method is seen; the number of iterations reduce as the mesh size is increased. While 122 iterations, on average for all schemes, were required on the coarse mesh, only 94 iterations were needed on the medium and 45 iterations on the fine grid, respectively. Compared to the FSAC-PP method, this means that over all 4.5 and 1.2 time more iterations were required on the coarse and medium mesh, however, on the fine grid, 5.3 times less iterations

were needed. Compared to the AC method, the overall speed-up on the coarse, medium and fine mesh is 7.7, 27.4 and 193.0 times, respectively. The FSAC-PP method already provided significant gains in terms of computational cost reduction, however, the FSAC-VP method is able to decrease the computational cost even further by a astounding factor of 193.0. This also explains why only the AC method was negatively affected in terms of computational times and results could only be presented up to 50 seconds of simulated times while the FSAC-PP and FSAC-VP method do not share the same problem. It is a known problem in the literature, see for example [183], that the solution of the pressure can take up to 80% of the overall simulation time. In this work, the FSAC-VP method has been specifically designed to represent a physical closure for incompressible flows rather than a numerical closure. The effect can be observed here were a drastic increase in the convergence rate for unsteady flows can be observed. Furthermore, the parabolic restriction on the flow, implying a fixed information propagation, may also explain why the FSAC-VP method is ultimately faster than the FSAC-PP method, where the infinite pressure propagation may induce pressure wave oscillations that require further iterations to be smoothed down to the convergence threshold.
The results for the FSVP method in Table 6.28 show similar results compared to the FSAC-PP method with slightly increased error norms and number of iterations that are required for convergence within a pseudo time-step.

In Figure 6.51 and 6.50, the error norms of pressure are shown for the full 200 seconds of simulated time to visualise the decay of error over time. Here, the y-axis is shown in log scale to further illustrate the exponential decay over time. As can be seen for the AC method in Figure 6.51 on the left-hand side, error curves are only available up to 50 seconds as discussed above on the fine grid. For all incompressible methods, the error is wider spread at $t = 200$ while the curves are closer together on the medium grid. The initial bump that can be observed for all methods in Figure 6.47 and 6.48 is still present, after which an exponential decay sets in, here shown as a linear decay through the log scale. The oscillations that are present in the FSAC-PP method can still be made out, although the long term trend shows that these oscillations are only present during the initial phase after which they decay. Overall, smooth profiles are obtained for all error curves starting at around $t = 50$.

At this point, we can make use of the fact that the kinetic energy is analytically available and start to make judgement on the numerical dissipation inherent to each numerical scheme. By comparing the computed to the calculated kinetic energy, as was done in qualitative way in Figure 6.47 and 6.48, a quantitative assessment of the effect of numerical dissipations can be made. An equation of the form

$$\nu_{num} \propto \frac{1}{n_x \times n_y} \int (k_{num} - k) \mathrm{d}t, \tag{6.4.4}$$

is used for this purpose, where ν_{num} is the numerical dissipation. In a strict sense, the numerical dissipation is defined to be the dissipation that is added by the numerical scheme and due to the truncation error of the Taylor-series. Through a modified

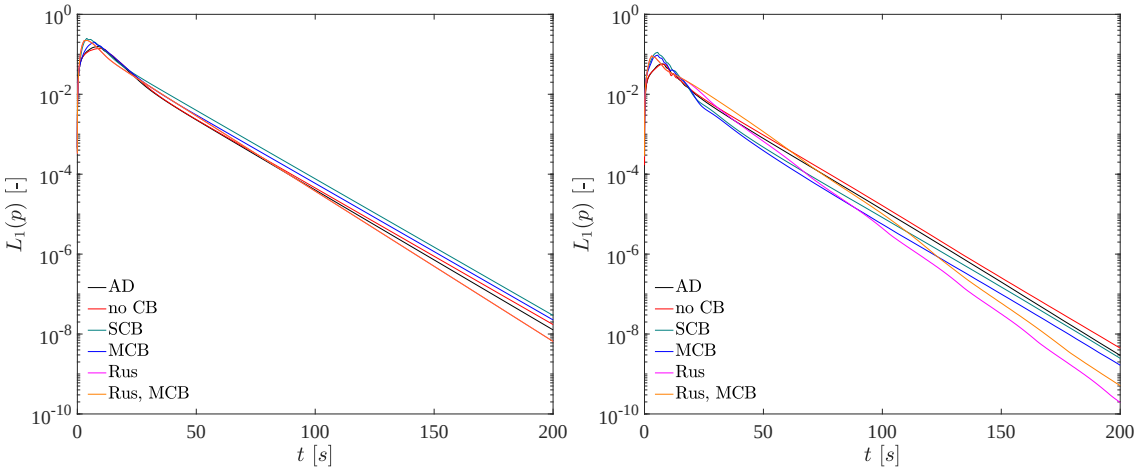

(a) AC, $n_x \times n_y = 32^2$

(b) FSAC-PP, $n_x \times n_y = 32^2$

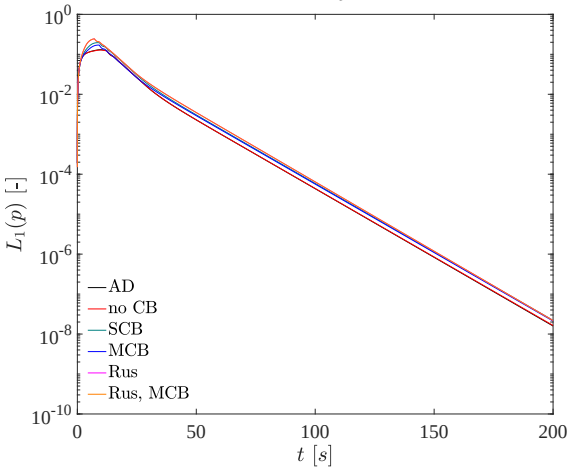

(c) AC, $n_x \times n_y = 64^2$

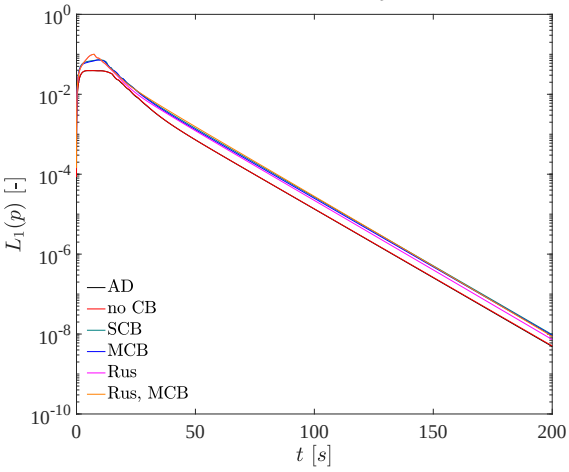

(d) FSAC-PP, $n_x \times n_y = 64^2$

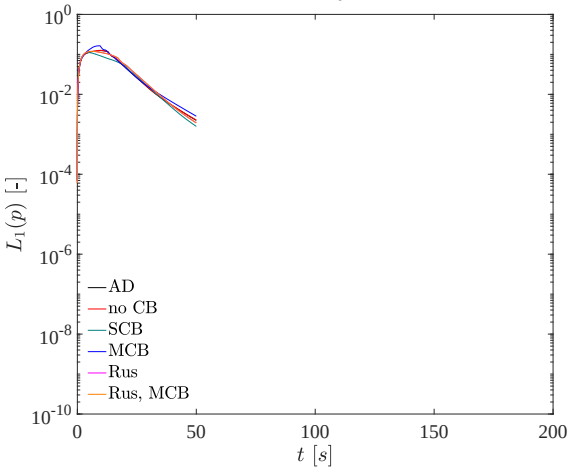

(e) AC, $n_x \times n_y = 128^2$

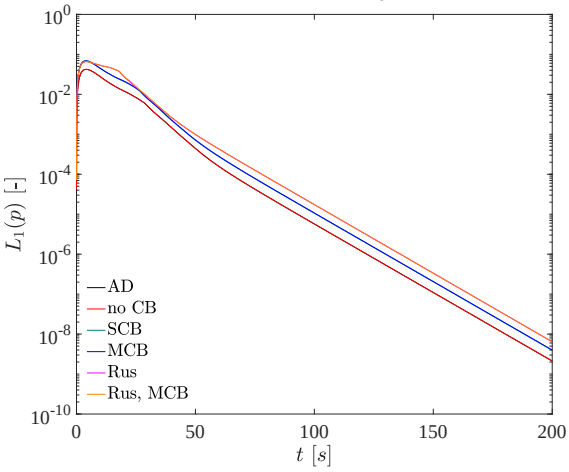

(f) FSAC-PP, $n_x \times n_y = 128^2$

Figure 6.51: Evolution of the L_1 error norm for the pressure over the full simulation period of 200 seconds for different grid sizes of $n_x \times n_y = 32^2$, 64^2 and 128^2 using the AC method (left) and FSAC-PP method (right).

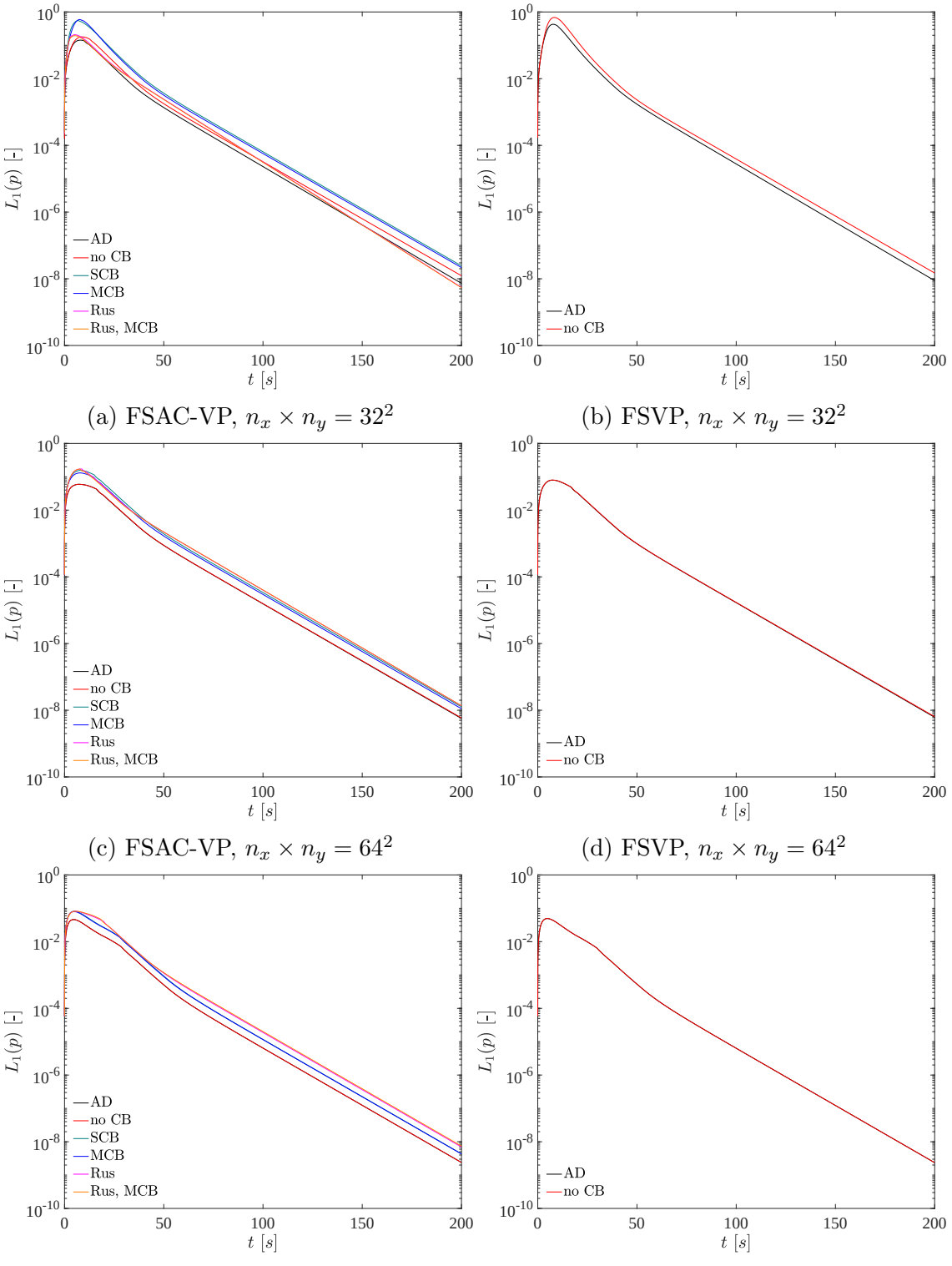

(a) FSAC-VP, $n_x \times n_y = 32^2$

(b) FSVP, $n_x \times n_y = 32^2$

(c) FSAC-VP, $n_x \times n_y = 64^2$

(d) FSVP, $n_x \times n_y = 64^2$

(e) FSAC-VP, $n_x \times n_y = 128^2$

(f) FSVP, $n_x \times n_y = 128^2$

Figure 6.52: Evolution of the L_1 error norm for the pressure over the full simulation period of 200 seconds for different grid sizes of $n_x \times n_y = 32^2$, 64^2 and 128^2 using the FSAC-VP method (left) and FSVP method (right).

equation analysis, this numerical dissipation can be given in an exact form. In the present case, however, no modified equation analysis was carried out which is usually restricted to model equations in one-dimensional space, although El Rafei *et al.* [153] showed that in principle the same approach can be applied to the Navier–Stokes equations, however, in its current form the result do not show a perfect match with the computed dissipation. Thus, we follow the general approach adopted in the literature where the numerical dissipation can be obtained from the difference in the analytic and computed kinetic energy. The result is scaled by the mesh size in Eq.(6.4.4) so as to normalise the result but most importantly, the numerical dissipation is set proportional to the expression on the right-hand side and not equal. This is done with respect to other possibilities through which numerical dissipation can be induced. For example, the time-integration, both in pseudo and dual time will have an effect on the numerical dissipation. Since those time integration schemes are the same for all simulations, they still permit a fair comparison among the schemes and different methods, but we are not able to obtain the exact value for the numerical dissipation.

In Figure 6.53, the numerical dissipation obtained for each method and scheme is shown for all mesh sizes. The AC method shows an increase of numerical dissipation from the coarse to medium grid for the non CB, central and both Rusanov approaches. The MCB scheme produces the same amount of dissipation on both grids while the SCB scheme is the only one capable or reducing the numerical dissipation. Going from the medium to fine grid, all schemes show a reduction. For the FSAC-PP method, only the two Rusanov variants show an increase in numerical dissipation from the coarse to medium grid. From the medium to the fine grid, however, those two approaches reduce the numerical dissipation, as does the SCB scheme, while the other schemes do not show a change in numerical dissipation, at best a slight increase can be observed. In contrast, the FSAC-VP and FSVP method both show a consistent reduction in numerical dissipation for all grid sizes. It is interesting to note here that the central scheme with artificial dissipation possesses the least amount of numerical dissipation for all grids and method, expect the FSAC-PP method. Despite its artificial nature, it still produces reliable results. As highlighted by Chapelier *et al.* [179], it was indeed the second-order central scheme in their work that provided the right amount of dissipation to obtain the correct transfer of kinetic energy from the larger to smaller scales.

In Table 6.29, the absolute values of the numerical dissipation are given for all methods and numerical schemes for each grid level to complement Figure 6.53. It can be seen that the central scheme is indeed the most accurate scheme for all grids and methods except the FSAC-PP method where the Rusanov RS together with the MCB scheme provides the least amount of numerical dissipation. On average, the AC and FSAC-PP method produces again very similar results where the FSAC-PP method is the more accurate approach. The FSAC-VP method, in turn, is more accurate than the FSVP method by itself for the non CB and central scheme but more dissipative than the FSAC-PP and AC method. On the fine grid with 128^2 elements, however, the absolute values of all methods are closer together than on

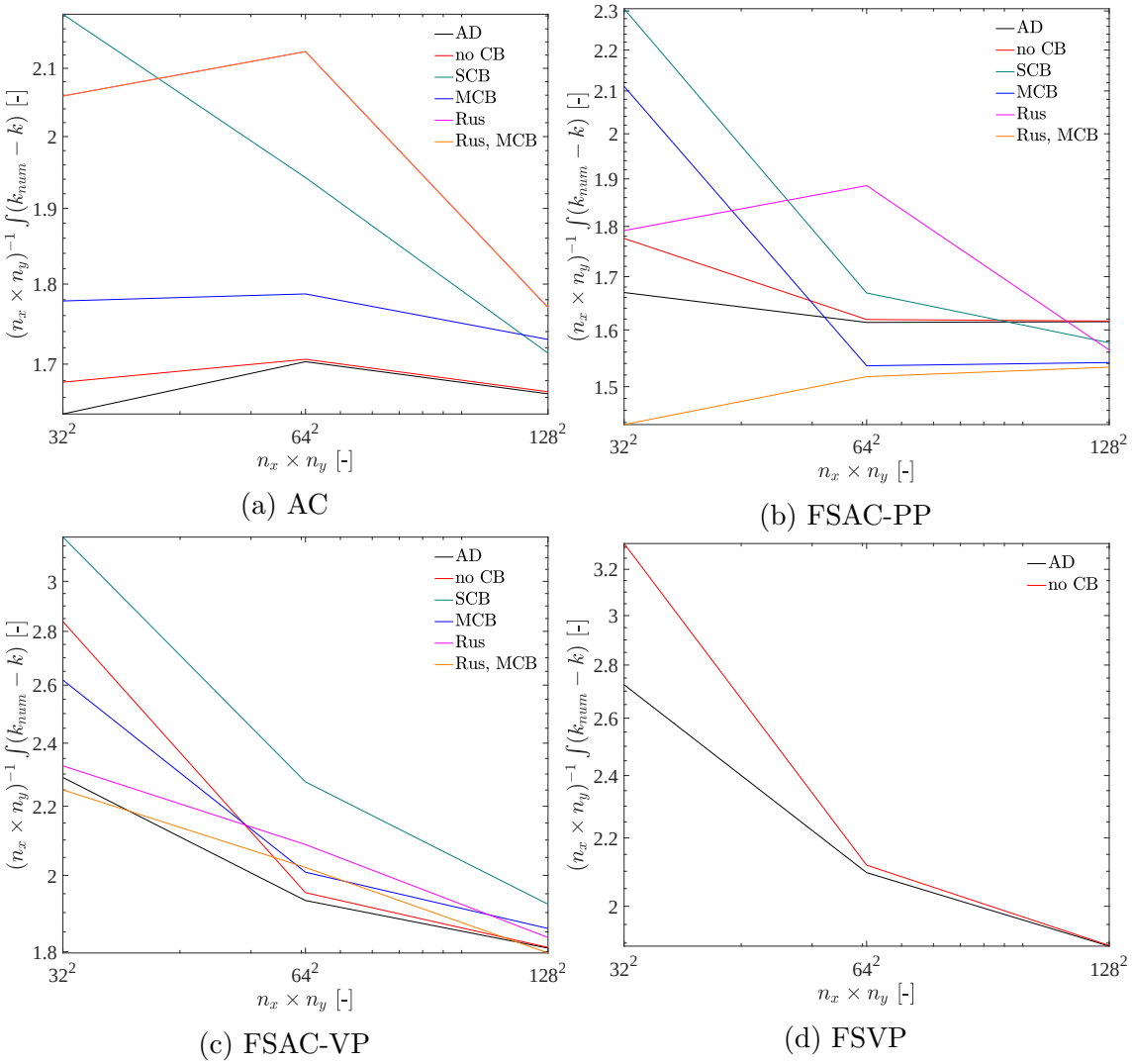

(a) AC

(b) FSAC-PP

(c) FSAC-VP

(d) FSVP

Figure 6.53: Integrated and normalised difference of computed and analytical kinetic energy for different mesh sizes for different incompressible methods and numerical schemes.

the medium or coarse mesh. In-fact, on this mesh level it was seen in Figure 6.47 and 6.48 for the kinetic energy, as well as in Figure 6.49 and 6.50 for the pressure, that the overall error curves were closely matched. The higher amount of numerical dissipation associated to the FSAC-VP and FSVP method may also provide extra stability to suppress numerical oscillations, as those seen in the FSAC-PP method, in addition to the discussion on the different pressure treatments through elliptic and parabolic equations. The Rusanov Riemann solver shows a reduction in numerical dissipation when it is combined with the MCB scheme for all grid levels using the FSAC-PP and FSAC-VP method, which are better than or similar to the MCB scheme by itself. For the AC method, there is no difference between the Rusanov RS and its combination with the MCB scheme and it generally shows more numerical dissipation than the MCB scheme by itself. For the AC, FSAC-PP and FSAC-VP method, the MCB scheme also provides less numerical dissipation compared to the

Table 6.29: Comparisons of the integrated numerical dissipation for different incompressible methods and numerical schemes on different meshes at a Reynolds number of Re=1000.

		AD	no RS			Rusanov RS	
	$n_x \times n_y$	no CB	no CB	SCB	MCB	no CB	MCB
AC	32×32	1.64	1.68	2.18	1.78	2.06	2.06
	64×64	1.70	1.71	1.94	1.79	2.13	2.13
	128×128	1.66	1.67	1.71	1.73	1.77	1.77
FSAC-PP	32×32	1.67	1.78	2.31	2.11	1.79	1.44
	64×64	1.61	1.62	1.67	1.54	1.89	1.52
	128×128	1.62	1.62	1.58	1.54	1.56	1.53
FSAC-VP	32×32	2.29	2.84	3.19	2.62	2.33	2.25
	64×64	1.93	1.95	2.28	2.01	2.09	2.02
	128×128	1.81	1.81	1.92	1.86	1.84	1.80
FSVP	32×32	2.72	3.32	-	-	-	-
	64×64	2.10	2.12	-	-	-	-
	128×128	1.89	1.89	-	-	-	-

SCB scheme, except on the fine mesh for the AC method, where the SCB scheme is 1.1% less dissipative. Overall the central scheme provides either the least amount of numerical dissipation or matches the least dissipative numerical scheme closely for all methods and grids. This may indicate that the default parameter for the artificial dissipation may work well for the current case. However, as highlighted in previous Sections, the artificial dissipation may be fine-tuned to give the best possible results and so is depending on the user's input. The advantages of providing the solution with a numerical scheme with inherent numerical dissipation is able to provide the right amount of numerical dissipation which requires no fine tuning, such as the Rusanov RS or the Godunov RS which forms part of the SCB scheme. Those RS may not always provide the lowest level of numerical dissipation, but they provide enough for a wide range of applications. As pointed out above, the dissipation may, however, be positively influenced by coupling the Rusanov RS with the MCB scheme. The gain of treating the flow with physical sound numerical methods is the reduction of numerical artefacts, as shown here through the analysis of numerical dissipation.

This concludes the discussion on the periodic vortex evolution of the Taylor–Green vortex problem. We saw that the difference in the computed to analytical kinetic energy showed smooth profiles for the AC, FSAC-VP and FSVP method but oscillatory results for the FSAC-PP method. It was argued that the parabolic treatment

of the pressure was able to prevent the same oscillations to occur in the FSAC-VP method due to a limit on the information propagation speed. The error curves for the pressure showed a similar oscillatory behaviour for the FSAC-PP but not the FSAC-VP method, which was taken as further evidence that a different pressure treatment can have a significant effect on the results. Over the full spectrum of simulated time, the pressure ultimately reached a smooth decay in error where no further oscillations were present. It was shown that the overall L_0 and L_1 error norms for the velocity and pressure were lowest for the FSAC-PP method, followed by the FSAC-VP method and then the AC and FSVP method. In terms of iterations, the FSAC-PP method was able to speed up the computations by a factor up to 36.5 times compared to the AC method, while the FSAC-VP was able to provide a speed up of up to 193.0 times compared to the AC method. The speed up obtained with the FSVP method were comparable to those of the FSAC-VP method and just slightly lower. In terms of numerical dissipation, it was shown that the FSAC-PP and AC method provided the overall least dissipative results while the FSAC-VP and FSVP method showed the most amount, especially on the coarse grid. On the fine grid, the error curves were generally closer matched which resulted in the numerical dissipation to be equally close together.

Chapter 7

Conclusions

In this concluding Chapter, the work conducted so far will be summarised and important findings highlighted. A list of possible extensions of the current work is given at the end of this Chapter.

7.1 Summary of the Current Work

This work has been concerned with mainly two research streams; the first was dealing with the method of characteristics and the Riemann problem while the second was looking at methods to solve the incompressible Navier–Stokes equations. For the method of characteristics, a single- and multi-directional approach can be found in the literature which has been, however, only applied to the hyperbolic AC method. While the single-directional CB scheme has been used for the FSAC-PP method, it has not been extended to the multi-directional CB scheme. This work provided first the application of the MCB scheme to the FSAC-PP method and secondly a generalisation procedure which makes the method applicable to any hyperbolic system of equations. To make the MCB scheme independent of the underlying numerical reconstruction scheme, it was further extended to include the Rusanov Riemann solver to provide needed numerical dissipation to avoid the onset of the pressure-velocity decoupling phenomenon at high Reynolds numbers. In this way, a multi-directional Godunov-type framework has been created, based on the Rusanov RS and the MCB scheme. In order to make the Rusanov Riemann solver fully compatible with the MCB scheme, it was necessary to construct a geometric multi-directional version of the RS to obtain the wave speeds at cell interfaces. This made the RS directly applicable to unstructured grids as well. Unlike the SCB scheme, the RS was not incorporated into the MCB scheme so that it can be exchanged for any other suitable RS which may depend on the application. The SCB scheme is relying on the Godunov RS internally which cannot be simply substituted or taken away from the scheme. Furthermore, the MCB scheme has been extended to unsteady flows through a dual time-stepping procedure which has not been done so far in the literature.
For the second research stream, dealing with the incompressible Navier–Stokes equations, a novel procedure was developed which was based on considerations of the pressure on the atomistic level. It has been shown that the expected behaviour

of the pressure should be parabolic, in a mathematical sense, so as to restrict the propagation of information through system-imposed propagation speeds. It has also been argued that the pressure should have a transport or evolution equation which determines the pressure in space and time uniquely. Starting from the FSAC-PP method, a velocity projection concept has been invoked on the perturbed continuity equation which led to a parabolic pressure transport equation. This new concept has been named the Fractional-Step with Velocity Projection, or FSVP, method, which was further extended by the perturbed continuity equation to form the FSAC-VP method. In this way, the pressure and velocity treatment are separated into a hyperbolic treatment of the velocity field while the pressure follows a parabolic transport equation. Thus, the developed multi-directional Godunov-type framework can also be applied to the FSAC-VP method through its hyperbolic Fractional-Step.
In essence, this research has been undertaken to solve the Navier–Stokes equations according to their expected physical behaviour. The pressure is hypothesised to be parabolic and therefore a parabolic transport equation has been derived. The non-linear term is expected to have an anisotropic behaviour and therefore a multi-directional CB scheme is developed for any hyperbolic incompressible method. This has been done to remove numerical modelling errors and to introduce physical features into the modelling approaches.

To validate the developed numerical schemes and incompressible methods, four validation cases were selected. The first consisted of the lid driven cavity to test the high Reynolds number capabilities of each scheme and method. The second was the flow over a backward facing step and mainly considered here due to biased results in the literature. Results have been obtained for two different geometries to show the shortcomings of the selected geometry in the literature while the second geometry with well-defined boundary conditions did not show any negative influence on the results. The third test case was an extension of the backward facing step where the flow through a sudden expansion was modelled. In this case, where a bifurcation of the Navier–Stokes equations is present, the behaviour of the different schemes and methods were tested to capture this symmetry breaking effect. The last test case was the time evolution of a symmetrical and vortical flow field, also known as the Taylor–Green vortex problem. The ability to retain the symmetry as well as the influence of the different methods on the computational costs were investigated.
Some trends that were observed in the results are highlighted in the following, based on available errors or other metrics to judge the accuracy of each scheme and incompressible method. The AC method generally showed best results with a non CB and central scheme with artificial dissipation, while the Rusanov RS-based approaches showed generally more error. The MCB and SCB schemes were located somewhere between these two extremes with no clear preference as to which performed better. For the FSAC-PP and FSAC-VP method, the SCB scheme produced the most discrepancies while the MCB scheme and its combination with the Rusanov RS compared more favourable to reference data or in terms of error norms. Similarly, the Rusanov RS produced equally good results. The central scheme with artificial dissipation cannot be dismissed which showed generally good results as well. It is, however, depending on the user-defined scaling parameters which control the

amount of numerical dissipation. Since classical test cases are considered here, it is possible that those scaling parameters have been fine tuned in the literature for exactly these test cases which would explain their good comparison. Despite their good results, the Rusanov-based approaches provided usually equally good or better results which required no user-defined parameters to be set. The FSVP method showed generally similar results to the FSAC-VP method but occasionally provided higher errors or less agreement with reference data. More interestingly, the FSAC-VP and FSVP method both showed a higher degree of scheme-independence than the FSAC-PP and AC method. The differences among the numerical schemes were less pronounced using the FSAC-VP and FSVP method compared to the other two methods. A similar trend was observed for the FSAC-PP method [21, 109] where flow structures usually captured only with higher-order schemes were resolved with first-order schemes. This behaviour may be attributed to the elliptic Poisson equation which provides an inherent smoothing of the pressure field. The results for the tested cases suggests that the FSAC-VP method is capable of increasing the scheme-independence even further. Thus, it is reasonable to expect the parabolic transport equation to have an equal effect on the results. This behaviour was especially pronounced for the backward facing step and sudden expansion geometry when judging the velocity profiles. The lid driven cavity did not show the same behaviour which was simply due to the fact that the simulations were run on purpose with low levels of inherent numerical dissipation to examine each scheme under such environments. For the lid driven cavity problem, it was shown that only numerical approaches relying on a RS were able to provide physical results up to a Reynolds number of Re=5000 while no onset in pressure-velocity decoupling was observed. The central scheme was able to provide equally well resolved results for the velocity field but was unable to prevent the oscillation in the pressure field.

When the different incompressible methods were tested for their computational cost, it was found that the FSAC-PP method performed usually fastest for steady state simulations. The FSAC-VP method performed similar but required slightly more iterations, as did the FSVP method. The AC method required consistently more iterations which could be up to six times more than the FSAC-PP method. Although it may be argued that the iterations are not the true indicator for computational cost, it was found to be the most reliable indicator as results were obtained on different HPC clusters and personal computers of different clock speeds. For unsteady flows, the parabolic pressure transport equation has been found to provide not only smoothing of the pressure in space but also in time, resulting in error curves free of oscillations (unlike the FSAC-PP method) for which speed-ups of a factor of up to 193.0 times were obtained, compared to the AC method. This behaviour is explained by the fact that the parabolic pressure transport equation represents the expected and hypothesised behaviour of the pressure in a real fluid. By aligning the mathematical equation of the pressure with the expected physical reality, it is possible that this approach fairs better in terms of convergence rate than an artificially constructed pressure equation based on the compressible Navier–Stokes equations. On the other hand, the parabolic behaviour may be unfavourable in other flow situations. Rezzolla and Zanotti [184], for example, argued that the parabolic behaviour introduces an instantaneous propagation speed into the governing equations

of a compressible or relativistic fluid. Here, however, the considered time scales are much smaller than those encountered for incompressible flows. In order to capture discontinuities it is important to retain the hyperbolic behaviour in these cases and a parabolic pressure treatment may not be favourable.
Some more specific observations may be highlighted here. The MCB scheme has shown capabilities to resolve vortical structures more favourably where other schemes may fail, see for example the lid driven cavity using the FSAC-PP and FSAC-VP methods at Re=5000. For the backward facing step, the tested Reynolds number of Re=389 was close to the critical Reynolds number after which a secondary recirculation area forms. The AC method incorrectly predicted the onset of the secondary recirculation area for all numerical schemes while the FSAC-PP method did not predict any secondary vortex structure. Using the FSAC-VP method, only the characteristic- and RS-based approaches were able to correctly predict that no secondary vortex should exist, while the non CB and central scheme with artificial dissipation failed to do so. For the sudden expansion test case, the bifurcation showed a high dependence on the incompressible method. The AC method showed that the numerical scheme was important to predict the bifurcation at all, while the FSAC-PP, FSAC-VP and FSVP predicted the bifurcation for all schemes. The FSAC-PP method showed a gradual prediction of the bifurcation which resulted in a smooth onset of symmetry breaking. The FSAC-VP and FSVP methods, however, showed a sharp transition close to the critical Reynolds number from the symmetric to the anti-symmetric state. For the AC method, the MCB scheme was able to sharply predict the bifurcation while the SCB scheme was not able to do so.

Thus, the discussion above can be summarised in the following. The multi-directional Godunov-type framework has shown favourable vortex treatment capabilities. Its full potential may only be observed, however, when it is applied to a three-dimensional space for which a four-dimensional MCB scheme needs to be developed first (see also next Section). But even for two-dimensional flows in space, a stronger pressure-velocity coupling could be observed using the current framework while the overall accuracy compared well with other schemes and reference data. The treatment of the pressure, however, had a stronger effect, even for just two-dimensional cases. In-fact, there is a lack of comparison of elliptic, parabolic and hyperbolic pressure treatments in the literature for which this study may have presented results for all treatments within the same framework. Keeping the geometry, boundary conditions, numerical schemes and parameters the same, it was observed that the different incompressible methods had a strong impact on the overall accuracy and general behaviour. It was concluded that the attention of numerical scheme development that has been undertaken to capture the non-linear properties of the Navier–Stokes equations needs to be given to incompressible method development as well. More specifically, while high-resolution numerical schemes try to capture the non-linear behaviour of the Navier–Stokes equations, incompressible methods should be equally constructed with a respect to the physical behaviour of the pressure. Despite the linearity of the pressure gradient, it is important to treat the pressure in a way which aligns with its expected behaviour, be it elliptic, parabolic or hyperbolic. Furthermore, due to the pressure-velocity coupling, some non-linear aspects of the velocity

field may influence the pressure field so that the interplay of numerical schemes to capture the non-linearities and the incompressible method to provide the correct pressure responds becomes even more important.

7.2 Future Work

Although all the aims of the projects have been met through the objectives, there are several areas which require further research. The following will give a list of possible extensions for future work.

As was already highlighted, the main bottleneck of the current form of the MCB is its two-dimensional restriction in space. A three-dimensional version is required for further observations on its capabilities to capture vortical and turbulent structures. The extension of the scheme to three-dimensional space is straight forward and follows the two-dimensional case, however, the normal vector is not readily available. Since in this case, the normal vector defined in Eq.(4.1.58) correspond to the unit normal vector of a cylindrical coordinate system, it may be postulated that the normal vector for a three-dimensional MCB scheme requires the normal vector from a spherical coordinate system, i.e.

$$\mathbf{n} = \begin{bmatrix} \cos\theta \sin\phi \\ \sin\theta \sin\phi \\ \cos\theta \end{bmatrix}, \tag{7.2.1}$$

where θ and ϕ are the azimuthal and polar angles, respectively. This is, however, not tested and may turn out to bear unforeseen complications.

Another extension of the MCB scheme is to include the viscous terms into the derivation, which is commonly neglected. There is, however, no general barrier to do so and Hoffmann and Chiang [4] have shown how second-order derivatives can be included in the classification of system of partial differential equations. The process to derive the MCB scheme is closely related to the classification of system of equations and thus the same approach can be done. If one wishes to do so, the result of the stream surface Ψ_2 in Eq.(4.1.40) has to be modified by the contribution of the second-order derivatives. Carrying out the derivation, one would arrive at

$$\mathbf{n} \cdot \nabla n_t + \frac{\rho}{\beta n_t} \left[n_t^2 + n_t(\mathbf{u} \cdot \mathbf{n}) \right] = 0 \tag{7.2.2}$$

which results in a differential equation for the normal vector component in space. With the MCB scheme being directly applicable to unstructured grids, another extension of this work could be the application of the presented and newly developed incompressible methods to unstructured grids together with the multi-directional Godunov-type framework. Although this extension is trivial, an unstructured meshing approach would allow for locally refined mesh topologies which may further help to increase the accuracies for the test cases presented in this work.

From the incompressible method point of view, there are a few possible extensions

as well. The AC method introduced the time derivative of the pressure into the continuity equation for which the functional relationship of the pressure and density was lumped together into the β parameter, which is a purely numerical artefact. Since the FSAC-PP method is based on the AC method, and the FSAC-VP and FSVP method are based on the FSAC-PP method, this artificial time-derivative problem is inherited by each method. In order to remove this shortcoming from the AC method, the physical relation for the β parameter needs to be established. Classical routes from thermodynamics may not work here but should not be discarded. A first theory which shows how the β parameter can be given physical meaning again has been developed and initial tests have shown its potential, however, at this stage the theory is not mature enough to be presented in this work and further work is required to establish its correctness. With this extension, the need for the dual time-stepping procedure would be eliminated. This would also support the discussion hold on the smoothing abilities of the parabolic pressure transport equation in time, which for the moment is only smoothing the pseudo time derivative. As discussed, however, the pseudo time derivative has a direct influence on the dual time-stepping procedure so that the smoothing in pseudo time is also affecting the real time derivative.

Finally, more tests for unsteady flows are required to establish the behaviour of the FSAC-VP and FSVP method for different test cases and to confirm the favourable convergence properties observed in the Taylor–Green vortex flow problem.

Bibliography

[1] P. D. Lax, "Weak solutions of nonlinear hyperbolic equations and their numerical computation," *Communications on Pure and Applied Mathematics*, vol. 7, no. 1, pp. 159–193, 1954.

[2] P. D. Lax and B. Wendroff, "Systems of conservation laws," *Communications on Pure and Applied Mathematics*, vol. 13, no. 2, pp. 217–237, 1960.

[3] S. K. Godunov, "A difference scheme for numerical solution of discontinuous solution of hydrodynamic equations," *Mathematics of the USSR-Sbornik*, vol. 47, pp. 271–306, 1959.

[4] K. A. Hoffmann and S. T. Chiang, *Computational Fluid Dynamics for Engineers, Vol 1.* Wichita: Engineering Education System, 1993.

[5] A. Harten, "High resolution schemes for hyperbolic conservation laws," *Journal of Computational Physics*, vol. 49, no. 3, pp. 357–393, 1983.

[6] H. K. Versteeg and W. Malalasekera, *An Introduction to Computational Fluid Dynamics: The Finite Volume Method.* Harlow, England: Prentice Hall, 2nd ed., 2007.

[7] A. Harten, P. D. Lax, and B. V. Leer, "On Upstream Differencing and Godunov-Type Schemes for Hyperbolic Conservation Laws," *SIAM Review*, vol. 25, no. 1, pp. 35–61, 1983.

[8] A. Harten, B. Engquist, S. Osher, and S. R. Chakravarthy, "Uniformly High Order Accurate Essentially Non-oscillatory Schemes, III," *Journal of Computational Physics*, vol. 71, pp. 231–303, 1987.

[9] X. D. Liu, "Weighted essentially non-oscillatory schemes," *Journal of Computational Physics*, vol. 115, no. 1, pp. 200–212, 1994.

[10] A. Jameson, W. Schmidt, and E. Turkel, "Numerical Solution of the Euler Equations by Finite Volume Methods Schemes," in *AIAA 14th Fluid and Plasma Dynamic Conference*, (Palo Alto, California, USA), pp. 1–19, 1981.

[11] A. N. Kolmogorov, "The Local Structure of Turbulence in Incompressible Viscous Fluid for Very Large Reynolds Numbers," *Proceedings of the USSR Academy of Sciences*, vol. 30, pp. 299–303, 1941.

[12] I. Grattan-Guinness and S. Engelsman, "The manuscripts of Paul Charpit," *Historia Mathematica*, vol. 9, no. 1, pp. 65–75, 1982.

[13] N. Saltykow, *Méthodes classiques d'intégration des équations aux dérivées partielles du premier ordre à une fonction inconnue.* Gauthier-Villars, 1931.

[14] V. V. Rusanov, "Characteristics of the General Equations of Gas Dynamics," *Noi Mathematiki Mathematicheskoi Fiziki*, vol. 3, no. 3, pp. 508–527, 1963.

[15] D. Drikakis, P. A. Govatsos, and D. E. Papantonis, "A Characteristic-based Method for Incompressible Flows," *International Journal for Numerical Methods in Fluids*, vol. 19, pp. 667–685, 1994.

[16] A. J. Chorin, "A Numerical Method for Solving Incompressible Viscous Flow Problems," *Journal of Computational Physics*, vol. 2, pp. 12–26, 1967.

[17] S. E. Razavi, K. Zamzamian, and A. Farzadi, "Genuinely multidimensional characteristic-based scheme for incompressible flows," *International Journal for Numerical Methods in Fluids*, vol. 57, no. 8, pp. 929–949, 2008.

[18] A. J. Chorin, "Numerical solution of the Navier-Stokes equations," *Mathematics of Computation*, vol. 22, no. 104, pp. 745–762, 1968.

[19] R. Témam, "Sur l'approximation de la solution des équations de Navier-Stokes par la méthode des pas fractionnaires (I)," *Archive for Rational Mechanics and Analysis*, vol. 33, pp. 377–385, 1969.

[20] S. Patankar and D. Spalding, "A calculation procedure for heat, mass and momentum transfer in three-dimensional parabolic flows," *International Journal of Heat and Mass Transfer*, vol. 15, pp. 1787–1806, oct 1972.

[21] L. Könözsy and D. Drikakis, "A Unified Fractional-Step, Artificial Compressibility and Pressure-Projection Formulation for Solving the Incompressible Navier-Stokes Equations," *Communications in Computational Physics*, vol. 16, no. 5, pp. 1135–1180, 2014.

[22] L. Könözsy, D. Drikakis, M. Ashcroft, A. Dixon, and J. Persson, "Experimental and numerical investigation for trapping and positioning cryogenic propellants," in *8th European Symposium on Aerothermodynamics for Space Vehicles*, (Lisbon, Portugal), 2015.

[23] J. D. Anderson, *Modern Compressible Flow: With Historical Perspective.* New York: McGraw-Hill Education, 2002.

[24] M. J. Zucrow and J. D. Hoffman, *Gas Dynamics, Vol 2: Multidimensional Flow.* New York: John Wiley & Sons, Inc., 1977.

[25] R. A. Delaney, *A second-order method of characteristics for two- dimensional unsteady flow with application to turbomachinery cascades.* PhD thesis, Iowa State University, 1974.

[26] M. C. Cline and J. D. Hoffman, "Comparison of Characteristic Schemes for Three-Dimensional, Steady, Isentropic Flow," *AIAA Journal*, vol. 10, no. 11, pp. 1452–1458, 1972.

[27] V. H. Ransom, J. D. Hoffman, and H. D. Thompson, "A Second-Order Bicharacteristics Method for Three-Dimensional, Steady, Supersonic Flow," *AIAA Journal*, vol. 10, no. 12, pp. 1573–1581, 1972.

[28] C. Ferrari, "Interference Between Wing and Body at Supersonic Speeds-Analysis by the Method Characteristics," *Journal of the Aeronautical Sciences*, vol. 16, no. 7, pp. 411–434, 1949.

[29] P. I. Chushkin and O. N. Katskova, "Three-dimensional supersonic equilibrium flow of a gas around bodies at the angle of attack," tech. rep., NASA, Washington, 1965.

[30] J. V. Rakich and J. W. Cleary, "Theoretical and Experimental Study of Supersonic Steady Flow around Inclined Bodies of Revolution," *AIAA Journal*, vol. 8, no. 3, pp. 511–518, 1970.

[31] H. Sauerwein, "The method of characteristics for the three-dimensional unsteady magnetofluid dynamics of a multi-component medium," *Journal of Fluid Mechanics*, vol. 25, 1966.

[32] M. C. Cline and J. D. Hoffman, "The analysis of nonequilibrium, chemically reacting, supersonic flow in three dimensions using a bicharacteristics method," *Journal of Computational Physics*, vol. 12, no. 1, pp. 1–23, 1973.

[33] J. D. Hoffman and A. R. Maykut, "Gas Dynamic Gain of Supersonic Thrust Nozzles," *Journal of Spacecrafts and Rockets*, vol. 11, no. 10, pp. 697–704, 1974.

[34] R. A. Delaney and P. Kavanagh, "Transonic Flow Analysis in Axial-Flow Turbomachinery Cascades by a Time-Dependent Method of Characteristics," *Journal of Engineering for Power*, vol. 98, no. 3, pp. 356–363, 1976.

[35] D. L. Marcum and J. D. Hoffman, "Calculation of Three-Dimensional Flowfields by the Unsteady Method of Cahracteristics," *AIAA Journal*, vol. 23, no. 10, pp. 1497–1505, 1985.

[36] P. Roe, "Characteristic-Based Schemes for the Euler Equations," *Annual Review of Fluid Mechanics*, vol. 18, no. 1, pp. 337–365, 1986.

[37] M. J. Zucrow and J. D. Hoffman, *Gas Dynamics, Vol 1.* New York: John Wiley & Sons, Inc., 1976.

[38] H. Sauerwein, *The Calculation of two- and three-dimensional inviscid unsteady flows by the method of characteristics.* PhD thesis, Massachusetts Institute of Technology, 1964.

[39] A. Eberle, "Characteristic flux averaging approach to the solution of Euler's equations," tech. rep., Von Karman Institute, 1987.

[40] D. Drikakis, "A parallel multiblock characteristic-based method for three-dimensional incompressible flows," *Advances in Engineering Software*, vol. 26, no. 95, pp. 111–119, 1996.

[41] D. Drikakis, O. Iliev, and D. Vassileva, "A Nonlinear Multigrid Method for the Three-Dimensional Incompressible Navier-Stokes Equations," *Journal of Computational Physics*, vol. 146, pp. 301–321, 1998.

[42] P. Neofytou, "Revision of the characteristics-based scheme for incompressible flows," *Journal of Computational Physics*, vol. 222, no. 2, pp. 475–484, 2007.

[43] X. Su, Y. Zhao, and X. Huang, "On the characteristics-based ACM for incompressible flows," *Journal of Computational Physics*, vol. 227, no. 1, pp. 1–11, 2007.

[44] C. H. Tai and Y. Zhao, "Parallel unsteady incompressible viscous flow computations using an unstructured multigrid method," *Journal of Computational Physics*, vol. 192, pp. 277–311, 2003.

[45] C. Tai, Y. Zhao, and K. Liew, "Parallel computation of unsteady three-dimensional incompressible viscous flow using an unstructured multigrid method," *Computers & Structures*, vol. 82, no. 28, pp. 2425–2436, 2004.

[46] C. Tai, Y. Zhao, and K. Liew, "Parallel-multigrid computation of unsteady incompressible viscous flows using a matrix-free implicit method and high-resolution characteristics-based scheme," *Computer Methods in Applied Mechanics and Engineering*, vol. 194, no. 36-38, pp. 3949–3983, 2005.

[47] C. Tai, Y. Zhao, and K. Liew, "Parallel computation of unsteady incompressible viscous flows around moving rigid bodies using an immersed object method with overlapping grids," *Journal of Computational Physics*, vol. 207, no. 1, pp. 151–172, 2005.

[48] Y. Zhao and B. Zhang, "High-order characteristics upwind FV method for incompressible flow and heat transfer simulation on unstructured grids," *Computer Methods in Applied Mechanics and Engineering*, vol. 190, no. 5-7, pp. 733–756, 2000.

[49] E. Shapiro and D. Drikakis, "Artificial compressibility, characteristics-based schemes for variable density, incompressible, multi-species flows. Part I. Derivation of different formulations and constant density limit," *Journal of Computational Physics*, vol. 210, no. 2, pp. 584–607, 2005.

[50] E. Shapiro and D. Drikakis, "Artificial compressibility, characteristics-based schemes for variable-density, incompressible, multispecies flows: Part II. Multigrid implementation and numerical tests," *Journal of Computational Physics*, vol. 210, no. 2, pp. 608–631, 2005.

[51] I. Abdollahi, K. Zamzamian, and R. Fathollahi, "High-accuracy upwind method using improved characteristics speeds for incompressible flows," *International Journal for Numerical Methods in Fluids*, p. Article in press, 2015.

[52] A. Atashbar Orang, "Genuinely characteristic-based scheme for the incompressible turbulent flows," *Computers & Fluids*, vol. 103, pp. 175–185, 2014.

[53] K. Zamzamian and S. E. Razavi, "Multidimensional upwinding for incompressible flows based on characteristics," *Journal of Computational Physics*, vol. 227, no. 19, pp. 8699–8713, 2008.

[54] S. E. Razavi, *Far Field Boundary Conditions for Computation of Compressible Aerodynamic flows*. PhD thesis, McGill University, 1995.

[55] M. Hashemi and K. Zamzamian, "Efficient and non-reflecting far-field boundary conditions for incompressible flow calculations," *Applied Mathematics and Computation*, vol. 230, pp. 248–258, 2014.

[56] K. Zamzamian and M. Y. Hashemi, "Multidimensional characteristic-based solid boundary condition for incompressible flow calculations," *Applied Mathematical Modelling*, vol. 39, no. 22, pp. 7032–7044, 2015.

[57] R. Fathollahi and K. Zamzamian, "An improvement for multidimensional characteristic-based scheme by using different selected waves," *International Journal for Numerical Methods in Fluids*, vol. 76, no. 10, pp. 722–736, 2014.

[58] M. Hashemi and K. Zamzamian, "A multidimensional characteristic-based method for making incompressible flow calculations on unstructured grids," *Journal of Computational and Applied Mathematics*, vol. 259, pp. 752–759, 2014.

[59] S. E. Razavi and M. Hanifi, "A Multi-Dimensional Virtual Characteristic Scheme for Laminar and Turbulent Incompressible Flows," *Journal of Applied Fluid Mechanics*, vol. 9, no. 4, pp. 1579–1590, 2016.

[60] S. E. Razavi and T. Adibi, "A Novel Multidimensional Characteristic Modeling of Incompressible Convective Heat Transfer," *Journal of Applied Fluid Mechanics*, vol. 9, no. 3, pp. 1135–1146, 2016.

[61] A. Atashbar Orang, S. E. Razavi, and H. Pourmirzaagha, "Computational study of incompressible turbulent flows with method of characteristics," *Journal of Computational and Applied Mathematics*, vol. 259, no. PART B, pp. 741–751, 2014.

[62] O. C. Zienkiewicz and R. Codina, "A general algorithm for compressible and incompressible flow - Part I. the split, characteristic-based scheme," *International Journal for Numerical Methods in Fluids*, vol. 20, no. 8-9, pp. 869–885, 1995.

[63] O. C. Zienkiewicz, K. Morgan, B. V. K. Satya Sai, R. Codina, and M. Vasquez, "A general algorithm for compressible and incompressible flow - Part II. tests on the explicit form," *International Journal for Numerical Methods in Fluids*, vol. 20, no. 8-9, pp. 887–913, 1995.

[64] P. Nithiarasu, "An efficient artificial compressibility (AC) scheme based on the characteristic based split (CBS) method for incompressible flows," *International Journal for Numerical Methods in Engineering*, vol. 56, no. 13, pp. 1815–1845, 2003.

[65] P. Nithiarasu, J. S. Mathur, N. P. Weatherill, and K. Morgan, "Three-dimensional incompressible flow calculations using the characteristic based split(CBS) scheme," *International Journal for Numerical Methods in Fluids*, vol. 44, pp. 1207–1229, apr 2004.

[66] P. Nithiarasu and C.-B. Liu, "An artificial compressibility based characteristic based split (CBS) scheme for steady and unsteady turbulent incompressible flows," *Computer Methods in Applied Mechanics and Engineering*, vol. 195, no. 23-24, pp. 2961–2982, 2006.

[67] A. G. Malan and R. W. Lewis, "An artificial compressibility CBS method for modelling heat transfer and fluid flow in heterogeneous porous materials," *International Journal for Numerical Methods in Engineering*, vol. 87, pp. 412–423, jul 2011.

[68] V. V. Rusanov, "The calculation of the interaction of non-stationary shock waves and obstacles," *USSR Computational Mathematics and Mathematical Physics*, vol. 1, no. 2, pp. 304–320, 1961.

[69] P. L. Roe, "Approximate Riemann solvers, parameter vectors, and difference schemes," *Journal of Computational Physics*, vol. 43, no. 2, pp. 357–372, 1981.

[70] E. F. Toro, M. Spruce, and W. Speares, "Restoration of the contact surface in the HLL-Riemann solver," *Shock Waves*, vol. 4, pp. 25–34, jul 1994.

[71] E. F. Toro, *Riemann Solvers and Numerical Methods for Fluid Dynamics*. Heidelberg: Springer, 2009.

[72] D. Drikakis and W. Rider, *High-Resolution Methods for Incompressible and Low-Speed Flows*. Heidelberg: Springer, 2005.

[73] R. Saurel, M. Larini, and J. C. Loraud, "Exact and Approximate Riemann Solvers for Real Gases," *Journal of Computational Physics*, vol. 112, pp. 126–137, 1994.

[74] W. Roger and L. David, "Implicit lower-upper/approximate-factorization algorithms for viscous incompressible flows," *12th Computational Fluid Dynamics Conference*, pp. 1091–1099, 1995.

[75] C. Sheng, L. Taylor, and D. Whitfield, "Multiblock multigrid solution of three-dimensional incompressible turbulent flows about appended submarine configurations," in *33rd Aerospace Sciences Meeting and Exhibit*, (Reston, Virigina), American Institute of Aeronautics and Astronautics, jan 1995.

[76] Y. Aiming, N. Yunhua, and W. Peifen, "Numerical Analysis of Low Reynolds Number Flows Around Thin Wings for Micro Air Vehicles," in *24th Congress of International Council of the Aeronautical Sciences*, (Yokohama, Japan), 2004.

[77] M. Azhdarzadeh and S. Razavi, "A Pseudo-Characteristic Based Method for Incompressible Flows with Heat Transfer," *Journal of Applied Sciences*, vol. 8, pp. 3183–3190, dec 2008.

[78] W. H. Wang and Y. Y. Wang, "An essential solution of water entry problems and its engineering applications," *Journal of Marine Science and Application*, vol. 9, no. 3, pp. 268–273, 2010.

[79] W.-H. Wang, Y. Huang, and Y.-Y. Wang, "Analysis of Mechanical Energy Transport on Free-Falling Wedge during Water-Entry Phase," *Journal of Applied Mathematics*, vol. 2012, pp. 1–21, 2012.

[80] H. Lee and S. Lee, "Artificial Compressibility Method and Preconditioning Method for Solving Two Dimensional Incompressibile Flow," in *ASME-JSME-KSME 2011 Joint Fluids Engineering Conference*, (Hamamatsu, Japan), 2011.

[81] H. Lee and S. Lee, "Convergence characteristics of upwind method for modified artificial compressibility method," *International Journal of Aeronautical and Space Sciences*, vol. 12, no. 4, pp. 318–330, 2011.

[82] C. Ma, Z. and Qian, L. and Causon, D. and Mingham, "Simulation of Solitary Breaking Waves Using a Two-Fluid Hybrid Turbulence Approach," *The Twenty-first International Offshore and Polar Engineering Conference*, vol. 8, pp. 231–237, 2011.

[83] Y. Y. Niu, C. H. Chang, W. Y. I. Tseng, H. H. Peng, and H. Y. Yu, "Numerical simulation of an aortic flow based on a HLLC type incompressible flow solver," *Communications in Computational Physics*, vol. 5, no. 1, pp. 142–162, 2009.

[84] J. C. Mandal, C. R. Sonawane, a. S. Iyer, and S. J. GosaviInamdar, "Incompressible flow computations over moving boundary using a novel upwind method," *Computers and Fluids*, vol. 46, no. 1, pp. 348–352, 2011.

[85] J. Mandal and C. R. Sonawane, "Simulation of flow inside differentially heated rotating cavity," *International Journal of Numerical Methods for Heat & Fluid Flow*, vol. 23, no. 1, pp. 23–54, 2013.

[86] J. C. Mandal and C. R. Sonawane, "Simulation of Moderator Flow and Temperature Inside Calandria of CANDU Reactor Using Artificial Compressibility Method," *Heat Transfer Engineering*, vol. 35, no. 14-15, pp. 1254–1266, 2014.

[87] Z. Qian and C. H. Lee, "Preconditioned HLLC scheme for incompressible viscous flow simulation," *WIT Transactions on Engineering Sciences*, vol. 74, pp. 85–96, 2012.

[88] Z. Qian and C.-H. Lee, "HLLC scheme for the preconditioned pseudo-compressibility Navier-Stokes equations for incompressible viscous flows," *International Journal of Computational Fluid Dynamics*, vol. 8562, no. November, pp. 1–11, 2015.

[89] L. K. Taylor, K. Sreenivas, R. S. Webster, and J. Kress, "An Artificial Compressibility Algorithm for Convective Heat Transfer," *44th AIAA Thermophysics Conference*, pp. 1–17, 2013.

[90] F. Golay and P. Helluy, "Numerical schemes for low Mach wave breaking," *International Journal of Computational Fluid Dynamics*, vol. 21, no. 2, pp. 69–86, 2007.

[91] A. N. Sambe, F. Golay, D. Sous, P. Fraunié, V. Rey, R. Marcer, and C. de Jouette, "Two-phase-flow unstructured grid solver: Application to tsunami wave impact," *International Journal of Offshore and Polar Engineering*, vol. 21, no. 3, pp. 186–191, 2011.

[92] A. N. Sambe, D. Sous, F. Golay, P. Fraunié, and R. Marcer, "Numerical wave breaking with macro-roughness," *European Journal of Mechanics, B/Fluids*, vol. 30, no. 6, pp. 577–588, 2011.

[93] D. G. Hyams, K. Sreenivas, R. Pankajakshan, D. Stephen Nichols, W. Roger Briley, and D. L. Whitfield, "Computational simulation of model and full scale Class 8 trucks with drag reduction devices," *Computers and Fluids*, vol. 41, no. 1, pp. 27–40, 2011.

[94] Z. Li, Y. Zhang, and H. Chen, "A low dissipation numerical scheme for Implicit Large Eddy Simulation," *Computers and Fluids*, vol. 117, pp. 233–246, 2015.

[95] K. Smith, T.-R. Teschner, and L. Könözsy, "On Approximate Riemann Solvers within the Concept of the Unified Fractional-Step, Articificial Compressibility and Pressure-Projection Method," in *MultiScience - XXXI. microCAD*, (Miskolc, Hungary, 20-21 April), 2017.

[96] O. San and K. Kara, "Evaluation of Riemann flux solvers for WENO reconstruction schemes: Kelvin-Helmholtz instability," *Computers and Fluids*, vol. 117, pp. 24–41, 2015.

[97] D. S. Balsara, "Multidimensional HLLE Riemann solver: Application to Euler and magnetohydrodynamic flows," *Journal of Computational Physics*, vol. 229, no. 6, pp. 1970–1993, 2010.

[98] D. S. Balsara, "A two-dimensional HLLC Riemann solver for conservation laws: Application to Euler and magnetohydrodynamic flows," *Journal of Computational Physics*, vol. 231, no. 22, pp. 7476–7503, 2012.

[99] D. S. Balsara, M. Dumbser, and R. Abgrall, "Multidimensional HLLC Riemann solver for unstructured meshes - With application to Euler and MHD flows," *Journal of Computational Physics*, vol. 261, pp. 172–208, 2014.

[100] S. V. Patankar, *Numerical Heat Transfer and Fluid Flow*. New-Work: McGraw-Hill, 1980.

[101] R. I. Issa, a. D. Gosman, and a. P. Watkins, "The Computation of Compressible and Incompressible Recirculating Flows by a Non-iterative Implicit Scheme," *Journal of Computational Physics*, vol. 62, pp. 66–82, 1986.

[102] J. L. Guermond, P. Minev, and J. Shen, "An overview of projection methods for incompressible flows," *Computer Methods in Applied Mechanics and Engineering*, vol. 195, pp. 6011–6045, 2006.

[103] J. B. Bell, P. Colella, and J. a. Trangenstein, "Higher order Godunov methods for general systems of hyperbolic conservation laws," *Journal of Computational Physics*, vol. 82, no. 2, pp. 362–397, 1989.

[104] J. B. Bell, P. Colella, and H. M. Glaz, "A second-order projection method for the incompressible navier-stokes equations," *Journal of Computational Physics*, vol. 85, no. 2, pp. 257–283, 1989.

[105] F. Xiao, "Unified fomulation for compressible and incompressible flows by using multi-integrated moments I: One-dimensional inviscid compressible flow," *Journal of Computational Physics*, vol. 195, no. 2, pp. 629–654, 2004.

[106] F. Xiao, R. Akoh, and S. Ii, "Unified formulation for compressible and incompressible flows by using multi-integrated moments II: Multi-dimensional version for compressible and incompressible flows," *Journal of Computational Physics*, vol. 213, no. 1, pp. 31–56, 2006.

[107] E. Turkel, "Preconditioned methods for solving the incompressible and low speed compressible equations," *Journal of Computational Physics*, vol. 72, no. 2, pp. 277–298, 1987.

[108] H. S. Tang and F. Sotiropoulos, "Fractional step artificial compressibility schemes for the unsteady incompressible Navier-Stokes equations," *Computers and Fluids*, vol. 36, no. 5, pp. 974–986, 2007.

[109] L. Könözsy, *Multiphysics CFD Modelling of Incompressible Flows at Low and Moderate Reynolds Numbers*. PhD thesis, Cranfield University, 2012.

[110] L. Könözsy and D. Drikakis, "A Coupled High-Resolution Fractional-Step Artificial Compressibility and Pressure-Projection Formulation for Solving Incompressible Multi-Species Variable Density Flow Problem At Low Reynolds Numbers," in *European Congress on Computational Methods in Applied Sciences and Engineering*, (Vienna, Austria), 2012.

[111] T.-R. Teschner, L. Könözsy, and K. W. Jenkins, "Numerical investigation of an incompressible flow over a backward facing step using a unified fractional-step, artificial compressibility and pressure-projection (fsac-pp) method," in *Multi-Science - XXX. microCAD International Multidisciplinary Scientific Conference*, (Miskolc, Hungary), 2016.

[112] J. D. Anderson, "Brief History of the Early Development of Theoretical and Experimental Fluid Dynamics," 2010.

[113] G. Hellwig, *Partial Differential Equations: An Introduction*. Heidelberg: Springer, 1960.

[114] A. Jameson, "Time Dependent Calculations Using Multigrid, with Applications to Unsteady Flows Past Airfoils and Wings," *AIAA 10th Computational Fluid Dynamics Conference*, p. 14, 1991.

[115] S. Davis, "Simplified Second-Order Godunov-Type Methods," *SIAM Journal on Scientific and Statistical Computing*, vol. 9, no. 3, pp. 445–473, 1988.

[116] R. Courant, K. Friedrichs, and H. Lewy, "Über die partiellen Differenzengleichungen der mathematischen Physik," *Mathematische Annalen*, vol. 100, pp. 32–74, dec 1928.

[117] V. Thomée, "From Finite diierences to Finite elements A short history of numerical analysis of partial diierential equations," *Journal of Computational and Applied Mathematics*, vol. 128, pp. 1–54, 2001.

[118] R. W. Clough, "The Finite Element Method in Plane Stress Analysis," in *Proceedings of American Society of Civil Engineers*, vol. 8, (Pittsburg, Pennsylvania), pp. 345–378, 1960.

[119] L. Rayleigh, *Theory of Sound, Vol. 1.* London: Macmillan, 1894.

[120] L. Rayleigh, *Theory of Sound, Vol. 2.* London: Macmillan, 1896.

[121] W. Ritz, "Über eine neue Methode zur Lösung gewisser Variationsprobleme der mathematischen Physik.," *Journal für die reine und angewandte Mathematik (Crelle's Journal)*, no. 135, pp. 1–61, 1908.

[122] J. H. Ferziger and M. Perić, *Computational Methods for Fluid Dynamics*. Berlin: Springer, 2002.

[123] J. Y. Murthy and S. R. Mathur, "Numerical Methods in Heat, Mass, and Momentum Transfer," tech. rep., Purdue University, West Lafayette, Indiana, 2002.

[124] C. Hirsch, *Numerical Computation of Internal and External Flows, Volume 1: Fundamentals of Numerical Discretization*. Chichester: John Wiley & Sons, Inc., 1988.

[125] C. Hirsch, *Numerical Computation of Internal and External Flows, Volume 2: Computational Methods for Inviscid and Viscous Flows by Charles Hirsch.* Chichester: John Wiley & Sons, Inc., 1990.

[126] J. Blazek, *Computational Fluid Dynamics: Principles and Application.* Oxford: Elsevier, 2006.

[127] R. LeVeque, *Finite Volume Methods for Hyperbolic Problems.* Cambridge: Cambridge University Press, 2002.

[128] R. LeVeque, *Numerical Methods for Conservation Law.* Basel: Birkhäuser Verlag, 2008.

[129] R. Löhner, *Applied Computational Fluid Dynamics Techniques: An Introduction Based on Finite Element Methods.* Chichester: Wiley, 2008.

[130] C. M. Rhie and W. L. Chow, "Numerical study of the turbulent flow past an airfoil with trailing edge separation," *AIAA Journal*, vol. 21, pp. 1525–1532, nov 1983.

[131] R. L. Sani and P. M. Gresho, "Résumé and remarks on the open boundary condition minisymposium," *International Journal for Numerical Methods in Fluids*, vol. 18, pp. 983–1008, may 1994.

[132] R. Steijl and G. Barakos, "Coupled Navier-Stokes/molecular dynamics simulations in nonperiodic domains based on particle forcing," *International Journal for Numerical Methods in Fluids*, vol. 69, pp. 1326–1349, 2012.

[133] M. K. Borg, G. Macpherson, and J. Reese, "Controllers for imposing continuum-to-molecular boundary conditions in arbitrary fluid flow geometries," *Molecular Simulation*, vol. 36, pp. 745–757, 2010.

[134] R. Delgado-Buscalioni and P. V. Coveney, "USHER: An algorithm for particle insertion in dense fluids," *Journal of Chemical Physics*, vol. 119, no. 2, pp. 978–987, 2003.

[135] R. Delgado-Buscalioni, J. Sablić, and M. Praprotnik, "Open boundary molecular dynamics," *The European Physical Journal Special Topics*, vol. 2349, pp. 1–19, 2015.

[136] G.-S. Jiang and C.-W. Shu, "Efficient Implementation of Weighted ENO Schemes," *Journal of Computational Physics*, vol. 126, no. 1, pp. 202–228, 1996.

[137] S. B. Pope, *Turbulent Flows.* Cambridge: Cambridge University Press, 2000.

[138] P. A. Davidson, *Turbulence.* Oxford: Oxford University Press, 2004.

[139] H. Tennekes and J. L. Lumley, *A first course in turbulence.* Cambridge: MIT Press, 1972.

[140] S. Kuksin and A. Shirikyan, *Mathematics of Two-Dimensional Turbulence*. Cambridge: Cambridge University Press, 2012.

[141] W. K. George, "Lectures in Turbulence for the 21st Century," Tech. Rep. January, Imperial College London, 2013.

[142] E. Erturk, "Discussions on driven cavity flow," *International Journal for Numerical Methods in Fluids*, vol. 60, no. 3, pp. 275–294, 2009.

[143] A. K. Prasad and J. R. Koseff, "Reynolds number and end-wall effects on a lid-driven cavity flow," *Physics of Fluids A: Fluid Dynamics*, vol. 1, no. 2, pp. 208–218, 1989.

[144] A. Fortin, M. Jardak, J. J. Gervais, and R. Pierre, "Localization of Hopf bifurcations in fluid flow problems," *International Journal for Numerical Methods in Fluids*, vol. 24, pp. 1185–1210, jun 1997.

[145] J. J. Gervais, D. Lemelin, and R. Pierre, "Some experiments with stability analysis of discrete incompressible flows in the lid-driven cavity," *International Journal for Numerical Methods in Fluids*, vol. 24, pp. 477–492, mar 1997.

[146] A. Abouhamza and R. Pierre, "A neutral stability curve for incompressible flows in a rectangular driven cavity," *Mathematical and Computer Modelling*, vol. 38, pp. 141–157, jul 2003.

[147] M. Sahin and R. G. Owens, "A novel fully implicit finite volume method applied to the lid-driven cavity problem?Part I: High Reynolds number flow calculations," *International Journal for Numerical Methods in Fluids*, vol. 42, pp. 57–77, may 2003.

[148] M. Poliashenko and C. K. Aidun, "A direct method for computation of simple bifurcations," *Journal of Computational Physics*, vol. 121, pp. 246–260, oct 1995.

[149] O. Goyon, "High-Reynolds number solutions of Navier-Stokes equations using incremental unknowns," *Computer Methods in Applied Mechanics and Engineering*, vol. 130, pp. 319–335, apr 1996.

[150] G. Tiesinga, F. Wubs, and A. Veldman, "Bifurcation analysis of incompressible flow in a driven cavity by the Newton-Picard method," *Journal of Computational and Applied Mathematics*, vol. 140, pp. 751–772, mar 2002.

[151] Y.-F. Peng, Y.-H. Shiau, and R. R. Hwang, "Transition in a 2-D lid-driven cavity flow," *Computers & Fluids*, vol. 32, pp. 337–352, mar 2003.

[152] U. Ghia, K. N. Ghia, and C. T. Shin, "High-Re solutions for incompressible flow using the Navier-Stokes equations and a multigrid method," *Journal of Computational Physics*, vol. 48, no. 3, pp. 387–411, 1982.

[153] M. El Rafei, L. Könözsy, and Z. Rana, "Investigation of Numerical Dissipation in Classical and Implicit Large Eddy Simulations," *Aerospace*, vol. 4, no. 4, p. 59, 2017.

[154] M. Dumbser, O. Zanotti, R. Loubère, and S. Diot, "A posteriori subcell limiting of the discontinuous Galerkin finite element method for hyperbolic conservation laws," *Journal of Computational Physics*, vol. 278, pp. 47–75, dec 2014.

[155] M. Dumbser, I. Peshkov, E. Romenski, and O. Zanotti, "High order ADER schemes for a unified first order hyperbolic formulation of continuum mechanics: Viscous heat-conducting fluids and elastic solids," *Journal of Computational Physics*, vol. 314, pp. 824–862, 2016.

[156] W. Boscheri, R. Loubère, and M. Dumbser, "Direct Arbitrary-Lagrangian-Eulerian ADER-MOOD finite volume schemes for multidimensional hyperbolic conservation laws," *Journal of Computational Physics*, vol. 292, pp. 56–87, jul 2015.

[157] J. Jeong and F. Hussain, "On the identification of a vortex," *Journal of Fluid Mechanics*, vol. 285, pp. 69–94, feb 1995.

[158] A. Leroy, D. Violeau, M. Ferrand, and C. Kassiotis, "Unified semi-analytical wall boundary conditions applied to 2-D incompressible SPH," *Journal of Computational Physics*, vol. 261, pp. 106–129, mar 2014.

[159] F. Archambeau, N. Méchitoua, and M. Sakiz, "Code Saturne: A Finite Volume Code for the Computation of Turbulent Incompressible Flows - Industrial Applications," *International Journal on Finite Volumes*, vol. 1, no. 1, 2004.

[160] M. Denham and M. Patrick, "Laminar flow over a downstream-facing step in a two-dimensional flow channel," *Chemical Engineering Research & Design*, vol. 52, pp. 361–367, 1974.

[161] B. Armaly, F. Durst, J. Pereira, and B. Schonung, "Experimental and theoretical investigation of backward-facing step flow," *J. Fluid Mech*, vol. 127, pp. 473–496, 1983.

[162] F. Durst, S. Ray, B. Unsal, and O. A. Bayoumi, "The Development Lengths of Laminar Pipe and Channel Flows," *J. Fluids Eng.*, vol. 127, no. 6, p. 1154, 2005.

[163] R. J. Goldstein, V. L. Eriksen, R. M. Olson, and E. R. G. Eckert, "Laminar separation, reattachment, and transition of flow over a downstream-facing step," *Journal of Basic Engineering*, vol. 94, no. 4, pp. 732–739, 1970.

[164] L. G. Leal and A. Acrivos, "The effect of base bleed on the steady separated flow past bluff objects," *Journal of Fluid Mechanics*, vol. 39, no. 04, pp. 735–752, 1969.

[165] P. J. Roache, "Perspective: A Method for Uniform Reporting of Grid Refinement Studies," *Journal of Fluids Engineering*, vol. 116, no. 3, p. 405, 1994.

[166] I. B. Celik, U. Ghia, P. J. Roache, C. J. Freitas, C. Hugh, and P. E. Raad, "Procedure for Estimation and Reporting of Uncertainty Due to Discretization in CFD Applications," *Journal of Fluids Engineering*, vol. 130, no. 7, p. 078001, 2008.

[167] David C. Wilcox, *Turbulence Modeling for CFD*. DCW Industries Inc., 1993.

[168] R. M. Fearn, T. Mullin, and K. a. Cliffe, "Nonlinear flow phenomena in a symmetric sudden expansion," *Journal of Fluid Mechanics*, vol. 211, no. -1, p. 595, 1990.

[169] P. J. Oliveira, "Asymmetric flows of viscoelastic fluids in symmetric planar expansion geometries," *Journal of Non-Newtonian Fluid Mechanics*, vol. 114, no. 1, pp. 33–63, 2003.

[170] F. Durst, J. C. F. Pereira, and C. Tropea, "The plane Symmetric sudden-expansion flow at low Reynolds numbers," *Journal of Fluid Mechanics*, vol. 248, pp. 567–581, 1993.

[171] K. Akselvoll and P. Moin, "Large-eddy simulation of turbulent confined coannular jets," *Journal of Fluid Mechanics*, vol. 315, no. -1, p. 387, 1996.

[172] R. Friedrich, T. J. Hüttl, M. Manhart, and C. Wagner, "Direct numerical simulation of incompressible turbulent flows," *Computers & Fluids*, vol. 30, pp. 555–579, 2001.

[173] T. Hawa and Z. Rusak, "The dynamics of a laminar flow in a symmetric channel with a sudden expansion," *Journal of Fluid Mechanics*, vol. 436, pp. 283–320, 2001.

[174] I. J. Sobey and P. G. Drazin, "Bifurcations of two-dimensional channel flows," *Journal of Fluid Mechanics*, vol. 171, no. 6, pp. 263–287, 1986.

[175] D. Drikakis, "Bifurcation phenomena in incompressible sudden expansion flows," *Physics of Fluids*, vol. 9, no. 1, pp. 76–87, 1997.

[176] D. Drikakis, C. Fureby, F. F. Grinstein, and D. Youngs, "Simulation of transition and turbulence decay in the Taylor-Green vortex," *Journal of Turbulence*, vol. 8, no. July 2013, p. N20, 2007.

[177] M. E. Brachet, D. I. Meiron, B. G. Nickel, R. H. Morf, U. Frisch, and S. A. Orszag, "Small-scale structure of the taylor-green vortex," *Journal of Fluid Mechanics*, vol. 130, pp. 411–452, 1983.

[178] M. E. Brachet, M. Meneguzzi, H. Politano, and P. L. Sulem, "The dynamics of freely decaying two-dimensional turbulence," *Journal of Fluid Mechanics*, vol. 194, pp. 333–349, 1988.

[179] J. B. Chapelier, M. de la Llave Plata, and E. Lamballais, "Development of a multiscale LES model in the context of a modal discontinuous Galerkin method," *Computer Methods in Applied Mechanics and Engineering*, vol. 307, pp. 275–299, 2016.

[180] J. R. Bull and A. Jameson, "Simulation of the Taylor-Green Vortex Using High-Order Flux Reconstruction Schemes," *AIAA Journal*, vol. 53, no. 9, pp. 2750–2761, 2015.

[181] C. W. Shu, W. S. Don, D. Gottlieb, O. Schilling, and L. Jameson, "Numerical convergence study of nearly incompressible, inviscid Taylor-Green vortex flow," *Journal of Scientific Computing*, vol. 24, no. 1, pp. 569–595, 2005.

[182] A. Sifounakis, S. Lee, and D. You, "A conservative finite volume method for incompressible Navier-Stokes equations on locally refined nested Cartesian grids," *Journal of Computational Physics*, vol. 326, pp. 845–861, 2016.

[183] K. N. Premnath, J.-C. Nave, and S. Banerjee, "Computation of Multiphase Flows With Lattice Boltzmann Methods," *Fluids Engineering*, vol. 2005, pp. 403–420, 2005.

[184] L. Rezzolla and O. Zanotti, *Relativistic Hydrodynamics*. Oxford: Oxford University Press, 2013.

Appendices

Appendix A

The Method of Characteristics for the Linear and non-Linear Advection Equation

In the following section, the Method of Characteristic (MOC) will be explained in its general form. To visualise the concept, we will apply the method to the linear and non-linear advection equation, the latter also being referred to as the Burger's equation.

A.1 General Derivation of the Method of Characteristics

The main idea behind the MOC is that each system governed by partial differential equations, either just one or a system of equations, possesses physical properties that are unique to these equations. From linear algebra we know that we can compute the eigenvalues and eigenvectors of a matrix which will give physical meaningful quantities, and a similar philosophy applies to the MOC. Take the advection equation, for example, which we will investigate in more detail in the following. It is written in general, 1D form as

$$\frac{\partial u}{\partial t} + \phi \frac{\partial u}{\partial x} = 0. \tag{A.1.1}$$

Here we have introduced ϕ as either linear ($\phi = a = const.$) or non-linear ($\phi = u(x,t) \neq const.$). If we use the linear coefficient a and provide an initial profile for u, then the profile for u will just get advected with the speed a in the positive or negative x-direction, depending on the sign of a. Similarly, if we use $\phi = u(x,t)$ instead, our initial profile would get advected with the local speed u and further the shape of the initial profile of u may change and form discontinuities. For simplicity we will stick with a for the moment. We could say that the physical properties of Eq.(A.1.1) is that any initial profile of u will simply get advected with speed a. This is demonstrated in Figure A.1. The arbitrary profile of u at t_0 is getting advected until a time t_1 and travels a distance $a(t_1 - t_0)$. If we follow a specific point on our

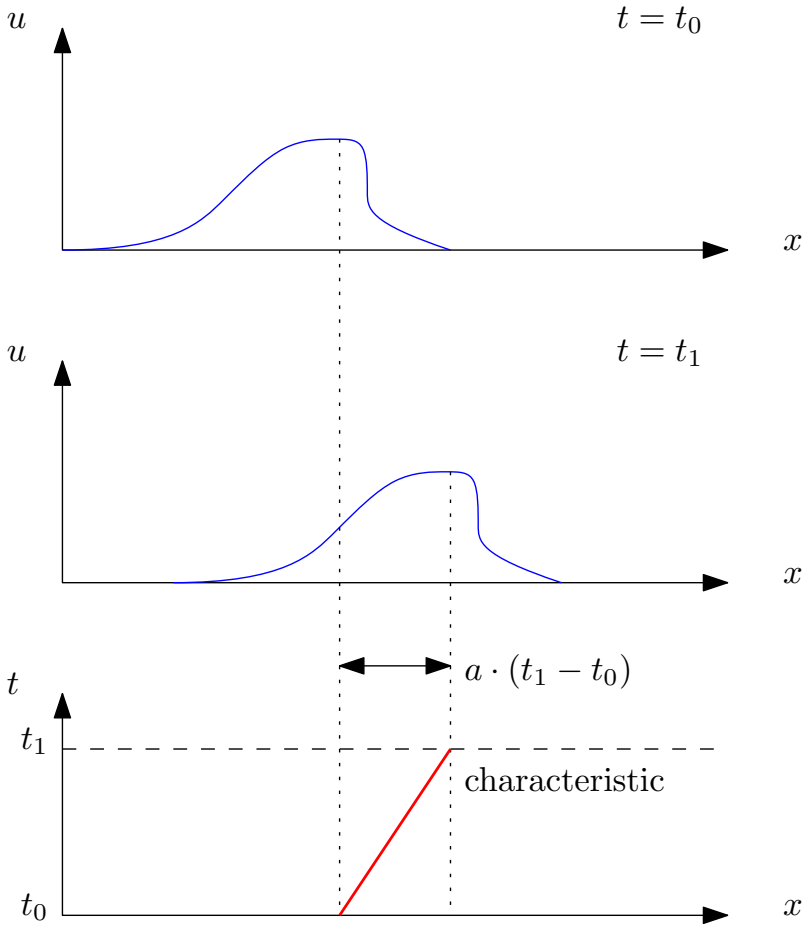

Figure A.1: Advection of the initial profile of u and the transformation from the u, x into the t, x space.

profile of u, say the peak as shown in Figure A.1, then we can follow the advection of the peak instead of the whole profile of u in time. We can show this by going from the u, x space into the t, x space and see that the peak is following a linear curve, as we would expect, which depends on the advection speed a. This line, shown here in red, is referred to as the characteristic curve. We could follow any other point on the profile of u, not just the peak and we would get the advected profile of u at an arbitrary time t_x. In this way we could obtain the solution at any point in time without having to perform any descritisation of Eq.(A.1.1).
This serves as a physical interpretation, but we need to develop the mathematical tools to apply the MOC to any general partial differential equation. In the following we will do so for the general advection equation.

A.2 Derivation based on the Advection Equation

The main idea of the MOC was developed in the previous section. We have characteristic curves in the physical space along which our solution (here the advection of the initial profile of u) changes according to the eigenstructure of the partial differential equation we are looking at. In case of the linear advection equation,

the initial profile did not change across our characteristic curve and was advected with a constant speed of a. Generally speaking, this does not need to be the case and the profile may change along the characteristic. The equation, which is valid along the characteristic curve is called the compatibility equation and is unique for each characteristic. The mathematical constraint of the characteristic is, that the function (here u) is continuous along the characteristic and the derivative of it *may* be discontinuous. In order to put this into a mathematical constraint, we need to find a system of equations to represent Eq.(A.1.1) in terms of its derivatives. We see that we have partial derivatives with respect to time and space. We can construct a second equation based on the total derivative as

$$du = \frac{\partial u}{\partial t}\mathrm{d}t + \frac{\partial u}{\partial x}\mathrm{d}x. \tag{A.2.1}$$

With Eq.(A.1.1) and Eq.(A.2.1), we express the system in matrix form as

$$\begin{bmatrix} 1 & \phi \\ \mathrm{d}t & \mathrm{d}x \end{bmatrix} \cdot \begin{bmatrix} u_t \\ u_x \end{bmatrix} = \begin{bmatrix} 0 \\ \mathrm{d}u \end{bmatrix}, \tag{A.2.2}$$

where we introduced the shorthand notation u_t and u_x for the partial time and space derivative, respectively. We have separated the derivatives from the coefficients, now we can apply the idea of the MOC. Solving the system for u_t via Cramer's rule we get

$$u_t = \frac{\begin{vmatrix} 0 & \phi \\ \mathrm{d}u & \mathrm{d}x \end{vmatrix}}{\begin{vmatrix} 1 & \phi \\ \mathrm{d}t & \mathrm{d}x \end{vmatrix}} = \frac{-\mathrm{d}u\phi}{\mathrm{d}x - \mathrm{d}t\phi} \tag{A.2.3}$$

and

$$u_x = \frac{\begin{vmatrix} 1 & 0 \\ \mathrm{d}t & \mathrm{d}u \end{vmatrix}}{\begin{vmatrix} 1 & \phi \\ \mathrm{d}t & \mathrm{d}x \end{vmatrix}} = \frac{\mathrm{d}u}{\mathrm{d}x - \mathrm{d}t\phi} \tag{A.2.4}$$

for u_x. Since we stated that the derivative *may* be discontinuous, the denominator of Eq.(A.2.3) and Eq.(A.2.4) has to become zero, and therefore, the numerator has to be zero as well. The numerator has to be zero in order to keep the derivative finite. The characteristic equation is obtained from the denominator while the compatibility equation is derived from the numerator. Therefore, we have for the characteristic equation

$$\mathrm{d}x - \phi\mathrm{d}t = 0. \tag{A.2.5}$$

After separating the variables, we have

$$\mathrm{d}x = \phi\mathrm{d}t. \tag{A.2.6}$$

Integrating yields

$$x = \phi t + C_1 \tag{A.2.7}$$

and the integration constant C_1 is obtained from data at the previous timestep (or initial conditions at the first timestep). Lets return to Section A.1, where we obtained the characteristic equation of the advection equation by physical arguments as $a(t_1 - t_0)$. Let us set $t_0 = 0$ and drop the subscript, then we have for the characteristic $x = at$. Let us insert a for ϕ in Eq.(A.2.7) and for the sake of argument assume that $C_1 = 0$, then we have $x_{char} = at$, which is what we obtained from physical reasoning. Also note that the characteristic equation for x_{char} can be obtained from both Eq.(A.2.3) and Eq.(A.2.4). The compatibility equation is obtained as well from both equations and we have from Eq.(A.2.3)

$$-\mathrm{d}u\phi = 0. \tag{A.2.8}$$

Divide by $(-1)\phi$ and integrate to obtain

$$u = C_2. \tag{A.2.9}$$

Eq.(A.2.9) is the general compatibility equation. From Eq.(A.2.4) we see that we would end up with the same compatibility equation if we were to derive it from the solution of u_x. The only thing left to do is to obtain values for C_1 and C_2 and we can solve Eq.(A.1.1). Before we do that, there are two comments in order. First, only hyperbolic partial differential equations can be used in conjunction with the MOC. Hyperbolic equations have the properties that its eigenvalues are all real and distinct. Non-hyperbolic equations result in complex eigenvalues and thus complex characteristics for which this method cannot be applied. Secondly, have a look at Eq.(A.2.5). We could also write this equation as

$$\frac{\mathrm{d}x}{\mathrm{d}t} = \phi. \tag{A.2.10}$$

Commonly it is said that the MOC transforms a system of *partial* differential equations (PDEs) into a system of *ordinary* differential equations (ODEs) which we can solve analytically. However, the compatibility equation, in general, changes along the characteristic and therefore we have to obtain a new compatibility equation at each timestep where a solution is sought. The MOC can thus be regarded as a semi-analytic solution.
Let us now return to a general approach to obtain the coefficients C_1 and C_2.

A.3 General Procedure to Obtain the Integration Constants

We assume the general advection equation (ϕ) for this example as we already have derived the characteristic equation, Eq.(A.2.7), and the compatibility equation, Eq.(A.2.9), previously. We need initial data to solve the PDE and lets simply assume that we have a profile of

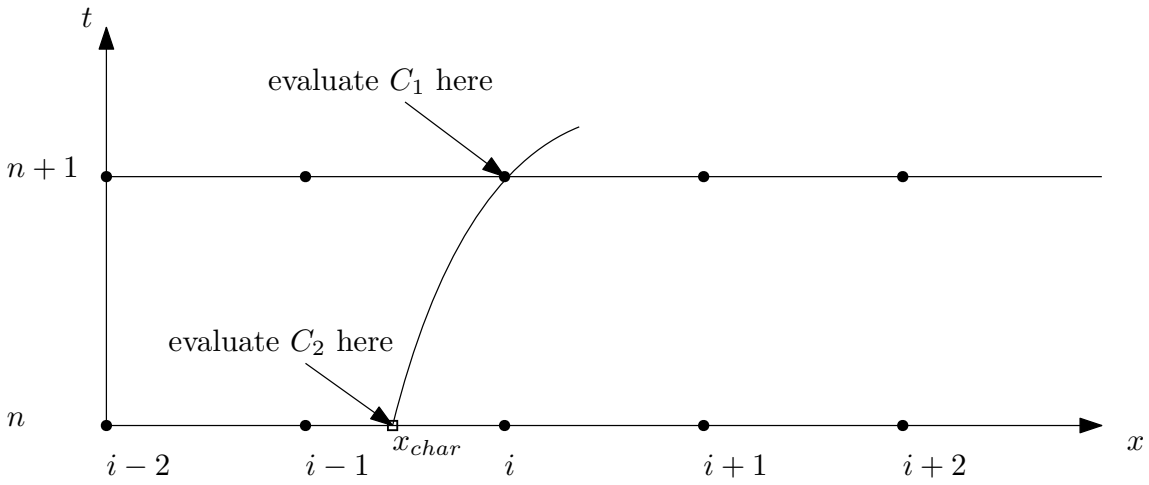

Figure A.2: Schematic showing how to evaluate the integration constants C_1 and C_2 along the characteristics.

$$u(x,0) = \sin(x) \tag{A.3.1}$$

at time $t = 0$. The general procedure is as follows:

1. Solve for C_1: Eq.(A.2.7) is solved for the integration constant and we have

$$C_1 = x - at. \tag{A.3.2}$$

   The location x is the position at which we want to to evaluate C_1 at the next time level, i.e. x_i^{n+1}. The product at can be expressed as $a(t^{n+1} - t^n)$ which simplifies to $a\Delta t$.

2. Insert C_1: We now substitute Eq.(A.3.2) back into Eq.(A.2.7) and obtain

$$x_{char} = at + C_1. \tag{A.3.3}$$

   Note that x_{char} is the intersection of the characteristic line with the x-axis. Thus, since the x-axis intersects the t-axis at $t = 0$, the above simplifies to $x_{char} = a \cdot 0 + C_1 = C_1$.

3. Obtain C2: We need to obtain the value for C2 from the initial data. We can do that because C2 is the integration constant of the compatibility equation which is, per definition, valid along the characteristic. Therefore, we can evaluate it at any point along that curve and have

$$C2 = u(x_{char}, t^n). \tag{A.3.4}$$

   Usually, we do not have data available for u at x_{char} and need to obtain values for u through interpolation from neighbouring points. Since u itself is simply the integration constant itself, we have found the solution at the next time level t^{n+1} and can iterate through time.

The procedure detailed above is shown schematically in Figure A.2. A matlab code is given which demonstrates the above for the general advection equation which can solve both the linear and non-linear case.

A.4 A Matlab Script for the Method of Characteristics

```
%==========================================================================
%
% The Method of Characteristics applied to the linear and non-linear
% advection equation in 1D.
%
% Tom-Robin Teschner, 2016, Cranfield Univeristy, UK
%
%==========================================================================

clear;
clc;
close all;

% number of points
n = 101;

% start and end of domain, start cannot be lower than zero
d_sta = 0;
d_end = 4*pi;

% time step
CFL = 1.0;
dt  = CFL*(d_end-d_sta)/(n-1);
tt  = 22;

% equation type, 1: linear, 2: non-linear
linear = 1;

% advection speed if linear equation is used
a = 1;

% 1D (line) domain
x = linspace(d_sta, d_end, n);

% initial profile for function
u = zeros(1,n);
  for i=1:n
u(i) = sin(x(i));
end

% initial value for advection speed, if linear, it is constant
phi = zeros(1,n);

if(linear == 1)
  phi(:) = a;
else
  phi = u;
end

% integration constants C1 and C2
C1 = zeros(1,n);
C2 = zeros(1,n);
```

```
53
54 %% main loop, use method of characteristics to advance in time
55 for t=1:tt
56
57 %=========================================================================
58 % 1: obtain C1 for the characteristic equation x = phi*t + C1 by
59 %    advancing in time by dt => C1 = x - phi*dt
60 %=========================================================================
61
62   for i=1:n
63     C1(i) = x(i) - phi(i)*dt;
64   end
65
66 %=========================================================================
67 % 2: obtain the location x at the previous time level t. Find closest
68 %    location in x array and linearly interpolate u to this position.
69 %    The compatibility equation is constant in this case and
70 %    corresponds to u = C2, therefore, we have u_char = C2
71 %=========================================================================
72
73   for i=1:n
74     x_char = C1(i);  % characteristic equation
75   if(x_char<d_sta) % periodic boundary conditions
76     x_char = x_char + d_end-d_sta;
77   elseif(x_char>d_end)
78     x_char = x_char - d_end-d_sta;
79   end
80
81   [~,j] = min(abs(x-x_char)); % find closest value of x_char in x
82   if(sign(x_char-x(j))>0) % right sided interpolation
83     u_char = interp1([x(j) x(j+1)],[u(j) u(j+1)],x_char);
84   elseif(sign(x_char-x(j))<0) % left sided interpolation
85     u_char = interp1([x(j) x(j-1)],[u(j) u(j-1)],x_char);
86   elseif(x_char == x(j))
87     u_char = u(j);
88   end
89     C2(i) = u_char;
90   end
91
92 %=========================================================================
93 % 3: update the solution at the next timelevel from the compatibility
94 %    equation. Therefore the new value for u will be u = C2
95 %=========================================================================
96   u(:) = C2(:); % compatibility equation
97
98   if(linear == 2) % update phi
99     phi(:) = u(:);
100  end
101 %=========================================================================
102 % 4: plot the solution
103 %=========================================================================
104   plot(x,u)
105   pause(0.1)
106 end
```